Autonomous Sun-Direction Estimation Using Partially Underdetermined Coarse Sun Sensor Configurations

by

Stephen A. O'Keefe

B.S., Georgia Institute of Technology, 2006

M.S., University of Colorado, 2012

A thesis submitted to the

Faculty of the Graduate School of the

University of Colorado in partial fulfillment

of the requirements for the degree of

Doctor of Philosophy

Department of Aerospace Engineering Sciences

2015

This thesis entitled:
Autonomous Sun-Direction Estimation Using Partially Underdetermined Coarse Sun Sensor Configurations
written by Stephen A. O'Keefe
has been approved for the Department of Aerospace Engineering Sciences

_____
Prof. Hanspeter Schaub

_____
Prof. Penina Axelrad

_____
Prof. Nikolaus Correll

_____
Prof. Brandon Jones

_____
Prof. Jay McMahon

Date _____

The final copy of this thesis has been examined by the signatories, and we find that both the content and the form meet acceptable presentation standards of scholarly work in the above mentioned discipline.

O'Keefe, Stephen A. (Ph.D., Aerospace Engineering Sciences)

Autonomous Sun-Direction Estimation Using Partially Underdetermined Coarse Sun Sensor Configurations

Thesis directed by Prof. Hanspeter Schaub

In recent years there has been a significant increase in interest in smaller satellites as lower cost alternatives to traditional satellites, particularly with the rise in popularity of the CubeSat. Due to stringent mass, size, and often budget constraints, these small satellites rely on making the most of inexpensive hardware components and sensors, such as coarse sun sensors (CSS) and magnetometers. More expensive high-accuracy sun sensors often combine multiple measurements, and use specialized electronics, to deterministically solve for the direction of the Sun. Alternatively, cosine-type CSS output a voltage relative to the input light and are attractive due to their very low cost, simplicity to manufacture, small size, and minimal power consumption. This research investigates using coarse sun sensors for performing robust attitude estimation in order to point a spacecraft at the Sun after deployment from a launch vehicle, or following a system fault.

As an alternative to using a large number of sensors, this thesis explores sun-direction estimation techniques with low computational costs that function well with underdetermined sets of CSS. Single-point estimators are coupled with simultaneous nonlinear control to achieve sun-pointing within a small percentage of a single orbit despite the partially underdetermined nature of the sensor suite. Leveraging an extensive analysis of the sensor models involved, sequential filtering techniques are shown to be capable of estimating the sun-direction to within a few degrees, with no a priori attitude information and using only CSS, despite the significant noise and biases present in the system. Detailed numerical simulations are used to compare and contrast the performance of the five different estimation techniques, with and without rate gyro measurements, their sensitivity to rate gyro accuracy, and their computation time.

One of the key concerns with reducing the number of CSS is sensor degradation and failure. In this thesis, a Modified Rodrigues Parameter based CSS calibration filter suitable for autonomous on-board operation is developed. The sensitivity of this method's accuracy to the available Earth albedo data is evaluated and compared to the required computational effort. The calibration filter is expanded to perform sensor fault detection, and promising results are shown for reduced resolution albedo models. All of the methods discussed provide alternative attitude, determination, and control system algorithms for small satellite missions looking to use inexpensive, small sensors due to size, power, or budget limitations.

Dedication

To Cheryl, for everything.

To the computers who worked even longer hours than I stoically performing all the Monte Carlo analyses I asked of them, especially the one that sacrificed its motherboard in the process.

Acknowledgements

I would like to express my deepest appreciation and gratitude to my advisor Dr. Hanspeter Schaub. He has continually believed in me, pushed me, and helped me grow both academically and personally. Without his guidance and persistent help this dissertation would not have been possible. Thank you also to the rest of my committee: Dr. Penina Axelrad, Dr. Nikolaus Correll, Dr. Brandon Jones (particularly for contributions regarding consider filters), and Dr. Jay McMahon.

While at the University of Colorado several professors have been especially kind offering guidance and mentoring with regards to academics, teaching, and research: thank you to Dr. Penina Axelrad, Dr. Jay McMahon, and Dr. Jeff Parker. Thank you to my colleagues in the Autonomous Vehicle Systems Laboratory: Lee Jasper, Erik Hogan, Paul Anderson, Trevor Bennett, Patrick Kenneally, and everyone else, for the feedback and insightful ideas.

A special thanks goes to my parents, Randy and Mary Lee, who always encouraged me to follow my dreams and, amongst innumerable other things, listened to me on many late nights despite the timezone difference. Finally, I would like to thank my girlfriend, Cheryl, who overcame my obliviousness, has proved to be a fountain of constant support and encouragement, and learned more about astrodynamics than she ever wanted. This thesis would have been immensely more difficult without you and your loving support.

This research was supported through several teaching assistantships generously provided by the Department of Aerospace Engineering Sciences, a research assistantship with the Laboratory for Atmospheric and Space Physics (LASP), and the Graduate Assistance in Areas of National Need (GAANN) fellowship.

Contents

Chapter

Tables

Table

Figures

Figure

Chapter 1

Introduction

1.1 Background and Motivation

A key function of satellite attitude, determination, and control systems (ADCS) is to provide a sun-pointing, or safe, mode. This mode is designed to successfully advance the spacecraft to nominal operation, following separation from a launch vehicle, by maneuvering to a power positive orientation, and to function as a safe mode to revert to in the event of a fault or failure. The ADCS must, therefore, be capable of quickly and robustly pointing the solar arrays at the Sun and maintaining power positiveness from any initial orientation, with no prior knowledge of attitude, in the presence of potentially large angular rates due to launch vehicle separation or other ADCS faults.

In recent years there has been a significant increase in interest in smaller satellites as a lower cost alternative to traditional satellites. From largest to smallest mass, these new classes of satellites are generally referred to as minisatellites, 500 kg to 100 kg, microsatellites, 100 kg to 10 kg, nanosatellites, 10 kg to 1 kg, and picosatellites, 1 kg to 0.1 kg. These satellites are commonly used for educational purposes or as technology demonstrators, but they have been identified as excellent candidates for distributed sensing and formation flying opportunities. While some systems, such as command and data handling and electrical power systems, have benefited from advances in commercial electronics, there has been a lag in the development of attitude control subsystems[1].

One of the reasons for the rise of small satellites is the definition of the CubeSat standard. CubeSats, or 10 cm cube satellites weighing less than 1.33 kg, were originally proposed by Profes-

sor Robert Twiggs of Stanford University and Professors Jordi Puig-Suari and Clarke Turner of California Polytechnic State University as a means of reducing satellite costs to enable academic participation in space science[2]. These nanosatellites have garnered international interest and approximately one hundred have been launched by universities, research institutes, and commercial entities with several demonstrating active ADCS. Due to stringent mass, size, and often budget constraints placed on these satellites, they typically rely on simple sensor hardware, such as coarse sun sensors (CSS) and magnetometers. In addition, with limited size and space for batteries, it is even more important for actively controlled small satellites to have a reliable method for determining the sun-direction and achieving sun-pointing following deployment from a launch vehicle.

CubeSats are not alone in their need of improved attitude, determination, and control subsystems. The FORMOSAT-3/COSMIC (Constellation Observing System for Meteorology, Ionosphere, and Climate) mission consists of six low Earth orbiting microsatellites launched jointly by the United States and Taiwan in 2006 to study the Earth's atmosphere using radio occultation (RO) measurements from Global Positioning System (GPS) satellites[3]. COSMIC provides data to over 1000 users worldwide for weather prediction and climate modeling. COSMIC has been highly successful, but some of the key spacecraft system lessons learned highlight the difficulties and importance of a robust sun-pointing mode: the satellites are equipped with no angular rate sensors and the sun-direction algorithm on board periodically generates poor estimates[4].

Literature on the use of coarse sun sensors for sun-direction estimation, sun acquisition, attitude control, or the on-orbit calibration of such sensors is sparse with most devoted to the use of more expensive and complicated digital sun sensors[5,6]. This research aims to investigate the use of inexpensive cosine-type coarse sun sensors and explores methods for sun-direction estimation, coupled with simultaneous attitude control, an important aspect of attitude, determination, and control systems, using partially underdetermined sets of CSS. Ideally, the sun direction can be uniquely determined at a given time for a spacecraft if three or more CSS measurements are available. For this research, an underdetermined sensor set is one for which there are spacecraft attitudes where the sun direction cannot be uniquely determined due to an insufficient number of sensors. In

addition, methods for performing autonomous calibration and fault detection of coarse sun sensors are investigated. Emphasis is placed on balancing accuracy with computational costs to improve autonomy and reduce ground testing and support costs.

1.2 Previous Work

As mentioned earlier, the literature on the use of cosine-type coarse sun sensors for performing sun-direction estimation, on-orbit calibration, and fault detection is limited. While it is known these sensors are flown in space, the relative cost savings of using analog sun sensors, as opposed to digital sensors, is not as important to large corporate satellites as it is to low-budget spacecraft produced in academia. An overview of previous research in the relevant aspects of sun sensors, based attitude estimation, on-orbit calibration, and fault detection is presented.

1.2.1 Coarse Sun Sensors

Spacecraft commonly use a number of sun sensors to determine the sun-direction vector in the body frame. There are two general types of sun sensors used: digital two-axis sensors and coarse analog cosine-type sensors. Digital two-axis sensors combine two or more image sensors and processing electronics into a single package that provides a complete sun vector. Coarse analog cosine-type sensors are composed of photodiodes with glass covers for filtering out undesired wavelengths, and optional baffles used for restricting the sensor's field of view, and return a scalar measurement.

Digital sun sensors are more expensive and complicated than analog sensors and an area of research unto themselves. These sensors often use an optical mask to filter incoming light onto linear-array-charge-couple-devices (linear CCDs)[7] or high-accuracy complementary metal-oxide-semiconductor (CMOS) active pixel sensors (APS)[8,9]. Using the geometry of the optical mask, incoming irradiance is confined to a specific area on the CCD and the incidence angle of the incoming ray is reconstructed. Multiple CCDs are usually incorporated into a single sensor package to provide a vector sun-direction measurement when the Sun is in view of the spacecraft. These sensors must often trade between field of view and accuracy due to the resolution available on the detector[10].

Current research into improving accuracy, while reducing the size of these devices, includes using miniaturized silicon photodiodes[11], high-accuracy complementary metal-oxide-semiconductors (CMOS)[8], and N-shaped slit masks[9].

Alternatively, analog cosine-type CSS are simply photodiodes that output a voltage proportional to the input irradiance. Digital sensors are capable of producing much higher accuracy estimates of the sun-direction than analog sensors, but do have several disadvantages. While research is ongoing to reduce the power consumption of digital sun sensors[12], power is still required to run their specialized electronics, and they must be coupled with on-board electronics to produce an estimate of the spacecraft's attitude. In addition, they are significantly more expensive than analog devices. This research focuses on using analog sun sensors because of their inexpensiveness, small size, and minimal power consumption. The algorithms investigated are advantageous for small satellite platforms because they reduce costs by incorporating the processing of measurements directly into the attitude estimation algorithms.

Sun sensors are sensitive to any light and in orbit the most significant light source, other than direct sunlight, is light from the Sun diffusely reflected by the Earth. NASA has published models for Earth's albedo[13] and its Total Ozone Mapping Spectrometer (TOMS) mission generated a wealth of data on Earth's reflectivity. More recently, Bhanderi looked extensively at modeling Earth's albedo with regards to coarse sun sensor observations and validating such models against flight data[14,15]. Research has been devoted to approximating the reflectivity of the Earth with a latitude dependent polynomial fit to reduce memory requirements[16].

Digital sun sensors use geometry of incoming light and order of magnitude thresholding to reject light due to albedo. Because Earth's albedo can account for significant amount of the input to analog coarse sun sensors, and accounting for Earth's albedo requires knowledge of the relative positions of the Sun, the Earth, and the satellite, analog sensors are often overlooked. This research shows how coarse sun sensors can be used without an on-board albedo model to achieve sun-direction accurate to a few degrees and autonomous on-orbit calibration.

Because CSS are relatively inexpensive, it is not uncommon for spacecraft to place a multitude of sensors around the exterior to achieve the coverage required for determining the sun direction geometrically. For example, RAX-2, a 3U CubeSat, is equipped with 17 coarse sun sensors[5]. The addition of so many sensors to the spacecraft is not without hazards. The fields of view of the CSS can become blocked by other instrumentation, the CSS can interfere with other payloads, cabling must be routed for all sensors, and extra sensors require additional testing time and complexity. The placement of these sensors is generally an iterative process based on experience and prior designs, but can be optimized to maximize redundant coverage[17] or minimize the angular uncertainty of the resulting sun vector estimate when three sensor coverage is available globally[18]. These approaches include methods to weight the solution to account for mission objectives and payload interference, but do not address, as this research aims to, what to do when the Sun is only observed by two or fewer sensors.

1.2.2 Sun Sensor Based Attitude Estimation

When using digital sun sensors, the output sun-direction observation is often combined with other vector observations, such as magnetometer readings[19], to solve for the true sun direction deterministically. Many methods exist for performing attitude estimation through the use of weighted vector observations. In particular, a large number of methods pose the attitude estimation problem as a quadratic cost function and use the optimality criteria introduced by Wahba[20]. Examples of this approach include Davenport's Q-Method[21], QUEST[22], and FOAM[23]. Alternatively, the TRIAD method[24] solves for an attitude deterministically using two measurements and reference vectors and the Optimal Linear Attitude Estimator (OLAE)[25] proposed by Mortari, Markley, and Singla uses the the Gibbs vector and the Cayley transformation. Satellite missions that use such methods include the Thrusted Vector Mission[26] and COMPASS-1[27].

With cosine-type CSS no vector observations are available, only scalar measurements proportional to the angle of incidence of the incoming light. Thus, the sun-direction vector must be determined through other means such as geometric methods or statistical filtering algorithms. A

spacecraft's attitude can generally be determined geometrically at any time if the Sun is simultaneously in the field of view of at least three CSS; a more reliable estimate is found if continuous 4π steradian coverage is achieved by a minimum of four sensors. Statistical filtering algorithms provide an estimate of the spacecraft's attitude based on a collection of measurements over time. In particular, sequential filtering algorithms process measurements as soon as they are received and are commonly derived from the Kalman filter[28] which produces a statistically optimal estimate for linear systems. The most popular non-linear variant used on spacecraft is the extended Kalman filter (EKF) which linearizes the nonlinear system about the current estimate.

Small satellite missions that have used an EKF for attitude estimation include HokieSat[29], CanX-2[30], and RAX[31]. Both HokieSat and CanX-2 performed attitude estimation in real-time on-board the spacecraft while RAX reconstructed its attitude using ground software. These missions, along with COMPASS-1, all performed full attitude estimation; i.e. determining the absolute attitude of the spacecraft relative to a reference frame. Unfortunately, such estimation requires knowledge of reference vectors, for example an inertial sun direction or the orientation of the local Earth magnetic field, and calculation of such reference vectors requires information about the satellite's orbital position and the current time. While this information can be acquired through GPS receivers or ground uploaded tracking data, this research investigates methods that do not require this information.

The use of coarse sun sensors provides interesting challenges. Because of the significant noise and biases present in cosine-type coarse sun sensor measurements they do not traditionally work well with linear estimation techniques such as the Kalman filter. However, fully nonlinear filters, for example the unscented Kalman filter[32] and divided difference filters[33], take significantly more computational power or time to evaluate[34] and are not well suited for real time operation on low-budget spacecraft. Alternatively, the Kalman filter can be transformed into a consider filter to better compensate for the the impact of biases on the state estimate. Initially presented by Schmidt[35], other derivations of the Consider Kalman Filter have been published by Friedland[36], Jazwinski[37]; Tapley, Shutz, and Born[38]; Woodbury and Junkins[39]; and Zanetti and Bishop[40]. The use of a

consider Kalman filter estimation strategy is investigated here, and while it does offer more rigorous treatment of the biases present in the system, it too suffers from increased computational needs as compared to a traditional EKF.

Sequential estimation algorithms, like the Kalman filter, require an angular rate measurement to propagate the spacecraft attitude between measurement updates. Most often these measurements come from a rate gyro, but in the extreme the rate gyro may fail or power critical situations may require it to be turned off. For HokieSat, a Virginia Tech student built satellite, the rate gyro consumed 24 % of the available system power[29]. When their rate gyro needs to be turned off they use a method proposed by Bar-Itzhack and Oshman that generates an estimate of the quaternion of rotation based on pairs of measured vectors[41]. Tsao and Chiang examine gyroless estimation using only sun sensors, but they require knowledge of the spacecraft's momentum vector in inertial space, and in estimating the spacecraft's inertial attitude they end up with a highly nonlinear problem that must be estimated using an unscented Kalman filter[42]. Alternatively, deterministic attitude estimation can be performed using only geomagnetic-field measurements[43]. This research shows how even a simple rate estimate based on successive sun-direction estimates is sufficient when performing simultaneous coarse sun-direction estimation and control.

1.2.3 On-Orbit Calibration

Previous spacecraft missions have shown that coarse sun sensors have the potential to significantly degrade over time[44]. Because the sun-pointing mode of an ADCS is not only used at the onset of a mission, but in the event of a fault, having the ability to calibrate sensors on-orbit greatly improves the effectiveness of the ADCS over the lifetime of a satellite. Significant literature is available on the calibration of attitude sensors and rate gyros[45,46], but little is published specifically pertaining to the calibration of coarse sun sensors. Ortega, López-Rodríguez, et. al., and Wu and Steyn both present calibration of two-axis sun sensors specific to an individual model[11,47]. Springmann examines the use of a quaternion-based EKF to calibrate coarse sun sensors, but all analysis is done through post-processing using ground based assets[5]. This research examines a Modified

Rodrigues Parameter (MRP) EKF based approach that is general to any cosine-type coarse sun sensor and presents the trade offs that can be made between accuracy and computational costs.

1.2.4 Fault Detection

A primary concern when using an underdetermined set of coarse sun sensors is the system's robustness to sensor failure or fault. Sensor failure in an underdetermined configuration of CSS can easily lead to the Sun being unobserved by all sensors, and while methods can be developed to handle these situations, the sensor failure must first be detected. Sensor faults are malfunctions of the sensor, or its controlling electronics, that lead to unacceptable anomalies in the state estimation. Fault and failure detection of coarse sun sensors is made difficult because null measurements are regular and routine, both when a sensor is pointed into deep space and when the spacecraft is in the shadow of the Earth, and significant noise is present in CSS measurements.

Considerable literature is available on fault detection. Frank[48], and more recently Betta and Pietrosanto[49], provide surveys of instrument fault detection and isolation, and Isermann provides overviews of model based fault detection and its application to machine tools[50,51]. Fault detection is often classified into two main groups: analytical and physical. Analytical fault detection uses mathematical models to determine if an anomaly has occurred, whereas mechanical or physical redundancy fault detection uses duplicate sensors to compare and detect malfunctions. As this research is interested in reducing sensor requirements, as opposed to adding more sensors for redundancy, analytical detection is considered.

Betta and Pietrodanto further classify analytical redundancy-based fault detection into methods focused on instruments: parity relations and Kalman filters; and methods focused on system modeling techniques: artificial neural networks, genetic algorithms, and Bayesian networks[49]. One system modeling technique, Finite Set Statistics (FISST), has gained popularity in applications of multi-target tracking and detection, and recent work has shown that FISST can be applied to Bayesian estimation filters[52] to estimate continuous and discrete random variables simultaneously[53]. This approach has promise, particularly due to its ability to estimate continuous and

discrete variables simultaneously; however, this approach, and those of neural networks and genetic algorithms, require significant computational power and are excessive for this application. A Kalman filter based instrument fault detection approach is used as it represents a logical expansion to the sun-direction estimation and CSS calibration filters developed.

Previous ADCS fault detection research has focused on performing statistical tests on the residuals of one or more sequential filters[54,55]. For nonlinear problems the use of an extended Kalman filter approach tends to suffer from poor detection or high false alarm rates[56]. Methods proposed for dealing with nonlinear problems include using the residuals of multiple nonlinear predictive filters[57], using the residuals of an unscented Kalman filter[58], and using multiple hypothesis tests using multiple EKFs operating on subsets of the available sensor data[59]. An innovations test based approach is used here as it is shown through use of detailed measurement models to accurately detect sensor failure without adding significant computational burden.

1.3 Research Overview

This research investigates using coarse sun sensors, due to budget, power, and size, for performing robust attitude estimation in order to point a spacecraft at the Sun after deployment from a launch vehicle or following a system fault. As noted earlier, the size and cost requirements of increasingly popular small satellites are a driving factor for making the most of small inexpensive sensors, and while there is significant research into improving sun sensors, investigation into maximizing the performance of existing sensors is needed. This work looks to address the following questions regarding the use of coarse sun sensors in attitude determination and control:

(1) How can spacecraft achieve required ADCS performance within the budget and computational constraints imposed on small satellites?

(2) Is it necessary to have complete coarse sun sensor coverage to perform sun-direction estimation or might it be done using underdetermined sets of sensors?

(3) Can sun-direction estimation be performed using only cosine-type coarse sun sensors?

(4) What is the minimum amount of information necessary to perform coarse sun sensor calibration and fault detection autonomously on-orbit?

This research will explore using inexpensive, analog, cosine-type CSS and making improvements to sun-direction estimation, autonomy, and robustness that will reduce satellite life-cycle costs. Work will be focused in three main tasks: simulation, estimation, and autonomy and robustness. The first task focuses on creating a simulation framework and sensor models to accurately simulate spacecraft ADCS operations. The second task applies estimation theory to determining the sun-direction using underdetermined sets of coarse sun sensors. Finally, the third task seeks to identify ways in which spacecraft autonomy can be increased to reduce ground support costs. The scope of these three areas is described below.

1.3.1 Simulation

Due to the high cost of launching and operating satellites, even relatively low-cost CubeSats, it is important to be able to develop flight algorithms efficiently. To accomplish this numerical simulations are often used; however, the simulations and models must be accurate enough to adequately simulate reality. This research will examine in detail, and validate through experimental data, the sensor models of coarse sun sensors and rate gyroscopes. A numerical simulation framework capable of interfacing with testbed hardware, simulating flight hardware functionality, and performing Monte Carlo analysis will be developed. The main research tasks include:

(1) Develop a satellite simulation framework suitable for developing and testing spacecraft ADCS algorithms.

(2) Review and implement detailed coarse sun sensor model complete with Earth albedo effects.

(3) Model any additional significant coarse sun sensor error sources.

(4) Verify sensor models using experimental data.

1.3.2 Estimation

This research will closely examine situations where full three sensor coverage is partially unavailable and apply estimation theory to determine the attitude of a spacecraft. This is in contrast to previous sun sensor attitude estimation research, which has focused on using more expensive digital sun sensors that incorporate their own electronics, maximizing the steradian coverage by three or more sensors, or optimizing placement of sensors when using overdetermined sensor sets. Models for coarse sun sensor and satellite dynamics on-orbit will be implemented into a simulation framework for studying the performance of all estimation methods developed.

Single-point and sequential filter algorithms for estimating the sun direction will be reviewed, developed, and tested. Emphasis is placed on developing algorithms that are computationally efficient enough to run on small satellite hardware and fully understanding measurement errors, inconsistencies, and noise. The highly nonlinear nature of the system model, and the biases and significant noise present in coarse sun sensor measurements, makes this a challenging task because the algorithms are intended for low cost small satellite missions with strict computational requirements. These algorithms will use a novel approach that does not calculate a satellite's inertial attitude in order to reduce the dependence on ground communication and more complicated sensors. The methods developed here will be suitable for use as a baseline for lower budget missions or as a robust safe mode for nominally fully determined configurations that have suffered from multiple sensor failures. The main research tasks of this focus area include:

(1) Review and develop single-point and sequential sun-direction estimation strategies.

(2) Study performance of all estimation methods using partially underdetermined sensor sets.

(3) Investigate how rate gyroscope accuracy affects the performance of estimation approaches.

(4) Evaluate performance of estimation strategies when no angular rate measurements are available.

1.3.3 Autonomy & Robustness

Traditionally satellite's are designed with continuous coverage by three or more CSS which inherently provides redundancy. One of the key concerns with reducing the number of sensors is CSS failure. This research will investigate strategies for compensating for known sensor failures and methods for autonomously detecting sensor failures so these strategies can be implemented as needed. As noted earlier, there is significant research into autonomous fault detection in other industries, and significant ADCS research is devoted to creating more accurate nonlinear fault detection methods. In contrast, this research will focus on understanding sensor models in order to apply computationally simpler fault detection methods. The goals of this topic are:

(1) Develop Modified Rodrigues Parameter based coarse sun sensor calibration filter.

(2) Evaluate to what accuracy coarse sun sensor calibration scale factors can be estimated.

(3) Determine what resources are necessary to perform autonomous on-orbit calibration of sun sensors.

(4) Explore sensitivity of calibration filter to model uncertainties.

(5) Study performance of sun-direction estimation techniques when coarse sun sensors fail.

(6) Investigate methods with low computational costs for performing autonomous fault detection of coarse sun sensors.

Increasing ADCS autonomy through on-orbit calibration will help reduce operations costs by decreasing the ground support needed to perform attitude estimation throughout the lifetime of a mission in addition to reducing the pre-launch testing required to calibrate sensors.

Chapter 2

Sensor and Simulation Models

The algorithms presented in this work are developed and evaluated using numerical simulations, not flight data. Because of this, care has been taken to develop a numerical simulation framework that is a sufficiently accurate representation of reality. The simulation code developed for this work originally started as an attitude dynamics and control analysis tool for the Community Initiative for Continuous Earth Remote Observation (CICERO)[60] satellite developed by the Laboratory for Atmospheric and Space Physics (LASP) and simulates the dynamics of, and the sensor inputs received by, a satellite in a low Earth orbit. It also has the ability to simulate flight software timing, sensor communication and associated fault detection, and perform hardware in the loop testing. The key simulation models, for the CSS and rate gyro, and the basic simulation framework are described.

2.1 Coarse Sun Sensors

The low-cost cosine-type CSS used in this study are composed of photodiodes with a glass cover for filtering out undesired wavelengths and protecting against radiation damage. Optional baffles are added to the sensors to restrict their field of view. An example of an individual CSS is shown in Figure 2.1a, and a complete pyramid assembly with associated controlling electronics is shown in Figure 2.1b. The following sections describe the basic CSS measurement model, the measurement model modifications necessary to account for Earth's albedo, and finally a detailed CSS measurement model that takes into account sensor misalignments, noise, and calibration biases.

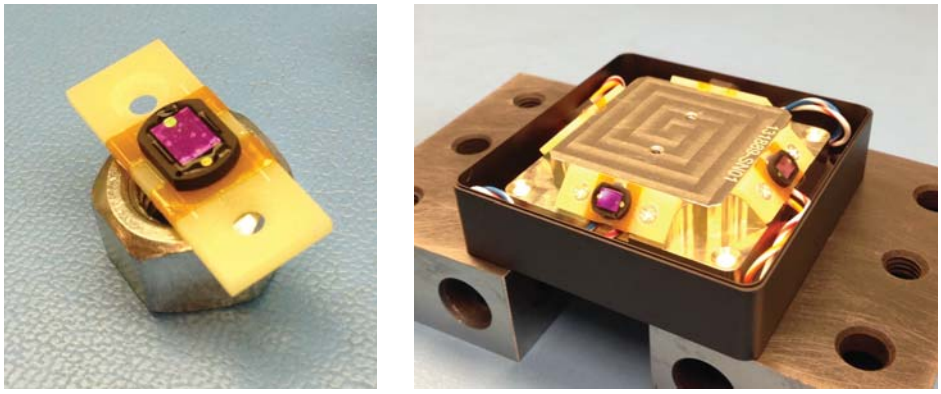

(a) Individual photodiode. (b) Photodiode pyramid assembly.

Figure 2.1: Photodiode and pyramid configuration of photodiodes complete with governing electronics.

2.1.1 Basic CSS Model

Assuming Lambert's cosine law, the solar flux F_d that impacts a CSS due to the direct solar flux of the Sun $F_\odot$ is given by[61]

$$F_d = F_\odot \left(\frac{\boldsymbol{n}^T \boldsymbol{s}}{\|\boldsymbol{n}\| \|\boldsymbol{s}\|} \right) \tag{2.1}$$

where $\boldsymbol{n}$ is the unit normal of the CSS, and $\boldsymbol{s}$ is the direction vector from the spacecraft to the Sun. An illustration of this model is shown in Figure 2.2 where θ is the angle between the CSS normal and the sun direction. It is assumed that that for any sun direction on the cone defined by θ the input flux is the same.

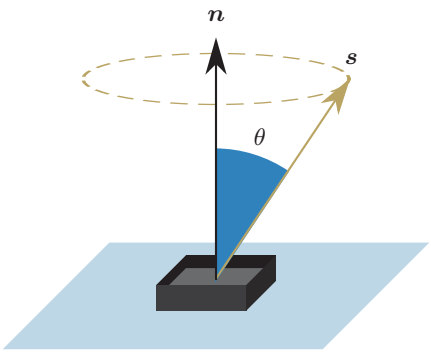

Figure 2.2: Illustration of basic CSS model geometry.

The output voltage of the CSS is assumed proportional to the input flux through the relation

$$V = C\left(\frac{\boldsymbol{n}^T\boldsymbol{s}}{\|\boldsymbol{n}\|\|\boldsymbol{s}\|}\right) \tag{2.2}$$

where the scale factor

$$C = \frac{V_{\max}}{F_{\text{cal}}}F_{\odot} \tag{2.3}$$

is determined during ground testing using a calibration flux, F_{cal} and the maximum voltage output of the CSS is given by $V_{\max}$. Ideally, the calibration flux will equal the flux due to direct sunlight on orbit $F_{\odot}$, but any ground-based testing of this calibration parameter for a particular CSS will have to account for atmospheric reduction of solar irradiance. While estimates are available for how much stronger the solar irradiance is in space, a sun-direction estimation algorithm that is insensitive to this calibration parameter will enable significantly simpler, and thus cheaper, CSS calibration and testing procedures.

2.1.2 Earth Albedo Model

Solar radiation that impacts the Earth is partially absorbed, partially specularly reflected, and partially diffusely reflected. Cosine-type CSS are sensitive to any light and on orbit the most significant light source other than direct sunlight is light from the Sun diffusely reflected by the Earth. Solar radiation that is absorbed by the Earth and later radiated at infrared wavelengths is easily filtered through mechanical means, while the energy due to specular reflectance is generally small and ignored[13].

Determining the output voltage of a CSS on a spacecraft due to Earth's albedo requires first determining the irradiance due to the diffuse reflectance of a differential area of the Earth. Consider the situation shown in Figure 2.3, where a spacecraft is located at point B with a CSS with unit normal $\boldsymbol{n}$; $\boldsymbol{s}$ is the direction vector from the spacecraft to the Sun; $\mathrm{d}A$ is a differential area on the surface of the Earth; $\boldsymbol{n}_A$ is the unit normal of $\mathrm{d}A$; $\boldsymbol{s}_{\oplus}$ is the unit direction vector from the Earth to the Sun; $\boldsymbol{r}_{AB}$ is a vector from $\mathrm{d}A$ to the body of the spacecraft; and α is the albedo, or reflectivity coefficient, of the differential area. The region of space in the Earth's shadow is defined as $\boldsymbol{\mathcal{S}}$. The

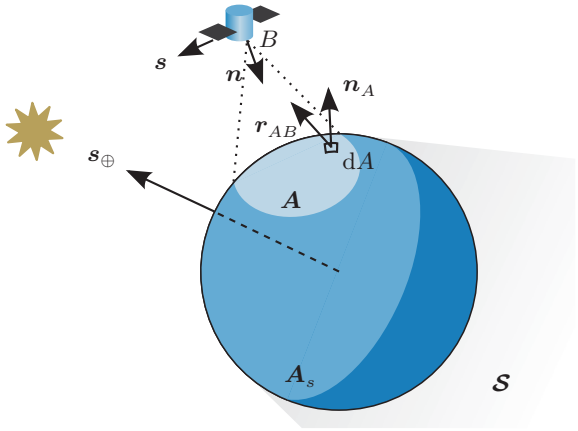

Figure 2.3: Illustration of Earth albedo geometry.

sunlit region of the Earth, $\boldsymbol{A}_s$, is defined by

$$\boldsymbol{A}_s \equiv \left\{ \mathrm{d}A : \boldsymbol{n}_A^T \boldsymbol{s}_\oplus > 0 \right\}. \tag{2.4}$$

The surface of the Earth visible to a CSS on the spacecraft, $\boldsymbol{A}_\psi$, is defined by

$$\boldsymbol{A}_\psi \equiv \left\{ \mathrm{d}A : \boldsymbol{n}_A^T \boldsymbol{r}_{AB} > 0 \ \wedge \ -\frac{\boldsymbol{n}^T \boldsymbol{r}_{AB}}{\|\boldsymbol{n}\| \|\boldsymbol{r}_{AB}\|} > \cos\psi \right\} \tag{2.5}$$

where ψ is the field of view half angle of the CSS. The surface of the Earth that is both sunlit and visible to the ith CSS on the spacecraft, $\boldsymbol{A}$, is defined as the intersection of these two regions

$$\boldsymbol{A} \equiv \boldsymbol{A}_s \cap \boldsymbol{A}_\psi. \tag{2.6}$$

The solar flux F_A^{in} at $\mathrm{d}A$ due to the solar irradiance in the vicinity of the Earth, assuming a Lambert's cosine law, is given by

$$F_A^{\text{in}} = F_\odot \left(\frac{\boldsymbol{n}_A^T \boldsymbol{s}_\oplus}{\|\boldsymbol{n}_A\| \|\boldsymbol{s}_\oplus\|} \right) \tag{2.7}$$

and the amount of irradiance that is reflected F_A^{out} is proportional to the albedo giving

$$\begin{aligned} F_A^{\text{out}} &= \alpha F_A^{\text{in}} \\ &= \alpha F_\odot \left(\frac{\boldsymbol{n}_A^T \boldsymbol{s}_\oplus}{\|\boldsymbol{n}_A\| \|\boldsymbol{s}_\oplus\|} \right). \end{aligned} \tag{2.8}$$

As the diffusely reflected irradiance F_A^{out} travels outward from $\mathrm{d}A$ its energy is distributed over a 2π steradian hemisphere $\mathcal{H}$. The total energy over $\mathcal{H}$ can be found using

$$E_{\mathcal{H}} = \int_0^{2\pi} \int_0^{\frac{\pi}{2}} \left(F_{\mathcal{H}_{\max}} \cos\theta \right) \left(r^2 \sin\theta \, \mathrm{d}\theta \, \mathrm{d}\phi \right) = F_{\mathcal{H}_{\max}} \pi r^2 \tag{2.9}$$

where $F_{\mathcal{H}_{\max}}$ is the maximum flux seen by the hemisphere due to the reflectance of $\mathrm{d}A$ and r is the radius of $\mathcal{H}$.

Using conservation of energy, the energy reflected by $\mathrm{d}A$, $F_A^{\text{out}} \, \mathrm{d}A$, can be related to the total energy spread out over this hemisphere $E_{\mathcal{H}}$. The quantity $F_{\mathcal{H}_{\max}}$ can then be solved for using Equation (2.8)

$$\begin{aligned} F_A^{\text{out}} \, \mathrm{d}A &= F_{\mathcal{H}_{\max}} \pi r^2 \\ \alpha F_{\odot} \left(\frac{\boldsymbol{n}_A^T \boldsymbol{s}_{\oplus}}{\|\boldsymbol{n}_A\| \|\boldsymbol{s}_{\oplus}\|} \right) \mathrm{d}A &= F_{\mathcal{H}_{\max}} \pi r^2 \\ F_{\mathcal{H}_{\max}} &= \frac{F_{\odot}}{\pi} \frac{\alpha}{r^2} \left(\frac{\boldsymbol{n}_A^T \boldsymbol{s}_{\oplus}}{\|\boldsymbol{n}_A\| \|\boldsymbol{s}_{\oplus}\|} \right) \mathrm{d}A. \end{aligned} \tag{2.10}$$

The flux at any point B on $\mathcal{H}$ is thus given by

$$\begin{aligned} F_B^{\text{in}} &= F_{\mathcal{H}_{\max}} \left(\frac{\boldsymbol{n}_A^T \boldsymbol{r}_{AB}}{\|\boldsymbol{n}_A\| \|\boldsymbol{r}_{AB}\|} \right) \\ &= \frac{F_{\odot}}{\pi} \frac{\alpha}{\|r_{AB}\|^2} \left(\frac{\boldsymbol{n}_A^T \boldsymbol{s}_{\oplus}}{\|\boldsymbol{n}_A\| \|\boldsymbol{s}_{\oplus}\|} \right) \left(\frac{\boldsymbol{n}_A^T \boldsymbol{r}_{AB}}{\|\boldsymbol{n}_A\| \|\boldsymbol{r}_{AB}\|} \right) \mathrm{d}A. \end{aligned} \tag{2.11}$$

Finally, the irradiance due to the diffuse reflectance of the incremental area of the Earth received by a CSS located at point B is given by

$$\begin{aligned} F_{\alpha} &= F_B^{\text{in}} \left(-\frac{\boldsymbol{n}^T \boldsymbol{r}_{AB}}{\|\boldsymbol{n}\| \|\boldsymbol{r}_{AB}\|} \right) \\ &= -\frac{F_{\odot}}{\pi} \frac{\alpha}{\|\boldsymbol{r}_{AB}\|^2} \left(\frac{\boldsymbol{n}_A^T \boldsymbol{s}_{\oplus}}{\|\boldsymbol{n}_A\| \|\boldsymbol{s}_{\oplus}\|} \right) \left(\frac{\boldsymbol{n}_A^T \boldsymbol{r}_{AB}}{\|\boldsymbol{n}_A\| \|\boldsymbol{r}_{AB}\|} \right) \left(\frac{\boldsymbol{n}^T \boldsymbol{r}_{AB}}{\|\boldsymbol{n}\| \|\boldsymbol{r}_{AB}\|} \right) \mathrm{d}A. \end{aligned} \tag{2.12}$$

Integrating over the surface of the Earth both lit by the Sun and visible to the spacecraft results in

$$F_{\alpha} = -\frac{F_{\odot}}{\pi} \iint_{\boldsymbol{A}} \frac{\alpha}{\|\boldsymbol{r}_{AB}\|^2} \left(\frac{\boldsymbol{n}_A^T \boldsymbol{s}_{\oplus}}{\|\boldsymbol{n}_A\| \|\boldsymbol{s}_{\oplus}\|} \right) \left(\frac{\boldsymbol{n}_A^T \boldsymbol{r}_{AB}}{\|\boldsymbol{n}_A\| \|\boldsymbol{r}_{AB}\|} \right) \left(\frac{\boldsymbol{n}^T \boldsymbol{r}_{AB}}{\|\boldsymbol{n}\| \|\boldsymbol{r}_{AB}\|} \right) \mathrm{d}A. \tag{2.13}$$

Adding this model to the output voltage given in Equation (2.2) results in

$$V = C\left(\frac{\boldsymbol{n}^T\boldsymbol{s}}{\|\boldsymbol{n}\|\|\boldsymbol{s}\|} - \frac{F_\alpha}{F_\odot}\right) \tag{2.14}$$

where the scale factor remains as shown in Equation (2.3).

2.1.2.1 Earth Albedo Data

For this work, albedo coefficients for the Earth are taken from NASA Total Ozone Mapping Spectrometer mission data. The data used in this study were acquired as part of the NASA's Earth-Sun System Division and archived and distributed by the Goddard Earth Sciences (GES) Data and Information Services Center (DISC) Distributed Active Archive Center (DAAC). The value of the Earth's albedo varies significantly with position, and due to seasonal, ground cover, and cloud cover changes.

To account for this significant variability, daily measurements from 2000 to 2005, corresponding to a $1^\circ \times 1.25^\circ$ latitude longitude grid, are used to calculate mean and standard deviation values that are shown in Figure 2.4. These values are used to generate statistically accurate values for the Earth's albedo coefficient used in the numerical simulations. Due to the computation time involved with solving the irradiance computation from each data point, the data set resolution can be reduced through interpolation or approximated through polynomials[16].

To illustrate the significance of Earth's albedo, the expected measurements for a satellite equipped with a dual pyramid CSS configuration, as described in Section 2.2, due to direct sunlight and Earth's albedo are shown in Figure 2.5. The spacecraft is simulated in a 400 km circular, polar orbit and it is actively controlled to point its $+z$-axis directly at the Sun. As can be seen the expected measurement due to albedo can be almost 50 % of the irradiance due to direct sunlight. Interestingly, it has been shown that the maximum albedo is not over the poles, but over Greenland during local summer at noon[14].

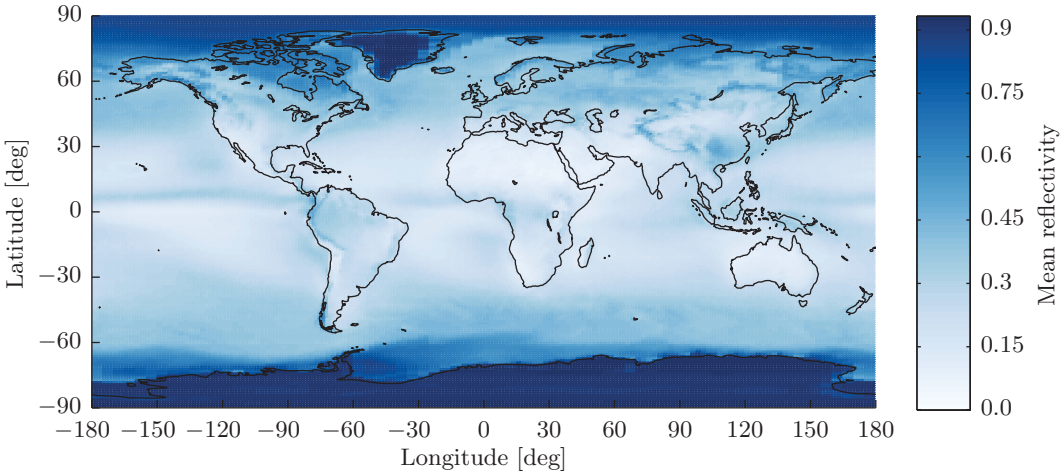

(a) Mean reflectivity.

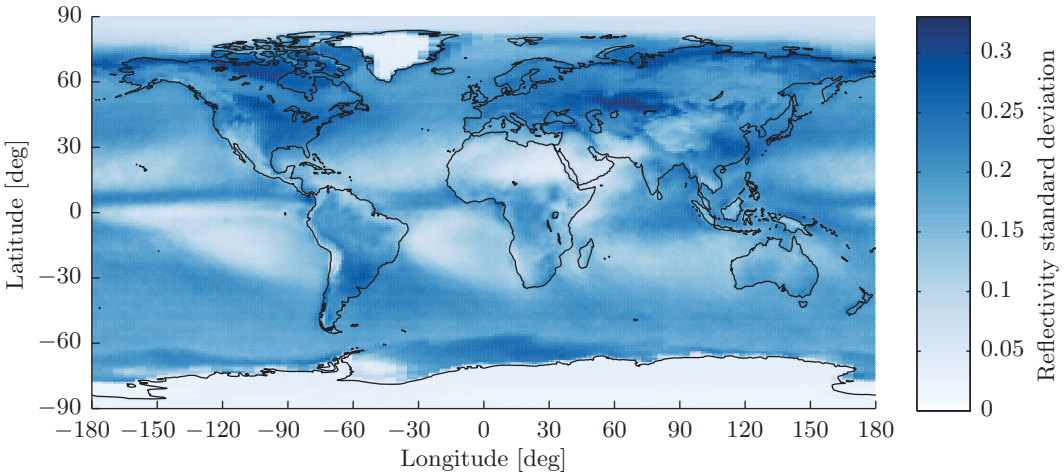

(b) Standard deviation of reflectivity.

Figure 2.4: Mean and standard deviation of the reflectivity of Earth as measured by TOMS mission between 2000 and 2005 used in numerical simulations.

2.1.2.2 Simulated Albedo Implementation

Due to the discrete nature of the available albedo data, Equation (2.13) is written as a finite sum using the position of the spacecraft $\boldsymbol{r}_B$ and the position of the differential area $\boldsymbol{r}_A$ as

$$F_\alpha = -\frac{F_\odot}{\pi} \sum_{j=0}^{N_A} \frac{\alpha}{\left\| \boldsymbol{r}_B - \boldsymbol{r}_{A_j} \right\|^4} \left(\boldsymbol{n}_{A_j}^T \boldsymbol{s}_\oplus \right) \left(\boldsymbol{n}_{A_j}^T \left[\boldsymbol{r}_B - \boldsymbol{r}_{A_j} \right] \right) \left(\boldsymbol{n}^T \left[\boldsymbol{r}_B - \boldsymbol{r}_{A_j} \right] \right) \Delta A_j \tag{2.15}$$

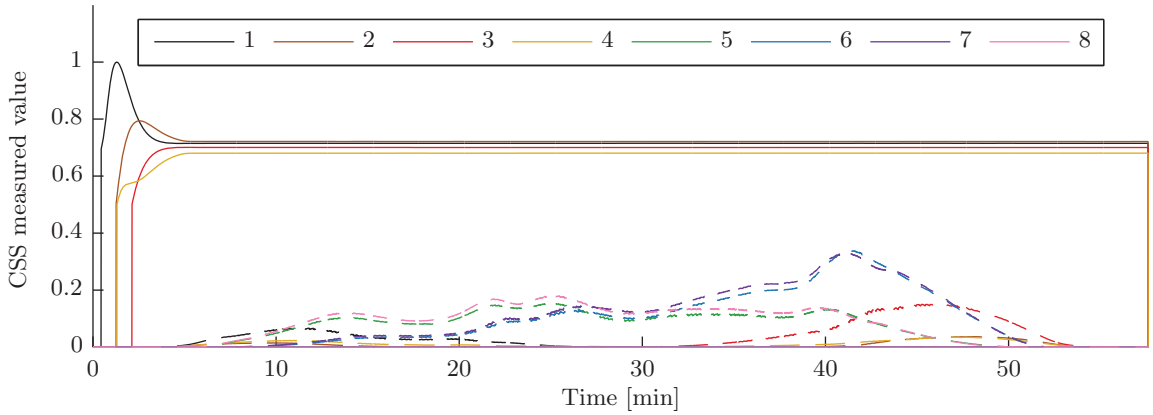

Figure 2.5: CSS expected measurements due to direct sunlight (solid) and Earth's albedo (dashed).

where N_A is the total number of differential areas within $\boldsymbol{A}$ and assuming $\|\boldsymbol{n}_A\| = 1$, $\|\boldsymbol{s}_\oplus\| = 1$, and $\|\boldsymbol{n}\| = 1$. The position, area, and surface normal of each differential area are precomputed for use in the estimation algorithms developed later. The position and normal of a differential area are calculated using the NASA Navigation and Ancillary Information Facility (NAIF) SPICE toolkit [62]. The surface area of the differential area is approximated by first calculating the authalic sphere for the Earth's ellipsoid. The authalic radius for the Earth is given by [63]

$$R_2 = \sqrt{\frac{a^2}{2}\left(1 + \frac{1-e^2}{2e}\ln\left(\frac{1+e}{1-e}\right)\right)} \tag{2.16}$$

where a is the Earth's equatorial radius, b is the Earth's polar radius, and $e = \sqrt{1 - \frac{b^2}{a^2}}$. Next, the geodetic latitude ϕ given in the TOMS data is converted to authalic latitude β using the series approximation

$$\begin{aligned}\beta = \phi &- \left(\frac{1}{3}e^2 + \frac{31}{180}e^4 + \frac{59}{560}e^6 + \ldots\right)\sin(2\phi) + \left(\frac{17}{360}e^4 + \frac{61}{1260}e^6 + \ldots\right)\sin(4\phi) \\ &- \left(\frac{383}{45360}e^6 + \ldots\right)\sin(6\phi) + \ldots.\end{aligned} \tag{2.17}$$

Finally, the surface area of the differential area is calculated using spherical geometry

$$\Delta A = \left|\lambda_1 - \lambda_0\right|\left|\sin\beta_1 - \sin\beta_0\right|R_2^2 \tag{2.18}$$

where λ_1 and λ_0 are the bounding longitudes, and β_1 and β_0 are the bounding authalic latitudes.

2.1.3 Unmodeled CSS Disturbances

As noted earlier, cosine-type CSS will report a measurement for any irradiance received. It is important to note there are two important sources of light on-orbit that are not considered in this study: lunar albedo and reflections.

The geometric albedo of the Moon has been shown to be between 0.05 and 0.15[64,65], but is highly uncertain, non-Lambertian, and dependent on the phase of the Moon[64–67]. In addition, due to the geometry of the Moon's orbit, the entire lunar disk will take up a maximum of approximately 0.5° of the CSS 120° edge-to-edge field of view for a spacecraft in LEO. In contrast, the Earth can fill the entire field of view of the sensor. Because the expected irradiance from lunar albedo is small it is neglected in this study.

Additionally, solar irradiance can be reflected into a CSS's field of view by structural components of the spacecraft. However, these disturbances can be minimized through careful placement of the sensors on the spacecraft. Because of this, these disturbances are also neglected in this work.

2.1.4 CSS Model Validation

To validate the model given in Equation (2.2), four CSS mounted in a pyramid configuration, as shown in Figure 2.1b, are tested in a heliostat. The results of sweeping the sensors through a variety of orientations are shown in Figure 2.6. The missing regions of the polar plots are due to the fields of view of the sensors being restricted by the local horizon of the surface to which the CSS are mounted.

Figure 2.7 shows the responses of two CSS with respect to the cosine of the angle between the incoming light and the CSS normal. A linear fit of the data and the associated R-squared values are shown along with the deviations of the experimental data from the linear fit. Higher order, sinusoidal, and Fourier fits are not found to improve the goodness of the fit.

From Figures 2.6 and 2.7 it can be seen that there is some variability in the output of a CSS due corresponding to rotation about the normal of the CSS. However, the magnitude of this

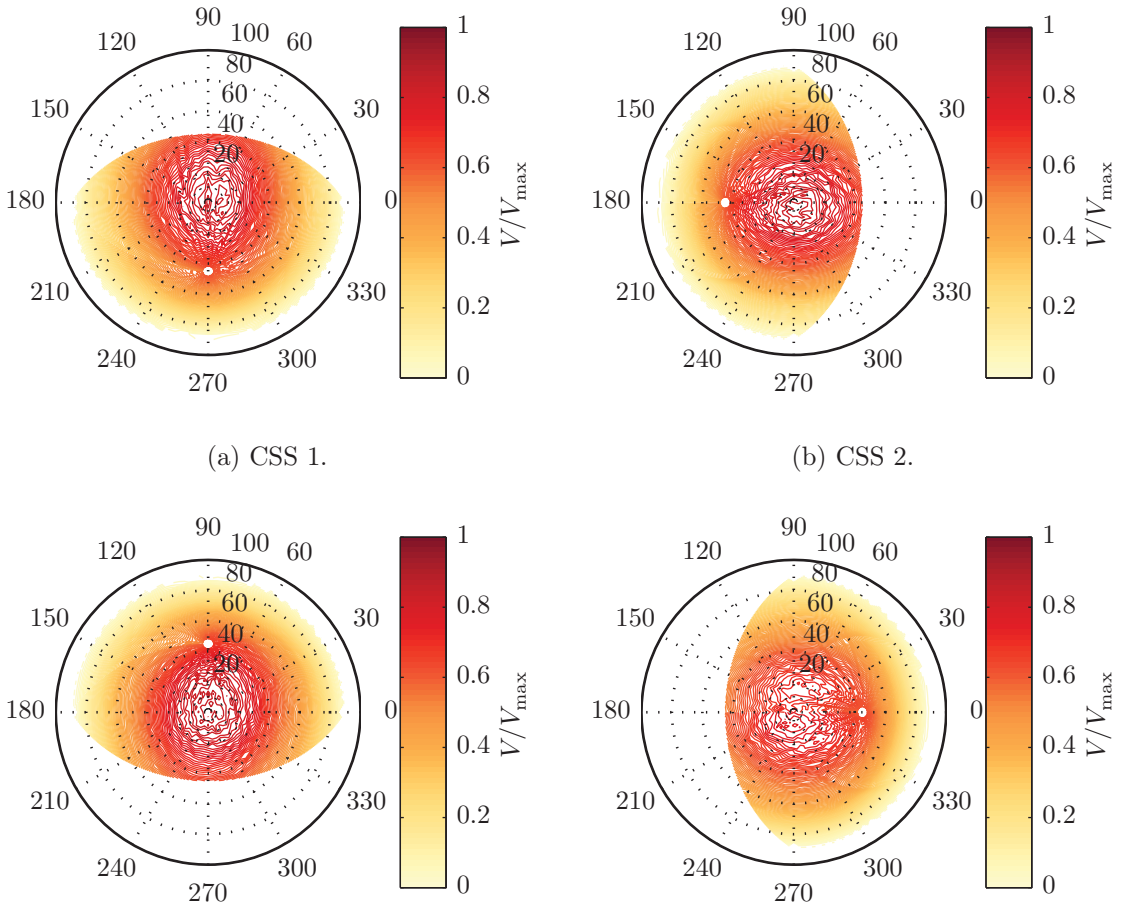

(a) CSS 1.

(b) CSS 2.

(c) CSS 3.

(d) CSS 4.

Figure 2.6: Output of CSS in heliostat.

variability is small and within the sensor noise, therefore, it is assumed the true unit direction vector for a CSS can be spherically expressed in the spacecraft body frame as

$$ {}^{\mathcal{B}}\boldsymbol{n} = \begin{bmatrix} \cos\left(\phi + \phi_\beta\right) \cos\left(\theta + \theta_\beta\right) \\ \cos\left(\phi + \phi_\beta\right) \sin\left(\theta + \theta_\beta\right) \\ \sin\left(\phi + \phi_\beta\right) \end{bmatrix} \tag{2.19} $$

where θ is the azimuth angle, measured positive from the body $+x$-axis around the $+z$-axis, and ϕ is the elevation angle, measured positive toward the body $+z$-axis from the x-y plane, of the CSS

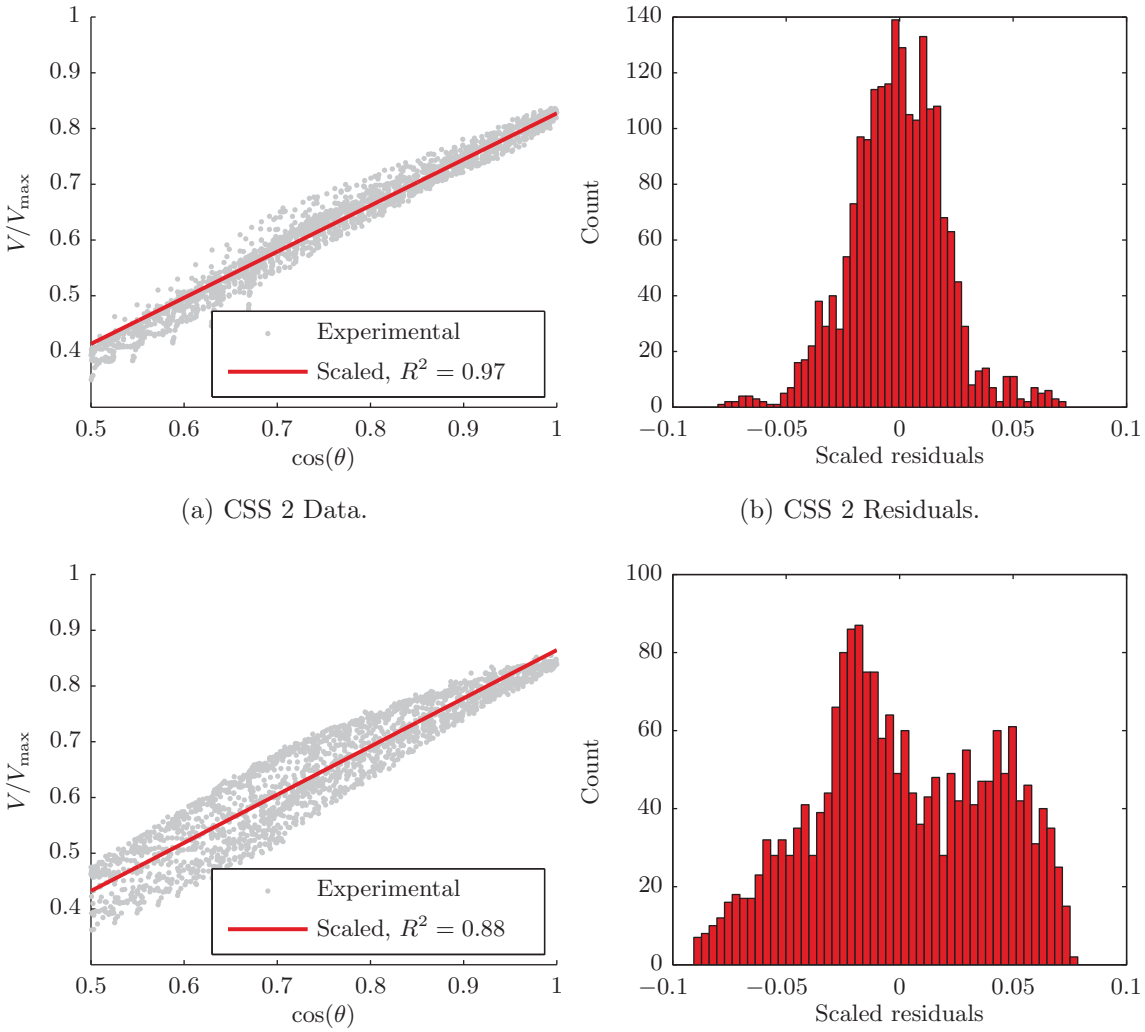

(a) CSS 2 Data.

(b) CSS 2 Residuals.

(c) CSS 3 Data.

(d) CSS 3 Residuals.

Figure 2.7: Result of fitting Equation (2.2) to data from CSS in heliostat.

unit direction vector; and θ_β and ϕ_β are uncorrelated random constants

$$\mathrm{E}\big[\theta_\beta\big] = 0, \quad \mathrm{E}\big[\theta_\beta^2\big] = \sigma_{\theta_\beta}^2, \quad \mathrm{E}\big[\phi_\beta\big] = 0, \quad \mathrm{E}\big[\phi_\beta^2\big] = \sigma_{\phi_\beta}^2, \quad \mathrm{E}\big[\phi_\beta\theta_\beta\big] = 0 \tag{2.20}$$

corresponding to misalignment errors.

A detailed model of the voltage output of a CSS on-board a spacecraft is arrived at by combining Equations (2.14) and (2.19). In order to simulate the behavior of actual hardware, discontinuities due to field of view limitations and noise are added to the measurement model

giving

$$V = C \cdot C_\kappa \left(V_d + V_\alpha + \nu_V \right)$$

$$V_d = \begin{cases} \frac{\boldsymbol{n}^T \boldsymbol{s}}{\|\boldsymbol{n}\| \|\boldsymbol{s}\|} & \text{if } \left(\frac{\boldsymbol{n}^T \boldsymbol{s}}{\|\boldsymbol{n}\| \|\boldsymbol{s}\|} \geq \cos\psi \right) \wedge (B \notin \boldsymbol{\mathcal{S}}) \\ 0 & \text{if } \left(\frac{\boldsymbol{n}^T \boldsymbol{s}}{\|\boldsymbol{n}\| \|\boldsymbol{s}\|} < \cos\psi \right) \vee (B \in \boldsymbol{\mathcal{S}}) \end{cases}$$

$$V_\alpha = \begin{cases} -\frac{1}{\pi} \iint\limits_{\boldsymbol{A}} \frac{\alpha}{\left\| \boldsymbol{r}_{AB} \right\|^2} \frac{\boldsymbol{n}_A^T \boldsymbol{s}_\oplus}{\left\| \boldsymbol{n}_A \right\| \left\| \boldsymbol{s}_\oplus \right\|} \frac{\boldsymbol{n}_A^T \boldsymbol{r}_{AB}}{\left\| \boldsymbol{n}_A \right\| \left\| \boldsymbol{r}_{AB} \right\|} \frac{\boldsymbol{n}^T \boldsymbol{r}_{AB}}{\left\| \boldsymbol{n} \right\| \left\| \boldsymbol{r}_{AB} \right\|} \, \mathrm{d}A & \text{if } B \notin \boldsymbol{\mathcal{S}} \\ 0 & \text{if } B \in \boldsymbol{\mathcal{S}} \end{cases} \tag{2.21}$$

where ν_V is zero-mean Gaussian noise with standard deviation σ_V, ψ is the half angle of the sensor's field of view, and C_κ is a constant random scale factor

$$\mathrm{E}[C_\kappa] = 1, \quad \mathrm{E}\left[C_\kappa^2\right] = \sigma_{C_\kappa}^2 \tag{2.22}$$

included to account for error in the knowledge of the calibration coefficient. Over time, radiation and other factors may cause the parameter C_κ to change, but it is assumed to be constant over short time scales[44]. Other hardware limitations, such as obstructions due to solar panels or instrumentation, must be evaluated on a mission specific basis.

2.2 Coarse Sun Sensor Configurations

Ideally, the sun direction can be uniquely determined at a given time for a spacecraft if three or more CSS measurements are available. For this research, a partially underdetermined sensor set is one for which there are spacecraft attitudes where the sun-direction cannot be uniquely determined due to an insufficient number of sensors. A fully underdetermined CSS set is one for which there are no attitudes with sufficient sensor coverage to uniquely determine the sun-direction in the absence of noise. The study of underdetermined CSS sets is important as they are a possibility for low-budget small satellites, and larger satellites suffering from sensor failure.

Two underdetermined CSS configurations are examined in this study. The first uses eight sensors arranged in a dual pyramid configuration that includes multiple sensor coverage when in

the desired sun-pointing orientation. The second is closer to a fully underdetermined configuration with one sensor on each of the six faces of a cube. The design of where to place these sensors is not investigated as it is usually an iterative process based on experience and heritage, and there are methods available in the literature[17,18].

2.2.1 Dual Pyramid Configuration

The first CSS configuration is a partially underdetermined configuration and includes eight cosine-type CSS in a dual pyramid setup. A basic dual pyramid configuration includes sensors with 120° edge-to-edge fields of view arranged on the $+z$ and $-z$ faces of the spacecraft oriented 90° apart and angled 45° from the body z axis. An illustration of this configuration is shown in Figure 2.8a and a list of the azimuth and elevation angles used are shown in Table 2.1. Multiple sensor coverage is provided along, $+z$, and opposite, $-z$, the solar array normal direction with minimal coverage along the equator of the spacecraft. This configuration leaves the sides of the spacecraft clear for scientific instrumentation and seeks to minimize both the CSS obstruction due to the solar arrays and the amount of internal cabling necessary for the sensors.

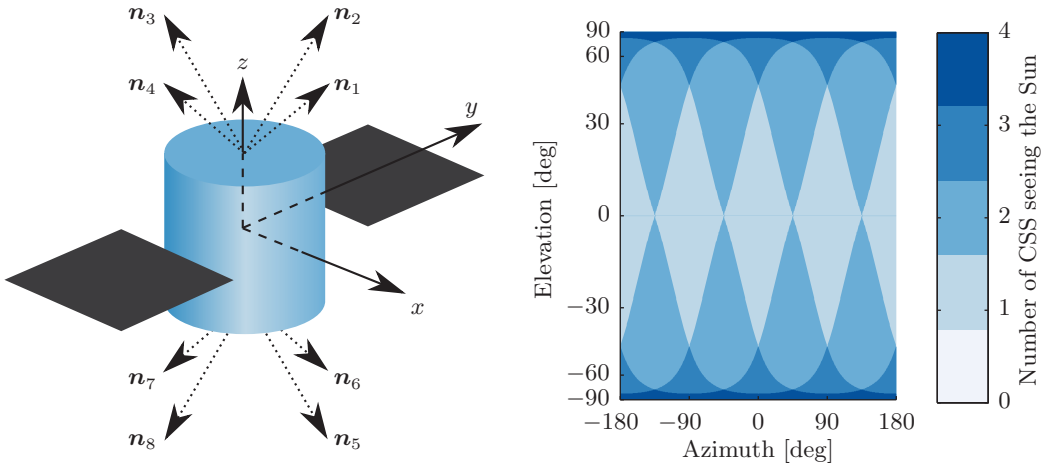

(a) Schematic of spacecraft.

(b) CSS coverage map.

Figure 2.8: Illustration of spacecraft, with CSS unit vectors, for a dual pyramid configuration and the associated coverage map.

Table 2.1: Azimuth and elevation angles of CSS in dual pyramid configuration.

Sensor	ϕ [deg]	θ [deg]
1	0	45
2	90	45
3	180	45
4	270	45
5	0	-45
6	90	-45
7	180	-45
8	270	-45

Figure 2.8b shows the number of CSS to which the Sun is visible for any relation of the Sun with respect to the spacecraft. Note that the fields of view of the CSS are clipped at the local-horizontal plane by the spacecraft structure and solar panel arrays. A Lambert cylindrical area preserving projection[63] is used so as to give a fair relative area comparison of the over, uniquely, and underdetermined regions of coverage. For this study, the ideal sun-pointing direction for a power-positive orientation has an elevation angle of 90°. It is not necessary to have the spacecraft point directly to the sun; being off by 20° to 30° is often acceptable for sufficient power generation.

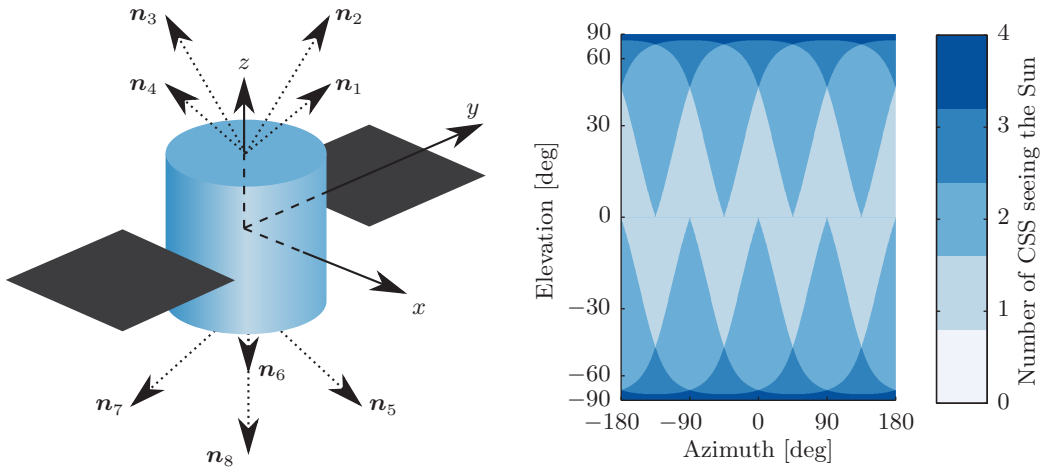

(a) Schematic of spacecraft.

(b) CSS coverage map.

Figure 2.9: Illustration of spacecraft, with CSS unit vectors, for an offset dual pyramid configuration and the associated coverage map.

In practice it is found this configuration can lead to numerical difficulties due to the collinear nature of the sensor normals. Figure 2.9 shows a slightly modified dual pyramid configuration. In this configuration the $-z$ facing sensors are rotated by 45° about the z axis with respect to the $+z$ facing sensors, thus adding 45° to the azimuth angles for sensors 5 to 8. This modified alignment prevents any of the sensor normals being collinear without sacrificing coverage and is the configuration used in this research.

2.2.2 Cube Configuration

The second CSS configuration uses only six sensors arranged on the faces of a cube. Depending on the field of view of the CSS used, a simple cube configuration with a single sensor on each face can represent either a partially or fully underdetermined sensor set. An illustration of this configuration and the associated coverage map are shown in Figure 2.10, and a list of the azimuth and elevation angles used are shown in Table 2.1.

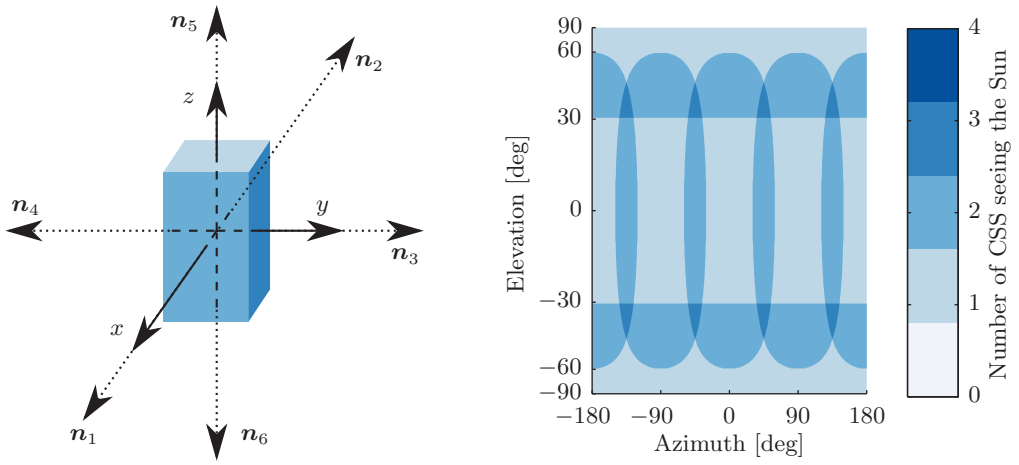

(a) Schematic of spacecraft.

(b) CSS coverage map, FOV = 60°.

Figure 2.10: Illustration of spacecraft for a simple cube configuration and the associated CSS coverage map.

Sensors with field of view half-angles of at least 55° are required in order for at least one CSS to detect the Sun at all times. Using sensors with smaller field of view half-angles results in

Table 2.2: Azimuth and elevation angles of CSS in cube configuration.

Sensor	ϕ [deg]	θ [deg]
1	0	0
2	0	90
3	0	180
4	0	20
5	90	0
6	270	0

uncovered zones near the corners of the cube and using sensors with larger field of view half-angles results in triple sensor coverage in these same regions. This configuration only requires six sensors, but if the solar panels of the spacecraft are aligned along one of the body axes, this configuration will suffer from minimal coverage in the goal orientation.

2.3 Rate Gyroscopes

The spacecraft simulated in this work is assumed to be equipped with a three axis rate gyro for measuring the body angular velocity. It is assumed the rate gyro measurements are corrupted by drive rate and zero mean additive white Gaussian noise according to Farrenkopf's approximation[68]. Crassidis provides a derivation of the discrete time propagation equations for a rate gyro noise model for a single-axis gyro model with no scale factor correction[69]. Pittelkau provides a rate gyro reference model that includes gyro alignment and scale factor error models[70,71].

The rate gyro noise model used here follows the derivation of Crassidis, expanded for vector-valued variables, with the scale factor and misalignment representations presented by Pittelkau. The derivation is included to highlight key assumptions made throughout. In addition, reference values for spacecraft rate gyros are provided. Both the reference values and the noise models are verified through comparison to data taken from a commercially available microelectromechanical systems (MEMS) gyro.

2.3.1 Basic Rate Gyro Model

A basic three-axis rate gyro model can be formed assuming the gyroscope dynamics follow Farrenkopf's approximation[68]

$$\tilde{\boldsymbol{\omega}}(t) = \boldsymbol{\omega}(t) + \boldsymbol{\omega}_\beta(t) + \boldsymbol{\eta}_\omega(t) \tag{2.23a}$$

$$\dot{\boldsymbol{\omega}}_\beta(t) = \boldsymbol{\eta}_{\omega_d}(t) \tag{2.23b}$$

where $\tilde{\boldsymbol{\omega}}(t)$ is the sensed angular velocity; $\boldsymbol{\omega}(t)$ is the true angular velocity; $\boldsymbol{\omega}_\beta(t)$ is the measurement bias, modeled as a rate random walk process; and $\boldsymbol{\eta}_\omega(t)$ and $\boldsymbol{\eta}_{\omega_d}(t)$ are zero-mean Gaussian rate and angular acceleration, respectively, white-noise processes with

$$\mathrm{E}\big[\boldsymbol{\eta}_\omega(t)\,\boldsymbol{\eta}_\omega^T(\tau)\big] = \sigma_\omega^2 \delta\,(t-\tau)\,\boldsymbol{I}_{3\times 3} \tag{2.24a}$$

$$\mathrm{E}\Big[\boldsymbol{\eta}_{\omega_d}(t)\,\boldsymbol{\eta}_{\omega_d}^T(\tau)\Big] = \sigma_{\omega_d}^2 \delta\,(t-\tau)\,\boldsymbol{I}_{3\times 3} \tag{2.24b}$$

were $\delta(\cdot)$ is the Dirac delta function.

2.3.2 Detailed Rate Gyro Model

Expanding Equation (2.23) to a more general form results in

$${}^{\mathcal{G}}\tilde{\boldsymbol{\omega}}(t) = (\boldsymbol{I} + \boldsymbol{K} + \boldsymbol{\Upsilon})\,(\boldsymbol{I} + \boldsymbol{\Delta})\,[GB]\,{}^{\mathcal{B}}\boldsymbol{\omega}(t) + {}^{\mathcal{G}}\boldsymbol{\omega}_d(t) + {}^{\mathcal{G}}\boldsymbol{\omega}_r + {}^{\mathcal{G}}\boldsymbol{\eta}_\omega(t) \tag{2.25a}$$

$$\dot{\boldsymbol{\omega}}_d(t) = \boldsymbol{\eta}_{\omega_d}(t) \tag{2.25b}$$

$$\dot{\boldsymbol{K}} = 0, \quad \dot{\boldsymbol{\Upsilon}} = 0, \quad \dot{\boldsymbol{\Delta}} = 0, \quad \dot{\boldsymbol{\omega}}_r = 0 \tag{2.25c}$$

where the left exponent $\mathcal{G}$ indicates a quantity expressed in the rate gyro frame, the left exponent $\mathcal{B}$ indicates a quantity expressed in the spacecraft body frame, and the bias term

$$\boldsymbol{\omega}_\beta \equiv \boldsymbol{\omega}_r + \boldsymbol{\omega}_d \tag{2.26}$$

has been broken down into a "bias repeatability" or "bias stability" term $\boldsymbol{\omega}_r$ and bias drift term $\boldsymbol{\omega}_d$. The processes given in Equation (2.25c) are constant random variables:

$$\boldsymbol{K} = \mathrm{diag}\big(\kappa_x, \kappa_y, \kappa_z\big)$$

is a matrix of symmetric scale factor errors,

$$\boldsymbol{\Upsilon} = \operatorname{diag}\left(\upsilon_x \operatorname{sgn}(\omega_x(t)), \upsilon_y \operatorname{sgn}\left(\omega_y(t)\right), \upsilon_z \operatorname{sgn}(\omega_z(t))\right)$$

is a matrix of asymmetric scale factor errors, $(\boldsymbol{I} + \boldsymbol{\Delta})$ is a nonorthogonal small angle misalignment error, and $[GB]$ is an assumed known transformation matrix from the spacecraft's body frame to the gyroscope sensing frame. Noting ${}^{\mathcal{G}}\boldsymbol{\omega} = [GB]\,{}^{\mathcal{B}}\boldsymbol{\omega}$, the quantity $(\boldsymbol{I} + \boldsymbol{\Delta})\,{}^{\mathcal{G}}\boldsymbol{\omega}$ can be expressed as the sum of orthogonal rotations β of the true angular rate about each axis

$$\begin{aligned}(\boldsymbol{I} + \boldsymbol{\Delta})\,{}^{\mathcal{G}}\boldsymbol{\omega} = &\begin{bmatrix} c\beta_{xy}c\beta_{xz} & -c\beta_{xy}s\beta_{xz} & s\beta_{xy} \\ s\beta_{xz} & c\beta_{xz} & 0 \\ -c\beta_{xz}s\beta_{xy} & s\beta_{xy}s\beta_{xz} & c\beta_{xy} \end{bmatrix}{}^{\mathcal{G}}\begin{bmatrix}\omega_x \\ 0 \\ 0\end{bmatrix} + \begin{bmatrix} c\beta_{yz} & -s\beta_{yz} & 0 \\ c\beta_{yx}s\beta_{yz} & c\beta_{yx}c\beta_{yz} & -s\beta_{yx} \\ s\beta_{yx}s\beta_{yz} & c\beta_{yz}s\beta_{yx} & c\beta_{yx} \end{bmatrix}{}^{\mathcal{G}}\begin{bmatrix}0 \\ \omega_y \\ 0\end{bmatrix} \\ &+ \begin{bmatrix} c\beta_{zy} & 0 & s\beta_{zy} \\ s\beta_{zx}s\beta_{zy} & c\beta_{zx} & -c\beta_{zy}s\beta_{zx} \\ -c\beta_{zx}s\beta_{zy} & s\beta_{zx} & c\beta_{zx}c\beta_{zy} \end{bmatrix}{}^{\mathcal{G}}\begin{bmatrix}0 \\ 0 \\ \omega_z\end{bmatrix} = \begin{bmatrix} c\beta_{xy}c\beta_{xz} & -s\beta_{yz} & s\beta_{zy} \\ s\beta_{xz} & c\beta_{yx}c\beta_{yz} & -c\beta_{zy}s\beta_{zx} \\ -c\beta_{xz}s\beta_{xy} & c\beta_{yz}s\beta_{yx} & c\beta_{zx}c\beta_{zy} \end{bmatrix}{}^{\mathcal{G}}\begin{bmatrix}\omega_x \\ \omega_y \\ \omega_z\end{bmatrix}\end{aligned} \tag{2.27}$$

where $c\beta$ is used as shorthand for $\cos(\beta)$ and $s\beta$ as shorthand for $\sin(\beta)$. Assuming small angle misalignments, this can be approximated to first-order as

$$\begin{aligned}(\boldsymbol{I} + \boldsymbol{\Delta})\,{}^{\mathcal{G}}\boldsymbol{\omega} \approx &\begin{bmatrix} 1 & -\beta_{xz} & \beta_{xy} \\ \beta_{xz} & 1 & 0 \\ -\beta_{xy} & 0 & 1 \end{bmatrix}{}^{\mathcal{G}}\begin{bmatrix}\omega_x \\ 0 \\ 0\end{bmatrix} + \begin{bmatrix} 1 & -\beta_{yz} & 0 \\ \beta_{yz} & 1 & -\beta_{yx} \\ 0 & \beta_{yx} & 1 \end{bmatrix}{}^{\mathcal{G}}\begin{bmatrix}0 \\ \omega_y \\ 0\end{bmatrix} \\ &+ \begin{bmatrix} 1 & 0 & \beta_{zy} \\ 0 & 1 & -\beta_{zx} \\ -\beta_{zy} & \beta_{zx} & 1 \end{bmatrix}{}^{\mathcal{G}}\begin{bmatrix}0 \\ 0 \\ \omega_z\end{bmatrix} = \begin{bmatrix} 1 & -\beta_{yz} & \beta_{zy} \\ \beta_{xz} & 1 & -\beta_{zx} \\ -\beta_{xy} & \beta_{yx} & 1 \end{bmatrix}{}^{\mathcal{G}}\begin{bmatrix}\omega_x \\ \omega_y \\ \omega_z\end{bmatrix}.\end{aligned} \tag{2.28}$$

Maintaining a first order approximation and taking a QR decomposition of Equation (2.28) results in

$$(\boldsymbol{I} + \boldsymbol{\Delta})\,{}^{\mathcal{G}}\boldsymbol{\omega} \approx \begin{bmatrix} 1 & -\beta_z & \beta_y \\ \beta_z & 1 & -\beta_x \\ -\beta_y & \beta_x & 1 \end{bmatrix}\begin{bmatrix} 1 & \xi_z & -\xi_y \\ 0 & 1 & \xi_x \\ 0 & 0 & 1 \end{bmatrix} \approx \begin{bmatrix} 1 & -(\beta_z - \xi_z) & \beta_y - \xi_y \\ \beta_z & 1 & -(\beta_x - \xi_x) \\ -\beta_y & \beta_x & 1 \end{bmatrix} \tag{2.29}$$

where

$$\beta_x = \beta_{yx}, \quad \beta_y = \beta_{xy}, \quad \beta_z = \beta_{xz}$$

$$\xi_x = \beta_{yx} - \beta_{zx}, \quad \xi_y = \beta_{xy} - \beta_{zy}, \quad \xi_z = \beta_{xz} - \beta_{yz} \tag{2.30}$$

are the orthogonal, $\boldsymbol{\beta}$, and nonorthogonal, $\boldsymbol{\xi}$, misalignments. Assuming small scale factor errors, the matrix $\boldsymbol{\Phi}$ is defined as the combination of scale factor and misalignment errors as

$$\boldsymbol{\Phi} = \begin{bmatrix} 1 + \kappa_x + \upsilon_x \operatorname{sgn}(\omega_x(t)) & -(\beta_z - \xi_z) & \beta_y - \xi_y \\ \beta_z & 1 + \kappa_y + \upsilon_y \operatorname{sgn}\big(\omega_y(t)\big) & -(\beta_x - \xi_x) \\ -\beta_y & \beta_x & 1 + \kappa_z + \upsilon_z \operatorname{sgn}(\omega_z(t)) \end{bmatrix} \tag{2.31}$$

allowing Equation (2.23) to be written as

$${}^{\mathcal{G}}\tilde{\boldsymbol{\omega}}(t) = \boldsymbol{\Phi}\,[GB]\,{}^{\mathcal{B}}\boldsymbol{\omega}(t) + {}^{\mathcal{G}}\boldsymbol{\omega}_d(t) + {}^{\mathcal{G}}\boldsymbol{\omega}_r + {}^{\mathcal{G}}\boldsymbol{\eta}_\omega(t) \tag{2.32a}$$

$$\dot{\boldsymbol{\omega}}_d(t) = \boldsymbol{\eta}_{\omega_d}(t)\,. \tag{2.32b}$$

2.3.2.1 Measured Rate Gyro Bias Drift Model

Integrating Equation (2.32b) gives an expression for the discrete propagation of the bias drift

$$\boldsymbol{\omega}_d(t_0 + \Delta t) = \boldsymbol{\omega}_d(t_0) + \int_{t_0}^{t_0+\Delta t} \boldsymbol{\eta}_{\omega_d}(t)\,\mathrm{d}t. \tag{2.33}$$

The variance of the bias drift is given by

$$\mathrm{E}\Big[\{\boldsymbol{\omega}_d(t_0 + \Delta t) - \mathrm{E}[\boldsymbol{\omega}_d(t_0 + \Delta t)]\}\,\{\boldsymbol{\omega}_d(t_0 + \Delta t) - \mathrm{E}[\boldsymbol{\omega}_d(t_0 + \Delta t)]\}^T\Big] = E\left[\left\{\int_{t_0}^{t_0+\Delta t} \boldsymbol{\eta}_{\omega_d}(t)\,\mathrm{d}t\right\}\left\{\int_{t_0}^{t_0+\Delta t} \boldsymbol{\eta}_{\omega_d}(\tau)\,\mathrm{d}\tau\right\}^T\right]. \tag{2.34}$$

Applying Equation (2.24b) gives

$$\mathrm{E}\Big[\{\boldsymbol{\omega}_d(t_0 + \Delta t) - \mathrm{E}[\boldsymbol{\omega}_d(t_0 + \Delta t)]\}\,\{\boldsymbol{\omega}_d(t_0 + \Delta t) - \mathrm{E}[\boldsymbol{\omega}_d(t_0 + \Delta t)]\}^T\Big] = \sigma^2_{\omega_d}\Delta t \boldsymbol{I}_{3\times 3}. \tag{2.35}$$

The bias drift variance, Equation (2.35), can be satisfied by modeling the bias drift using

$$\boldsymbol{\omega}_{d_m}(t_0 + \Delta t) = \boldsymbol{\omega}_{d_m}(t_0) + \sigma_{\omega_d}\sqrt{\Delta t}\boldsymbol{N}_{\omega_d} \tag{2.36}$$

where the subscript m indicates a modeled quantity and $\boldsymbol{N}_{\omega_d}$ is a 3×1 matrix of uncorrelated zero-mean random variables with unit variance, thus, $\mathrm{E}\Big[\boldsymbol{N}_{\omega_d}\boldsymbol{N}^T_{\omega_d}\Big] = \boldsymbol{I}_{3\times 3}$.

2.3.2.2 Measured Rate Gyro Rate Model

Assuming the measurement and truth are constant over the time interval, integrating Equation (2.32a), and dividing by Δt gives an expression for the discrete propagation of the rate measurement

$$ {}^{\mathcal{G}}\tilde{\boldsymbol{\omega}}(t_0+\Delta t) = \boldsymbol{\Phi}\,[GB]\,{}^{\mathcal{B}}\boldsymbol{\omega}(t_0+\Delta t) + {}^{\mathcal{G}}\boldsymbol{\omega}_r + \frac{1}{\Delta t}\int_{t_0}^{t_0+\Delta t}\left\{{}^{\mathcal{G}}\boldsymbol{\omega}_d(t) + {}^{\mathcal{B}}\boldsymbol{\eta}_\omega(t)\right\}\mathrm{d}t. \tag{2.37} $$

Generalizing the discrete propagation of the measurement bias, Equation (2.33),

$$ \boldsymbol{\omega}_d(t) = \boldsymbol{\omega}_d(t_0) + \int_{t_0}^{t}\boldsymbol{\eta}_{\omega_d}(\tau)\,\mathrm{d}\tau \tag{2.38} $$

and substituting the result into the discrete propagation of the rate measurement, Equation (2.37), gives

$$ \begin{aligned} {}^{\mathcal{G}}\tilde{\boldsymbol{\omega}}(t_0+\Delta t) = \boldsymbol{\Phi}\,[GB]\,{}^{\mathcal{B}}\boldsymbol{\omega}(t_0+\Delta t) + {}^{\mathcal{G}}\boldsymbol{\omega}_r + {}^{\mathcal{G}}\boldsymbol{\omega}_d(t_0) + \frac{1}{\Delta t}\int_{t_0}^{t_0+\Delta t}\int_{t_0}^{t}{}^{\mathcal{G}}\boldsymbol{\eta}_{\omega_d}(\tau)\,\mathrm{d}\tau\,\mathrm{d}t \\ + \frac{1}{\Delta t}\int_{t_0}^{t_0+\Delta t}{}^{\mathcal{G}}\boldsymbol{\eta}_\omega(t)\,\mathrm{d}t. \end{aligned} \tag{2.39} $$

The variance of the rate measurement, Equation (2.39), is given by

$$ \begin{aligned} &\mathrm{E}\Big[\left\{{}^{\mathcal{G}}\tilde{\boldsymbol{\omega}}(t_0+\Delta t) - \mathrm{E}\big[{}^{\mathcal{G}}\tilde{\boldsymbol{\omega}}(t_0+\Delta t)\big]\right\}\left\{{}^{\mathcal{G}}\tilde{\boldsymbol{\omega}}(t_0+\Delta t) - \mathrm{E}\big[{}^{\mathcal{G}}\tilde{\boldsymbol{\omega}}(t_0+\Delta t)\big]\right\}^T\Big] \\ &\quad = E\left[\left\{\frac{1}{\Delta t}\int_{t_0}^{t_0+\Delta t}\int_{t_0}^{\tau}\boldsymbol{\eta}_{\omega_d}(\gamma)\,\mathrm{d}\gamma\,\mathrm{d}\tau + \frac{1}{\Delta t}\int_{t_0}^{t_0+\Delta t}\boldsymbol{\eta}_\omega(\tau)\,\mathrm{d}\tau\right\}\right. \\ &\quad\quad \left.\times\left\{\frac{1}{\Delta t}\int_{t_0}^{t_0+\Delta t}\int_{t_0}^{t}\boldsymbol{\eta}_{\omega_d}(\zeta)\,\mathrm{d}\zeta\,\mathrm{d}t + \frac{1}{\Delta t}\int_{t_0}^{t_0+\Delta t}\boldsymbol{\eta}_\omega(t)\,\mathrm{d}t\right\}^T\right]. \end{aligned} \tag{2.40} $$

Again noting $\boldsymbol{\eta}_{\omega_d}(t)$ and $\boldsymbol{\eta}_\omega(t)$ are uncorrelated, and using Equation (2.24), gives

$$ \begin{aligned} &\mathrm{E}\Big[\left\{{}^{\mathcal{G}}\tilde{\boldsymbol{\omega}}(t_0+\Delta t) - \mathrm{E}\big[{}^{\mathcal{G}}\tilde{\boldsymbol{\omega}}(t_0+\Delta t)\big]\right\}\left\{{}^{\mathcal{G}}\tilde{\boldsymbol{\omega}}(t_0+\Delta t) - \mathrm{E}\big[{}^{\mathcal{G}}\tilde{\boldsymbol{\omega}}(t_0+\Delta t)\big]\right\}^T\Big] \\ = \frac{\sigma_{\omega_d}^2}{\Delta t^2}\left(\int_{t_0}^{t_0+\Delta t}\int_{t_0}^{t_0+\Delta t}\int_{t_0}^{t}\int_{t_0}^{\tau}\delta(\gamma-\zeta)\,\mathrm{d}\gamma\,\mathrm{d}\zeta\,\mathrm{d}\tau\,\mathrm{d}t\right) + \frac{\sigma_\omega^2}{\Delta t^2}\left\{\int_{t_0}^{t_0+\Delta t}\int_{t_0}^{t_0+\Delta t}\delta(\tau-t)\,\mathrm{d}\tau\,\mathrm{d}t\right\} \\ = \frac{\sigma_{\omega_d}^2}{\Delta t^2}\left(\frac{\Delta t^3}{3}\right) + \frac{\sigma_\omega^2}{\Delta t^2}\{\Delta t\} \\ = \frac{1}{3}\sigma_{\omega_d}^2\Delta t + \frac{\sigma_\omega^2}{\Delta t}. \end{aligned} \tag{2.41} $$

The covariance between the rate measurement bias, Equation (2.33), and the rate measurement, Equation (2.39), is given by

$$\begin{aligned}
&\mathrm{E}\Big[\left\{{}^{\mathcal{G}}\boldsymbol{\omega}_d(t_0+\Delta t)-\mathrm{E}\big[{}^{\mathcal{G}}\boldsymbol{\omega}_d(t_0+\Delta t)\big]\right\}\left\{{}^{\mathcal{G}}\tilde{\boldsymbol{\omega}}(t_0+\Delta t)-\mathrm{E}\big[{}^{\mathcal{G}}\tilde{\boldsymbol{\omega}}(t_0+\Delta t)\big]\right\}^T\Big]= \\
&E\left[\left\{\int_{t_0}^{t_0+\Delta t}{}^{\mathcal{G}}\boldsymbol{\eta}_{\omega_d}(\tau)\,\mathrm{d}\tau\right\}\left\{\frac{1}{\Delta t}\int_{t_0}^{t_0+\Delta t}\int_{t_0}^{t}{}^{\mathcal{G}}\boldsymbol{\eta}_{\omega_d}(\zeta)\,\mathrm{d}\zeta\,\mathrm{d}t+\frac{1}{\Delta t}\int_{t_0}^{t_0+\Delta t}{}^{\mathcal{G}}\boldsymbol{\eta}_{\omega}(t)\,\mathrm{d}t\right\}\right]. \qquad (2.42)
\end{aligned}$$

Noting $\boldsymbol{\eta}_{\omega_d}(t)$ and $\boldsymbol{\eta}_{\omega}(t)$ are uncorrelated, and using Equation (2.24b) gives

$$\begin{aligned}
&\mathrm{E}\Big[\left\{{}^{\mathcal{G}}\boldsymbol{\omega}_d(t_0+\Delta t)-\mathrm{E}\big[{}^{\mathcal{G}}\boldsymbol{\omega}_d(t_0+\Delta t)\big]\right\}\left\{{}^{\mathcal{G}}\tilde{\boldsymbol{\omega}}(t_0+\Delta t)-\mathrm{E}\big[{}^{\mathcal{G}}\tilde{\boldsymbol{\omega}}(t_0+\Delta t)\big]\right\}^T\Big] \\
&\quad=\frac{\sigma_{\omega_d}^2}{\Delta t}\left(\int_{t_0}^{t_0+\Delta t}\int_{t_0}^{t_0+\Delta t}\int_{t_0}^{t}\delta\left(\tau-\zeta\right)\mathrm{d}\zeta\,\mathrm{d}\tau\,\mathrm{d}t\right) \\
&\quad=\frac{\sigma_{\omega_d}^2}{\Delta t}\left(\frac{\Delta t^2}{2}\right) \\
&\quad=\frac{1}{2}\sigma_{\omega_d}^2\Delta t. \qquad (2.43)
\end{aligned}$$

assuming $t-t_0<\Delta t$. The covariance between the rate measurement bias and the rate measurement, Equation (2.43), can be satisfied by modeling the rate measurement as

$${}^{\mathcal{G}}\tilde{\boldsymbol{\omega}}_m(t_0+\Delta t)=\boldsymbol{\Phi}\left[GB\right]{}^{\mathcal{B}}\boldsymbol{\omega}_m(t_0+\Delta t)+{}^{\mathcal{G}}\boldsymbol{\omega}_{r_m}+{}^{\mathcal{G}}\boldsymbol{\omega}_{d_m}(t_0)+\frac{1}{2}\sigma_{\omega_d}\sqrt{\Delta t}\boldsymbol{N}_{\omega_d}+a\boldsymbol{N}_{\omega} \qquad (2.44)$$

where $\boldsymbol{N}_{\omega}$ is a 3×1 matrix of uncorrelated zero-mean random variables with unit variance, thus $\mathrm{E}\big[\boldsymbol{N}_{\omega}\boldsymbol{N}_{\omega}^T\big]=\boldsymbol{I}_{3\times 3}$, that are uncorrelated with $\boldsymbol{N}_{\omega_d}$, thus $\mathrm{E}\Big[\boldsymbol{N}_{\omega}\boldsymbol{N}_{\omega_d}^T\Big]=\boldsymbol{0}_{3\times 3}$, and a is yet to be determined.

The variance of the proposed rate measurement model, Equation (2.44), is given by

$$\begin{aligned}
&\mathrm{E}\Big[\left\{{}^{\mathcal{G}}\tilde{\boldsymbol{\omega}}_m(t_0+\Delta t)-\mathrm{E}\big[{}^{\mathcal{G}}\tilde{\boldsymbol{\omega}}_m(t_0+\Delta t)\big]\right\}\left\{{}^{\mathcal{G}}\tilde{\boldsymbol{\omega}}_m(t_0+\Delta t)-\mathrm{E}\big[{}^{\mathcal{G}}\tilde{\boldsymbol{\omega}}_m(t_0+\Delta t)\big]\right\}^T\Big] \\
&\quad=E\left[\left\{\frac{1}{2}\sigma_{\omega_d}\sqrt{\Delta t}\boldsymbol{N}_{\omega_d}+a\boldsymbol{N}_{\omega}\right\}\left\{\frac{1}{2}\sigma_{\omega_d}\sqrt{\Delta t}\boldsymbol{N}_{\omega_d}+a\boldsymbol{N}_{\omega}\right\}^T\right] \\
&\quad=\frac{1}{4}\sigma_{\omega_d}^2\Delta t+a^2. \qquad (2.45)
\end{aligned}$$

Equating Equation (2.41) and Equation (2.45) gives

$$a^2=\frac{1}{12}\sigma_{\omega_d}^2\Delta t+\frac{\sigma_{\omega}^2}{\Delta t} \qquad (2.46)$$

and solving Equation (2.36) for $\boldsymbol{N}_{\omega_d}$ and substituting into Equation (2.44) results in

$$ {}^{\mathcal{G}}\tilde{\boldsymbol{\omega}}_m(t_0+\Delta t) = \boldsymbol{\Phi}\,[GB]\,{}^{\mathcal{B}}\boldsymbol{\omega}_m(t_0+\Delta t) + {}^{\mathcal{G}}\boldsymbol{\omega}_{r_m} + \frac{1}{2}\left\{{}^{\mathcal{G}}\boldsymbol{\omega}_{d_m}(t_0) + {}^{\mathcal{G}}\boldsymbol{\omega}_{d_m}(t_0+\Delta t)\right\} + a\boldsymbol{N}_\omega. \quad (2.47) $$

Substituting Equation (2.46) into Equation (2.47) gives

$$ \begin{aligned} {}^{\mathcal{G}}\tilde{\boldsymbol{\omega}}_m(t_0+\Delta t) = \boldsymbol{\Phi}\,[GB]\,{}^{\mathcal{B}}\boldsymbol{\omega}_m(t_0+\Delta t) + {}^{\mathcal{G}}\boldsymbol{\omega}_{r_m} + \frac{1}{2}\left({}^{\mathcal{G}}\boldsymbol{\omega}_{d_m}(t_0) + {}^{\mathcal{G}}\boldsymbol{\omega}_{d_m}(t_0+\Delta t)\right) \\ + \sqrt{\frac{1}{12}\sigma^2_{\omega_d}\Delta t + \frac{\sigma^2_\omega}{\Delta t}}\boldsymbol{N}_\omega \end{aligned} \quad (2.48) $$

and, finally, substituting in the bias drift propagation model, Equation (2.36), gives

$$ \begin{aligned} {}^{\mathcal{G}}\tilde{\boldsymbol{\omega}}_m(t_0+\Delta t) = \boldsymbol{\Phi}\,[GB]\,{}^{\mathcal{B}}\boldsymbol{\omega}_m(t_0+\Delta t) + {}^{\mathcal{G}}\boldsymbol{\omega}_{r_m} + {}^{\mathcal{G}}\boldsymbol{\omega}_{d_m}(t_0) + \frac{1}{2}\sigma_{\omega_d}\sqrt{\Delta t}\boldsymbol{N}_{\omega_d} \\ + \sqrt{\frac{1}{12}\sigma^2_{\omega_d}\Delta t + \frac{\sigma^2_\omega}{\Delta t}}\boldsymbol{N}_\omega. \end{aligned} \quad (2.49) $$

Generalizing Equation (2.49) and Equation (2.36) for all time gives the following discrete-time rate measurement and rate bias propagation equations

$$ {}^{\mathcal{G}}\tilde{\boldsymbol{\omega}}_{k+1} = \boldsymbol{\Phi}\,[GB]\,{}^{\mathcal{B}}\boldsymbol{\omega}_k + {}^{\mathcal{G}}\boldsymbol{\omega}_r + {}^{\mathcal{G}}\boldsymbol{\omega}_{d_k} + \frac{1}{2}\sigma_{\omega_d}\sqrt{\Delta t}\boldsymbol{N}_{\omega_d} + \sqrt{\frac{1}{12}\sigma^2_{\omega_d}\Delta t + \frac{\sigma^2_\omega}{\Delta t}}\boldsymbol{N}_\omega \quad (2.50a) $$

$$ \boldsymbol{\omega}_{d_{k+1}} = \boldsymbol{\omega}_{d_k} + \sigma_{\omega_d}\sqrt{\Delta t}\boldsymbol{N}_{\omega_d}. \quad (2.50b) $$

2.3.3 Model Validation and Performance Grades

Table 2.3 lists the values of rate gyro accuracy used in this study. These values are adapted from a table of generally accepted performance grades listed in References 72 and 73. The angular acceleration white-noise process variance $\sigma^2_{\omega_d}$ is computed from the bias stability typically quoted by gyro manufacturers as $\sigma^2_{\omega_d} = \left(2/\tau_{\omega_r}\right)\sigma^2_{\omega_r}$, where τ_{ω_r} is the specified drift stability interval.[71].

In order to validate the values shown in Table 2.3, data from a smartphone equipped with an InvenSense MPU6515 MEMS gyroscope is analyzed. The rate gyro noise statistics are calculated using the Allan variance of data recorded while the sensor is at rest. The fully overlapping Allan

Table 2.3: Rate gyro accuracy levels.

Parameter	Units	Inertial	Intermediate	Moderate	Low
Rate Noise (σ_ω)	$^\circ/\sqrt{\text{s}}$	10^{-6}	10^{-4}	10^{-2}	10^{-1}
Bias Stability $\left(\sigma_{\omega_r}\right)$	$^\circ/\text{s}$	10^{-8}	10^{-6}	10^{-3}	10^{-2}

variance $\sigma_y^2(\tau)$ at a specific sampling time τ is calculated for a set of rate gyro measurements y using[74]

$$\sigma_y^2(\tau) = \frac{1}{2m^2\left(M-2m+1\right)} \sum_{j=0}^{M-2m} \left[\sum_{i=j}^{j+m-1} \left(y_{i+m} - y_i\right) \right]^2 \tag{2.51}$$

where M is the total number of measurements, and m is the averaging factor equal to the number of samples taken within a single sampling time. Due to the high computational costs of Equation (2.51) the rate gyroscope measurements are usually integrated to give phase measurements x at each time. The Allan variance is then calculated from these phase measurements using

$$\sigma_y^2(\tau) = \frac{1}{2m^2\tau^2\left(M-2m\right)} \sum_{i=0}^{M-2m-1} \left(x_{i+2m} - 2x_{i+m} + x_i\right)^2 . \tag{2.52}$$

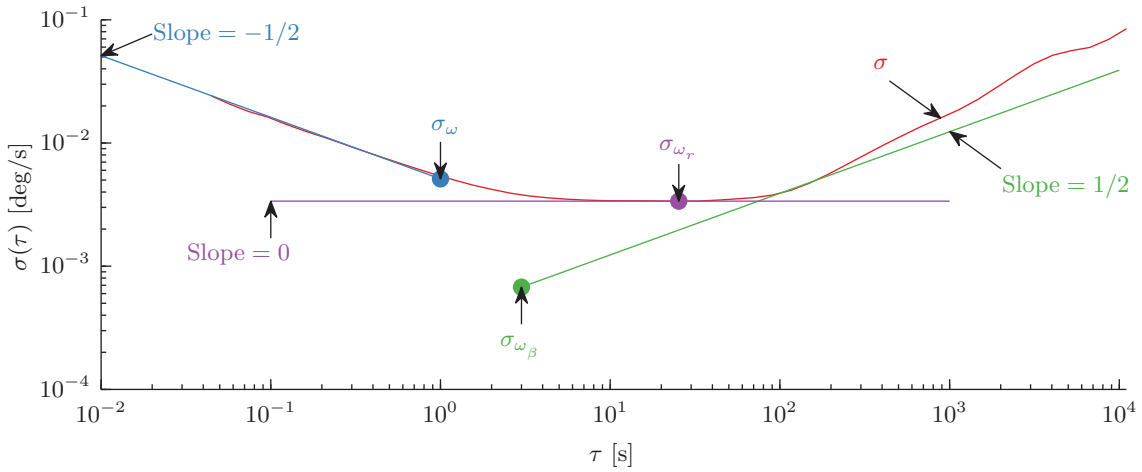

Figure 2.11: Important rate gyroscope noise statistics noted on sample Allan variance plot.

The IEEE standard for single-axis interferometric fiber optic gyros[75] states that the angle random walk, denoted here as σ_ω, is obtained from the Allan deviation value by reading the $-\frac{1}{2}$ slope line at $\tau = 1\,\text{s}$. The bias instability, σ_{ω_r}, is given by the minimum point on the Allan deviation

curve. The rate ramp, or angular acceleration white-noise process variance, σ_{ω_d} is obtained from the Allan deviation value by reading the $\frac{1}{2}$ slope line at $\tau = 3\,\text{s}$. These values are illustrated using the Allan variance of the x-axis measurements of the InvenSense MPU6515 MEMS gyroscope in Figure 2.11.

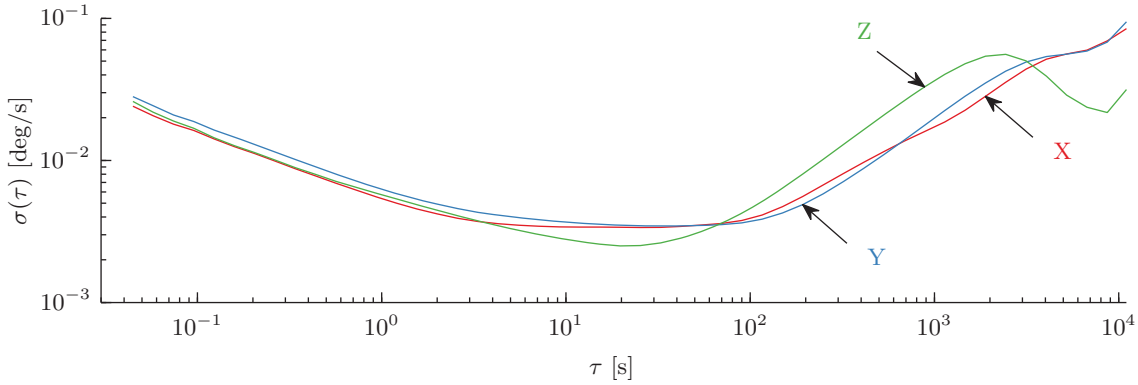

Figure 2.12: Allan variance analysis results for InvenSense MPU6515 gyroscope.

Table 2.4: Calculated rate gyro noise statistics for InvenSense MPU6515 gyroscope.

Axis	σ_ω [°/$\sqrt{\text{s}}$]	σ_{ω_r} [°/s]	σ_{ω_d} [°/s$^{3/2}$]
X	0.0051	0.0034	0.00068
Y	0.0059	0.0035	0.00062
Z	0.0052	0.0025	0.00076
Average	0.0054	0.0031	0.00068

The Allan deviations of data from all three axes of the InvenSense MPU6515 MEMS gyroscope data are shown in Figure 2.12. According to the manufacturer specifications[76] the gyro is expected to have a rate noise spectral density of $0.01\,°/(\text{s}\sqrt{\text{Hz}})$. The calculated noise statistics for the gyro are shown in Table 2.4. The measured values are fairly consistent across all three axes and the measurement rate noise spectral density is lower than the manufacturer specification. The experimentally obtained values classify this gyro as moderate grade according to Table 2.3.

The raw data for the InvenSense MPU6515 MEMS gyroscope and simulated measurements generated using Equation (2.50) are shown in Figure 2.13. Due to the randomness involved with generating the simulated data, and the discretization of the measurements, it is not expected that

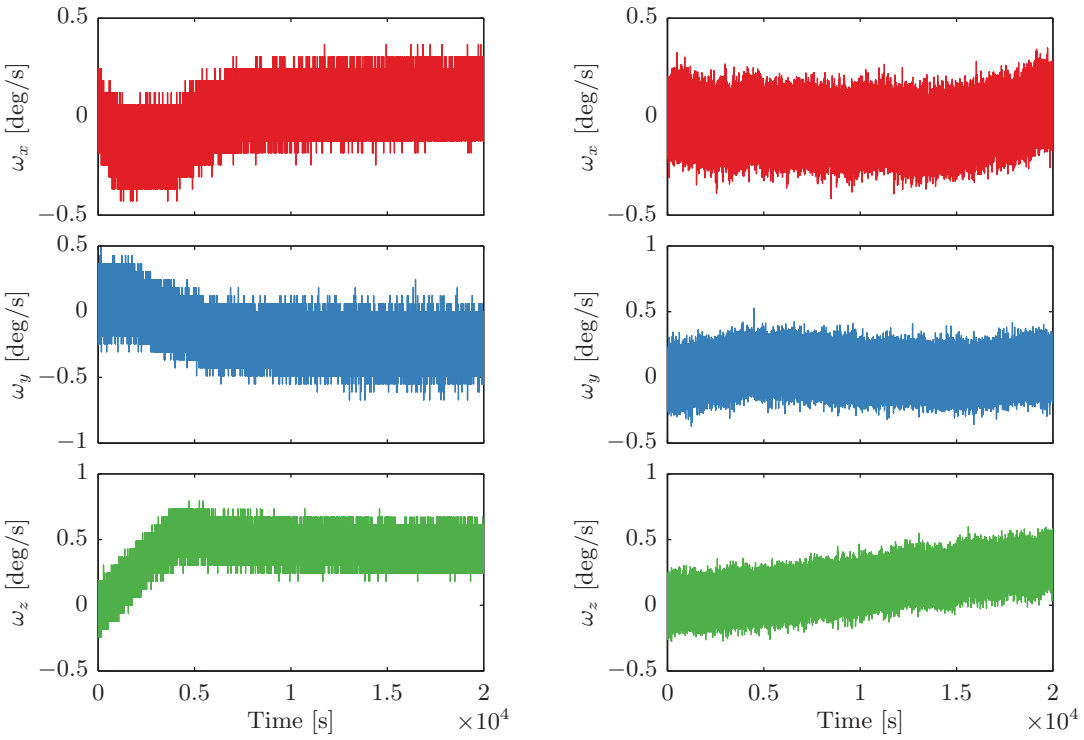

(a) Measured rate gyro data.

(b) Simulated rate gyro data.

Figure 2.13: Measured and simulated InvenSense MPU6515 gyro data.

the simulated data will exactly match the measured data. However, there is a good match between the level of noise and the magnitude of the drift after approximately 5.5 h validating the model is a good approximation of reality.

The values listed in Table 2.3 cover the noise characteristics of a rate gyros, but they do not address another key aspect of rate gyro performance for space applications: resolution. Most rate gyros are designed to provide a full scale range of hundreds, if not thousands, of degrees per second. However, in space applications it is also important to be able to distinguish very slow rotations. For MEMS gyros the minimum rotation rate that can be detected is a function of mechanical noise equivalent rotation and electronic noise equivalent rotation[77]. For the InvenSense MPU6515 gyro, the stated gyro sensitivity is between 131 LSB/°/s and 16.4 LSB/°/s depending on the maximum range of the sensor. These values correspond to a resolution of approximately 0.0076 °/s (27 °/h)

and $0.061\,^\circ/\mathrm{s}\,(220\,^\circ/\mathrm{h})$, respectively. Therefore, care must be taken when selecting rate gyros, particularly if there are high accuracy requirements with little expected motion.

2.4 ADCS Simulation Tool

The simulation software framework to be used in this research was originally created for the Community Initiative for Continuous Earth Remote Observation (CICERO)[60] satellite developed by the Laboratory for Atmospheric and Space Physics (LASP), but continues to be developed for the specific needs of this study. The framework successfully simulates the dynamics of, and the sensor inputs received by, a satellite in a low Earth orbit. Written using a combination of C and C++ programming languages, this framework contains over 250 options changeable via an input file for altering the simulation to be performed, over half of which are designed to be changed at any time to simulate the failure or fault of any of the 15 different subcomponents modeled. In addition, the framework has the ability to run Monte Carlo analyses using any of the 28 different preprogrammed perturbations and is easily modifiable to include additional perturbations.

Using this tool, a spacecraft is modeled in a 400 km altitude circular orbit with an inclination of 90° and a 60° longitude of the ascending node starting on 2015 June 1, 00:00 UTC. The accelerations due to the J_2 through J_6 Earth zonal gravitational perturbations, atmospheric drag, and solar radiation pressure (SRP) are modeled. The spacecraft is assumed to have a mass of 100 kg, a drag area of approximately $0.38\,\mathrm{m}^2$, a ballistic coefficient of 2.1, and a cross sectional area of $1.3\,\mathrm{m}^2$ subject to SRP. This orbit has a period of approximately 92.5 min and the spacecraft spends approximately 56.6 min in view of the Sun per orbit. The relative positions of the Earth and Sun are simulated using ephemeris from the NASA Navigation and Ancillary Information Facility (NAIF) SPICE toolkit[62].

For Monte Carlo analyses, the spacecraft's initial true anomaly and attitude are uniformly distributed amongst all possible values and its initial angular velocity is uniformly distributed about all three axes with a maximum value of $2.0\,^\circ/\mathrm{s}$ about each axis. Rate gyroscope measurements are simulated at 10 Hz and the rate white noise standard deviation is assumed to be $1 \times 10^{-4}\,^\circ/\sqrt{\mathrm{s}}$ with

a drift stability standard deviation of $1 \times 10^{-6}\,^{\circ}/\mathrm{s}$ over 1000 s. The spacecraft inertia is assumed $[I] = \mathrm{diag}\begin{bmatrix} 10.5 & 8.0 & 7.5 \end{bmatrix}\,\mathrm{kg\,m^2}$, and the spacecraft is assumed equipped with four reaction wheels for control purposes. In the spacecraft body frame the spin, or alignment, axes $\boldsymbol{g}_s$ for these reaction wheels are given by

$$\boldsymbol{G}_s = \begin{bmatrix} \boldsymbol{g}_{s_1} & \cdots & \boldsymbol{g}_{s_4} \end{bmatrix} = \begin{bmatrix} 0 & 0 & \cos(45^\circ) & -\cos(45^\circ) \\ \cos(45^\circ) & \sin(45^\circ) & -\sin(45^\circ) & -\sin(45^\circ) \\ \sin(45^\circ) & -\cos(45^\circ) & 0 & 0 \end{bmatrix}$$

Each reaction wheel is assumed to have a spin-axis inertia of $J_s = 0.001\,\mathrm{kgm^2}$ and a maximum torque of 30 mN m.

The alignment azimuth and elevation of each CSS is perturbed by a normally distributed angle with a standard deviation of 1°. All CSS are assumed to be affected by a common uniformly distributed calibration error between 0 % to 50 %, and normally distributed individual calibration errors with standard deviation of 2.0 %. CSS measurements are processed at 2 Hz and white Gaussian noise is added to each sensor with a standard deviation of 0.05. Irradiance due to Earth's albedo is modeled as explained in Section 2.1.2.

Chapter 3

Sun-Direction Estimators

Two classes of sun-direction estimators are examined: deterministic single-point methods and filtering algorithms. Deterministic single-point methods use sensor measurements available at a specific time while filtering algorithms combine sensor measurements over a continuous range of time with a dynamic model to estimate the sun direction.

It is important to note that accounting for the effects of Earth albedo in the measurement model of the CSS requires both orbital position information and a inertial reference sun-direction vector. For this work, it is assumed such information is not available; an example of such a situation is immediately after launch vehicle separation before ground communication has been established or an orbit determination solution has been calculated. Thus, for the estimators that follow the input due to Earth's albedo must be treated as a systematic bias V_{α_β} and Equation (2.21) is changed to

$$V = C \cdot C_\kappa \left(V_d + V_{\alpha_\beta} + \nu_V \right)$$

$$V_d = \begin{cases} \boldsymbol{n}^T \frac{\boldsymbol{s}}{\|\boldsymbol{s}\|} & \text{if } \left(\boldsymbol{n}^T \frac{\boldsymbol{s}}{\|\boldsymbol{s}\|} \geq \cos\psi \right) \wedge (B \notin \boldsymbol{\mathcal{S}}) \\ 0 & \text{if } \left(\boldsymbol{n}^T \frac{\boldsymbol{s}}{\|\boldsymbol{s}\|} < \cos\psi \right) \vee (B \in \boldsymbol{\mathcal{S}}) \end{cases} . \tag{3.1}$$

Despite this significant assumption, the estimation algorithms developed here are shown to perform coarse sun-direction estimation adequate for satellite health monitoring and safe-mode maneuvering to power-positive orientations. For the estimators that follow the quantity

$$\boldsymbol{d} \equiv C\boldsymbol{s} \tag{3.2}$$

is defined as a scaled sun-direction vector where, as noted earlier, it is assumed that all CSS share a common gross calibration factor C and some individual variation C_κ from this value.

3.1 Deterministic Single-Point Estimators

Three deterministic single-point estimators are reviewed. The first method examined is a single-point approach derived from the weighted average of all CSS measurements at a given time. A more mathematically robust, but also more complicated, single-point method follows that combines a least squares estimate and a minimum norm estimate based on the number of sensor measurements available. This second method is then expanded to include a weighting matrix to better reject noise.

3.1.1 Weighted Average (WAVG) Method

A simple deterministic estimate for the sun-direction vector is formed by taking a vector average of all the CSS capable of seeing the Sun at a single time using

$$\hat{\boldsymbol{s}} = \frac{\sum_{i=1}^{N} \hat{C}_{\kappa_i} V_i \hat{\boldsymbol{n}}_i \left[V_i > 0\right]}{\left\| \sum_{i=1}^{N} \hat{C}_{\kappa_i} V_i \hat{\boldsymbol{n}}_i \left[V_i > 0\right] \right\|} \tag{3.3}$$

where Iverson bracket notation[78] is used,

$${}^{\mathcal{B}}\hat{\boldsymbol{n}}_i = \begin{bmatrix} \cos\left(\phi_i + \hat{\phi}_{\beta_i}\right) \cos\left(\theta_i + \hat{\theta}_{\beta_i}\right) \\ \cos\left(\phi_i + \hat{\phi}_{\beta_i}\right) \sin\left(\theta_i + \hat{\theta}_{\beta_i}\right) \\ \sin\left(\phi_i + \hat{\phi}_{\beta_i}\right) \end{bmatrix} \tag{3.4}$$

is the best estimate of the ith CSS normal vector, N is the total number of CSS, $\hat{C}_{\kappa_i}$ is the best estimate of the ith CSS individual calibration scale factor nominally set to one, and the direction vectors of the CSS seeing the Sun are "weighted" by their output voltage. Nominally the bias parameters are set to $\hat{C}_{\kappa i} = 1.0$, $\hat{\theta}_\beta = 0.0$, and $\hat{\phi}_\beta = 0.0$, but they should be adjusted if better estimates become available. Because the weighted average method is a deterministic approach, the noise-free error of this method is easily calculated for any orientation of the Sun relative to the spacecraft; the resulting error map is shown in Figure 3.1.

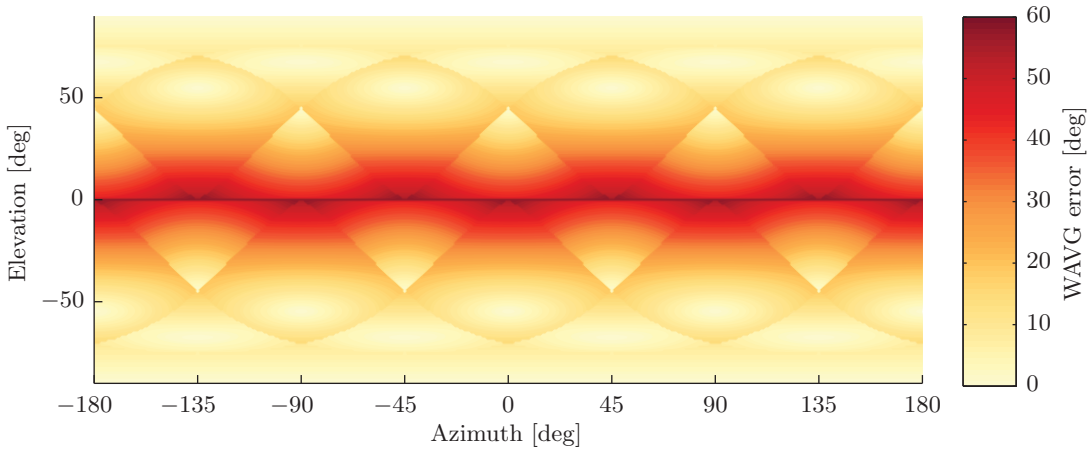

(a) Dual pyramid CSS configuration.

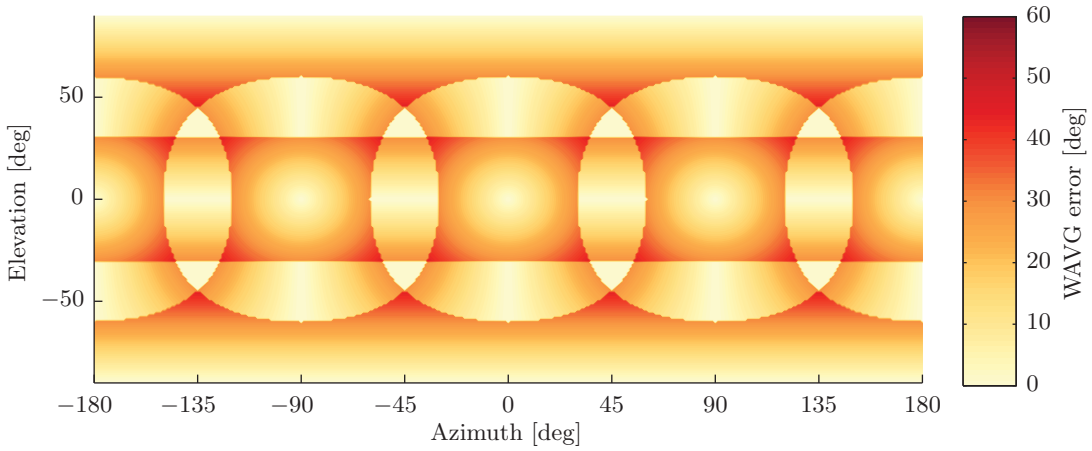

(b) Cube CSS configuration.

Figure 3.1: Weighted average method error map assuming no noise.

The desired attitude of the spacecraft requires the sun-direction vector be aligned with the $+z$ axis. For the WAVG method an error of less than 10° is maintained for the dual pyramid configuration when aligned within 19° of the reference axis; thus, the estimate becomes more precise near the goal orientation. However, for the dual pyramid configuration in Figure 3.1a, a large band near the equator of the spacecraft in which the error is greater than 30° is evident. If the Sun is within this region, near 90° from the desired orientation, a large estimation error results. But

when coupled with a control algorithm, even an approximate sun-direction estimate provides enough knowledge to apply an appropriate control effort.

This weighted average method is attractive as it is computationally simple, provides an estimate when only one sensor is seeing the Sun, and is ideally capable of estimating the sun-direction vector to within a few degrees using the configuration described previously. Additionally, if the individual CSS calibration factor deviations are assumed small, the gross calibration factor falls out of the formulation, and the WAVG method becomes insensitive to large scale calibration errors common to all sensors.

3.1.2 Least Squares Minimum Norm (LSMN) Method

A more mathematically robust method is the Least Squares Minimum Norm method that combines two methods, least squares and minimum norm, based on the number of CSS measurements available. When the number of measurements available is equal to or greater than three the least squares method is used, and when the system is underdetermined the minimum norm criteria is used.

Starting with Equation (3.1), and assuming input due to albedo V_{α_β} is small[1], the measurements for the CSS can be written in matrix form as

$$\begin{bmatrix} V_1 \\ \vdots \\ V_N \end{bmatrix} = C \left(\begin{bmatrix} \hat{C}_{\kappa_1} \hat{\boldsymbol{n}}_1 \\ \vdots \\ \hat{C}_{\kappa_N} \hat{\boldsymbol{n}}_N \end{bmatrix} \boldsymbol{s} + \begin{bmatrix} \hat{C}_{\kappa_1} \nu_{V_1} \\ \vdots \\ \hat{C}_{\kappa_N} \nu_{V_N} \end{bmatrix} \right). \tag{3.5}$$

If the calibration constant C is known, it can be substituted in and these equations solved in a least squares manner for the unit sun-direction vector $\boldsymbol{s}$. However, if C is not known, the equation can

[1] Assuming the bias due to albedo is small is a significant assumption, however, this leads to a linear form and numerical Monte Carlo results show that the resulting coarse pointing performance, when coupled with a control algorithm, is sufficiently good for coarse sun pointing.

be rewritten in terms of $\boldsymbol{d}$ instead

$$\begin{bmatrix} V_1 \\ \vdots \\ V_N \end{bmatrix} = \begin{bmatrix} \hat{C}_{\kappa_1}\hat{\boldsymbol{n}}_1 \\ \vdots \\ \hat{C}_{\kappa_N}\hat{\boldsymbol{n}}_N \end{bmatrix} \boldsymbol{d} + \begin{bmatrix} \nu_1 \\ \vdots \\ \nu_N \end{bmatrix}, \tag{3.6}$$

giving an implementation that doesn't require a priori knowledge of the calibration parameter C, reducing ground calibration requirements, and the sun-pointing control, presented later in Section 3.3.2, operates on $\boldsymbol{d}$ as well. If an estimate of C is desired, then it is simply found through $\hat{C} = \left\|\hat{\boldsymbol{d}}\right\|$ and if estimates of the individual biases are available, from ground or on-orbit calibration, they can be substituted instead of the nominal values.

The measurement equation is now in the traditional least squares form

$$\tilde{\boldsymbol{y}} = \boldsymbol{H}\boldsymbol{x} + \boldsymbol{\nu} \tag{3.7}$$

where $\tilde{\boldsymbol{y}}$ is a vector of measured CSS voltages, $\boldsymbol{H}$ is a mapping matrix, $\boldsymbol{x} = \boldsymbol{d}$ is the state vector, and $\boldsymbol{\nu}$ is a vector of measurement errors. Using the cost function

$$J_{\text{LS}}(\boldsymbol{x}) = \frac{1}{2}\boldsymbol{\nu}^T\boldsymbol{\nu} = \frac{1}{2}(\tilde{\boldsymbol{y}} - \boldsymbol{H}\boldsymbol{x})^T(\tilde{\boldsymbol{y}} - \boldsymbol{H}\boldsymbol{x}) \tag{3.8}$$

if there are at least three measurements, the best estimate of the state is given by the least squares solution[38]

$$\hat{\boldsymbol{x}} = \left(\boldsymbol{H}^T\boldsymbol{H}\right)^{-1}\boldsymbol{H}^T\tilde{\boldsymbol{y}}. \tag{3.9}$$

If, however, there are only one or two observations, the system is underdetermined and the minimum norm criterion[38]

$$\hat{\boldsymbol{x}} = \boldsymbol{H}^T\left(\boldsymbol{H}\boldsymbol{H}^T\right)^{-1}\tilde{\boldsymbol{y}} \tag{3.10}$$

is used to determine a unique solution.

The error of the LSMN method is calculated for any orientation of the Sun relative to the spacecraft, in the absence of noise, and is shown in Figure 3.2. Comparing Figure 3.1 and Figure 3.2, it can be seen that the least squares minimum norm estimate has an error that is equal to or less than the weighted average method for all orientations, and particularly less error, up to 18° less,

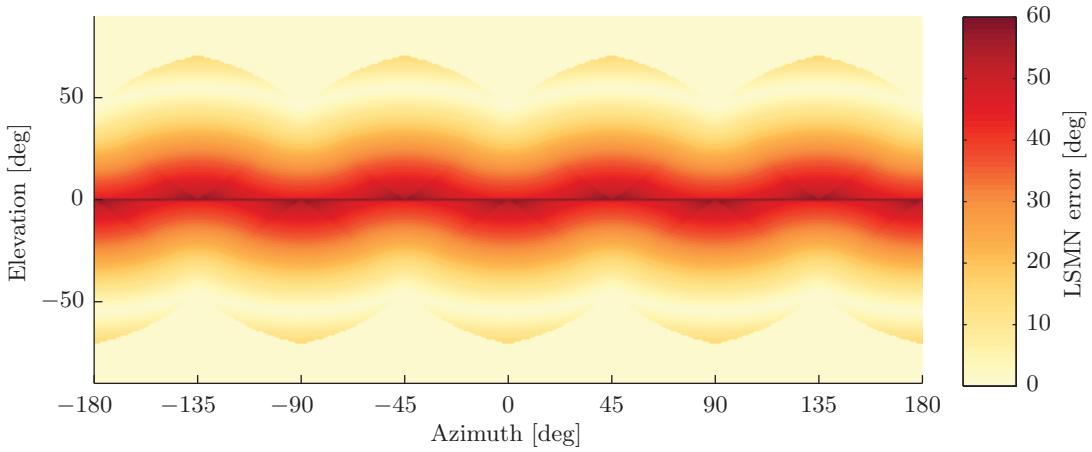

(a) Dual pyramid CSS configuration.

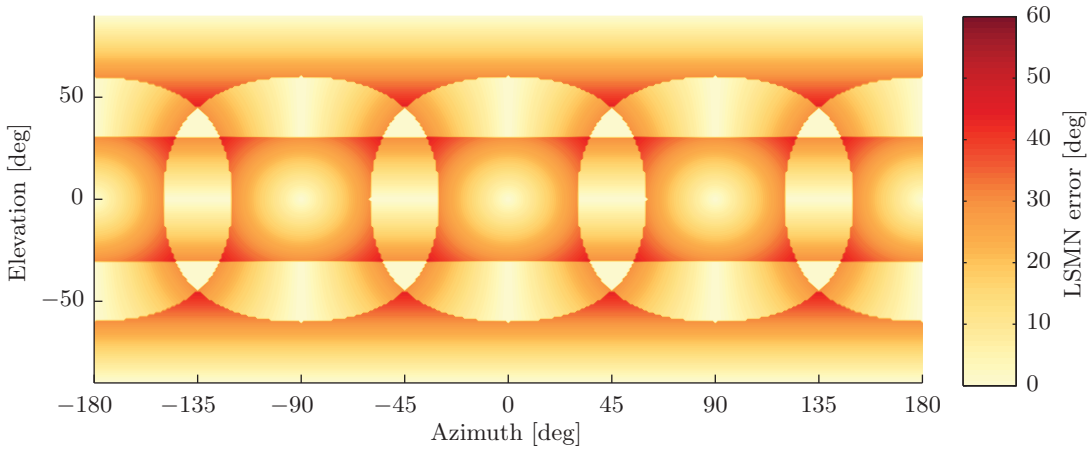

(b) Cube CSS configuration.

Figure 3.2: Least squares minimum norm method error map assuming no noise.

in regions of only two or three sensor coverage for the dual pyramid configuration. The large error regions are again near 90° from the desired orientation. For the cube configuration of CSS, the LSMN and WAVG methods are identical due to the orthogonality of the CSS normal vectors.

This method is also insensitive to large scale calibration errors, which can reduce costly pre-flight calibration requirements. As long as all CSS are calibrated to return the same voltage for a given amount of irradiance, and the common calibration factor is set so that the output doesn't saturate, there is no need to know the exact voltage when pointing straight at the Sun while in

orbit. It is important to remember that several key assumptions have been made, most notably negligible calibration errors and biases, that are not always true in flight. However, numerical simulation results, shown later, demonstrate that this method is capable of achieving coarse sun pointing despite these biases.

3.1.3 Weighted Least Squares Minimum Norm (WLSMN) Method

Least squares estimates are significantly affected by outliers, caused by noise, and in particular the LSMN method exhibits poor performance when the ratio between the voltage due to direct sunlight and the voltage due to Earth's albedo is large. The errors introduced by the inability to properly model the affect of Earth albedo, due to a lack of information, can be somewhat mitigated by augmenting the cost function in Equation (3.8) to

$$J_{\text{WLS}}(\boldsymbol{x}) = \frac{1}{2}\boldsymbol{\nu}^T\bar{\boldsymbol{W}}\boldsymbol{\nu} = \frac{1}{2}(\tilde{\boldsymbol{y}} - \boldsymbol{H}\boldsymbol{x})^T\bar{\boldsymbol{W}}(\tilde{\boldsymbol{y}} - \boldsymbol{H}\boldsymbol{x}). \tag{3.11}$$

The best estimate of the state is now given by the classic weighted least squares solution[38]

$$\hat{\boldsymbol{x}} = \left(\boldsymbol{H}^T\bar{\boldsymbol{W}}\boldsymbol{H}\right)^{-1}\boldsymbol{H}^T\bar{\boldsymbol{W}}\tilde{\boldsymbol{y}} \tag{3.12}$$

where $\bar{\boldsymbol{W}}$ is a diagonal weighting matrix. The weights of the individual CSS are set equal to their measurement; thus, the stronger voltage signals from sensors seeing the sun are weighted more than weaker signals induced by Earth's albedo. This modified method retains the desirable property of being robust to gross calibration errors common to all CSS.

Without noise, the WLSMN method has the same error map as the LSMN method shown in Figure 3.2. However, when noise is applied to the CSS measurements, differences appear. Figure 3.3 shows the difference in errors between the WLSMN and LSMN methods when $\sigma_V = 0.05$. The red regions indicate where the LSMN error is greater and the blue regions where the WLSMN error is greater. In particular, between 55° to 75° elevation, the WLSMN method is on average 5.75° more accurate then the LSMN method.

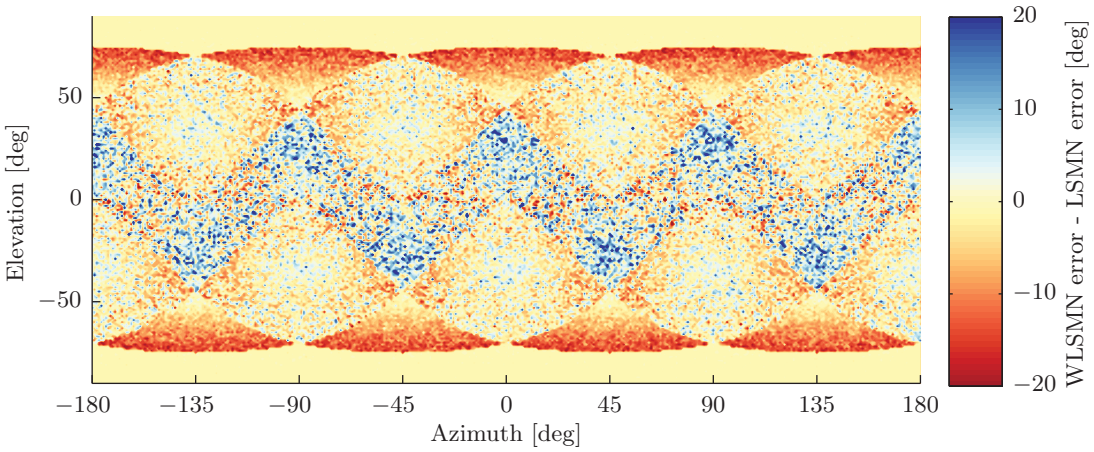

Figure 3.3: Difference in WLSMN and LSMN errors with noise for dual pyramid configuration.

3.2 Sequential Estimators

A common attitude estimation problem involves propagating the state dynamics and correcting that estimate using a direct measurement of the body's attitude. Thus, instead of solving the geometry of the CSS measurement values at any instant in time, sensor measurements are used to correct a propagated estimate of the sun-direction vector. While a single CSS measurement cannot fully determine the sun direction for the partially under-determined CSS configuration used in this study, a series of measurements coupled with the differential rotation information can determine the proper sun direction.

Two sequential filter estimators based on an extended Kalman filter approach are presented. First, a continuous-discrete extended Kalman filter formulated with non-additive noise that estimates the scaled sun-direction vector in the spacecraft body frame is presented. Second, a continuous-discrete extended consider Kalman filter is applied in which information on measurement and process biases are used to more robustly estimate the sun-direction vector. Due to the significant noise and biases present in the system care must be taken when processing measurements or measurement inconsistency can lead to filter divergence. Therefore, analysis of the measurement model inconsistencies and methods for addressing them are provided.

3.2.1 Extended Kalman Filter (EKF) Method

The Kalman filter[28] produces a statistically optimal estimate for linear systems. For nonlinear systems, such as the one investigated in this work, a linearized version of the Kalman filter, the extended Kalman filter, is commonly applied. The extended Kalman filter is based on the first-order Taylor series approximation of the state and observation equations about a reference trajectory and is a weighted least-squares or minimum l_2 norm estimator[38,79].

Because the problem being investigated is nonlinear, with non-Gaussian noise, a class of filters known as Sigma Point Kalman Filters (SPKF) could be used instead. Similar to the basic Kalman Filter, SPKFs seek to determine a state estimate which minimizes the l_2 norm of the residuals. In contrast to the EKF, they do so without linearizing the state and observation equations by propagating a discrete cluster of points that can be used to parameterize the mean and covariance of the system. One such algorithm is the Unscented Kalman Filter (UKF) proposed by Julier and Uhlmann[32] and another is the Divided Difference Filter proposed by Nørgaard, Poulsen and Ravn[33]. The UKF is based on the unscented transformation and uses a discrete set of points chosen according to a deterministic algorithm propagated through the full nonlinear equations to estimate the state and state covariance at a later time[32]. The first-order (DD1) and second-order (DD2) Divided Difference Filters are based on the work of Schei[80] and use a polynomial approximation of the nonlinear state equations obtained via interpolation[33]. These filters show performance equivalent to the linear Kalman filter and are 2nd order accurate for all nonlinear systems and 3rd order accurate for Gaussian error source distributions.

As the estimation algorithms presented will ideally be used autonomously on-board spacecraft, including small satellites with stringent computer processing restrictions, computational speed is important. Unfortunately, the UKF and divided difference filters have been shown to take three times the computation time as the EKF for even basic problems[34]. The EKF approach is used as it is computationally faster and exhibits promising results. Future work will have to investigate the implementation of a nonlinear estimation approach.

3.2.1.1 Continuous-Discrete Extended Kalman Filter

The equations for a continuous-discrete extended Kalman filter with non-additive noise are presented here as review. Detailed derivations of the extended Kalman filter can be found in References 38, 79, and 81. Assume the continuous-time state dynamics, for a nonlinear system with discrete-time measurements, are given by

$$\dot{\boldsymbol{x}}(t) = \boldsymbol{f}(\boldsymbol{x}(t)\,, \boldsymbol{u}(t)\,, \boldsymbol{\eta}(t)\,, t) \tag{3.13a}$$

$$\boldsymbol{y}_k = \boldsymbol{h}_k(\boldsymbol{x}_k, \boldsymbol{\nu}_k, t_k) \tag{3.13b}$$

where $\boldsymbol{x}(t)$ is the state vector, $\boldsymbol{f}$ represents the system dynamics, $\boldsymbol{u}(t)$ is the control input, and $\boldsymbol{y}_k$ is the discrete-time measurement expression. The process noise $\boldsymbol{\eta}(t)$ is continuous-time white-noise with spectral density $\boldsymbol{Q}(t)$

$$\mathrm{E}[\boldsymbol{\eta}(t)] = \boldsymbol{0} \tag{3.14a}$$

$$\mathrm{E}\big[\boldsymbol{\eta}(t)\,\boldsymbol{\eta}^T(\tau)\big] = \boldsymbol{Q}(t)\,\delta(t-\tau) \tag{3.14b}$$

and the measurement noise $\boldsymbol{\nu}_k$ is discrete-time white-noise with covariance $\boldsymbol{R}_k$ [79,81]

$$\mathrm{E}[\boldsymbol{\nu}_k] = \boldsymbol{0} \tag{3.15a}$$

$$\mathrm{E}\big[\boldsymbol{\nu}_k\boldsymbol{\nu}_j^T\big] = \boldsymbol{R}_k\delta_{jk} \;\forall\; j,k \tag{3.15b}$$

where δ_{jk} is the Kronecker delta. It is assumed that the process and measurement noises are uncorrelated.

The extended Kalman filter operates as a "predictor-corrector" algorithm where the state and covariance are first propagated, denoted by a superscript $-$, using the state dynamics model and then updated, denoted by a superscript $+$, when measurements are available. The state and covariance estimates, $\hat{\boldsymbol{x}}(t)$ and $\hat{\boldsymbol{P}}(t)$, are initialized using

$$\hat{\boldsymbol{x}}(t_0) = \mathrm{E}[\boldsymbol{x}(t_0)] \tag{3.16}$$

$$\hat{\boldsymbol{P}}(t_0) = \mathrm{E}\Big[\left(\hat{\boldsymbol{x}}(t_0) - \boldsymbol{x}(t_0)\right)\left(\hat{\boldsymbol{x}}(t_0) - \boldsymbol{x}(t_0)\right)^T\Big] \tag{3.17}$$

where E[·] is the expected value operator. The continuous-time state and covariance propagations equations are given by

$$\dot{\hat{\boldsymbol{x}}}(t) = \boldsymbol{f}(\hat{\boldsymbol{x}}(t)\,, \boldsymbol{u}(t)\,, \boldsymbol{\eta}_0(t)\,, t) \tag{3.18}$$

$$\dot{\boldsymbol{P}}(t) = \boldsymbol{F}(t)\,\boldsymbol{P}(t) + \boldsymbol{P}(t)\,\boldsymbol{F}^T(t) + \boldsymbol{G}(t)\,\boldsymbol{Q}(t)\,\boldsymbol{G}^T(t) \tag{3.19}$$

where the nominal process noise $\boldsymbol{\eta}_0(t) = 0$ and

$$\boldsymbol{F}(t) \equiv \left.\frac{\partial \boldsymbol{f}}{\partial \boldsymbol{x}}\right|_{\hat{\boldsymbol{x}},\boldsymbol{u}} \tag{3.20a}$$

$$\boldsymbol{G}(t) \equiv \left.\frac{\partial \boldsymbol{f}}{\partial \boldsymbol{\eta}}\right|_{\hat{\boldsymbol{x}},\boldsymbol{u}} \tag{3.20b}$$

. Finally, the discrete-time state and covariance measurement update equations are given by

$$\boldsymbol{W}_k = \boldsymbol{H}_k \boldsymbol{P}_k^- \boldsymbol{H}_k^T + \boldsymbol{M}_k \boldsymbol{R}_k \boldsymbol{M}_k^T \tag{3.21}$$

$$\boldsymbol{K}_k = \boldsymbol{P}_k^- \boldsymbol{H}_k^T \boldsymbol{W}_k^{-1} \tag{3.22}$$

$$\hat{\boldsymbol{x}}_k^+ = \hat{\boldsymbol{x}}_k^- + \boldsymbol{K}_k \left[\boldsymbol{y}_k - \boldsymbol{h}_k\big(\hat{\boldsymbol{x}}_k^-, \boldsymbol{v}_0, t_k\big)\right] \tag{3.23}$$

$$\hat{\boldsymbol{P}}_k^+ = (\boldsymbol{I} - \boldsymbol{K}_k \boldsymbol{H}_k)\,\hat{\boldsymbol{P}}_k^-\,(\boldsymbol{I} - \boldsymbol{K}_k \boldsymbol{H}_k)^T + \boldsymbol{K}_k \boldsymbol{M}_k \boldsymbol{R}_k \boldsymbol{M}_k^T \boldsymbol{K}_k^T \tag{3.24}$$

where $\boldsymbol{W}_k$ is the innovation covariance, the nominal measurement noise $\boldsymbol{v}_0 = 0$, the Joseph form[82] of the covariance update is used to improve numerical stability, and

$$\boldsymbol{H}_k \equiv \left.\frac{\partial \boldsymbol{h}_k}{\partial \boldsymbol{x}_k}\right|_{\hat{\boldsymbol{x}}_k^-} \tag{3.25a}$$

$$\boldsymbol{M}_k \equiv \left.\frac{\partial \boldsymbol{h}_k}{\partial \boldsymbol{\nu}_k}\right|_{\hat{\boldsymbol{x}}_k^-} \tag{3.25b}$$

are evaluated using the current best estimate of the state. Note that when Equation (3.22) is used for the Kalman gain, Equation (3.24) can be reduced to

$$\hat{\boldsymbol{P}}_k^+ = \hat{\boldsymbol{P}}_k^- - \boldsymbol{K}_k \boldsymbol{W}_k \boldsymbol{K}_k^T, \tag{3.26}$$

but may suffer from numerical issues in this form.

3.2.1.2 EKF Based Sun-Direction Estimator

When using a sequential filter to perform attitude estimation it is common to estimate an absolute attitude, expressed as a quaternion or Modified Rodrigues Parameter (MRP) set [83]. It has been shown that one can estimate such an attitude, in addition to scale factor and alignment calibration factors, for coarse sun sensors [5]. However, this approach requires additional information, such as measurements from a star tracker or orbit information, to generate a reference sun-direction vector. An analysis of the posterior Cramér-Rao lower bound for systems with only CSS measurements available shows the rate gyro bias to be unobservable. More information on the calculation of the Cramér-Rao Lower Bound and the Fisher information matrix can be found in Appendix C. Estimation approaches for when additional measurement information is available are discussed in detail in Chapter 4, whereas here the estimation of the sun-direction vector using only CSS and a rate gyro is investigated.

The state vector is chosen to be the scaled sun-direction vector, defined in Equation (3.2), in the body frame

$$\boldsymbol{x}(t) = \left[{}^{\mathcal{B}}\boldsymbol{d}(t) \right]. \tag{3.27}$$

While it would be more optimal to enforce the unit-norm constraint on the unit sun-direction and estimate the common calibration coefficient separately, for a system with only CSS and rate gyro measurements the common calibration coefficient is unobservable; and the measurement equation requires an estimate of the common calibration scale factor. However, combining the common scale factor and the unit sun-direction vector into a single vector value results in a quantity that can be estimated with the added benefit that the estimator is insensitive to uncertainty in the common CSS scale factor.

It is assumed that angular velocity measurements are provided via a rate gyro and that the rate gyro measurements follow Farrenkopf's approximation [68] modified to account for angular velocity measurements taken in a frame $\mathcal{G}$ local to the rate gyro, as opposed to the body frame $\mathcal{B}$,

$${}^{\mathcal{G}}\tilde{\boldsymbol{\omega}}(t) = [GB]\, {}^{\mathcal{B}}\boldsymbol{\omega}(t) + {}^{\mathcal{G}}\boldsymbol{\omega}_{\beta}(t) + {}^{\mathcal{G}}\boldsymbol{\eta}_{\omega}(t) \tag{3.28a}$$

$$^{\mathcal{G}}\dot{\boldsymbol{\omega}}_{\beta}(t) = {}^{\mathcal{G}}\boldsymbol{\eta}_{\omega_d}(t) \tag{3.28b}$$

where $^{\mathcal{B}}\boldsymbol{\omega}$ is the true body angular velocity in the body frame, $^{\mathcal{G}}\tilde{\boldsymbol{\omega}}$ is the measured body angular velocity in the frame of the rate gyro, $[GB]$ maps vectors written in the body frame $\mathcal{B}$ into vectors written in the gyroscope frame $\mathcal{G}$, $^{\mathcal{G}}\boldsymbol{\omega}_{\beta}$ is the measurement bias, and $^{\mathcal{G}}\boldsymbol{\eta}_{\omega}$ and $^{\mathcal{G}}\boldsymbol{\eta}_{\omega_d}$ are zero-mean Gaussian white-noise processes with spectral densities given by $\sigma_{\omega}^2\boldsymbol{I}_{3\times3}$ and $\sigma_{\omega_d}^2\boldsymbol{I}_{3\times3}$, respectively. Assuming for time scales of interest the inertial sun vector is constant, the dynamics of the scaled sun-direction vector are written as

$$\frac{^{\mathcal{B}}\mathrm{d}}{\mathrm{d}t}\left[{}^{\mathcal{B}}\boldsymbol{d}(t)\right] = {}^{\mathcal{B}}\boldsymbol{d}(t) \times [BG]\left({}^{\mathcal{G}}\tilde{\boldsymbol{\omega}}(t) - {}^{\mathcal{G}}\hat{\boldsymbol{\omega}}_{\beta}(t) - {}^{\mathcal{G}}\boldsymbol{\eta}_{\omega}(t)\right) - {}^{\mathcal{B}}\boldsymbol{\eta}_{s}(t) \tag{3.29}$$

where $^{\mathcal{G}}\hat{\boldsymbol{\omega}}_{\beta}(t)$ is the best estimate of the rate gyro bias, determined a priori, and $\boldsymbol{\eta}_s$ is a zero-mean Gaussian white-noise process with $\mathrm{E}\left[\boldsymbol{\eta}_s(t)\,\boldsymbol{\eta}_s(\tau)^T\right] = \sigma_s^2\delta(t-\tau)\,\boldsymbol{I}_{3\times3}$. Equation (3.1) is modified

$$V = \|\boldsymbol{d}_k\| \cdot \hat{C}_{\kappa}\left(V_d + \nu_V\right)$$

$$V_d = \begin{cases} \boldsymbol{n}^T\frac{\boldsymbol{d}}{\|\boldsymbol{d}\|} & \text{if } \left(\boldsymbol{n}^T\frac{\boldsymbol{d}}{\|\boldsymbol{d}\|} \geq \cos\psi\right) \wedge \left(B \notin \boldsymbol{\mathcal{S}}\right) \\ 0 & \text{if } \left(\boldsymbol{n}^T\frac{\boldsymbol{d}}{\|\boldsymbol{d}\|} < \cos\psi\right) \vee \left(B \in \boldsymbol{\mathcal{S}}\right) \end{cases}$$

and used for the measurement model.

It is important to note that the rate gyro bias is not estimated, but neither is it random Gaussian noise. Similarly, the calibration coefficients C_{κ_i}, θ_{β_i}, and ϕ_{β_i}, also represent systematic biases. One common method, and the method used here, of dealing with such biases is suitably inflating the state and measurement process noise through numerical Monte Carlo simulation to ensure the covariance of the system encompasses the expected statistical error due to this bias[39]. It is acknowledged that this method is not optimal, due to the significant nature of the biases, but it does provide a bounded estimate for this system when no other information is available. More rigorous methods for dealing with these biases include: estimating the biases; however, an analysis of the posterior Cramér-Rao lower bound[84,85] for this system shows the rate gyro bias is unobservable given only CSS and rate gyro measurements; and considering them, as will be explored in Section 3.2.2.

Defining the noise vectors as

$$\boldsymbol{\eta}(t) = \begin{bmatrix} {}^{\mathcal{B}}\boldsymbol{\eta}_s(t) \\ {}^{\mathcal{G}}\boldsymbol{\eta}_\omega(t) \end{bmatrix}, \quad \boldsymbol{\nu}_k = \boldsymbol{\nu}_{V_k} \tag{3.30}$$

the key values for the implementation of this EKF are given by

$$\boldsymbol{F}(t) = \begin{bmatrix} -\left[[BG]\,{}^{\mathcal{G}}\tilde{\boldsymbol{\omega}}(t)\right]_\times \end{bmatrix} \tag{3.31a}$$

$$\boldsymbol{G}(t) = \begin{bmatrix} -\boldsymbol{I}_{3\times 3} & -\left[{}^{\mathcal{B}}\hat{\boldsymbol{d}}(t)\right]_\times [BG] \end{bmatrix} \tag{3.31b}$$

$$\boldsymbol{H}_k = \begin{bmatrix} H_{1,k} & \cdots & H_{N,k} \end{bmatrix}^T$$

$$H_{i,k} = \begin{cases} \hat{C}_{\kappa_i}\,{}^{\mathcal{B}}\hat{\boldsymbol{n}}_i & \text{if } \hat{\boldsymbol{n}}_i^T \frac{\hat{\boldsymbol{d}}_k}{\|\hat{\boldsymbol{d}}_k\|} \geq \cos\psi_i \\ \boldsymbol{0} & \text{if } \hat{\boldsymbol{n}}_i^T \frac{\hat{\boldsymbol{d}}_k}{\|\hat{\boldsymbol{d}}_k\|} < \cos\psi_i \end{cases} \tag{3.31c}$$

$$\boldsymbol{M}_k = \left\|\hat{\boldsymbol{d}}_k\right\| \operatorname{diag}\left(\hat{\boldsymbol{C}}_\kappa\right) \tag{3.31d}$$

where $[\cdot]_\times$ represents the skew-symmetric cross product matrix given by

$$\boldsymbol{a} = \begin{bmatrix} a_1 \\ a_2 \\ a_3 \end{bmatrix}, \quad [\boldsymbol{a}]_\times = \begin{bmatrix} 0 & -a_3 & a_2 \\ a_3 & 0 & -a_1 \\ -a_2 & a_1 & 0 \end{bmatrix}.$$

The measurement model given by Equation (3.1) does a good job of approximating the physical response of the CSS, but if the current estimate of the sun direction is not within the field of view of the sensor the corresponding row of the Kalman gain is equal to zero and the measurement does not impact the current state estimate. This results in strong measurements due to direct sunlight being ignored if the current estimate of the sun direction is in significant error, which can significantly impact performance when starting with no knowledge of the spacecraft attitude. Therefore, the measurement model is modified to include observations, albeit with increased measurement uncertainty, that are above 50 % of the expected maximum output. This improves the performance when initially lost in space, but does not impact steady state performance[2].

[2]Care should be taken when including strong measurements that don't align with the current estimate. While this can significantly improve performance for a lost in space scenario, it can also result in albedo measurements

This EKF estimation method offers a novel attitude estimation solution when faced with minimal sensor input due to sensor failure or power restrictions. While not optimal, numerical simulation shows this approach does provide significant improvement over the estimates given by the single-point estimation techniques described previously. Similar to those single-point techniques, the EKF-based approach is also insensitive to gross calibration errors common to all CSS.

3.2.2 Continuous-Discrete Extended Consider Kalman Filter (ECKF) Method

As noted previously, the measurement model for the CSS, Equation (2.21), and the dynamics model for the rate gyro, Equation (2.23a), have several biases. These parameters have a known a priori distribution, but remain unknown throughout the estimation procedure. Such bias errors can be treated in four ways: neglected, compensated for with process noise, estimated, or considered[38,39].

Neglecting the impact of the biases is a reasonable solution when the parameters have low impact on the dynamics. Compensation via process noise usually involves Monte Carlo analysis to numerically bound the uncertainty that is unaccounted for mathematically, and can be time consuming and tedious. Expanding the state vector of the system to estimate such biases is an excellent way to account for their effects, if doing so doesn't overly increase the computational burden and the system is sufficiently observable. The final option is to "consider" the effect of the biases; in this case the biases are not estimated directly, but their uncertainty is included in the calculation of the system covariance. Consider analysis provides an excellent middle ground between ignoring and estimating the biases when the biases themselves have low observability.

3.2.2.1 Continuous-Discrete Extended Consider Kalman Filter

Initially presented by Schmidt[35], more recent derivations of the Consider Kalman Filter have been published by Jazwinski[37]; Tapley, Shutz, and Born[38]; Woodbury and Junkins[39]; and Zanetti and Bishop[40]. The continuous-discrete extended consider Kalman filter presented here is

being considered if the calibration scale factors of the CSS are significantly uncertain. The erroneous inclusion of strong albedo measurements can subsequently cause the filter to become inconsistent.

adapted from the work of Zanetti and Bishop with modifications for continuous-time propagation and non-constant biases.

Consider a system with the augmented state vector given by

$$\boldsymbol{z}(t) = \begin{bmatrix} \boldsymbol{x}(t) \\ \boldsymbol{\beta}_\eta(t) \\ \boldsymbol{\beta}_\nu(t) \end{bmatrix} \tag{3.32}$$

where $\boldsymbol{x}$ is the vector of states to be estimated, $\boldsymbol{\beta}_\eta$ is a dynamic model bias with

$$\begin{aligned} \mathrm{E}\Big[\Big(\hat{\boldsymbol{\beta}}_\eta(t) - \boldsymbol{\beta}_\eta(t)\Big)\Big] &= \mathbf{0} \\ \mathrm{E}\Big[\Big(\hat{\boldsymbol{\beta}}_\eta(t) - \boldsymbol{\beta}_\eta(t)\Big)\Big(\hat{\boldsymbol{\beta}}_\eta(\tau) - \boldsymbol{\beta}_\eta(\tau)\Big)^T\Big] &= \boldsymbol{B}_\eta(t)\,\delta\left(t-\tau\right) \\ \mathrm{E}\Big[\left(\hat{\boldsymbol{x}}(t) - \boldsymbol{x}(t)\right)\Big(\hat{\boldsymbol{\beta}}_\eta(\tau) - \boldsymbol{\beta}_\eta(\tau)\Big)^T\Big] &= \boldsymbol{L}(t)\,\delta\left(t-\tau\right) \\ \mathrm{E}\Big[\Big(\hat{\boldsymbol{\beta}}_\eta(t) - \boldsymbol{\beta}_\eta(t)\Big)\left(\hat{\boldsymbol{x}}(\tau) - \boldsymbol{x}(\tau)\right)^T\Big] &= \boldsymbol{L}^T(t)\,\delta\left(t-\tau\right) \end{aligned} \tag{3.33}$$

and $\boldsymbol{\beta}_\nu$ is a measurement equation bias with

$$\begin{aligned} \mathrm{E}\Big[\Big(\hat{\boldsymbol{\beta}}_\nu(t) - \boldsymbol{\beta}_\nu(t)\Big)\Big] &= \mathbf{0} \\ \mathrm{E}\Big[\Big(\hat{\boldsymbol{\beta}}_\nu(t) - \boldsymbol{\beta}_\nu(t)\Big)\Big(\hat{\boldsymbol{\beta}}_\nu(\tau) - \boldsymbol{\beta}_\nu(\tau)\Big)^T\Big] &= \boldsymbol{B}_\nu(t)\,\delta\left(t-\tau\right) \\ \mathrm{E}\Big[\left(\hat{\boldsymbol{x}}(t) - \boldsymbol{x}(t)\right)\Big(\hat{\boldsymbol{\beta}}_\nu(\tau) - \boldsymbol{\beta}_\nu(\tau)\Big)^T\Big] &= \boldsymbol{\Lambda}(t)\,\delta\left(t-\tau\right) \\ \mathrm{E}\Big[\Big(\hat{\boldsymbol{\beta}}_\nu(t) - \boldsymbol{\beta}_\nu(t)\Big)\left(\hat{\boldsymbol{x}}(\tau) - \boldsymbol{x}(\tau)\right)^T\Big] &= \boldsymbol{\Lambda}^T(t)\,\delta\left(t-\tau\right). \end{aligned} \tag{3.34}$$

Similar to the augmented state vector, the covariance matrix can be written in block form as

$$\boldsymbol{P}_z(t) = \mathrm{E}\Big[\left(\hat{\boldsymbol{z}}(t) - \boldsymbol{z}(t)\right)\left(\hat{\boldsymbol{z}}(t) - \boldsymbol{z}(t)\right)^T\Big] = \begin{bmatrix} \boldsymbol{P}_x(t) & \boldsymbol{L}(t) & \boldsymbol{\Lambda}(t) \\ \boldsymbol{L}^T(t) & \boldsymbol{B}_\eta(t) & \mathbf{0} \\ \boldsymbol{\Lambda}^T(t) & \mathbf{0} & \boldsymbol{B}_\nu(t) \end{bmatrix} \tag{3.35}$$

where it is assumed the bias vectors are uncorrelated with either the measurement or dynamic process noise. The process noise is written as

$$\boldsymbol{\eta}(t) = \begin{bmatrix} \boldsymbol{\eta}_x(t) \\ \boldsymbol{\eta}_{\beta_\eta}(t) \end{bmatrix} \tag{3.36}$$

with

$$\mathrm{E}\big[\boldsymbol{\eta}(t)\,\boldsymbol{\eta}^T(\tau)\big] = \boldsymbol{Q}_z\delta(t-\tau) = \begin{bmatrix} \boldsymbol{Q}_x(t) & \mathbf{0} \\ \mathbf{0} & \boldsymbol{Q}_{\beta_\eta}(t) \end{bmatrix} \tag{3.37}$$

to allow for time varying process noise values, for example rate gyroscopes biases exhibiting random walk.

The continuous-time state dynamics are assumed to be of the form

$$\begin{bmatrix} \dot{\boldsymbol{x}}(t) \\ \dot{\boldsymbol{\beta}}_\eta(t) \\ \dot{\boldsymbol{\beta}}_\nu(t) \end{bmatrix} = \begin{bmatrix} \boldsymbol{f}_x\big(\boldsymbol{x}(t)\,,\boldsymbol{\beta}_\eta(t)\,,\boldsymbol{u}(t)\,,\boldsymbol{\eta}_x(t)\,,t\big) \\ \boldsymbol{f}_{\beta_\eta}\Big(\boldsymbol{\eta}_{\beta_\eta}(t)\,,t\Big) \\ 0.0 \end{bmatrix} \tag{3.38}$$

assuming the measurement biases are constant and the dynamic model biases are functions of time. It can be shown that the propagation of the state covariance for this system is given by

$$\dot{\boldsymbol{P}}_z(t) = \boldsymbol{\Theta}(t)\,\boldsymbol{P}_z(t) + \boldsymbol{P}_z(t)\,\boldsymbol{\Theta}^T(t) + \boldsymbol{\Upsilon}(t)\,\boldsymbol{Q}_z(t)\,\boldsymbol{\Upsilon}^T(t) \tag{3.39}$$

where

$$\boldsymbol{\Theta}(t) = \begin{bmatrix} \boldsymbol{F}(t) & \boldsymbol{S}(t) & \mathbf{0} \\ \mathbf{0} & \mathbf{0} & \mathbf{0} \\ \mathbf{0} & \mathbf{0} & \mathbf{0} \end{bmatrix}, \quad \boldsymbol{\Upsilon}_k = \begin{bmatrix} \boldsymbol{G}(t) & \mathbf{0} \\ \mathbf{0} & \boldsymbol{G}_{\beta_\eta}(t) \\ \mathbf{0} & \mathbf{0} \end{bmatrix}, \tag{3.40}$$

and

$$\boldsymbol{F}(t) = \left.\frac{\partial \boldsymbol{f}_x}{\partial \boldsymbol{x}}\right|_{\hat{\boldsymbol{z}},\hat{\boldsymbol{\beta}}_\eta,\boldsymbol{u}} \tag{3.41a}$$

$$\boldsymbol{S}(t) = \left.\frac{\partial \boldsymbol{f}_x}{\partial \boldsymbol{\beta}_\eta}\right|_{\hat{\boldsymbol{z}},\hat{\boldsymbol{\beta}}_\eta,\boldsymbol{u}} \tag{3.41b}$$

$$\boldsymbol{G}(t) = \left.\frac{\partial \boldsymbol{f}_x}{\partial \boldsymbol{\eta}_x}\right|_{\hat{\boldsymbol{z}},\hat{\boldsymbol{\beta}}_\eta,\boldsymbol{u}} \tag{3.41c}$$

$$\boldsymbol{G}_{\beta_\eta}(t) = \left.\frac{\partial \boldsymbol{f}_{\beta_\eta}}{\partial \boldsymbol{\eta}_{\beta_\eta}}\right|_{\hat{\boldsymbol{z}},\hat{\boldsymbol{\beta}}_\eta,\boldsymbol{u}}. \tag{3.41d}$$

Alternatively, using Equation (3.35) this can be written in terms of the block matrices as

$$\dot{\boldsymbol{P}}_x(t) = \boldsymbol{F}(t)\,\boldsymbol{P}_x(t) + \boldsymbol{P}_x(t)\,\boldsymbol{F}^T(t) + \boldsymbol{S}(t)\,\boldsymbol{L}^T(t) + \boldsymbol{L}(t)\,\boldsymbol{S}^T(t) + \boldsymbol{G}(t)\,\boldsymbol{Q}_x(t)\,\boldsymbol{G}^T(t) \tag{3.42a}$$

$$\dot{\boldsymbol{L}}(t) = \boldsymbol{F}(t)\,\boldsymbol{L}(t) + \boldsymbol{S}(t)\,\boldsymbol{B}_{\eta}(t) \tag{3.42b}$$

$$\dot{\boldsymbol{\Lambda}}(t) = \boldsymbol{F}(t)\,\boldsymbol{\Lambda}(t) \tag{3.42c}$$

$$\dot{\boldsymbol{B}}_{\eta}(t) = \boldsymbol{G}_{\beta_\eta}(t)\,\boldsymbol{Q}_{\beta_\eta}(t)\,\boldsymbol{G}_{\beta_\eta}^{T}(t) \tag{3.42d}$$

$$\dot{\boldsymbol{B}}_{\nu}(t) = \boldsymbol{0}. \tag{3.42e}$$

The discrete-time measurements are assumed to be of the form

$$\boldsymbol{y}_k = \boldsymbol{h}(\boldsymbol{z}_k, \boldsymbol{u}_k, \boldsymbol{\nu}_k, t_k) \tag{3.43}$$

where the measurement noise $\boldsymbol{\nu}_k$ is as defined in Section 3.2.1.1. The state update due to a measurement is given by

$$\hat{\boldsymbol{z}}_k^{+} = \hat{\boldsymbol{z}}_k^{-} + \boldsymbol{K}_k\,(\boldsymbol{y}_k - \hat{\boldsymbol{y}}_k) \tag{3.44}$$

where the Kalman gain, written in block matrix form,

$$\boldsymbol{K}_k = \begin{bmatrix} \boldsymbol{K}_{x,k} \\ \boldsymbol{K}_{b_\eta,k} \\ \boldsymbol{K}_{b_\nu,k} \end{bmatrix} \tag{3.45}$$

is not yet specified. The state covariance update equations are given by

$$\boldsymbol{P}_{z,k}^{+} = \boldsymbol{P}_{z,k}^{-} - \boldsymbol{P}_{z,k}^{-}\boldsymbol{Y}_k^{T}\boldsymbol{K}_k - \boldsymbol{K}_k\boldsymbol{Y}_k\boldsymbol{P}_{z,k}^{-} + \boldsymbol{K}_k\boldsymbol{W}_k\boldsymbol{K}_k^{T} \tag{3.46}$$

where

$$\begin{aligned} \boldsymbol{W}_k &= \boldsymbol{Y}_k\boldsymbol{P}_{z,k}^{-}\boldsymbol{Y}_k^{T} + \boldsymbol{M}_k\boldsymbol{R}_k\boldsymbol{M}_k^{T} \\ &= \boldsymbol{H}_k\boldsymbol{P}_{x,k}^{-}\boldsymbol{H}_k^{T} + \boldsymbol{J}_k\left(\boldsymbol{\Lambda}_k^{-}\right)^{T}\boldsymbol{H}_k^{T} + \boldsymbol{H}_k\boldsymbol{\Lambda}_k^{-}\boldsymbol{J}_k^{T} + \boldsymbol{J}_k\boldsymbol{B}_{\nu}\boldsymbol{J}_k^{T} + \boldsymbol{M}_k\boldsymbol{R}_k\boldsymbol{M}_k^{T} \end{aligned} \tag{3.47}$$

$$\boldsymbol{Y}_k = \begin{bmatrix} \boldsymbol{H}_k & \boldsymbol{0} & \boldsymbol{J}_k \end{bmatrix} \tag{3.48}$$

and

$$\boldsymbol{H}_k = \left.\frac{\partial \boldsymbol{h}_k}{\partial \boldsymbol{x}_k}\right|_{\hat{\boldsymbol{x}}_k^{-},\hat{\boldsymbol{\beta}}_{\nu,k}^{-}} \tag{3.49a}$$

$$\boldsymbol{J}_k = \left.\frac{\partial \boldsymbol{h}_k}{\partial \boldsymbol{\beta}_{\nu}}\right|_{\hat{\boldsymbol{x}}_k^{-},\hat{\boldsymbol{\beta}}_{\nu,k}^{-}} \tag{3.49b}$$

$$\boldsymbol{M}_k = \left.\frac{\partial \boldsymbol{h}_k}{\partial \boldsymbol{\nu}_k}\right|_{\hat{\boldsymbol{x}}_k^-, \hat{\boldsymbol{\beta}}_{\nu,k}^-}. \tag{3.49c}$$

Alternatively, using Equation (3.35), Equation (3.46) can be written in terms of the block matrices as

$$\boldsymbol{P}_{x,k}^+ = \boldsymbol{P}_{x,k}^- - \boldsymbol{K}_{x,k}\left(\boldsymbol{H}_k\boldsymbol{P}_{x,k}^- + \boldsymbol{J}_k\left(\boldsymbol{\Lambda}_k^-\right)^T\right) - \left(\boldsymbol{P}_{x,k}^-\boldsymbol{H}_k^T + \boldsymbol{\Lambda}_k^-\boldsymbol{J}_k^T\right)\boldsymbol{K}_{x,k}^T + \boldsymbol{K}_{x,k}\boldsymbol{W}_k\boldsymbol{K}_{x,k}^T \tag{3.50a}$$

$$\boldsymbol{L}_k^+ = \left(\boldsymbol{I} - \boldsymbol{K}_{x,k}\boldsymbol{H}_k\right)\boldsymbol{L}_k^- - \left(\boldsymbol{P}_{x,k}^-\boldsymbol{H}_k^T + \boldsymbol{\Lambda}_k^-\boldsymbol{J}_k^T\right)\boldsymbol{K}_{b_\eta,k}^T + \boldsymbol{K}_{x,k}\boldsymbol{W}_k\boldsymbol{K}_{b_\eta,k}^T \tag{3.50b}$$

$$\boldsymbol{\Lambda}_k^+ = \left(\boldsymbol{I} - \boldsymbol{K}_{x,k}\boldsymbol{H}_k\right)\boldsymbol{\Lambda}_k^- - \boldsymbol{K}_{x,k}\boldsymbol{J}_k\boldsymbol{B}_\nu - \left(\boldsymbol{P}_{x,k}^-\boldsymbol{H}_k^T + \boldsymbol{\Lambda}_k^-\boldsymbol{J}_k^T\right)\boldsymbol{K}_{b_\nu,k}^T + \boldsymbol{K}_{x,k}\boldsymbol{W}_k\boldsymbol{K}_{b_\nu,k}^T \tag{3.50c}$$

$$\boldsymbol{B}_\eta^+ = \boldsymbol{B}_\eta^- - \boldsymbol{K}_{b_\eta,k}\boldsymbol{H}_k\boldsymbol{L}_k^- - \left(\boldsymbol{L}_k^-\right)^T\boldsymbol{H}_k^T\boldsymbol{K}_{b_\eta,k}^T + \boldsymbol{K}_{b_\eta,k}\boldsymbol{W}_k\boldsymbol{K}_{b_\eta,k}^T \tag{3.50d}$$

$$\boldsymbol{B}_\nu^+ = \boldsymbol{B}_\nu^- - \boldsymbol{K}_{b_\nu,k}\left(\boldsymbol{H}_k\boldsymbol{\Lambda}_k^- + \boldsymbol{J}_k\boldsymbol{B}_\nu\right) - \left(\left(\boldsymbol{\Lambda}_k^-\right)\boldsymbol{H}_k^T + \boldsymbol{B}_\nu\boldsymbol{J}_k^T\right)\boldsymbol{K}_{b_\nu}^T + \boldsymbol{K}_{b_\nu}\boldsymbol{W}_k\boldsymbol{K}_{b_\nu}^T. \tag{3.50e}$$

A consider filter is one in which the bias parameters are not updated. Examining Equation (3.44) shows this can be achieved by setting $\boldsymbol{K}_{b_\eta,k} = \boldsymbol{K}_{b_\nu,k} = \boldsymbol{0}$. Similar to an EKF, the Kalman gain is found by minimizing the trace of the measurement updated covariance matrix giving

$$\boldsymbol{K}_k = \begin{bmatrix} \boldsymbol{P}_{x,k}^-\boldsymbol{H}_k^T + \boldsymbol{\Lambda}_k^-\boldsymbol{J}_k^T \\ \boldsymbol{0} \\ \boldsymbol{0} \end{bmatrix}\boldsymbol{W}_k^{-1} \tag{3.51}$$

Substituting this into Equation (3.50) gives the measurement update for a consider Kalman filter

$$\boldsymbol{P}_{x,k}^+ = \boldsymbol{P}_{x,k}^- - \boldsymbol{K}_{x,k}\boldsymbol{W}_k\boldsymbol{K}_{x,k}^T \tag{3.52a}$$

$$\boldsymbol{L}_k^+ = \left(\boldsymbol{I} - \boldsymbol{K}_{x,k}\boldsymbol{H}_k\right)\boldsymbol{L}_k^- \tag{3.52b}$$

$$\boldsymbol{\Lambda}_k^+ = \left(\boldsymbol{I} - \boldsymbol{K}_{x,k}\boldsymbol{H}_k\right)\boldsymbol{\Lambda}_k^- - \boldsymbol{K}_{x,k}\boldsymbol{J}_k\boldsymbol{B}_\nu^- \tag{3.52c}$$

$$\boldsymbol{B}_\eta^+ = \boldsymbol{B}_\eta^- \tag{3.52d}$$

$$\boldsymbol{B}_\nu^+ = \boldsymbol{B}_\nu^-. \tag{3.52e}$$

As noted by Bierman[86] and Zanetti and D'Souza[87] the consider filter applied recursively results in a suboptimal estimate because all measurements are not processed simultaneously. The globally optimal Kalman gain $\boldsymbol{K}_k^*$ is that for which all parameters of the state are estimated and is given by

$$\begin{aligned}\boldsymbol{K}_k^* &= \boldsymbol{P}_{z,k}^- \boldsymbol{Y}_k^T \boldsymbol{W}_k^{-1} \\ &= \begin{bmatrix} \boldsymbol{P}_{x,k}^- \boldsymbol{H}_k^T + \boldsymbol{\Lambda}_k^- \boldsymbol{J}_k^T \\ \left(\boldsymbol{L}_k^-\right)^T \boldsymbol{H}_k^T \\ \left(\boldsymbol{\Lambda}_k^-\right)^T \boldsymbol{H}_k^T + \boldsymbol{B}_\nu^- \boldsymbol{J}_k^T \end{bmatrix} \boldsymbol{W}_k^{-1}\end{aligned} \tag{3.53}$$

Substituting the values for the optimal Kalman gain into Equation (3.50) gives

$$\boldsymbol{P}_{x,k}^+ = \boldsymbol{P}_{x,k}^- - \boldsymbol{K}_{x,k}^* \boldsymbol{W}_k \boldsymbol{K}_{x,k}^{*T} \tag{3.54a}$$

$$\boldsymbol{L}_k^+ = \left(\boldsymbol{I} - \boldsymbol{K}_{x,k}^* \boldsymbol{H}_k\right) \boldsymbol{L}_k^- \tag{3.54b}$$

$$\boldsymbol{\Lambda}_k^+ = \left(\boldsymbol{I} - \boldsymbol{K}_{x,k}^* \boldsymbol{H}_k\right) \boldsymbol{\Lambda}_k^- - \boldsymbol{K}_{x,k}^* \boldsymbol{J}_k \boldsymbol{B}_\nu^- \tag{3.54c}$$

$$\boldsymbol{B}_\eta^+ = \boldsymbol{B}_\eta^- - \boldsymbol{K}_{b_\eta,k}^* \boldsymbol{W}_k \boldsymbol{K}_{b_\eta,k}^{*T} \tag{3.54d}$$

$$\boldsymbol{B}_\nu^+ = \boldsymbol{B}_\nu^- - \boldsymbol{K}_{b_\nu,k}^* \boldsymbol{W}_k \boldsymbol{K}_{b_\nu,k}^{*T}. \tag{3.54e}$$

By comparing Equations (3.52) and (3.54) it can be seen that the optimal equations will result in a smaller update due to the differences in $\boldsymbol{B}_\eta^+$ and $\boldsymbol{B}_\nu^+$ and so incremental updates, as applied in a sequential filter, will result in a different state covariance. Zanetti and D'Souza propose a method for obtaining an optimal estimate when using a consider filter[87]. Equation (3.54) is used instead of Equation (3.52) with the understanding that the calculated bias covariances $\boldsymbol{B}_\eta$ and $\boldsymbol{B}_\nu$ are not the true bias covariances, but the bias covariances if the biases were being optimally estimated; the actual bias covariances are given by $\boldsymbol{B}_\eta(t_0)$ and $\boldsymbol{B}_\nu(t_0)$.

3.2.2.2 ECKF Based Sun-Direction Estimator

Similar to Section 3.2.1.2, the state vector is chosen to be the scaled sun-direction vector in the body frame

$$\boldsymbol{x}(t) = \left[{}^{\mathcal{B}}\boldsymbol{d}(t)\right].$$

As before, the dynamics of the scaled sun-direction vector are written as in Equation (3.29). However, instead of assuming the inertial sun vector is constant, the time derivative of the inertial sun vector is retained as a consider parameter because statistics about this bias can be obtained from ephemeris data. While this bias is not constant, and definitely not Gaussian, this method will allow for the estimate uncertainty to be conservatively bounded. The state dynamics are, thus, given by

$$\frac{{}^{\mathcal{B}}\mathrm{d}}{\mathrm{d}t}\left[{}^{\mathcal{B}}\boldsymbol{d}(t)\right] = {}^{\mathcal{B}}\boldsymbol{d}(t) \times [BG]\left({}^{\mathcal{G}}\tilde{\boldsymbol{\omega}}(t) - {}^{\mathcal{G}}\boldsymbol{\omega}_{\beta}(t) - {}^{\mathcal{G}}\boldsymbol{\eta}_{\omega}(t)\right) + {}^{\mathcal{B}}\dot{\boldsymbol{d}}(t) - {}^{\mathcal{B}}\boldsymbol{\eta}_{s}(t)\,. \tag{3.55}$$

Equation (3.1), repeated here, is used for the measurement equation.

$$V = \|\boldsymbol{d}\| \cdot C_{\kappa}\left(V_d + V_{\alpha_\beta} + \nu_V\right)$$

$$V_d = \begin{cases} \boldsymbol{n}^T \frac{\boldsymbol{d}}{\|\boldsymbol{d}\|} & \text{if } \boldsymbol{n}^T \frac{\boldsymbol{d}}{\|\boldsymbol{d}\|} \geq \cos\psi \\ 0 & \text{if } \boldsymbol{n}^T \frac{\boldsymbol{d}}{\|\boldsymbol{d}\|} < \cos\psi \end{cases}$$

and the noises and biases are set to

$$\boldsymbol{\eta}_x(t) = \begin{bmatrix} {}^{\mathcal{B}}\boldsymbol{\eta}_s(t) \\ {}^{\mathcal{G}}\boldsymbol{\eta}_{\omega}(t) \end{bmatrix}, \quad \boldsymbol{\eta}_{\beta_\eta}(t) = \left[{}^{\mathcal{G}}\boldsymbol{\eta}_{\omega_\beta}(t)\right], \quad \boldsymbol{\nu}_k = \left[\boldsymbol{\nu}_{V_k}\right], \quad \boldsymbol{\beta}_\eta = \begin{bmatrix} {}^{\mathcal{B}}\dot{\boldsymbol{d}}(t) \\ {}^{\mathcal{G}}\boldsymbol{\omega}_{\beta} \end{bmatrix}, \quad \boldsymbol{\beta}_\nu = \begin{bmatrix} \boldsymbol{C}_{\kappa} \\ \boldsymbol{\theta}_{\beta} \\ \boldsymbol{\phi}_{\beta} \\ \boldsymbol{V}_{\alpha_\beta} \end{bmatrix}. \tag{3.56}$$

The estimator is initialized using $\boldsymbol{L}(t_0) = \boldsymbol{\Lambda}(t_0) = \boldsymbol{0}$, and the pertinent Jacobians are given by

$$\boldsymbol{F}(t) = \left[-\left[[BG]\,{}^{\mathcal{G}}\tilde{\boldsymbol{\omega}}(t)\right]_{\times}\right] \tag{3.57a}$$

$$\boldsymbol{G}(t) = \left[-\boldsymbol{I}_{3\times 3} \quad -\left[{}^{\mathcal{B}}\hat{\boldsymbol{d}}(t)\right]_{\times}[BG]\right] \tag{3.57b}$$

$$\boldsymbol{S}(t) = \left[\boldsymbol{I}_{3\times 3} \quad -\left[{}^{\mathcal{B}}\hat{\boldsymbol{d}}(t)\right]_{\times}[BG]\right] \tag{3.57c}$$

$$\boldsymbol{H}_k = \begin{bmatrix} H_{1,k} & \cdots & H_{N,k} \end{bmatrix}^T$$

$$H_{i,k} = \begin{cases} \hat{C}_{\kappa_i}\, {}^{\mathcal{B}}\hat{\boldsymbol{n}}_i & \text{if } \hat{\boldsymbol{n}}_i^T \frac{\hat{\boldsymbol{d}}_k}{\|\hat{\boldsymbol{d}}_k\|} \geq \cos\psi_i \\ \boldsymbol{0} & \text{if } \hat{\boldsymbol{n}}_i^T \frac{\hat{\boldsymbol{d}}_k}{\|\hat{\boldsymbol{d}}_k\|} < \cos\psi_i \end{cases} \tag{3.57d}$$

$$\boldsymbol{M}_k = \left\|\hat{\boldsymbol{d}}_k\right\| \operatorname{diag}\left(\hat{\boldsymbol{C}}_\kappa\right) \tag{3.57e}$$

$$\boldsymbol{J}_k = \begin{bmatrix} \operatorname{diag}\left(a_{1,k},\ldots,a_{N,k}\right) & \operatorname{diag}\left(b_{1,k},\ldots,b_{N,k}\right) & \operatorname{diag}\left(c_{1,k},\ldots,c_{N,k}\right) & \left\|{}^{\mathcal{B}}\hat{\boldsymbol{d}}_k\right\| \operatorname{diag}\left(\hat{\boldsymbol{C}}_\kappa\right) \end{bmatrix}$$

$$(\cdot)_{i,k} = \begin{cases} (\bar{\cdot})_{i,k} & \text{if } \hat{\boldsymbol{n}}_i^T \frac{\hat{\boldsymbol{d}}_k}{\left\|\hat{\boldsymbol{d}}_k\right\|} \geq \cos\psi_i \\ 0 & \text{if } \hat{\boldsymbol{n}}_i^T \frac{\hat{\boldsymbol{d}}_k}{\left\|\hat{\boldsymbol{d}}_k\right\|} < \cos\psi_i \end{cases}$$

$$\bar{a}_{i,k} = \hat{\boldsymbol{n}}_i^T \hat{\boldsymbol{d}}_k$$

$$\bar{b}_{i,k} = \hat{C}_{\kappa_i} \cos\left(\phi_i + \hat{\phi}_{\beta_i}\right) \left\{ -{}^{\mathcal{B}}\hat{\boldsymbol{d}}_{x_k} \sin\left(\theta_i + \hat{\theta}_{\beta_i}\right) + {}^{\mathcal{B}}\hat{\boldsymbol{d}}_{y_k} \cos\left(\theta_i + \hat{\theta}_{\beta_i}\right) \right\}$$

$$\begin{aligned} \bar{c}_{i,k} = \hat{C}_{\kappa_i} \Big[& - \left\{ {}^{\mathcal{B}}\hat{\boldsymbol{d}}_{x_k} \cos\left(\theta_i + \hat{\theta}_{\beta_i}\right) + {}^{\mathcal{B}}\hat{\boldsymbol{d}}_{y_k} \sin\left(\theta_i + \hat{\theta}_{\beta_i}\right) \right\} \sin\left(\phi_i + \hat{\phi}_{\beta_i}\right) \\ & + {}^{\mathcal{B}}\hat{\boldsymbol{d}}_{z_k} \cos\left(\phi_i + \hat{\phi}_{\beta_i}\right) \Big]. \end{aligned} \tag{3.57f}$$

In contrast to the EKF method of Section 3.2.1.2, the ECKF measurement update for sensors without the Sun in their field of view is non-zero. According to the measurement model, any sensor pointed away from the Sun should register zero; however, noise and albedo input will almost always create a non-zero observation, and negative measurements are not possible. Over time the presence of these positive measurements can cause the filter to develop a bias exceeding the calculated covariance bounds. Similar to the EKF, only those sensors expected to have direct sunlight measurements and those with measurements above some threshold are processed to alleviate this problem.

It is found in practice that the optimal consider filter, presented in Section 3.2.2.1, works well for relatively small biases. In the case of significant biases, for example due to albedo or rate gyro bias, the optimal consider Kalman gain can cause the filter to become overconfident and diverge.

Because of the omnipresent and significant nature of the biases being considered, the traditional, non-optimal, version of the ECKF is implemented to retain robustness.

Note that both this approach, and the EKF, only increase the uncertainty of the state to account for biases, they do not estimate the actual bias values. Nominally, it is assumed $\hat{C}_{\kappa_i} = 1.0$, $\hat{\theta}_\beta = 0.0$, and $\hat{\phi}_\beta = 0.0$, and if additional information is available the solution is improved by substituting in better estimates for these values. In order to properly estimate these biases requires additional measurement information. A method for calibrating CSS on orbit is discussed in detail in Chapter 4 and examines what is necessary to estimate these model parameters.

3.2.3 Measurement Consistency

Both sequential filters derived previously can suffer from divergence due to inconsistencies in the measurement model caused by the discontinuity in Equation (3.1). A filter is consistent if the estimated state and measurement innovations are zero-mean and have covariances within the filter predicted covariance[55,88]. Applying this to Equation (3.1) requires that

$$\mathrm{E}[\boldsymbol{y}_k - \hat{\boldsymbol{y}}_k] = 0 \tag{3.58a}$$

$$\mathrm{E}\Big[(\boldsymbol{y}_k - \hat{\boldsymbol{y}}_k)\,(\boldsymbol{y}_k - \hat{\boldsymbol{y}}_k)^T\Big] = \boldsymbol{W}_k \tag{3.58b}$$

where $\hat{\boldsymbol{y}}_k$ is the computed measurement at time t_k based on the best estimate of the state, and $\boldsymbol{W}_k$ is the expected covariance of the measurement innovation as defined in Equation (3.47).

Consider a single CSS with the true CSS normal vector given by

$$\boldsymbol{n} = \begin{bmatrix} \cos\Big(\phi + \phi_\beta\Big)\cos\Big(\theta + \theta_\beta\Big) \\ \cos\Big(\phi + \phi_\beta\Big)\sin\Big(\theta + \theta_\beta\Big) \\ \sin\Big(\phi + \phi_\beta\Big) \end{bmatrix} \tag{3.59}$$

whereas the CSS normal vector is modeled as

$$\hat{\boldsymbol{n}} = \begin{bmatrix} \cos(\phi)\cos(\theta) \\ \cos(\phi)\sin(\theta) \\ \sin(\phi) \end{bmatrix} \tag{3.60}$$

and θ_β and ϕ_β are normally distributed biases with standard deviations of 10.0°; note these uncertainties are exaggerated for illustrative purposes.

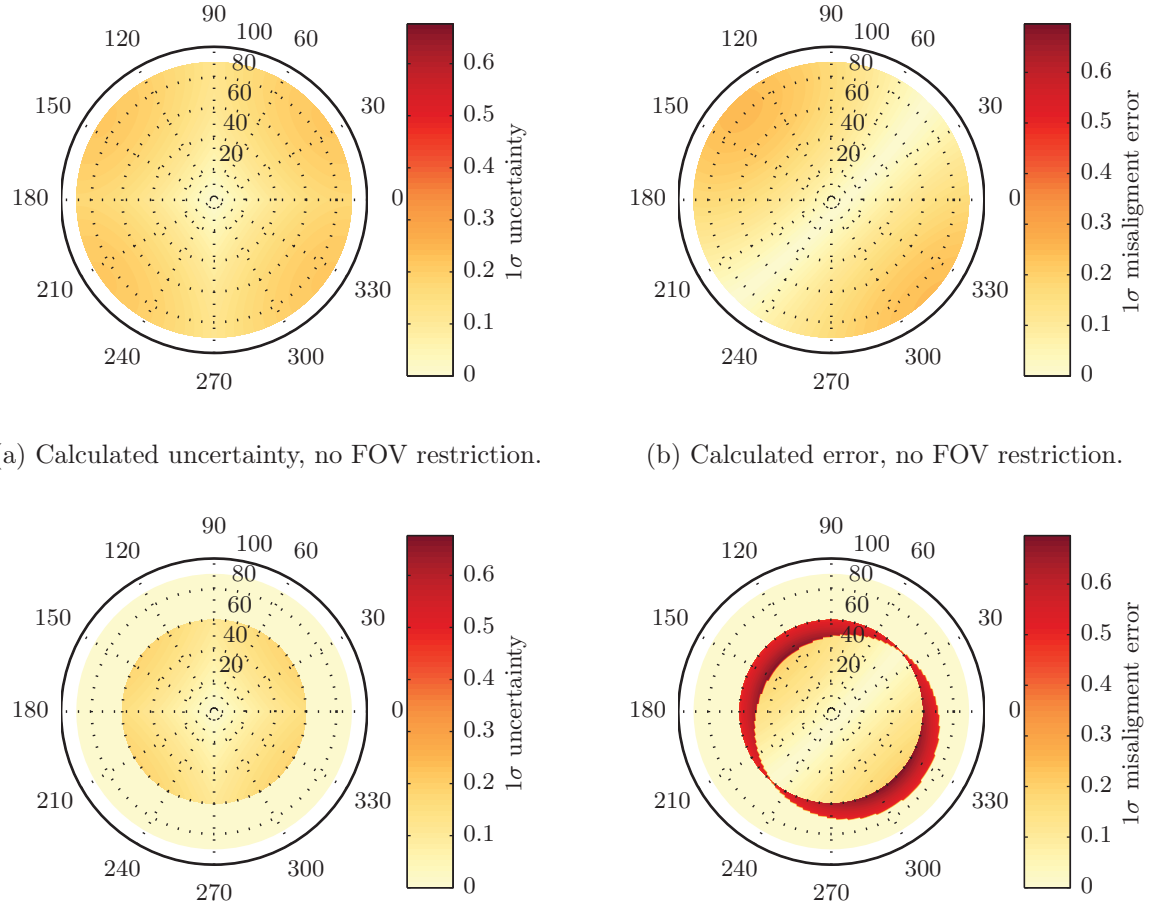

(a) Calculated uncertainty, no FOV restriction.

(b) Calculated error, no FOV restriction.

(c) Calculated uncertainty, FOV = 60°.

(d) Calculated error, FOV = 60°.

Figure 3.4: Calculated uncertainty and measured error for 1σ CSS misalignment.

Assuming no other errors results in the profiles shown in Figure 3.4, where the hemisphere visible to the CSS has been projected onto a 2D plane. Figures 3.4a and 3.4c show the calculated 1σ uncertainties, and Figures 3.4b and 3.4d show the associated possible σ errors with and without field of restrictions. Without any field of view restriction the errors from a 1σ misalignment are, as expected, within the predicted uncertainty bounds. However, when the field of view for the sensor is set to 60°, and all measurements outside are assumed zero, errors due to a 1σ misalignment are much

greater than the predicted uncertainty bounds. Due to this discontinuity, even small misalignments can lead to measurement innovations that are inconsistent and subsequent filter divergence.

Uncertainty in the sun-direction vector has a similar effect. Consider now a single CSS modeled using Equation (3.1). The misalignment biases θ_β and ϕ_β are normally distributed with standard deviations of 1.0°, $\sigma_V = 0.05$, $\sigma_{V_\alpha} = 0.1$, and the scale factor bias is assumed to have a mean of 1.0 and a standard deviation of 0.02. It is assumed the state uncertainty matrix is diagonal with equal variances about each axis, as when the filter is initialized, and sun-direction uncertainties up to 60° are considered, as beyond this angle the maximum error saturates. The range of possible measurement errors for these 1σ noises and biases, and the predicted covariance bounds, are shown in Figure 3.5 without a field of view discontinuity, and in Figure 3.6 with a 60° field of view restriction.

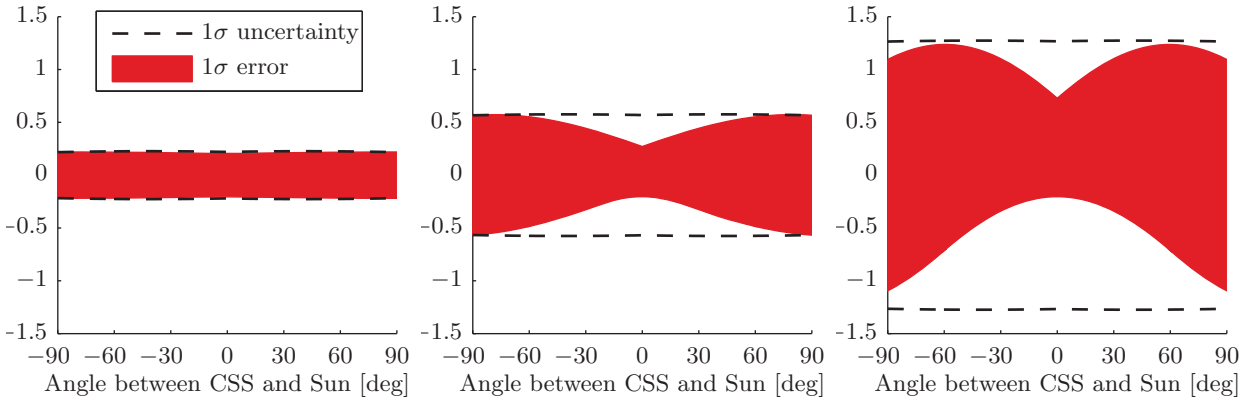

(a) 0° sun-direction uncertainty. (b) 20° sun-direction uncertainty. (c) 60° sun-direction uncertainty.

Figure 3.5: 2D slices, through 135° azimuth, of measurement 1σ uncertainty and possible errors without field of view restriction.

Without field of view restrictions, the calculated measurement uncertainty does not exactly match the possible errors, due to linearization, but it does bound the errors. In contrast, when a discontinuous cutoff is applied at the edge of a 60° field of view, several regions of possible errors appear outside the calculated covariance bounds. These regions are small for perfect sun-direction knowledge, but increase as the sun-direction uncertainty is increased.

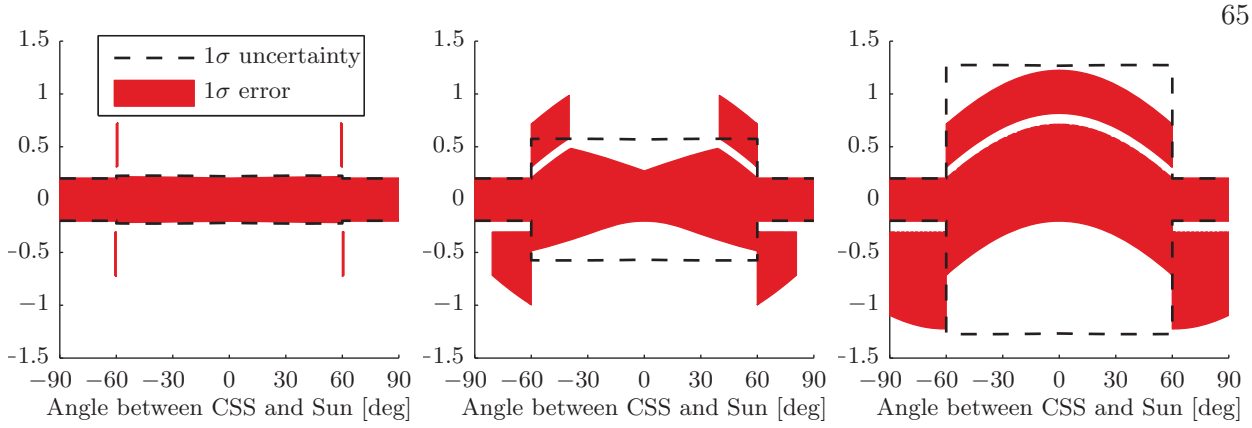

(a) 0° sun-direction uncertainty. (b) 20° sun-direction uncertainty. (c) 60° sun-direction uncertainty.

Figure 3.6: 2D slices, through 135° azimuth, of measurement 1σ uncertainty and possible errors for 60° FOV.

To counteract this measurement inconsistency, additional measurement uncertainty is added to the measurement model[89]. While inflating the measurement uncertainty will decrease the information content of the result, for a spacecraft orienting itself at the Sun the goal orientation will result in the actual offset angle being near zero. Thus, the added measurement noise will improve robustness while not impacting the steady state performance of the estimator when combined with simultaneous control effort. Alternatively, all inconsistent measurements could be rejected. However, with a sufficiently uncertain initial guess this results in all measurements being rejected and the filter never converges. This is particularly important for a spacecraft attempting to orient itself from a lost in space scenario in which it has no sun-direction knowledge.

The maximum angle from the field of view boundary at which inconsistent errors occur γ is modeled by adding the offset angle a 1σ misalignment can impose

$$\gamma_m = \arccos\left(\boldsymbol{n}^T\hat{\boldsymbol{n}}\right) = \arccos\left(\cos\left(\sigma_{\theta_\beta}\right)\cos(\phi)\cos\left(\phi+\sigma_{\phi_\beta}\right)+\sin(\phi)\sin\left(\phi+\sigma_{\phi_\beta}\right)\right) \tag{3.61}$$

to the angular uncertainty of the current scaled sun-direction estimate, where the variance of the angular offset of the sun-direction estimate from a reference unit-vector in the body frame $\boldsymbol{c}$ is given

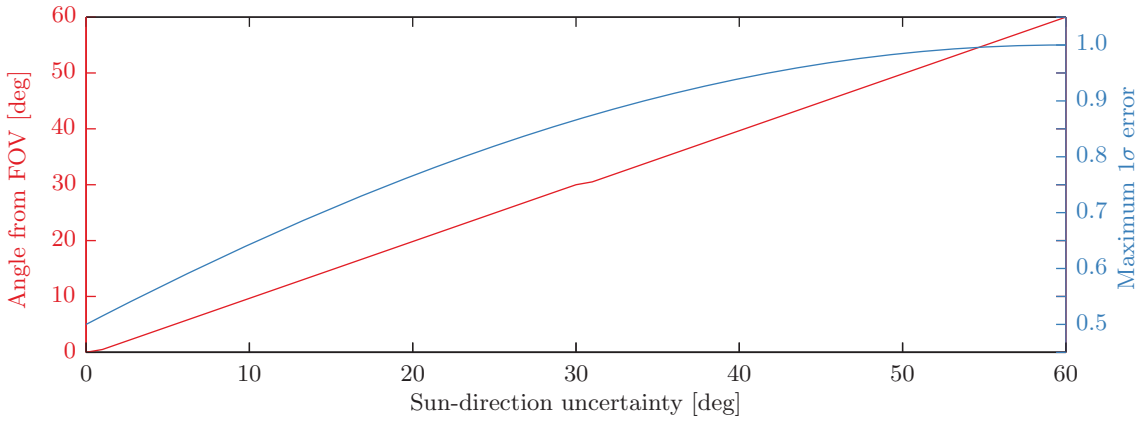

Figure 3.7: Maximum angle from FOV boundary inconsistent measurement errors extend and maximum 1σ error.

to first order by

$$\boldsymbol{\Sigma}\left(\gamma_{\hat{d}}\right) = \boldsymbol{J}_{\gamma}\boldsymbol{P}\boldsymbol{J}_{\gamma}^{T}$$

$$\boldsymbol{J}_{\gamma} = \left[\frac{1}{\sqrt{1-\left(\boldsymbol{c}^{T}\frac{\hat{\boldsymbol{d}}}{\|\hat{\boldsymbol{d}}\|}\right)^{2}}}\left(\frac{\hat{\boldsymbol{d}}^{T}}{\|\hat{\boldsymbol{d}}\|}\left(\boldsymbol{c}^{T}\frac{\hat{\boldsymbol{d}}}{\|\hat{\boldsymbol{d}}\|}\right)-\boldsymbol{c}^{T}\right)\right] \tag{3.62}$$

as shown in Appendix D. The maximum measurement error is calculated using

$$\max(\boldsymbol{y}_{k}-\hat{\boldsymbol{y}}_{k}) = \sigma_{C}\sigma_{C_{\kappa}}\left\{\cos(\psi-\min(\psi,\gamma))+\sigma_{V_{\alpha}}+\sigma_{\nu_{V}}\right\} \tag{3.63}$$

Figure 3.7 shows the maximum angle from the field of view boundary that the inconsistent errors extend along with the maximum value of the error assuming only errors in sun-direction knowledge. In practice, the implementation of increased innovation variance is done through logic statements and a bound larger than 1σ, such as 3σ, must be used to ensure measurement inconsistencies do not drive the filter to divergence.

The dual pyramid CSS configuration, discussed in Section 2.2, has a second measurement discontinuity imparted by the local horizon of the face of the spacecraft to which each pyramid is mounted. For example, even though CSS 1 in Figure 2.8 has a 60° field of view, it view is blocked by the $+z$ face of the spacecraft resulting in a measurement profile similar to those shown in Figure 2.6. The discontinuity on one side now occurs at an angle between 45° to 60° depending on the azimuth

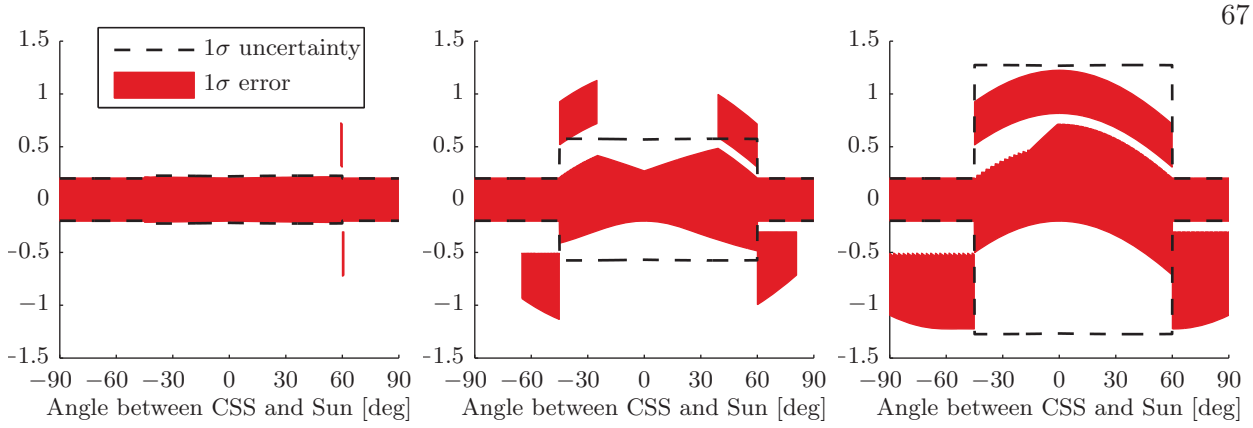

(a) 0° sun-direction uncertainty. (b) 20° sun-direction uncertainty. (c) 60° sun-direction uncertainty.

Figure 3.8: 2D slices, through 180° azimuth, of measurement 1σ uncertainty and possible errors for CSS 1 with 60° FOV and horizon cutoff.

of the slice. The calculation of the maximum uncertainty and angle at which is occurs are very similar to the field of view restriction with the exception that the minimum angle between the CSS normal and the local horizon is used instead of the field of view half angle in Equation (3.63).

3.3 Numerical Simulation Results

The results of several numerical Monte Carlo simulations are shown to illustrate and compare the performance of the sun-direction estimation methods presented. First the sun-direction estimators' performances are compared without attitude control to establish a performance baseline. Next the estimators are run with simultaneous nonlinear control and compared with and without rate gyro measurements. Finally, the sensitivity of the estimators to rate gyro accuracy is explored.

The single-point estimators use all available sensor input to calculate the sun-direction vector. Theoretically, the performance of these methods could be improved by implementing a form of noise rejection logic where the expected ratio of direct Sun measurements to albedo measurements is used to reject measurements below some threshold. Such logic will necessarily be governed by the specific mission of a spacecraft, the a priori knowledge of irradiance levels, and sensor calibration, therefore, the performance of the single-point estimators is evaluated without any such logic as a worst case.

The numerical simulation parameters are the same as outlined in Section 2.4. For the EKF estimator, the measurement noise standard deviation σ_V is very conservatively inflated to 1.84 to encompass all possible 1σ errors. The rate gyro noise value is set equal to the value specified for the appropriate level of gyro performance and σ_s is set to $5 \times 10^{-4}\,\mathrm{rad}/\sqrt{\mathrm{s}}$ for inertial and intermediate gyros, $4 \times 10^{-3}\,\mathrm{rad}/\sqrt{\mathrm{s}}$, and $4 \times 10^{-2}\,\mathrm{rad}/\sqrt{\mathrm{s}}$ for low gyros. For the ECKF estimator, the process noise σ_s is set to $1 \times 10^{-15}\,\mathrm{rad}/\sqrt{\mathrm{s}}$, and the standard deviations of the inertial rate of change of the sun-direction vector ${}^{\mathcal{B}}\dot{\boldsymbol{d}}$ are set to $\left[2.4 \times 10^{-7}, 2.4 \times 10^{-7}, 1.3 \times 10^{-7}\right]\mathrm{rad/s}$.

3.3.1 Sun-Direction Estimation Without Attitude Control

An initially uncontrolled tumbling spacecraft is simulated to investigate the baseline performance of the various sun-direction estimation methods described if they are not assisted with a simultaneously active attitude control. The resulting statistics for a 1000 case, 100 min, Monte Carlo analysis, run using the parameters listed in Section 2.4, and assuming the spacecraft is equipped with a dual-pyramid CSS configuration, are shown in Figure 3.9. The statistics are calculated for the time the spacecraft has at least one CSS with a valid direct Sun measurement; the time spent in the shadow of the Earth has been removed.

While the estimators output a solution for the scaled sun-direction vector, what is of interest is the total angular error of the estimate shown in Figure 3.9d. As can be seen, the single-point estimation algorithms, WAVG, LSMN, and WLSMN, all show significant error in the resulting scaled sun-direction vector estimation; the 99th percentile bounds for the estimated angular errors for all three methods are above 45°. This is expected due to the underdetermined nature of the CSS configuration. This is also evident in the non-zero mean of the sun-direction angular error. The EKF based methods, however, are capable of quickly achieving estimation accuracy below 5°. The EKF method performs the best, reducing the attitude estimation error to 1.75° within a few minutes and maintaining that level of accuracy throughout the trajectory. The ECKF is, as expected, more conservative, but still maintains a 99th percentile accuracy of approximately 3.1°. Both the EKF and ECKF exhibit a mean error just below 1° that corresponds well with the control deadband.

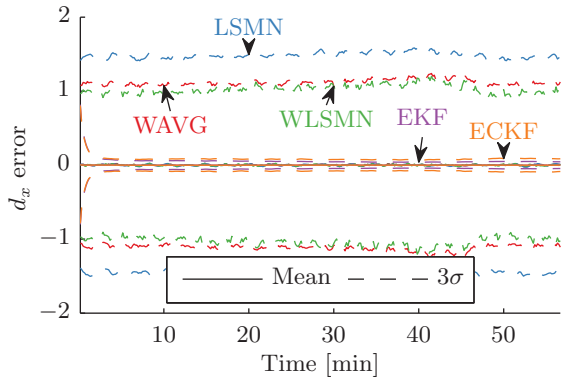

(a) Error in x-component of scaled sun-direction vector.

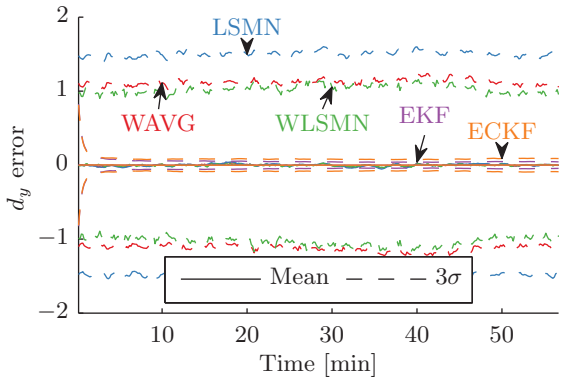

(b) Error in y-component of scaled sun-direction vector.

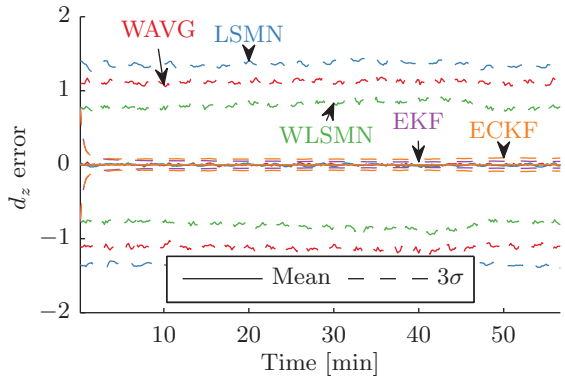

(c) Error in z-component of scaled sun-direction vector.

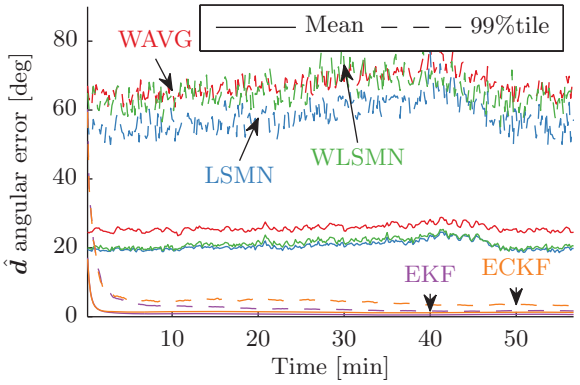

(d) Angular error of sun-direction vector estimate.

Figure 3.9: Calculated statistics for 1000 case Monte Carlo run without control using a dual pyramid CSS configuration.

Figure 3.10 shows similar results for a spacecraft equipped with a cube CSS configuration. The angular errors of the steady state solutions for the sequential estimators are nearly the same as when using the dual pyramid configuration; the ECKF achieves 5° and the EKF achieves 2° accuracy at the 99th percentile. As noted previously, the angular error in the three single-point methods are all the same due to the orthogonality of the measurements.

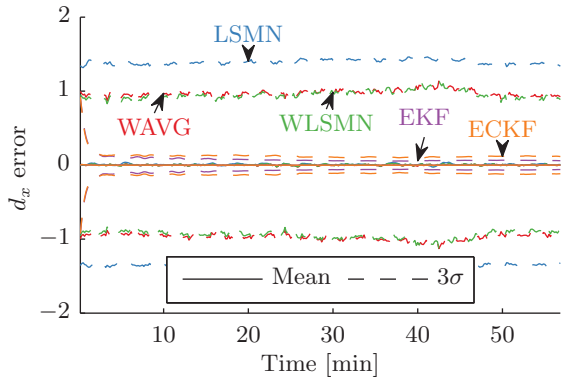

(a) Error in x-component of scaled sun-direction vector.

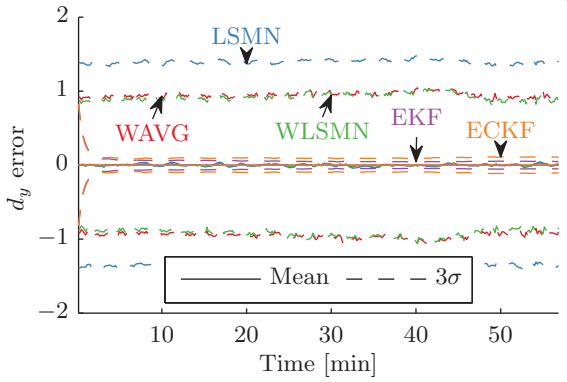

(b) Error in y-component of scaled sun-direction vector.

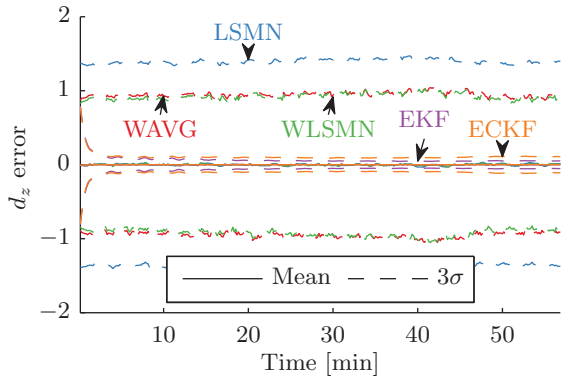

(c) Error in z-component of scaled sun-direction vector.

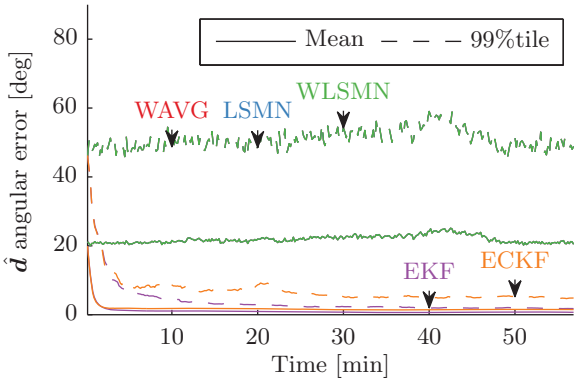

(d) Angular error of sun-direction vector estimate.

Figure 3.10: Calculated statistics for 1000 case Monte Carlo run without control using a cube CSS configuration.

3.3.2 Sun-Direction Estimation & Control With Rate Gyro Measurements

A nonlinear three-axis attitude control is used in the numerical simulation to reorient the spacecraft using redundant reaction wheels[90,91]. This control law is designed for detumbling with the goal of orienting the spacecraft body frame $\mathcal{B}$ with a reference frame $\mathcal{R}$ where the attitude error between the body and reference frames is described using the Modified Rodrigues Parameter (MRP)

set $\boldsymbol{\sigma}_{\mathcal{BR}}$. The control law is given by

$$\begin{aligned}\boldsymbol{G}_s\boldsymbol{u}_s = &- [I]\left(\dot{\boldsymbol{\omega}}_R - [\boldsymbol{\omega}]_\times \boldsymbol{\omega}_R\right) + K\boldsymbol{\sigma}_{\mathcal{BR}} + \boldsymbol{P}\Delta\boldsymbol{\omega} + \boldsymbol{P}\boldsymbol{K}_I\boldsymbol{z} \\ &- \left([\boldsymbol{\omega}_R]_\times - [\boldsymbol{K}_I\boldsymbol{z}]_\times\right)\left([I]\,\boldsymbol{\omega} + \boldsymbol{G}_s\left\{\boldsymbol{J}_s \circ \left(\boldsymbol{\Omega} + \boldsymbol{G}_s^T\boldsymbol{\omega}\right)\right\}\right) + \boldsymbol{L}\end{aligned} \tag{3.64}$$

where $\Delta\boldsymbol{\omega} = \boldsymbol{\omega} - \boldsymbol{\omega}_R$, $\boldsymbol{\omega}_R$ is a time-varying reference angular velocity, K is a scalar gain, $\boldsymbol{P}$ is a positive definite gain matrix, $\boldsymbol{K}_I$ is a gain matrix, $\boldsymbol{z}$ is the integral term, $\boldsymbol{J}_s$ is a vector of wheel spin-axis inertias, the $\circ$ operator indicates a Hadamard, or Schur, product[92], $\boldsymbol{\Omega}$ is a vector of wheel speeds, and $\boldsymbol{L}$ are the known external torques acting on the vehicle. The control is proven to be asymptotically stabilizing and guarantees if $\boldsymbol{\sigma}$ converges to zero, so will $\Delta\boldsymbol{\omega}$. For further discussion of this control law, and its development, the reader is referred to Reference 90. In this analysis, the control gains $K = 0.041\,\mathrm{N\,m}$, $\boldsymbol{P} = 0.5\boldsymbol{I}_{3\times3}\mathrm{N\,m\,s}$, and $\boldsymbol{K}_I = 0.001\boldsymbol{I}_{3\times3}/(\mathrm{Ns}^2)$ are used, $\boldsymbol{\omega}_r = \dot{\boldsymbol{\omega}}_r = \begin{bmatrix}0 & 0 & 0\end{bmatrix}^T$, and a control deadband of 1° is used.

The estimation algorithms compute a sun-direction vector in the body frame, not an attitude error. The error MRP $\boldsymbol{\sigma}_{\mathcal{BR}}$ is formed by finding the principal rotation vector necessary to rotate the sun-direction vector to align with the solar panel unit normal vector $\boldsymbol{c}$ expressed in the body frame. This vector is used in the definition of the MRP vector

$$\boldsymbol{\sigma} = \hat{\boldsymbol{e}}\tan\left(\frac{\Phi}{4}\right) \tag{3.65}$$

to create an error MRP given by

$$\boldsymbol{\sigma}_{\mathcal{BR}} = \frac{\hat{\boldsymbol{d}}\times\boldsymbol{c}}{\left\|\hat{\boldsymbol{d}}\times\boldsymbol{c}\right\|}\tan\left(\frac{1}{4}\arccos\left(\frac{\boldsymbol{c}^T\hat{\boldsymbol{d}}}{\|\boldsymbol{c}\|\|\hat{\boldsymbol{d}}\|}\right)\right). \tag{3.66}$$

Because of the normalization included in the error MRP, this control approach is able to operate on the current scaled sun-direction estimate $\hat{\boldsymbol{d}}$, not just the unit sun-direction vector $\boldsymbol{s}$. Equation (3.66) has a singularity when the denominator approaches zero, or the sun-direction vector approaches alignment with the goal orientation. However, at the same time the trigonometric function in the numerator will also approach zero. This issue is avoided by simply setting the control to zero when the dot product inside the inverse cosine function falls below a threshold.

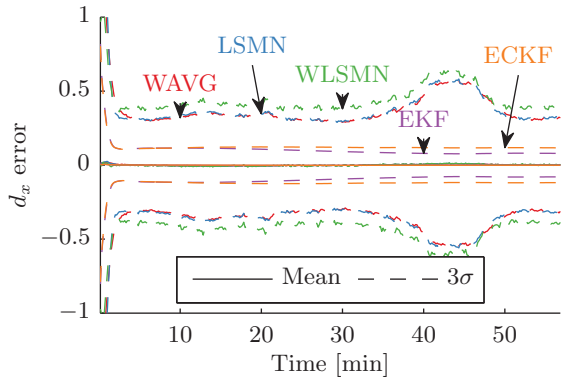

(a) Error in x-component of scaled sun-direction vector.

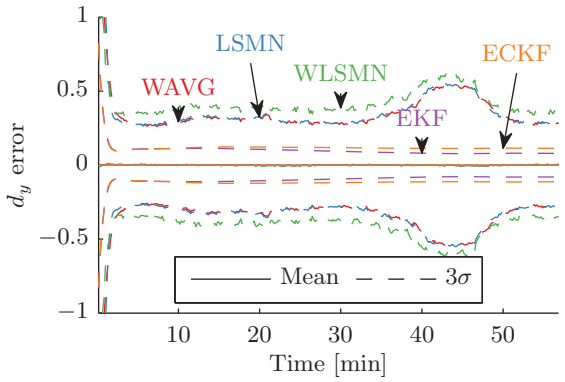

(b) Error in y-component of scaled sun-direction vector.

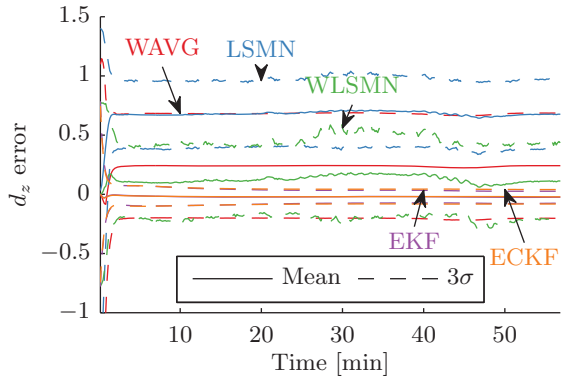

(c) Error in z-component of scaled sun-direction vector.

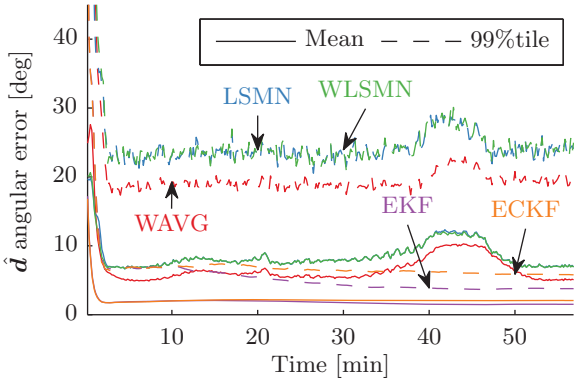

(d) Angular error of sun-direction vector estimate.

Figure 3.11: Calculated statistics for 1000 case Monte Carlo run with control using a dual pyramid CSS configuration.

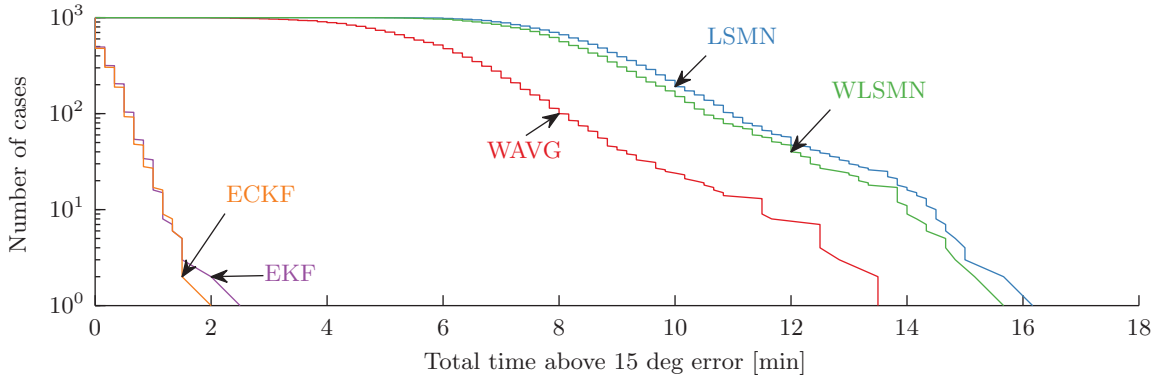

Figure 3.12: Total time spent with estimate in error of more than 15° for 1000 case Monte Carlo run with control using a dual pyramid CSS configuration.

Figures 3.11 and 3.12 show the statistics for a 1000 case Monte Carlo analysis with a dual pyramid CSS configuration and nonlinear control turned on; these results emphasize the positive impact of simultaneously estimating and controlling when using the single-point estimators with a partially underdetermined CSS configuration. As noted earlier, the control attempts to orient the spacecraft's z-axis to be pointed at the Sun while simultaneously estimating the sun direction. Due to the configuration of CSS used, this increases the number of CSS observations available, which is reflected in the significant decrease in estimation error as compared to the uncontrolled cases. Figure 3.12 shows the sorted total time above 15° for all the Monte Carlo runs on a log scale where the 15° threshold is an arbitrary limit used for comparison purposes. The discretized nature of the lines in Figure 3.12 are a result of the frequency of data output from the simulation.

All of the estimators are found to spend less than 17 min, of the approximately 56.5 min in view of the Sun for a single orbit, with angular accuracy greater than 15°. The EKF and ECKF methods spend the least amount of time above the threshold, 2 min, and achieve much higher estimate accuracy than the single-point estimators. Interestingly, of the single-point estimators the WAVG shows the least angular error and least total time, 14 min, above the threshold.

All of the single point estimators exhibit increased 3σ bounds for d_x and d_y and an increase in the mean angular error bias between 40 min and 50 min. This time corresponds to the region of the orbit where the spacecraft's sensors are most affected by Earth's albedo. Despite this, all three methods are able to maintain less than 15° angular error for 87 % of the time spent in view of the Sun.

Several biases are assumed small in the formulation of the estimation methods and the impact of that assumption can be seen in Figure 3.11c, particularly for the WAVG and LSMN methods. The results show a significant bias in the estimate of d_z, the axis desired to be pointing directly at the Sun, due to the biases present in the system dynamics and measurement models. Despite the significant biases and noise, all methods are shown capable of achieving a power positive orientation using only CSS, a rate gyro, and reaction wheels. The EKF method is able to achieve approximately 4° accuracy, and the ECKF method achieves 6° accuracy, at the 99th percentile. These results are

slightly less accurate that the results achieved without the control because the control eliminates all angular motion within a few minutes, thus reducing the number of new distinct measurements. If more accurate results are required while using a simultaneous control, a maneuver as benign as maintaining nadir pointing is capable of providing enough new information. Similarly, control dithering could be used to increase the information content of the CSS measurements.

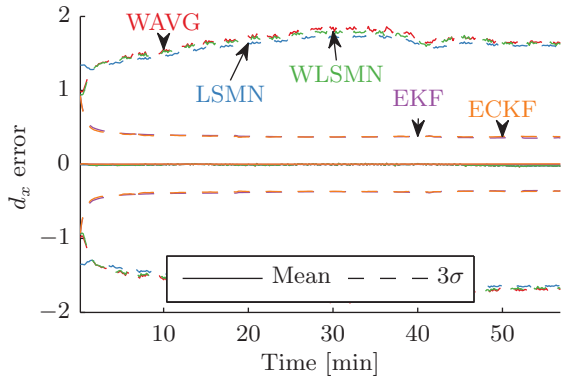

(a) Error in x-component of scaled sun-direction vector.

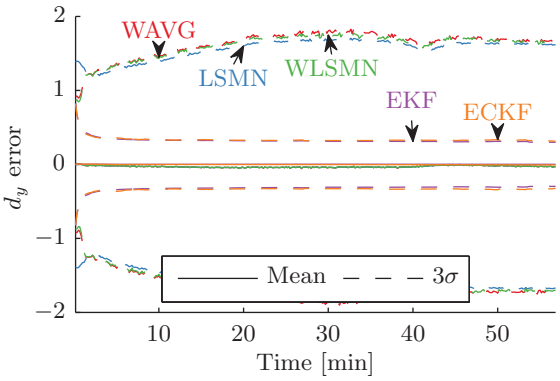

(b) Error in y-component of scaled sun-direction vector.

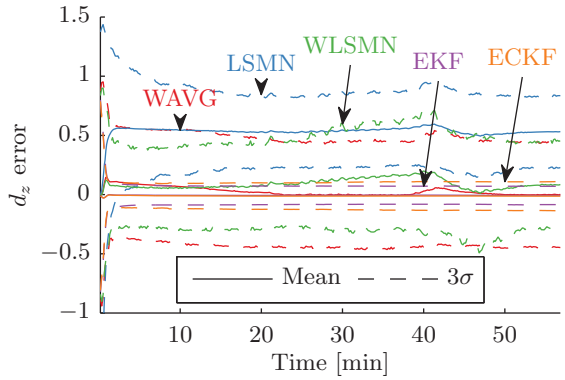

(c) Error in z-component of scaled sun-direction vector.

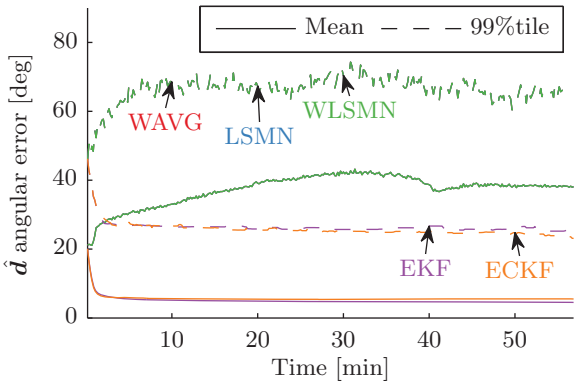

(d) Angular error of sun-direction vector estimate.

Figure 3.13: Calculated statistics for 1000 case Monte Carlo run with control using a cube CSS configuration.

Figures 3.13 and 3.14 show the statistics for a 1000 case Monte Carlo analysis with a cube CSS configuration and the nonlinear control turned on. As expected, all of the estimation approaches perform poorly due to the lack of measurement information available when in the goal orientation.

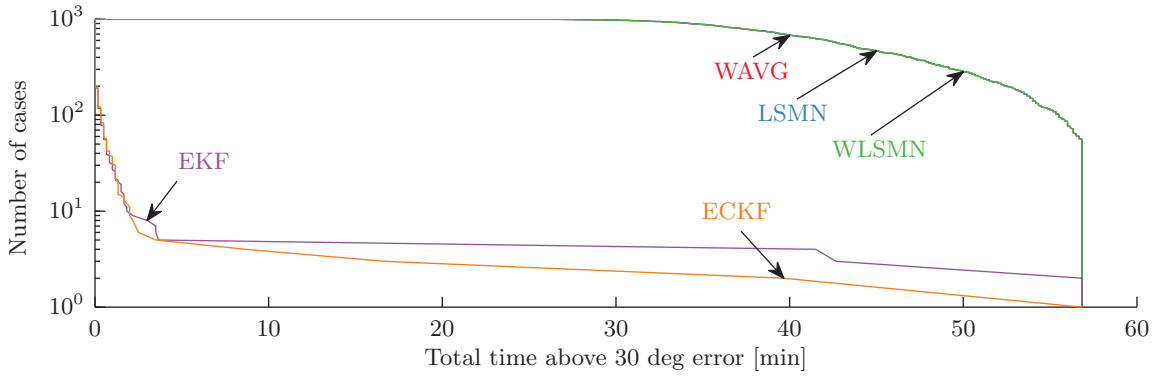

Figure 3.14: Total time spent with estimate in error of more than 30° for 1000 case Monte Carlo run with control using a cube CSS configuration.

Similar to the no control case, all three single point estimators have identical angular error statistics. Because there is only one sensor in view of the Sun for the goal orientation, the control actuates on a constantly changing sun-direction estimate, due to noise, and the spacecraft is unable to maintain sun pointing. In comparison, the sequential filtering algorithms perform quite well. The biased average angular error for these estimators is a result of the unestimated biases in the system, but the estimators are able to maintain pointing within 25° at the 99th percentile in a single orbit.

3.3.3 Sun-Direction Estimation & Control Without Rate Gyro Measurements

The control used to reorient the spacecraft to a power positive state requires a measure of the spacecraft's angular velocity $\boldsymbol{\omega}$ in order to arrest any rotational rates. In addition, the EKF method requires the spacecraft's angular velocity for state propagation. It is assumed the angular velocity of the spacecraft is nominally provided by a rate gyro, but it may be necessary to turn off the rate gyro in a power critical situation, or in a worst case scenario the rate gyro might fail. For these situations, the estimation approaches outlined previously are modified to use a simple estimate of the vehicle's angular velocity vector, a scaling of the cross product of the current and previous estimates of the sun-direction vector, given by

$$\bar{\boldsymbol{\omega}}_k = \frac{\hat{\boldsymbol{d}}_k \times \hat{\boldsymbol{d}}_{k-1}}{\left\|\hat{\boldsymbol{d}}_k \times \hat{\boldsymbol{d}}_{k-1}\right\|} \arccos\left(\frac{\hat{\boldsymbol{d}}_k^T \hat{\boldsymbol{d}}_{k-1}}{\left\|\hat{\boldsymbol{d}}_k\right\|\left\|\hat{\boldsymbol{d}}_{k-1}\right\|}\right) \frac{1}{t_k - t_{k-1}} \tag{3.67}$$

where $\hat{\boldsymbol{d}}_k$ is the best estimate of the scaled sun-direction unit vector at time t_k. This value is used in place of rate gyro measurements in the control to arrest vehicle rates. To counteract the additional error introduced by numerical differencing, the estimate is conservatively bounded about each axis and run through a first order low-pass filter. Since the numerical simulation assumes maximum initial angular rates of $2.0\,^\circ/\text{s}$ about each axis, the rates are conservatively constrained to $10\,^\circ/\text{s}$ about each axis before applying a 10 Hz low pass filter. Additionally, the single-point estimators are found to suffer significantly due to the noise in the angular rate measurements, but applying a 10 Hz low pass filter to the commanded reaction wheel torques and CSS measurements alleviates this issue. Because the rate gyro model is no longer valid, for the EKF and ECKF the values of σ_ω and σ_{ω_β} are set to zero and the sun-direction rate spectral density is increased to $1.0\,\text{rad}/\sqrt{\text{s}}$.

Results show that even though this simple backward-difference method does not provide new information, it does provide an adequate estimate for achieving a power positive orientation. More complicated methods for estimating the angular rate of a satellite exist; for example Azor, Bar-Itzhack, and Harman propose using an extended interlaced Kalman filter composed of three separate Kalman filters[93] and Mortari and Akela propose two filtering techniques that use quaternions to estimate the angular velocity[94]. Because the EKF and ECKF based methods are shown to perform quite well using the simple method proposed here, the investigation of these more complicated methods is left to future work.

Statistics are shown in Figures 3.15 and 3.16 for a 1000 case Monte Carlo analysis where the control is operating, but no rate gyro measurements are available. It is important to remember this represents a worst case safe-mode scenario in which only CSS and reaction wheels are available, and is presented here as a preliminary look into the robustness of the estimation algorithms examined. Nominally with rate gyro measurements, the sequential estimators propagate the spacecraft's orientation while in the shadow of the Earth. However, because the rate estimate is entirely dependent on having a sun-direction estimate, the sequential estimator propagation and all control effort are suspended when the spacecraft is in the shadow of the Earth if no rate gyro measurements are available.

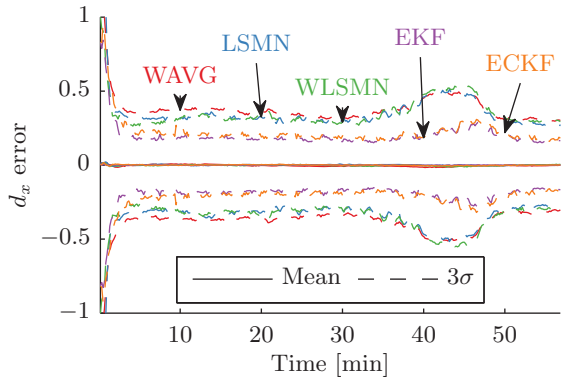

(a) Error in x-component of scaled sun-direction vector.

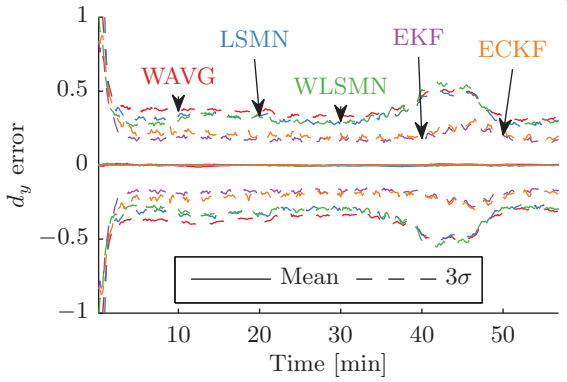

(b) Error in y-component of scaled sun-direction vector.

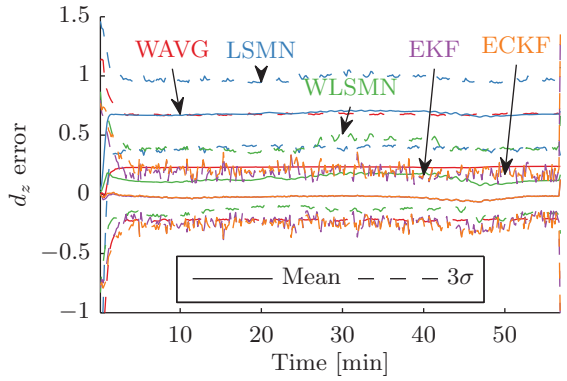

(c) Error in z-component of scaled sun-direction vector.

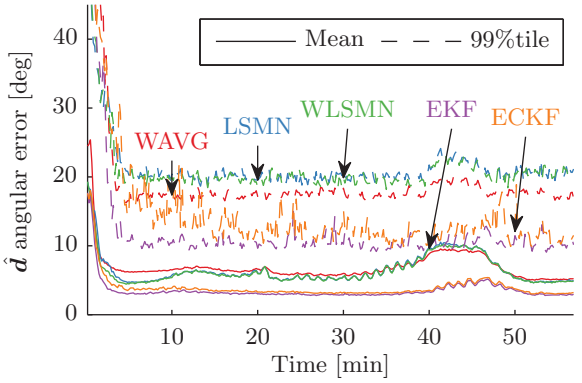

(d) Angular error of sun-direction vector estimate.

Figure 3.15: Calculated statistics for 1000 case Monte Carlo run with control, but no rate gyro measurements.

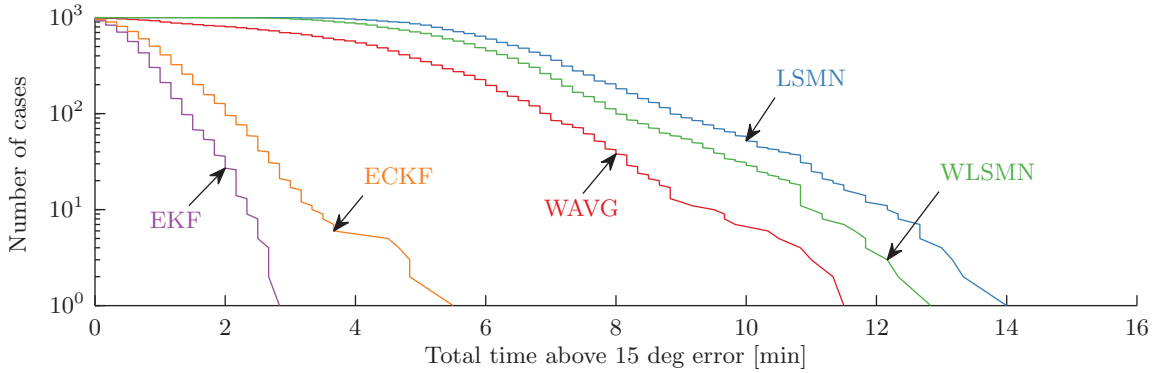

Figure 3.16: Total time spent with estimate in error of more than 15° for 1000 case Monte Carlo run with control, but no rate gyro measurements.

As a result of the numerical differentiation, the single-point estimators perform approximately the same, albeit with much greater variability in the estimate, as when using an intermediate level gyro as long as the low pass filtering mentioned is implemented. This is expected as the rate gyro measurement is only used by the control algorithm to damp out the spacecraft angular velocity. It is interesting that the EKF and ECKF still perform quite well despite the significant noise of the rate gyro measurements. All EKF cases spend less than approximately 5 min of the 56 min in view of the Sun per orbit with estimation error greater than 15°. The ECKF is more conservative in its estimate, and as a result, spends slightly more time with greater than 15° angular error than the EKF.

3.3.4 Sun-Direction Estimation & Control Sensitivity to Rate Gyro Accuracy

The results of 1000 case Monte Carlo analyses, in which the level of gyroscope accuracy is varied, are shown in Figures 3.17 to 3.20. The rate gyro accuracy levels correspond to those listed in Table 2.3. Results are shown for the EKF and ECKF methods and the single point estimators are omitted, as the estimators themselves do not use the angular rate measurements and the fidelity of angular rate measurements will only impact the control system's ability to arrest all rates.

Figures 3.17 and 3.18 show the results of using the EKF estimator with varying levels of rate gyro performance. Interestingly, the inertial and intermediate level gyro levels have nearly identical results, and examining the total time above 15° error they provide almost no improvement over the moderate gyro. This is because for those levels of rate gyro performance the noise levels are below the uncertainty in the inertial sun-direction rate of change and, thus, the increased rate gyro performance does not improve the estimate. Also of interest is that the use of low level gyro results in estimation error that is very close to the error when not using gyro measurements. The use of a gyro does help to increase the smoothness of the estimate, but for low level gyros, the noise level and bias uncertainty are so large that the estimation accuracy is on par with the accuracy attained without using a gyro.

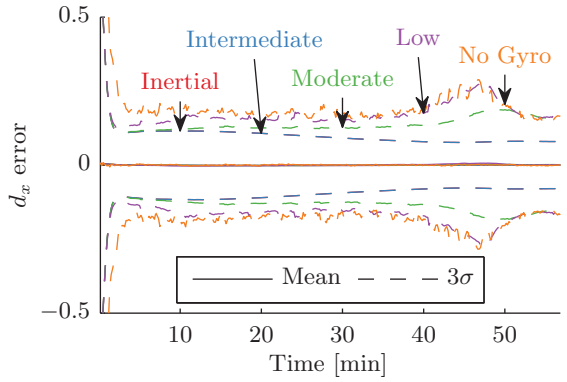

(a) Error in x-component of scaled sun-direction vector.

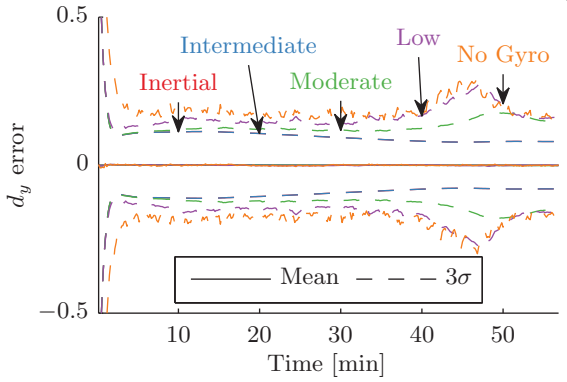

(b) Error in y-component of scaled sun-direction vector.

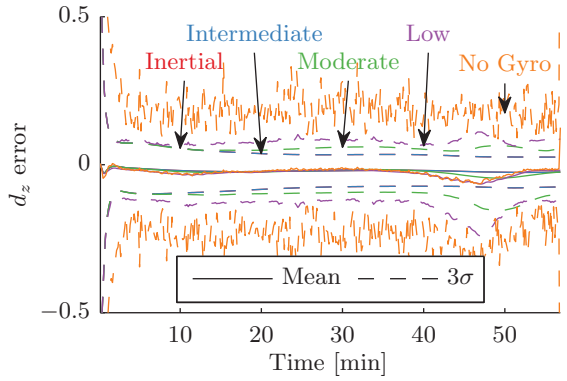

(c) Error in z-component of scaled sun-direction vector.

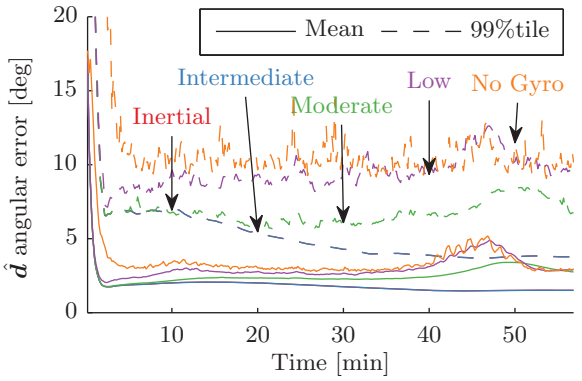

(d) Angular error of sun-direction vector estimate.

Figure 3.17: Calculated statistics for 1000 case Monte Carlo run with control and EKF estimator using varying levels of rate gyro measurements.

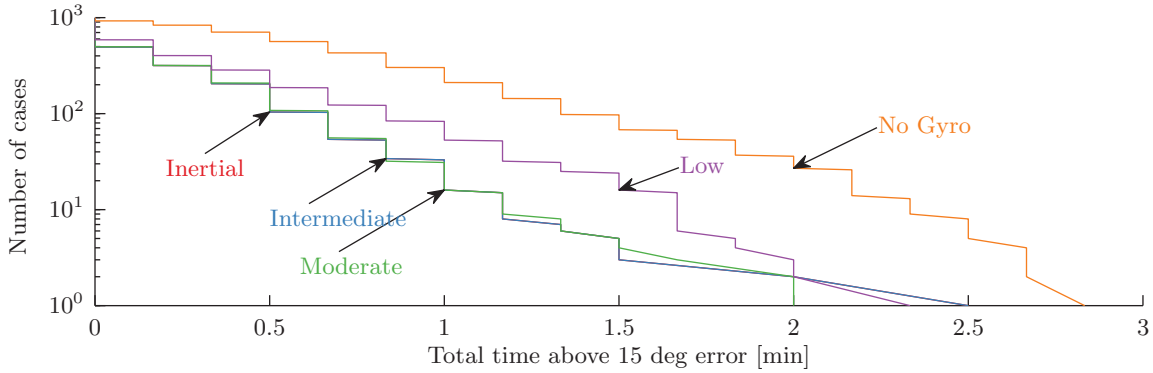

Figure 3.18: Total time spent with estimate in error of more than 15° for 1000 case Monte Carlo run with control and EKF method using varying levels of rate gyro measurements.

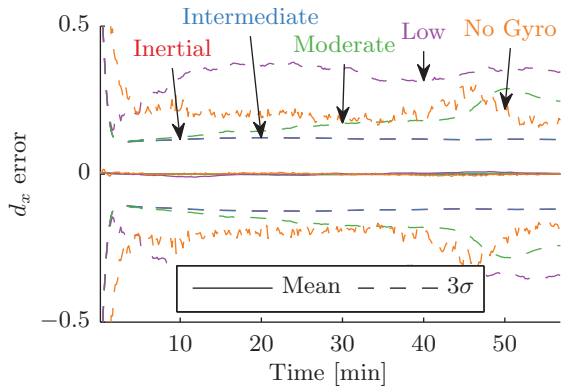

(a) Error in x-component of scaled sun-direction vector.

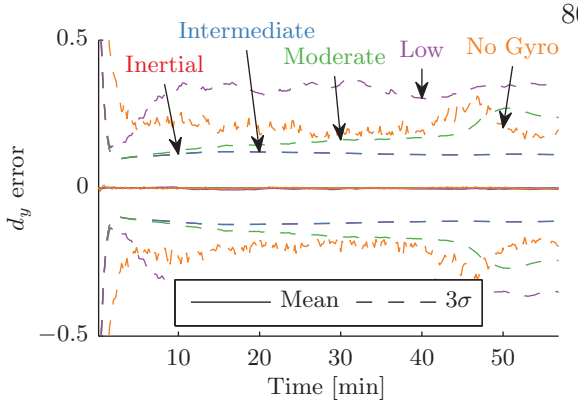

(b) Error in y-component of scaled sun-direction vector.

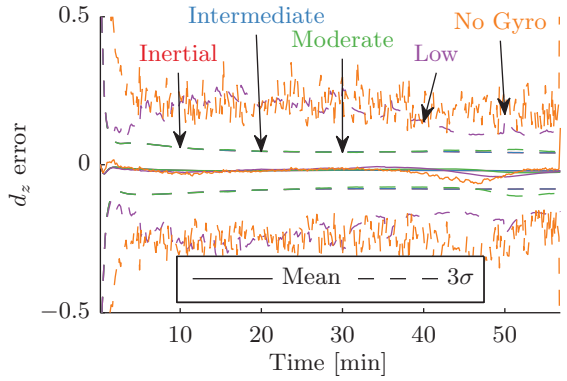

(c) Error in z-component of scaled sun-direction vector.

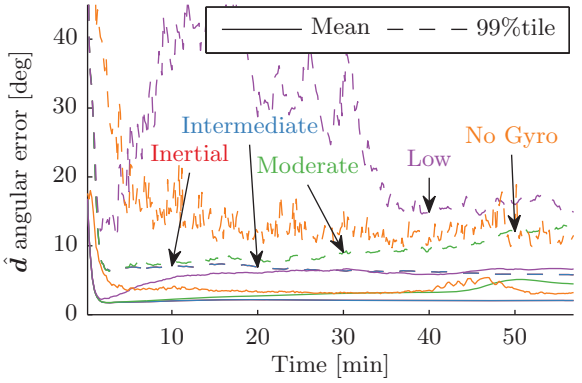

(d) Angular error of sun-direction vector estimate.

Figure 3.19: Calculated statistics for 1000 case Monte Carlo run with control and ECKF estimator using varying levels of rate gyro measurements.

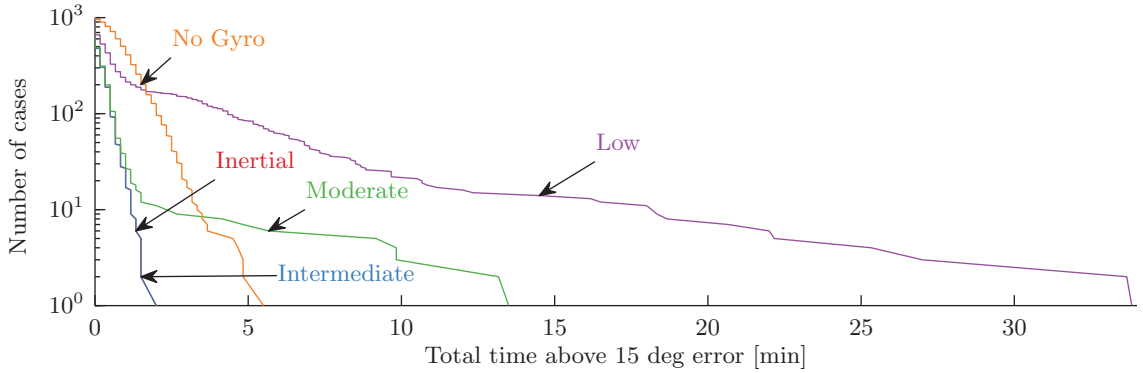

Figure 3.20: Total time spent with estimate in error of more than 15° for 1000 case Monte Carlo run with control and ECKF method using varying levels of rate gyro measurements.

Figures 3.19 and 3.20 show the results of using the ECKF estimator with varying levels of rate gyro performance. The angular error plot highlights a key point between the EKF and ECKF estimators. The EKF method uses a set value for the process noise in the system, that because of the unmodeled bias must be adjusted based on the estimated longest period of estimation, whereas the ECKF estimator includes a term to inflate the process noise over time. Thus, the uncertainty in the angular error of the ECKF grows to a value at which the information from the CSS balances the increasing uncertainty in the propagation. Also as a result of this, when the spacecraft is in the shadow of the Earth, the uncertainty in the ECKF estimate grows extremely large and the estimator spends several minutes of the next pass in view of the Sun recovering. Because of the dispersion in the initial true anomaly of the spacecraft in the Monte Carlo analysis, this manifests as a large dispersion, caused by an accumulation of short duration large sun-direction angular errors across the many Monte Carlo runs, in the sun-direction angle as seen in Figure 3.19d between 10 min and 30 min.

It is important to note that the gyro and the no gyro cases assume slightly different control algorithms. The with gyro cases attempt to propagate the attitude of the spacecraft through the shadow of the Earth using the rate gyro measurements. Because of the large biases present in the low performance gyro, the control spends the entire 36 min in the shadow of the Earth driving the spacecraft away from the true sun-direction. In contrast, the no gyro case turns off all control effort while in the shadow of the Earth and resumes active control when new CSS measurements become available. Despite using a noisy numerical backward difference rate estimate, the sun-direction estimator without rate gyro measurements is able to quickly achieve sun-pointing. The 99th percentile bounds for the low performance gyro case can be reduced by adopting a similar control approach.

Also, it is worth reiterating that the EKF and ECKF estimation filters are not optimal filters. As a result of the significant noise and biases present in the system, the EKF and ECKF are extremely conservative. Because of this, the Monte Carlo calculated 3σ bounds are much tighter than the estimator predicted bounds. Figure 3.21 shows the scaled sun-direction estimate error

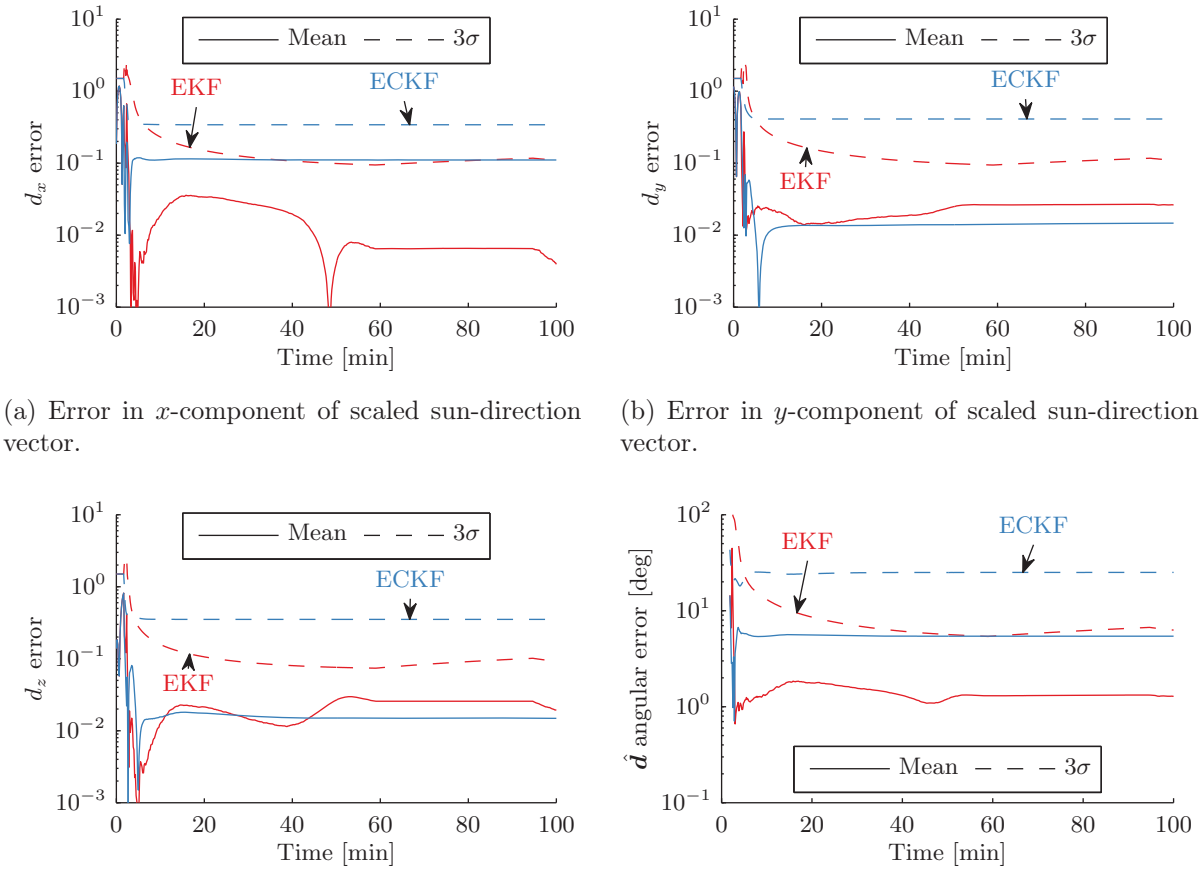

(a) Error in x-component of scaled sun-direction vector.

(b) Error in y-component of scaled sun-direction vector.

(c) Error in z-component of scaled sun-direction vector.

(d) Angular error of sun-direction vector estimate.

Figure 3.21: EKF and ECKF estimator performance for a single case.

and predicted covariance bounds for a single case using the EKF and ECKF estimators and an intermediate level gyro. As these estimators are designed to be used in a safe mode, conservatism is chosen over possible divergence.

3.3.5 Computation Time

An important factor when determining what algorithm to use is the available computation power. The total calculation time of the propagation and measurement updates are computed for the various estimation methods over an entire 100 min simulation. None of the algorithms have been optimized and they use the same routines to compute matrix algebra. The average and standard

deviations of the computation times, for C code compiled on a Windows i7 2.5 GHz machine, are shown in Table 3.1. The EKF and ECKF propagation updates are computed using an RK4 integrator. While this is not flight hardware, the relative difference is used to evaluate the relative computational costs of the these algorithms.

Table 3.1: Averages and standard deviations for computation times of various filters.

Method	Propagation Update [µs]	Measurement Update [µs]
WAVG	-	0.95 ± 0.54
LSMN	-	1.25 ± 0.69
WLSMN	-	1.26 ± 0.80
EKF	1.83 ± 0.81	1.32 ± 0.96
ECKF	3.86 ± 1.40	13.4 ± 10.8

All of the single point algorithms benefit from a lack of propagation update. The WAVG algorithm is the simplest and executes the fastest as expected. The LSMN and WLSMN methods are slightly slower due to the logic necessary to determine whether to use the least squares or minimum norm algorithm, but execute in nearly the same amount of time. The EKF measurement update evaluates in nearly the same amount of time as the WLSMN and LSMN algorithms, but requires a propagation update that takes longer than the measurement update. The ECKF is the slowest, by far, of the algorithms. This is due to the additional matrix math required to propagate and update the expanded state. This method provides a more robust mathematical modeling of the biases in the system, but it does come with increased computational costs.

Chapter 4

On-Orbit CSS Calibration

Expanding the estimation method developed in Section 3.2.1.2 to use an extended consider Kalman filter approach provides a method for accounting for the uncertainty associated with several systematic biases. A better approach is to estimate these biases directly. As noted by Springmann, literature on the on-orbit calibration of sun sensors is sparse[5]. Ortega, López-Rodríguez, et. al., and Wu and Steyn both present calibration of two-axis sun sensors specific to an individual model[11,47] and Springmann presents a CSS calibration filter capable of calculating CSS scale factor and misalignment[5]. The filter is a quaternion based EKF approach that assumes the albedo contributions to the EKF Jacobians are small, and the filter performance is shown for flight data.

Presented here are two CSS calibration filters, formulated using Modified Rodrigues Parameters (MRPs) and based on an ECKF approach. A MRP based filter is chosen because MRP based attitude estimation filters have been shown to have equal accuracy to and faster initial convergence than quaternion filters with slightly faster numerical evaluation and vastly simpler coding implementation[95]. An extended consider Kalman filter is used, instead of a traditional EKF, in order to account for known biases in the measurement model. In addition, the impact of the irradiance due to albedo is included to first order in the system Jacobians. The first filter uses an Earth albedo model to estimate the irradiance received by a CSS due to Earth's albedo, whereas the second treats the irradiance due to albedo as an unmodeled bias that is considered. The goal is to compare the relative accuracy and computation time of the two methods in order that the amount of ground-based support required by small satellites may be reduced and autonomy increased.

4.1 MRP Attitude Estimator

In order to estimate several of the systematic biases present in both the rate gyro and CSS models, an approach similar to a traditional MRP attitude estimation EKF formulation is used. The properties of MRPs and an MRP based attitude filter are presented here as review. For more detailed information regarding MRPs and MRP attitude estimation the reader is referred to References 83, 95, 96, and 97.

4.1.1 Modified Rodrigues Parameters

The MRP vector $\boldsymbol{\sigma}$ is defined in terms of the principal rotation elements as

$$\boldsymbol{\sigma} = \hat{\boldsymbol{e}} \tan\left(\frac{\Phi}{4}\right) \tag{4.1}$$

where $\hat{\boldsymbol{e}}$ is the principal rotation axis, and Φ is the principal rotation angle[83,96]. The MRP shadow set is defined as

$$\boldsymbol{\sigma}^S = -\frac{\boldsymbol{\sigma}}{\boldsymbol{\sigma}^T\boldsymbol{\sigma}} \tag{4.2}$$

and both MRPs satisfy the differential equation

$$\dot{\boldsymbol{\sigma}} = \frac{1}{4}\left[\left(1-\boldsymbol{\sigma}^T\boldsymbol{\sigma}\right)\left[\boldsymbol{I}_{3\times 3}\right] + 2\left[\boldsymbol{\sigma}\right]_\times + 2\boldsymbol{\sigma}\boldsymbol{\sigma}^T\right]\boldsymbol{\omega} = \frac{1}{4}\left[B(\boldsymbol{\sigma})\right]\boldsymbol{\omega} \tag{4.3}$$

where $[\cdot]_\times$ represents the skew-symmetric cross product matrix given by

$$[\boldsymbol{\sigma}]_\times = \begin{bmatrix} 0 & -\sigma_3 & \sigma_2 \\ \sigma_3 & 0 & -\sigma_1 \\ -\sigma_2 & \sigma_1 & 0 \end{bmatrix}.$$

The inverse MRP is given by $\boldsymbol{\sigma}^{-1} \equiv -\boldsymbol{\sigma}$ and the successive rotation of two MRPs is computed using the MRP product

$$\bar{\bar{\boldsymbol{\sigma}}} = \bar{\boldsymbol{\sigma}} \otimes \boldsymbol{\sigma} = \frac{\left(1-\boldsymbol{\sigma}^T\boldsymbol{\sigma}\right)\bar{\boldsymbol{\sigma}} + \left(1-\bar{\boldsymbol{\sigma}}^T\bar{\boldsymbol{\sigma}}\right)\boldsymbol{\sigma} - 2\left[\bar{\boldsymbol{\sigma}}\right]_\times\boldsymbol{\sigma}}{1+\left(\boldsymbol{\sigma}^T\boldsymbol{\sigma}\right)\left(\bar{\boldsymbol{\sigma}}^T\bar{\boldsymbol{\sigma}}\right) - 2\bar{\boldsymbol{\sigma}}^T\boldsymbol{\sigma}}. \tag{4.4}$$

4.1.2 Extended Kalman Filter Based MRP Attitude Estimator

A MRP attitude estimator uses an extended Kalman filter approach with the state vector

$$\boldsymbol{x}(t) = \begin{bmatrix} \boldsymbol{\sigma}(t) \\ {}^{\mathcal{G}}\boldsymbol{\omega}_{\beta}(t) \end{bmatrix} \tag{4.5}$$

The state dynamics are found by combining Equation (4.3) and Equation (3.28b)

$$\begin{bmatrix} \dot{\boldsymbol{\sigma}}(t) \\ {}^{\mathcal{G}}\dot{\boldsymbol{\omega}}_{\beta}(t) \end{bmatrix} = \begin{bmatrix} \frac{1}{4}\left[B\left(\boldsymbol{\sigma}(t)\right)\right] {}^{\mathcal{B}}\boldsymbol{\omega}(t) \\ {}^{\mathcal{G}}\boldsymbol{\eta}_{\omega_d}(t) \end{bmatrix} = \begin{bmatrix} \frac{1}{4}\left[B\left(\boldsymbol{\sigma}(t)\right)\right][BG]\left\{{}^{\mathcal{G}}\tilde{\boldsymbol{\omega}}(t) - {}^{\mathcal{G}}\boldsymbol{\omega}_{\beta}(t) - {}^{\mathcal{G}}\boldsymbol{\eta}_{\omega}(t)\right\} \\ {}^{\mathcal{G}}\boldsymbol{\eta}_{\omega_d}(t) \end{bmatrix} \tag{4.6}$$

Defining the process noise as

$$\boldsymbol{\eta} = \begin{bmatrix} {}^{\mathcal{G}}\boldsymbol{\eta}_{\omega}(t) \\ {}^{\mathcal{G}}\boldsymbol{\eta}_{\omega_d}(t) \end{bmatrix} \tag{4.7}$$

the quantities given in Equation (3.20) are

$$\boldsymbol{F} = \begin{bmatrix} \frac{1}{2}\left(\hat{\boldsymbol{\sigma}}(t)\,{}^{\mathcal{B}}\hat{\boldsymbol{\omega}}^{T}(t) - {}^{\mathcal{B}}\hat{\boldsymbol{\omega}}(t)\,\hat{\boldsymbol{\sigma}}^{T}(t) - \left[{}^{\mathcal{B}}\hat{\boldsymbol{\omega}}(t)\right]_{\times} + \hat{\boldsymbol{\sigma}}^{T}(t)\,{}^{\mathcal{B}}\hat{\boldsymbol{\omega}}(t)\,\boldsymbol{I}_{3\times 3}\right) & -\frac{1}{4}\left[B\left(\hat{\boldsymbol{\sigma}}(t)\right)\right][BG] \\ \boldsymbol{0}_{3\times 3} & \boldsymbol{0}_{3\times 3} \end{bmatrix} \tag{4.8a}$$

$$\boldsymbol{G} = \begin{bmatrix} -\frac{1}{4}\left[B\left(\hat{\boldsymbol{\sigma}}(t)\right)\right][BG] & \boldsymbol{0}_{3\times 3} \\ \boldsymbol{0}_{3\times 3} & \boldsymbol{I}_{3\times 3} \end{bmatrix} \tag{4.8b}$$

where $\hat{\boldsymbol{\sigma}}$ is the current best estimate of the attitude MRP, ${}^{\mathcal{G}}\hat{\boldsymbol{\omega}}_{b}$ is the best estimate of the total rate gyro bias in the rate gyro frame, and

$${}^{\mathcal{B}}\hat{\boldsymbol{\omega}} = [BG]\left[{}^{\mathcal{G}}\tilde{\boldsymbol{\omega}} - {}^{\mathcal{G}}\hat{\boldsymbol{\omega}}_{b}\right] \tag{4.9}$$

is the current best estimate of the angular velocity in the body frame.

Assuming measurements are taken of the body's attitude, via a star tracker or other generic attitude sensor, the measurement model is given by

$$\boldsymbol{y}_k = \boldsymbol{\sigma}_k + \boldsymbol{\nu}_k \tag{4.10}$$

where $\boldsymbol{\nu}_k$ is discrete-time white-noise with covariance $\boldsymbol{R}_k$. Thus, the EKF measurement Jacobians in Equation (3.25) are

$$\boldsymbol{H} = \begin{bmatrix} \boldsymbol{I}_{3\times 3} & \boldsymbol{0}_{3\times 3} \end{bmatrix} \tag{4.11a}$$

$$\boldsymbol{M} = \boldsymbol{I}_{3\times 3}. \tag{4.11b}$$

4.2 Full CSS Calibration Filter

The full CSS calibration filter assumes the spacecraft has CSS, inertial attitude, and angular rate measurements available, as well as an orbit solution and an estimate of the reference Earth-Sun vector, which requires the current Julian date. A continuous-discrete extended consider Kalman filter, as outlined in Section 3.2.2.1 is used as some of the measurement errors are better modeled as biases than white noise. The state vector is chosen to be

$$\boldsymbol{x}(t) = \begin{bmatrix} \boldsymbol{\sigma}(t) \\ {}^{\mathcal{G}}\boldsymbol{\omega}_{\beta}(t) \\ \boldsymbol{C}(t) \\ \boldsymbol{\theta} \\ \boldsymbol{\phi} \end{bmatrix} \tag{4.12}$$

where $\boldsymbol{\sigma}(t)$ is the MRP attitude description of the spacecraft. The MRP dynamics, assuming the rate gyro dynamics are modeled as shown in Section 2.3, are given by

$$\dot{\boldsymbol{\sigma}}(t) = \frac{1}{4}\left[B(\boldsymbol{\sigma}(t))\right]\left[BG\right]\left({}^{\mathcal{G}}\tilde{\boldsymbol{\omega}}(t) - {}^{\mathcal{G}}\boldsymbol{\omega}_{\beta}(t) - {}^{\mathcal{G}}\boldsymbol{\eta}_{\omega}(t)\right) \tag{4.13}$$

and the individual sensor calibration factors are assumed to be governed by

$$\dot{\boldsymbol{C}}(t) = \boldsymbol{\eta}_{C}(t)\,. \tag{4.14}$$

As mentioned in Section 2.1.4, it is expected $\boldsymbol{C}$ will be affected by changes in solar irradiance and over time the values of $\boldsymbol{C}$ will slowly decrease as CSS degrade due to radiation damage. For short time scales the individual sensor calibration factors are expected to remain constant and are modeled as having a random walk as a worst case analysis. Defining the best estimate of the true spacecraft angular velocity in the body frame as

$${}^{\mathcal{B}}\hat{\boldsymbol{\omega}}(t) = \left[BG\right]\left({}^{\mathcal{G}}\tilde{\boldsymbol{\omega}}(t) - {}^{\mathcal{G}}\hat{\boldsymbol{\omega}}_{b}(t)\right), \tag{4.15}$$

and the process noise vector as

$$\boldsymbol{\eta}(t) = \begin{bmatrix} {}^{\mathcal{G}}\boldsymbol{\eta}_{\omega}(t) \\ {}^{\mathcal{G}}\boldsymbol{\eta}_{\omega_d}(t) \\ \boldsymbol{\eta}_C(t) \end{bmatrix}, \tag{4.16}$$

the pertinent propagation Jacobians are given by

$$\boldsymbol{F}(t) = \begin{bmatrix} \frac{1}{2}\left(\hat{\boldsymbol{\sigma}}{}^{\mathcal{B}}\hat{\boldsymbol{\omega}}^T + {}^{\mathcal{B}}\hat{\boldsymbol{\omega}}\hat{\boldsymbol{\sigma}}^T - \left[{}^{\mathcal{B}}\hat{\boldsymbol{\omega}}\right]_\times + \hat{\boldsymbol{\sigma}}^T{}^{\mathcal{B}}\hat{\boldsymbol{\omega}}\boldsymbol{I}_{3\times3}\right) & -\frac{1}{4}\left[B(\boldsymbol{\sigma})\right][BG] & \boldsymbol{0}_{3\times3N} \\ \boldsymbol{0}_{(3+3N)\times3} & \boldsymbol{0}_{(3+3N)\times3} & \boldsymbol{0}_{(3+3N)\times3N} \end{bmatrix} \tag{4.17a}$$

$$\boldsymbol{G}(t) = \begin{bmatrix} -\frac{1}{4}\left[B(\boldsymbol{\sigma})\right][BG] & \boldsymbol{0}_{3\times3} & \boldsymbol{0}_{3\times N} \\ \boldsymbol{0}_{3\times3} & \boldsymbol{I}_{3\times3} & \boldsymbol{0}_{3\times N} \\ \boldsymbol{0}_{N\times3} & \boldsymbol{0}_{N\times3} & \boldsymbol{I}_{N\times N} \\ \boldsymbol{0}_{2N\times3} & \boldsymbol{0}_{2N\times3} & \boldsymbol{0}_{2N\times N} \end{bmatrix} \tag{4.17b}$$

where $\hat{\boldsymbol{\sigma}}$ is the current best estimate of the attitude MRP. The block structure of the Jacobians, particularly the sections equal to zero, should be considered when implementing the state update in order to reduce the total computations necessary.

As noted previously, it is assumed direct measurements of the body's attitude, via a star tracker or other generic attitude sensor, are available in addition to CSS measurements. Because these measurements may be sampled at different frequencies, and their noise values are uncorrelated, they are presented here as separate measurement updates.

Attitude measurements, for example from a star tracker, are modeled by

$$\boldsymbol{y}_k = \boldsymbol{\sigma}_k + \boldsymbol{\nu}_{\sigma,k} \tag{4.18}$$

where $\boldsymbol{\nu}_{\sigma,k}$ is discrete-time white noise with covariance $\boldsymbol{R}_{\sigma,k}$. The measurement update Jacobians are given by

$$\boldsymbol{H}_k = \begin{bmatrix} \boldsymbol{I}_{3\times3} & \boldsymbol{0}_{3\times(3+3N)} \end{bmatrix} \tag{4.19a}$$

$$\boldsymbol{M}_k = \boldsymbol{I}_{3\times3} \tag{4.19b}$$

$$\boldsymbol{J}_k = \boldsymbol{0} \tag{4.19c}$$

because there are no measurement biases modeled.

The CSS measurement model is based on Equation (3.1), however, it is modified so that it is written in terms of the state parameters given in Equation (4.12). It is initially assumed that the spacecraft has some estimate of the Earth-Sun vector $\boldsymbol{s}_{\oplus}$, obtained via ephemeris or a periodic model like those examined in Section 4.4.4, and its own position relative to the Earth $\boldsymbol{r}_B$, obtained from GPS or a ground generated orbit solution. The actual sun-direction vector can be written as

$$^{\mathcal{B}}\boldsymbol{s} = [BN]\,^{\mathcal{N}}\left(\boldsymbol{s}_{\oplus} - \boldsymbol{r}_B\right) \tag{4.20}$$

where $\boldsymbol{r}_B$ is the actual position of the spacecraft relative to the Earth, $\boldsymbol{s}_{\oplus}$ is the actual direction vector from the Earth to the Sun, and the direction cosine matrix $[BN]$ is written in terms of the attitude MRP as

$$[BN] = \left[I_{3\times 3}\right] + \frac{8\left[\boldsymbol{\sigma}\right]_{\times}^{2} - 4\left(1-\sigma^{2}\right)\left[\boldsymbol{\sigma}\right]_{\times}}{\left(1+\sigma^{2}\right)^{2}} \tag{4.21}$$

where $\sigma^{2n} = \left(\boldsymbol{\sigma}^{T}\boldsymbol{\sigma}\right)^{n}$. Because the estimation algorithm is assumed to only have estimates of the spacecraft position and Earth-Sun reference vector, the best estimate of the sun-direction vector is given by

$$^{\mathcal{B}}\hat{\boldsymbol{s}} = [BN]\,^{\mathcal{N}}\left(\hat{\boldsymbol{s}}_{\oplus} - \hat{\boldsymbol{r}}_B\right) \tag{4.22}$$

with $\boldsymbol{r}_B = \hat{\boldsymbol{r}}_B - \boldsymbol{r}_{B_\beta}$ where $\boldsymbol{r}_{B_\beta}$ is a bias in the uncertainty in the spacecraft position

$$\begin{aligned} \mathrm{E}\left[\left(\hat{\boldsymbol{r}}_{B_\beta} - \boldsymbol{r}_{B_\beta}\right)\right] &= \boldsymbol{0}, \\ \mathrm{E}\left[\left(\hat{\boldsymbol{r}}_{B_\beta} - \boldsymbol{r}_{B_\beta}\right)\left(\hat{\boldsymbol{r}}_{B_\beta} - \boldsymbol{r}_{B_\beta}\right)^{T}\right] &= \boldsymbol{B}_{r_B,k}\delta_{jk}\ \forall\ j,k \end{aligned} \tag{4.23}$$

and $\boldsymbol{s}_{\oplus} = \hat{\boldsymbol{s}}_{\oplus} - \boldsymbol{s}_{\oplus_\beta}$ where $\boldsymbol{s}_{\oplus_\beta}$ is a measurement bias due to model errors in the reference Earth-Sun vector with

$$\begin{aligned} \mathrm{E}\left[\left(\hat{\boldsymbol{s}}_{\oplus_\beta,k} - \boldsymbol{s}_{\oplus_\beta,k}\right)\right] &= \boldsymbol{0}, \\ \mathrm{E}\left[\left(\hat{\boldsymbol{s}}_{\oplus_\beta,k} - \boldsymbol{s}_{\oplus_\beta,k}\right)\left(\hat{\boldsymbol{s}}_{\oplus_\beta,k} - \boldsymbol{s}_{\oplus_\beta,k}\right)^{T}\right] &= \boldsymbol{B}_{s_\oplus,k}\delta_{jk}\ \forall\ j,k. \end{aligned} \tag{4.24}$$

The error in a properly post-processed orbit solution should resemble white noise. However, the error in a real time estimate of the spacecraft position will more likely exhibit bias-like characteristics.

Similarly, as shown in Figure 4.11, the error in the sun-direction reference vector is treated as a bias. The vector from the differential area on the surface of the Earth to the spacecraft is written as

$$^{\mathcal{N}}\boldsymbol{r}_{AB} = {}^{\mathcal{N}}\boldsymbol{r}_{B} - {}^{\mathcal{N}}\boldsymbol{r}_{A} \tag{4.25}$$

and the best estimate of this vector is given by

$$^{\mathcal{N}}\hat{\boldsymbol{r}}_{AB} = {}^{\mathcal{N}}\hat{\boldsymbol{r}}_{B} - {}^{\mathcal{N}}\boldsymbol{r}_{A} \tag{4.26}$$

using the definitions given previously.

Removing the biases from Equation (2.19), because the angles are being estimated directly, results in a modified measurement model

$$V = C\left(V_d + V_\alpha + \nu_V\right)$$

$$V_d = \begin{cases} {}^{\mathcal{B}}\begin{bmatrix}\cos\phi\cos\theta & \cos\phi\sin\theta & \sin\phi\end{bmatrix}[BN]\,\frac{{}^{\mathcal{N}}\boldsymbol{s}_{\oplus} - {}^{\mathcal{N}}\boldsymbol{r}_{B}}{\left\|{}^{\mathcal{N}}\boldsymbol{s}_{\oplus} - {}^{\mathcal{N}}\boldsymbol{r}_{B}\right\|} & \text{if } \frac{\boldsymbol{n}^T\boldsymbol{s}}{\|\boldsymbol{n}\|\|\boldsymbol{s}\|} \geq \cos\psi \\ 0 & \text{if } \frac{\boldsymbol{n}^T\boldsymbol{s}}{\|\boldsymbol{n}\|\|\boldsymbol{s}\|} < \cos\psi \end{cases}$$

$$V_\alpha = \begin{cases} -\frac{1}{\pi}\iint_{\boldsymbol{A}} (\alpha+\nu_\alpha)\,\frac{{}^{\mathcal{N}}\boldsymbol{n}_A^T\,{}^{\mathcal{N}}\boldsymbol{s}_{\oplus}}{\left\|{}^{\mathcal{N}}\boldsymbol{r}_{AB}\right\|^2\left\|{}^{\mathcal{N}}\boldsymbol{s}_{\oplus}\right\|}\left({}^{\mathcal{N}}\boldsymbol{n}_A^T\frac{{}^{\mathcal{N}}\boldsymbol{r}_{AB}}{\left\|{}^{\mathcal{N}}\boldsymbol{r}_{AB}\right\|}\right) \\ \qquad * \left({}^{\mathcal{B}}\begin{bmatrix}\cos\phi\cos\theta & \cos\phi\sin\theta & \sin\phi\end{bmatrix}[BN]\,\frac{{}^{\mathcal{N}}\boldsymbol{r}_{AB}}{\left\|{}^{\mathcal{N}}\boldsymbol{r}_{AB}\right\|}\right)\mathrm{d}A & \text{if } B \notin \boldsymbol{\mathcal{S}} \\ 0 & \text{if } B \in \boldsymbol{\mathcal{S}} \end{cases} \tag{4.27}$$

where ν_α is zero-mean Gaussian noise representing the uncertainty in the albedo coefficient of $\mathrm{d}A$ calculated from the NASA TOMS data, and it is assumed $\left\|\boldsymbol{n}_A\right\| = 1$. Defining the measurement noise and bias vectors as

$$\boldsymbol{\nu}_k = \begin{bmatrix}\boldsymbol{\nu}_{V,k} \\ \boldsymbol{\nu}_{\alpha,k}\end{bmatrix}, \quad \boldsymbol{\beta}_\nu = \begin{bmatrix}{}^{\mathcal{N}}\boldsymbol{s}_{\oplus_\beta,k} \\ {}^{\mathcal{N}}\boldsymbol{r}_{B_\beta,k}\end{bmatrix} \tag{4.28}$$

where $\boldsymbol{\nu}_{\alpha,k}$ is vector, of length N_α, of all the albedo coefficient uncertainty terms in $\boldsymbol{A}$, the measurement update Jacobians are given by

$$\boldsymbol{H}_k = \boldsymbol{H}_{d,k} + \boldsymbol{H}_{\alpha,k} \tag{4.29a}$$

$$\boldsymbol{H}_{d,k} = \begin{bmatrix} \begin{bmatrix} \boldsymbol{a}_{1,k} \\ \vdots \\ \boldsymbol{a}_{N,k} \end{bmatrix} & \boldsymbol{0}_{N\times 3} & \operatorname{diag}\Big(b_{1,k},\ldots,b_{N,k}\Big) & \operatorname{diag}\Big(c_{1,k},\ldots,c_{N,k}\Big) & \operatorname{diag}\Big(d_{1,k},\ldots,d_{N,k}\Big) \end{bmatrix}$$

$$(\cdot)_{i,k} = \begin{cases} (\bar{\cdot})_{i,k} & \text{if } \frac{\boldsymbol{n}_i^T \hat{\boldsymbol{s}}_k}{\|\boldsymbol{n}_i\|\|\hat{\boldsymbol{s}}_k\|} \geq \cos\psi_i \\ \boldsymbol{0} & \text{if } \frac{\boldsymbol{n}_i^T \hat{\boldsymbol{s}}_k}{\|\boldsymbol{n}_i\|\|\hat{\boldsymbol{s}}_k\|} < \cos\psi_i \end{cases}$$

$$\bar{\boldsymbol{a}}_{i,k} = \hat{C}_{i,k}^{\ \mathcal{B}}\begin{bmatrix} \cos\phi_i\cos\theta_i & \cos\phi_i\sin\theta_i & \sin\phi_i \end{bmatrix} \frac{\partial}{\partial\boldsymbol{\sigma}} \left([BN] \frac{{}^{\mathcal{N}}\hat{\boldsymbol{s}}_k}{\|{}^{\mathcal{N}}\hat{\boldsymbol{s}}_k\|} \right)\Bigg|_{\hat{\boldsymbol{\sigma}}_k}$$

$$\bar{b}_{i,k} = {}^{\mathcal{B}}\begin{bmatrix} \cos\phi_i\cos\theta_i & \cos\phi_i\sin\theta_i & \sin\phi_i \end{bmatrix} [BN] \frac{{}^{\mathcal{N}}\hat{\boldsymbol{s}}_k}{\|{}^{\mathcal{N}}\hat{\boldsymbol{s}}_k\|}$$

$$\bar{c}_{i,k} = \hat{C}_{i,k}^{\ \mathcal{B}}\begin{bmatrix} -\cos\phi_i\sin\theta_i & \cos\phi_i\cos\theta_i & 0 \end{bmatrix} [BN] \frac{{}^{\mathcal{N}}\hat{\boldsymbol{s}}_k}{\|{}^{\mathcal{N}}\hat{\boldsymbol{s}}_k\|}$$

$$\bar{d}_{i,k} = \hat{C}_{i,k}^{\ \mathcal{B}}\begin{bmatrix} -\sin\phi_i\cos\theta_i & -\sin\phi_i\sin\theta_i & \cos\phi_i \end{bmatrix} [BN] \frac{{}^{\mathcal{N}}\hat{\boldsymbol{s}}_k}{\|{}^{\mathcal{N}}\hat{\boldsymbol{s}}_k\|} \tag{4.29b}$$

$$\boldsymbol{H}_{\alpha,k} = \begin{bmatrix} \begin{bmatrix} \boldsymbol{a}_{1,k} \\ \vdots \\ \boldsymbol{a}_{N,k} \end{bmatrix} & \boldsymbol{0}_{N\times 3} & \operatorname{diag}\Big(b_{1,k},\ldots,b_{N,k}\Big) & \operatorname{diag}\Big(c_{1,k},\ldots,c_{N,k}\Big) & \operatorname{diag}\Big(d_{1,k},\ldots,d_{N,k}\Big) \end{bmatrix}$$

$$(\cdot)_{i,k} = \begin{cases} (\bar{\cdot})_{i,k} & \text{if } B \notin \boldsymbol{\mathcal{S}} \\ \boldsymbol{0} & \text{if } B \in \boldsymbol{\mathcal{S}} \end{cases}, \quad \varrho = \frac{\alpha^{\mathcal{N}}\boldsymbol{n}_A^{T\,\mathcal{N}}\hat{\boldsymbol{s}}_{\oplus}}{\|{}^{\mathcal{N}}\hat{\boldsymbol{r}}_{AB,k}\|^2\|{}^{\mathcal{N}}\hat{\boldsymbol{s}}_{\oplus}\|} \left({}^{\mathcal{N}}\boldsymbol{n}_A^T \frac{{}^{\mathcal{N}}\hat{\boldsymbol{r}}_{AB,k}}{\|{}^{\mathcal{N}}\hat{\boldsymbol{r}}_{AB,k}\|} \right)$$

$$\bar{\boldsymbol{a}}_{i,k} \approx -\frac{\hat{C}_{i,k}}{\pi} \iint_{\boldsymbol{A}} \varrho \left({}^{\mathcal{B}}\begin{bmatrix} \cos\phi_i\cos\theta_i & \cos\phi_i\sin\theta_i & \sin\phi_i \end{bmatrix} \frac{\partial}{\partial\boldsymbol{\sigma}} \left([BN] \frac{{}^{\mathcal{N}}\hat{\boldsymbol{r}}_{AB,k}}{\|{}^{\mathcal{N}}\hat{\boldsymbol{r}}_{AB,k}\|} \right)\Bigg|_{\hat{\boldsymbol{\sigma}}_k} \right) \mathrm{d}A$$

$$\bar{b}_{i,k} = -\frac{1}{\pi} \iint_{\boldsymbol{A}} \varrho \left({}^{\mathcal{B}}\begin{bmatrix} \cos\phi_i\cos\theta_i & \cos\phi_i\sin\theta_i & \sin\phi_i \end{bmatrix} [BN] \frac{{}^{\mathcal{N}}\hat{\boldsymbol{r}}_{AB,k}}{\|{}^{\mathcal{N}}\hat{\boldsymbol{r}}_{AB,k}\|} \right) \mathrm{d}A$$

$$\bar{c}_{i,k} \approx -\frac{\hat{C}_{i,k}}{\pi} \iint_{\boldsymbol{A}} \varrho \left({}^{\mathcal{B}}\begin{bmatrix} -\cos\phi_i\sin\theta_i & \cos\phi_i\cos\theta_i & 0 \end{bmatrix} [BN] \frac{{}^{\mathcal{N}}\hat{\boldsymbol{r}}_{AB,k}}{\|{}^{\mathcal{N}}\hat{\boldsymbol{r}}_{AB,k}\|} \right) \mathrm{d}A$$

$$\bar{d}_{i,k} \approx -\frac{\hat{C}_{i,k}}{\pi} \iint_{\boldsymbol{A}} \varrho \left({}^{\mathcal{B}}\begin{bmatrix} -\sin\phi_i\cos\theta_i & -\sin\phi_i\sin\theta_i & \cos\phi_i \end{bmatrix} [BN] \frac{{}^{\mathcal{N}}\hat{\boldsymbol{r}}_{AB,k}}{\|{}^{\mathcal{N}}\hat{\boldsymbol{r}}_{AB,k}\|} \right) \mathrm{d}A \tag{4.29c}$$

$$\boldsymbol{M}_k = \boldsymbol{M}_{\alpha_k} + \begin{bmatrix} \operatorname{diag}\Big(\hat{\boldsymbol{C}}_k^T\Big) & \boldsymbol{0}_{N\times N_\alpha} \end{bmatrix} \tag{4.30a}$$

$$\boldsymbol{M}_{\alpha,k} = \begin{bmatrix} \mathbf{0}_{N\times N} & \boldsymbol{\mathcal{L}}_k \end{bmatrix}$$

$$\mathcal{L}_{ij,k} = \begin{cases} -\frac{\hat{C}_{i,k}}{\pi} \frac{{}^{\mathcal{N}}\boldsymbol{n}_{A_j}^T \, {}^{\mathcal{N}}\hat{\boldsymbol{s}}_{\oplus,k}}{\left\| {}^{\mathcal{N}}\hat{\boldsymbol{r}}_{A_jB} \right\|^2 \left\| {}^{\mathcal{N}}\boldsymbol{s}_{\oplus,k} \right\|} \left(\mathcal{N}\boldsymbol{n}_{A_j}^T \frac{{}^{\mathcal{N}}\hat{\boldsymbol{r}}_{A_jB}}{\left\| {}^{\mathcal{N}}\hat{\boldsymbol{r}}_{A_jB} \right\|} \right) \\ \quad \left(\mathcal{N}\boldsymbol{n}_i^T \frac{{}^{\mathcal{N}}\hat{\boldsymbol{r}}_{A_jB}}{\left\| {}^{\mathcal{N}}\hat{\boldsymbol{r}}_{A_jB} \right\|} \right) \Delta A_j & \text{if } \mathrm{d}A \in \boldsymbol{A} \\ \mathbf{0} & \text{if } \mathrm{d}A \notin \boldsymbol{A} \end{cases} \tag{4.30b}$$

and

$$\boldsymbol{J}_k = \boldsymbol{J}_{d_k} + \boldsymbol{J}_{\alpha_k} \tag{4.31a}$$

$$\boldsymbol{J}_{d_k} = \begin{bmatrix} \boldsymbol{a}_{1,k} & -\boldsymbol{a}_{1,k} \\ \vdots & \vdots \\ \boldsymbol{a}_{N,k} & -\boldsymbol{a}_{N,k} \end{bmatrix}$$

$$\boldsymbol{a}_{i,k} = \begin{cases} -\hat{C}_{i,k} \, {}^{\mathcal{B}}\begin{bmatrix} \cos\phi_i \cos\theta_i & \cos\phi_i \sin\theta_i & \sin\phi_i \end{bmatrix} [BN] \\ \quad * \frac{1}{\left\| {}^{\mathcal{N}}\hat{\boldsymbol{s}}_k \right\|} \left(\boldsymbol{I}_{3\times 3} - \frac{{}^{\mathcal{N}}\hat{\boldsymbol{s}}_k \, {}^{\mathcal{N}}\hat{\boldsymbol{s}}_k^T}{\left\| {}^{\mathcal{N}}\hat{\boldsymbol{s}}_k \right\| \left\| {}^{\mathcal{N}}\hat{\boldsymbol{s}}_k \right\|} \right) & \text{if } \frac{\boldsymbol{n}_i^T \hat{\boldsymbol{s}}_k}{\left\| \boldsymbol{n}_i \right\| \left\| \hat{\boldsymbol{s}}_k \right\|} \geq \cos\psi_i \\ 0 & \text{if } \frac{\boldsymbol{n}_i^T \hat{\boldsymbol{s}}_k}{\left\| \boldsymbol{n}_i \right\| \left\| \hat{\boldsymbol{s}}_k \right\|} < \cos\psi_i \end{cases} \tag{4.31b}$$

$$\boldsymbol{J}_{\alpha,k} = \begin{bmatrix} \boldsymbol{a}_{1,k} & \boldsymbol{b}_{1,k} \\ \vdots & \vdots \\ \boldsymbol{a}_{N,k} & \boldsymbol{b}_{N,k} \end{bmatrix}, \quad (\cdot)_{i,k} = \begin{cases} (\dot{\cdot})_{i,k} & \text{if } B \notin \boldsymbol{\mathcal{S}} \\ \boldsymbol{0} & \text{if } B \in \boldsymbol{\mathcal{S}} \end{cases}$$

$$\bar{\boldsymbol{a}}_{i,k} \approx \frac{\hat{C}_{i,k}}{\pi} \iint_{\boldsymbol{A}} \frac{\alpha}{\left\|{}^{\mathcal{N}}\hat{\boldsymbol{r}}_{AB,k}\right\|^2 \left\|{}^{\mathcal{N}}\hat{\boldsymbol{s}}_{\oplus,k}\right\|} {}^{\mathcal{N}}\boldsymbol{n}_A^T \left(\boldsymbol{I}_{3\times3} - \frac{{}^{\mathcal{N}}\hat{\boldsymbol{s}}_{\oplus,k} {}^{\mathcal{N}}\hat{\boldsymbol{s}}_{\oplus,k}^T}{\left\|{}^{\mathcal{N}}\hat{\boldsymbol{s}}_{\oplus,k}\right\| \left\|{}^{\mathcal{N}}\hat{\boldsymbol{s}}_{\oplus,k}\right\|} \right) \left({}^{\mathcal{N}}\boldsymbol{n}_A^T \frac{{}^{\mathcal{N}}\hat{\boldsymbol{r}}_{AB,k}}{\left\|{}^{\mathcal{N}}\hat{\boldsymbol{r}}_{AB,k}\right\|} \right) \left({}^{\mathcal{N}}\boldsymbol{n}_i^T \frac{{}^{\mathcal{N}}\hat{\boldsymbol{r}}_{AB,k}}{\left\|{}^{\mathcal{N}}\hat{\boldsymbol{r}}_{AB,k}\right\|} \right) \mathrm{d}A$$

$$\begin{aligned} \bar{\boldsymbol{b}}_{i,k} \approx -\frac{\hat{C}_{i,k}}{\pi} \iint_{\boldsymbol{A}} \alpha \frac{{}^{\mathcal{N}}\boldsymbol{n}_A^T {}^{\mathcal{N}}\hat{\boldsymbol{s}}_{\oplus,k}}{\left\|{}^{\mathcal{N}}\hat{\boldsymbol{r}}_{AB,k}\right\|^3 \left\|{}^{\mathcal{N}}\hat{\boldsymbol{s}}_{\oplus,k}\right\|} \Bigg[& 2 \frac{{}^{\mathcal{N}}\hat{\boldsymbol{r}}_{AB,k}^T}{\left\|{}^{\mathcal{N}}\hat{\boldsymbol{r}}_{AB,k}\right\|} \left({}^{\mathcal{N}}\boldsymbol{n}_A^T \frac{{}^{\mathcal{N}}\hat{\boldsymbol{r}}_{AB,k}}{\left\|{}^{\mathcal{N}}\hat{\boldsymbol{r}}_{AB,k}\right\|} \right) \left({}^{\mathcal{N}}\boldsymbol{n}_i^T \frac{{}^{\mathcal{N}}\hat{\boldsymbol{r}}_{AB,k}}{\left\|{}^{\mathcal{N}}\hat{\boldsymbol{r}}_{AB,k}\right\|} \right) \\ & - {}^{\mathcal{N}}\boldsymbol{n}_A^T \left(\boldsymbol{I}_{3\times3} - \frac{{}^{\mathcal{N}}\hat{\boldsymbol{r}}_{AB,k} {}^{\mathcal{N}}\hat{\boldsymbol{r}}_{AB,k}^T}{\left\|{}^{\mathcal{N}}\hat{\boldsymbol{r}}_{AB,k}\right\|^2} \right) \left({}^{\mathcal{N}}\boldsymbol{n}_i^T \frac{{}^{\mathcal{N}}\hat{\boldsymbol{r}}_{AB,k}}{\left\|{}^{\mathcal{N}}\hat{\boldsymbol{r}}_{AB,k}\right\|} \right) \\ & - \left({}^{\mathcal{N}}\boldsymbol{n}_A^T \frac{{}^{\mathcal{N}}\hat{\boldsymbol{r}}_{AB,k}}{\left\|{}^{\mathcal{N}}\hat{\boldsymbol{r}}_{AB,k}\right\|} \right) {}^{\mathcal{N}}\boldsymbol{n}_i^T \left(\boldsymbol{I}_{3\times3} - \frac{{}^{\mathcal{N}}\hat{\boldsymbol{r}}_{AB,k} {}^{\mathcal{N}}\hat{\boldsymbol{r}}_{AB,k}^T}{\left\|{}^{\mathcal{N}}\hat{\boldsymbol{r}}_{AB,k}\right\|^2} \right) \Bigg] \mathrm{d}A \end{aligned} \tag{4.31c}$$

where the partial derivative of the DCM $[BN]$ multiplied by some 3×1 vector $\boldsymbol{a}$ with respect to the MRP attitude $\boldsymbol{\sigma}$ is given by

$$\begin{aligned} \frac{\partial}{\partial \boldsymbol{\sigma}} \left([BN]\, \boldsymbol{a} \right) \Big|_{\hat{\boldsymbol{\sigma}}} = \frac{8}{\left(1+\hat{\sigma}^2\right)^3} \Bigg[& \left(1+\hat{\sigma}^2\right) \left\{ \left(-\left[\hat{\boldsymbol{\sigma}}\right]_\times + \frac{1}{2}\left(1-\hat{\sigma}^2\right) \boldsymbol{I}_{3\times3} \right) \left[\boldsymbol{a}\right]_\times - \left[\hat{\boldsymbol{\sigma}} \times \boldsymbol{a}\right]_\times \right. \\ & \left. + \left(\hat{\boldsymbol{\sigma}} \times \boldsymbol{a}\right) \hat{\boldsymbol{\sigma}}^T \right\} + 4 \left(-\left[\hat{\boldsymbol{\sigma}}\right]_\times + \frac{1}{2}\left(1-\hat{\sigma}^2\right) \boldsymbol{I}_{3\times3} \right) \left(\hat{\boldsymbol{\sigma}} \times \boldsymbol{a}\right) \hat{\boldsymbol{\sigma}}^T \Bigg]. \end{aligned} \tag{4.32}$$

While these partial derivatives may appear intense, several quantities are repeated throughout. Taking advantage of this can greatly simplify coding of these equations.

It is important to note that several of the Jacobians associated with V_α are approximate. This is because V_α involves an area integral of the form

$$V_\alpha = \iint_{\boldsymbol{A}} f \, \mathrm{d}A \tag{4.33}$$

for which the partial derivatives are found using Leibniz's rule[98]

$$\frac{\partial V_\alpha}{\partial \boldsymbol{x}} = \iint_{\boldsymbol{A}} \frac{\partial f}{\partial \boldsymbol{x}} \, \mathrm{d}A + \left[f \frac{\partial A}{\partial \boldsymbol{x}} \right]_{\boldsymbol{\mathcal{C}_A}} \tag{4.34}$$

where $\boldsymbol{\mathcal{C}_A}$ is the bounding contour of the area $\boldsymbol{A}$. The Jacobians given above include the variations of f with respect to the state vector, but not the variations of the area being integrated with respect

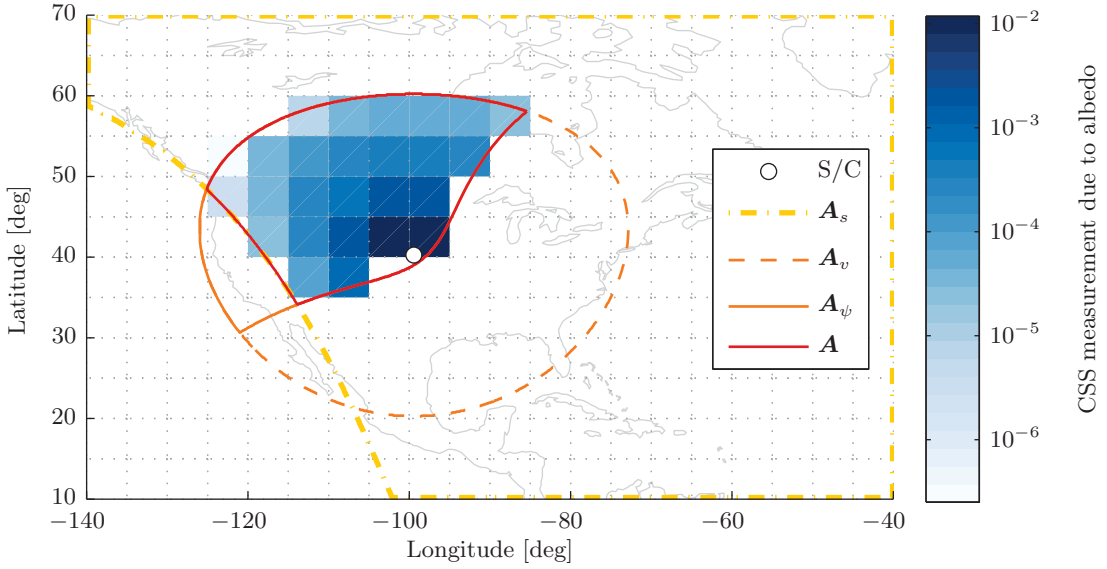

(a) Area of albedo contribution.

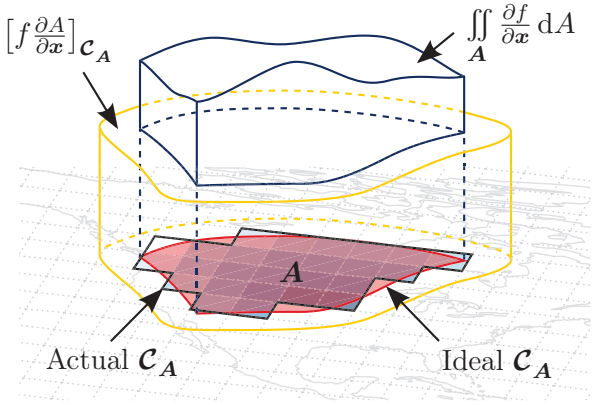

(b) Illustration of Leibnitz integral.

Figure 4.1: Illustration of complexities induced by gridded nature of albedo data.

to the state evaluated along the bounding contour. This is due to the uncertainty in the albedo model and numerical issues associated with evaluating Equation (4.34) using gridded data.

Consider the situation illustrated in Figure 4.1. The area $\boldsymbol{A}$ that is visible to a CSS for a nadir pointing spacecraft in a low-Earth orbit, along with a $5° \times 5°$ albedo grid are shown. Figure 4.1b provides an illustration of the two terms that make up Equation (4.34). As can be seen the ideal bounding contour of $\boldsymbol{A}$ is a complex shape; the calculation of which involves solving the intersection

of several cones and spheroids. The calculation of the second term also requires evaluating the partials of $\boldsymbol{A}$ with respect to $\boldsymbol{\sigma}$, $\boldsymbol{\theta}$, $\boldsymbol{\phi}$, $\boldsymbol{s}_{\oplus_\beta}$, and $\boldsymbol{r}_{B_\beta}$. Finally, it is important to note the albedo data is only available in gridded form and the albedo contributions for each grid square are calculated using the data point for the center of the grid square. To complete this calculation on board a spacecraft would involve either significant time or approximations. Coupled with the discrete and highly uncertain nature of the albedo data, this would result in a computationally expensive, or inherently imprecise calculation, for what is nominally a small value. Therefore, the measurement noise is inflated to account for this inconsistency.

While the full calibration filter will theoretically work for the full range of CSS measurement values, in practice CSS measurements near zero present additional challenges. In this region the signal to noise ratio is particularly low and the noise distribution is no longer Gaussian, as negative measurements are not possible. To address these issues a minimum CSS measurement value, or noise floor, is set, to twice the value of the CSS measurement noise, below which measurements are not considered.

4.3 Reduced CSS Calibration Filter Without Albedo Model

The reduced CSS calibration filter assumes the spacecraft has CSS, inertial attitude, angular rate measurements, and an estimate of the current time for calculating a reference Earth-Sun vector. In contrast to the full CSS calibration filter, it is assumed the received irradiance due to Earth's albedo is treated as an unmodeled measurement bias. This method aims to reduce the total computation time, at the cost of estimation accuracy, by eliminating the costly evaluation of the irradiance contributions caused by the Earth's albedo[1]. A continuous-discrete extended consider Kalman filter is used again and the state and process noise vectors are unchanged, along with the attitude measurement update, from the full CSS calibration filter.

[1]Evaluating the full NASA TOMS albedo model involves looping through 51 840 elements, for each of the CSS, every measurement update, and evaluating several equations at each element; a process which can take significant time as shown later in the results.

Because the input irradiance due to Earth's albedo is treated as a bias, Equation (4.27) is simplified to

$$V = C\left(V_d + V_\alpha + \nu_V\right)$$

$$V_d = \begin{cases} {}^{\mathcal{B}}\begin{bmatrix}\cos\phi\cos\theta & \cos\phi\sin\theta & \sin\phi\end{bmatrix}[BN]\,\frac{{}^{\mathcal{N}}\boldsymbol{s}_\oplus - {}^{\mathcal{N}}\boldsymbol{r}_B}{\left\|{}^{\mathcal{N}}\boldsymbol{s}_\oplus - {}^{\mathcal{N}}\boldsymbol{r}_B\right\|} & \text{if } \boldsymbol{n}^T\frac{\boldsymbol{s}}{\|\boldsymbol{s}\|} \geq \cos\psi \\ 0 & \text{if } \boldsymbol{n}^T\frac{\boldsymbol{s}}{\|\boldsymbol{s}\|} < \cos\psi \end{cases} \tag{4.35}$$

and the measurement noise and bias vectors are changed to

$$\boldsymbol{\nu}_k = \begin{bmatrix}\boldsymbol{\nu}_{V,k}\end{bmatrix}, \quad \boldsymbol{\beta}_\nu = \begin{bmatrix} {}^{\mathcal{N}}\boldsymbol{s}_{\oplus_\beta,k} \\ {}^{\mathcal{N}}\boldsymbol{r}_{B_\beta,k} \\ \boldsymbol{V}_{\alpha_\beta,k}\end{bmatrix} \tag{4.36}$$

where, without an orbit solution, the spacecraft position relative to the Earth is treated as a systematic bias. It is expected that this bias will have minimal impact on the estimate, especially when compared to the effect of Earth's albedo.

The measurement update Jacobians are given by Equation (4.29), where now $\boldsymbol{H}_{\alpha,k} = \boldsymbol{0}$,

$$\boldsymbol{M}_k = \operatorname{diag}\left(\hat{\boldsymbol{C}}_k^T\right) \tag{4.37}$$

and

$$\boldsymbol{J}_k = \begin{bmatrix}\begin{bmatrix}\boldsymbol{a}_{1,k}\\ \vdots \\ \boldsymbol{a}_{N,k}\end{bmatrix} & \begin{bmatrix}\boldsymbol{a}_{1,k}\\ \vdots \\ \boldsymbol{a}_{N,k}\end{bmatrix} & \operatorname{diag}\left(\hat{\boldsymbol{C}}_k^T\right)\end{bmatrix}$$

$$\boldsymbol{a}_{i,k} = \begin{cases} -\hat{C}_{i,k}\,{}^{\mathcal{B}}\begin{bmatrix}\cos\phi_i\cos\theta_i & \cos\phi_i\sin\theta_i & \sin\phi_i\end{bmatrix}[BN] \\ \quad * \frac{1}{\left\|{}^{\mathcal{N}}\hat{\boldsymbol{s}}_k\right\|}\left(\boldsymbol{I}_{3\times3} - \frac{{}^{\mathcal{N}}\hat{\boldsymbol{s}}_k\,{}^{\mathcal{N}}\hat{\boldsymbol{s}}_k^T}{\left\|{}^{\mathcal{N}}\hat{\boldsymbol{s}}_k\right\|\left\|{}^{\mathcal{N}}\hat{\boldsymbol{s}}_k\right\|}\right) & \text{if } \boldsymbol{n}_i^T\frac{\hat{\boldsymbol{s}}_k}{\left\|\hat{\boldsymbol{s}}_k\right\|} \geq \cos\psi_i \\ 0 & \text{if } \boldsymbol{n}_i^T\frac{\hat{\boldsymbol{s}}_k}{\left\|\hat{\boldsymbol{s}}_k\right\|} < \cos\psi_i \end{cases} \tag{4.38}$$

where, because the nominal value for the bias estimate ${}^{\mathcal{N}}\hat{\boldsymbol{r}}_{B_\beta,k}$ is a zero vector, ${}^{\mathcal{N}}\hat{\boldsymbol{s}}_k \approx {}^{\mathcal{N}}\hat{\boldsymbol{s}}_{\oplus,k}$.

4.4 Numerical Simulation Results

Numerical simulations, with significant noise and biases as outlined in Section 2.4, are used to demonstrate the performance of the two calibration filters. For these cases the spacecraft is assumed to have no active control. If the spacecraft is under active control, it must be made sure that during calibration all CSS have sufficient time with the Sun in their field of view. Even a slow maneuver that exposes all CSS to direct sunlight is sufficient, for example maintaining nadir pointing when equipped with a dual pyramid configuration, but may take more time to reduce the estimation uncertainty to the desired levels.

Chapter 3 shows that simultaneous sun-direction estimation and pointing can be performed when scale factor uncertainties are normally distributed with a standard deviation of 2 %. Here those scale factors are distributed by 30 %, an order of magnitude larger. For comparison, the total solar irradiance changes by 0.1 % between minimum and maximum solar activity and has only changed by 0.09 % over the last 400 years[99], but photodiode calibration is typically on the order of a few percent for visible light.

The performance of the full and reduced calibration filters are compared for a a tumbling spacecraft equipped with a dual pyramid CSS configuration and separately for a cube CSS configuration. Next, the accuracy and computation time of the full calibration filter run with reduced albedo resolution are compared. Finally, the sensitivity of the calibration filter to other error sources is examined.

4.4.1 Dual Pyramid CSS Configuration

A single orbit is simulated with the truth albedo model, and the full calibration filter albedo model, set to the full $1^\circ \times 1.25^\circ$ data set. The spacecraft is assumed uncontrolled and equipped with a dual pyramid CSS configuration. Figure 4.2 shows the error in the MRP and rate gyro bias estimates and their calculated covariance bounds. Both estimators give nearly identical estimates and covariance bounds because the attitude and rate bias estimates are dominated by the star

tracker measurements. While the MRP estimates quickly converge, the rate gyro bias estimate uncertainty grows as time progresses. This is because the initial rate gyro uncertainty is more accurate than the system can produce during one orbit; using a lower fidelity gyro results in the expected initial drop in uncertainty. Because the CSS have little impact on the attitude estimate for a sufficiently accurate attitude observation computation can be saved by combining this filter with an existing attitude estimator.

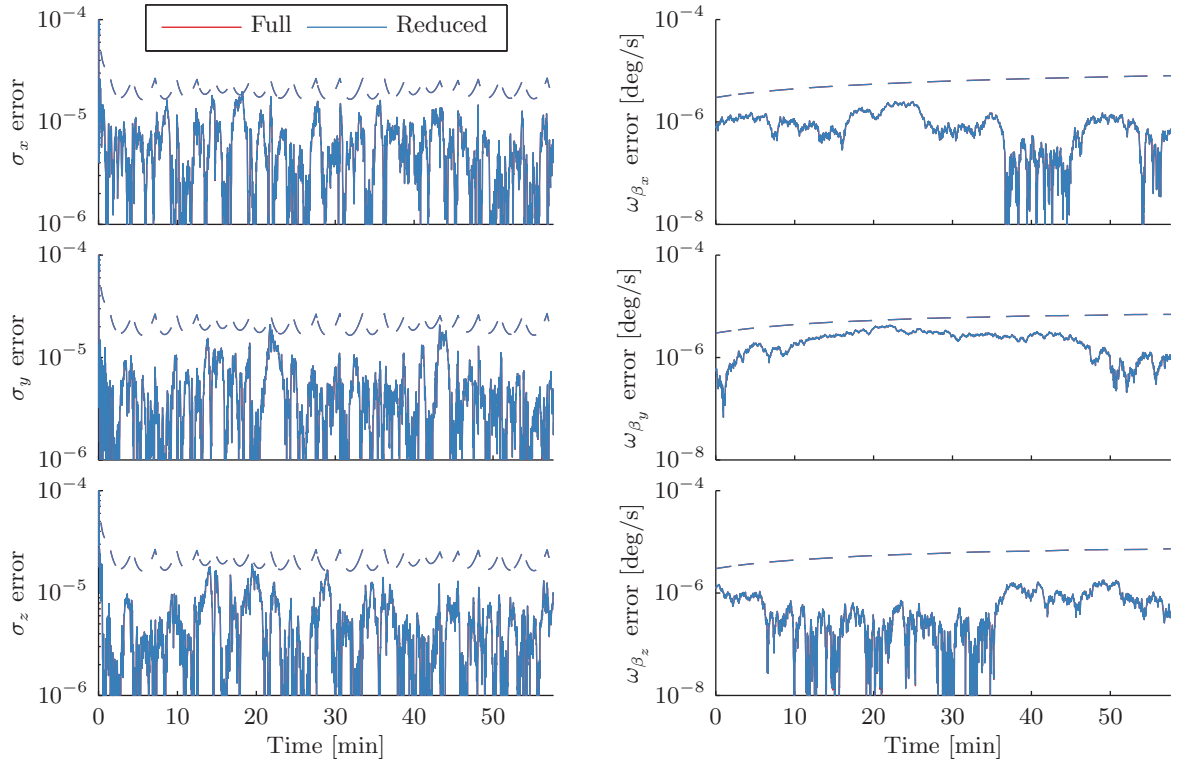

(a) Error in MRP attitude.

(b) Error in rate gyro bias.

Figure 4.2: Error in estimated (solid) MRP and rate gyro bias values, and estimated 3σ bounds (dashed), for nominal full and reduced calibration filters using dual pyramid CSS configuration.

Figure 4.3 shows the calibration results for the CSS with the greatest and least time receiving direct sunlight; and Table 4.1 lists the maximum and minimum estimated 3σ covariance bounds of the calibration coefficient and misalignment angles for the eight CSS after one orbit. As expected, the full calibration filter far outperforms the reduced calibration filter. The reduced filter is only able to make minimal reduction in the uncertainty in the calibration parameters, and needs far

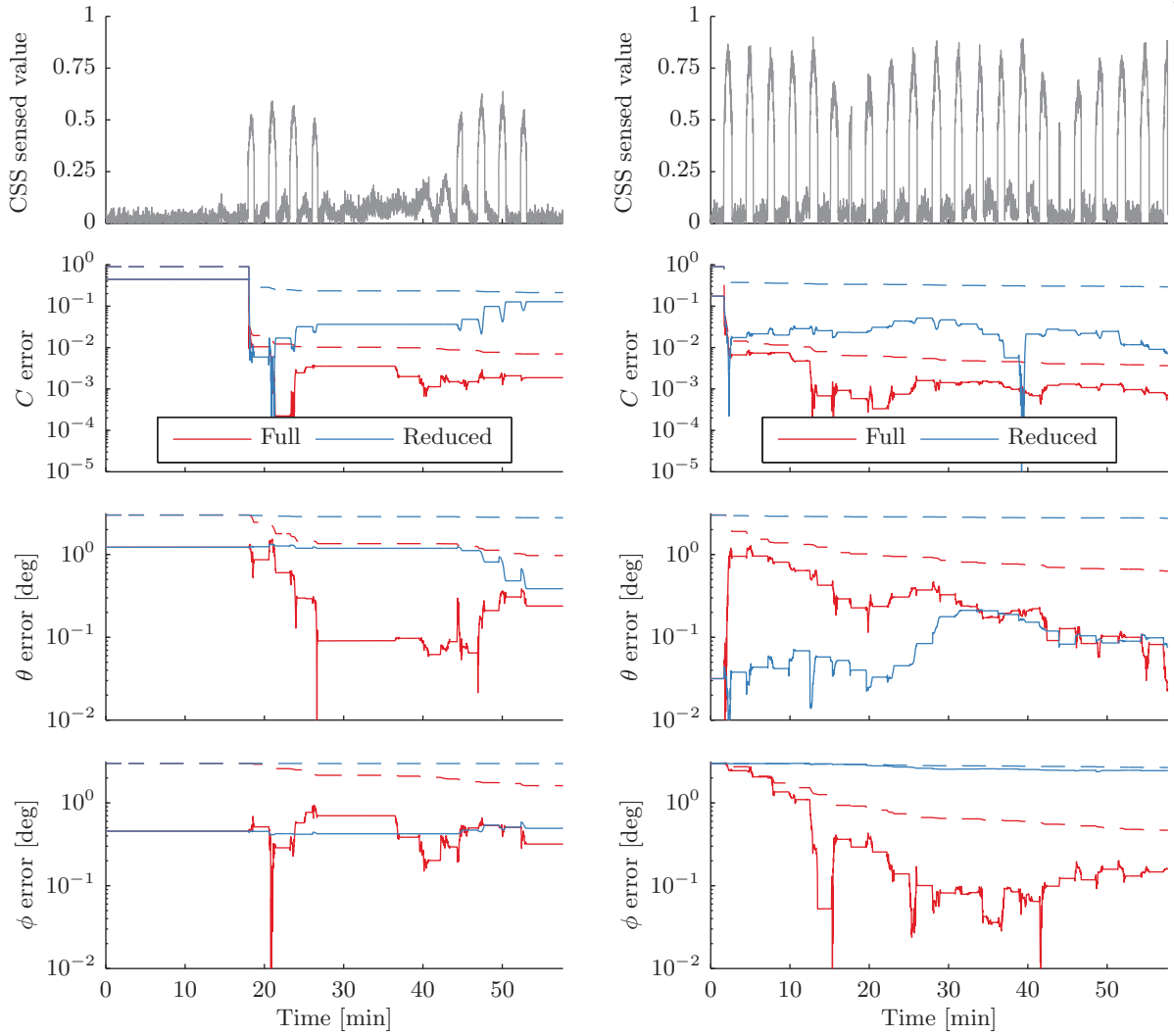

(a) CSS 2.

(b) CSS 6.

Figure 4.3: Error in estimated (solid) CSS 2 and 6 calibration values, and estimated 3σ bounds (dashed), for nominal full and reduced calibration filters using dual pyramid CSS configuration.

more than one orbit to reduce the uncertainty significantly. In contrast, the full calibration filter is able to reduce the uncertainty in the calibration coefficient by an order of magnitude, and reduce the uncertainty in the misalignment angles by a factor of two, in a single orbit.

Because the level of calibration accuracy for the CSS is a function of the measurements received, and the single case presented may not represent average results, a Monte Carlo analysis is run to statistically bound the performance of the calibration filters. The statistics of the calibration

Table 4.1: Estimated covariance values after one orbit for full and reduced calibration filters assuming a dual pyramid CSS configuration.

Parameter		Initial	Full Filter	Reduced Filter
$3\sigma_C$	max	0.9	0.018	0.61
	min		0.0036	0.21
$3\sigma_\theta$	max	3.0°	0.97°	2.9°
	min		0.59°	2.7°
$3\sigma_\phi$	max	3.0°	1.6°	3°
	min		0.47°	2.6°

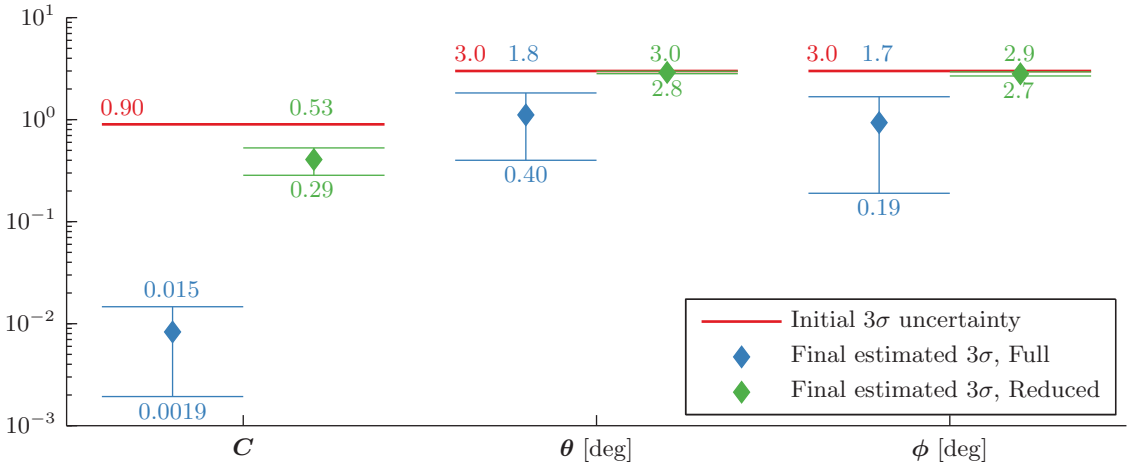

Figure 4.4: Monte Carlo generated statistics of CSS calibration parameter uncertainties for spacecraft using a dual pyramid CSS configuration after one orbit.

parameter uncertainties, for all CSS combined, after one orbit, for a 300 case Monte Carlo analysis, are shown in Figure 4.4. In some of the cases one or more CSS never experience direct irradiance from the Sun as a result of the particular random tumble of the spacecraft; the statistics are calculated with the data for these sensors omitted. The error bars represent one standard deviation from the mean of the estimated 3σ bounds. The results correlate well with the individual run; the results of which fall within or very near the one standard deviation bounds shown in Figure 4.4. The most significant difference between the full and reduced filter is in the estimate of the individual scale factors.

4.4.2 Cube CSS Configuration

A single orbit is again simulated with the truth albedo model, and the full calibration filter albedo model, set to the full $1° \times 1.25°$ data set. The spacecraft is assumed uncontrolled, but is now equipped with a cube CSS configuration. Similar to the dual pyramid configuration, the attitude and rate gyro bias errors, shown in Figure 4.5, are driven by the star tracker accuracy and are, therefore, indistinguishable at the scale shown.

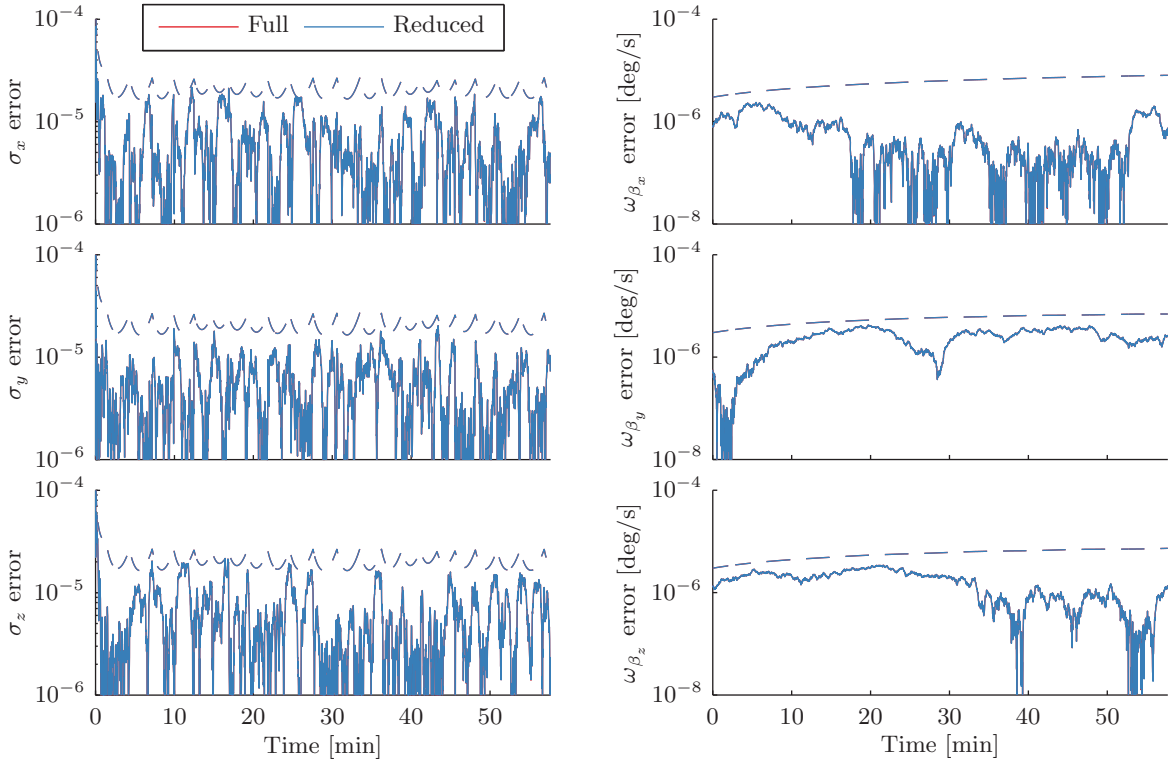

(a) Error in MRP attitude.

(b) Error in rate gyro bias.

Figure 4.5: Error in estimated (solid) MRP and rate gyro bias values, and estimated 3σ bounds (dashed), for nominal full and reduced calibration filters using cube CSS configuration.

Figure 4.6 shows the calibration results for the CSS with the greatest and least time receiving direct sunlight; and Table 4.2 lists the maximum and minimum estimated 3σ covariance bounds of the calibration coefficient and misalignment angles for the six CSS after one orbit. CSS 5 has almost zero time during which it receives direct sunlight. The filter does initialize for CSS 5 at

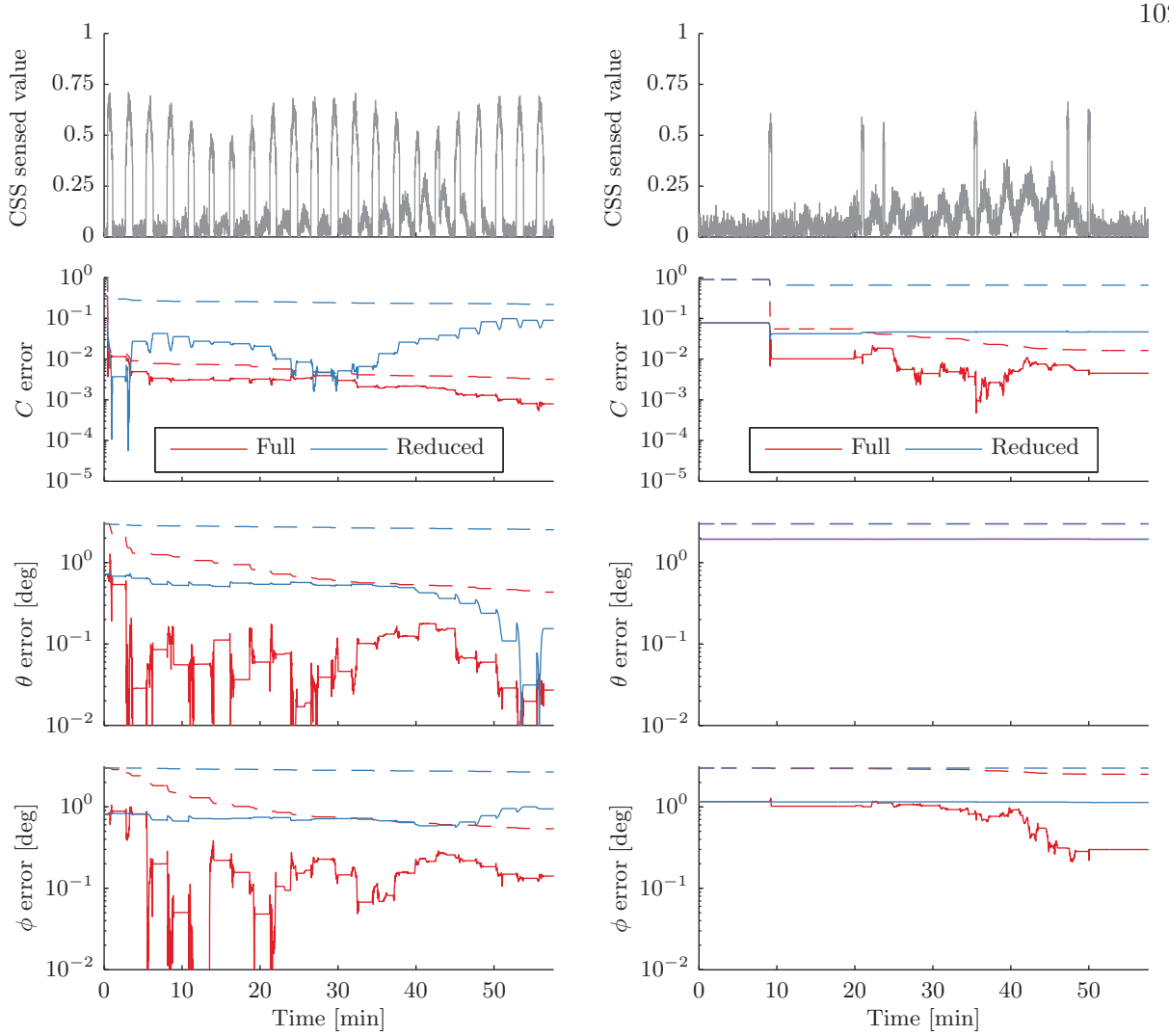

(a) CSS 1.

(b) CSS 5.

Figure 4.6: Error in estimated (solid) CSS 1 and 5 calibration values, and estimated 3σ bounds (dashed), for nominal full and reduced calibration filters using cube CSS configuration.

550 s, and although the misalignment uncertainties are only minimally improved, the 3σ scale factor uncertainty is reduced from 0.9 to 0.016 demonstrating the superior performance when accurately accounting for the Earth's albedo in the measurement model.

The statistics of the CSS calibration parameter uncertainties after one orbit for a 300 case Monte Carlo analysis are shown in Figure 4.7. Similar to thee results of the previous section, the results correlate well with the individual runs. The scale factor uncertainties are very close to the

Table 4.2: Estimated covariance values after one orbit for full and reduced calibration filters assuming a cube CSS configuration.

Parameter		Initial	Full Filter	Reduced Filter
$3\sigma_C$	max	0.9	0.016	0.66
	min		0.0022	0.22
$3\sigma_\theta$	max	3.0°	3°	3°
	min		0.43°	2.4°
$3\sigma_\phi$	max	3.0°	2.5°	3°
	min		0.33°	2.4°

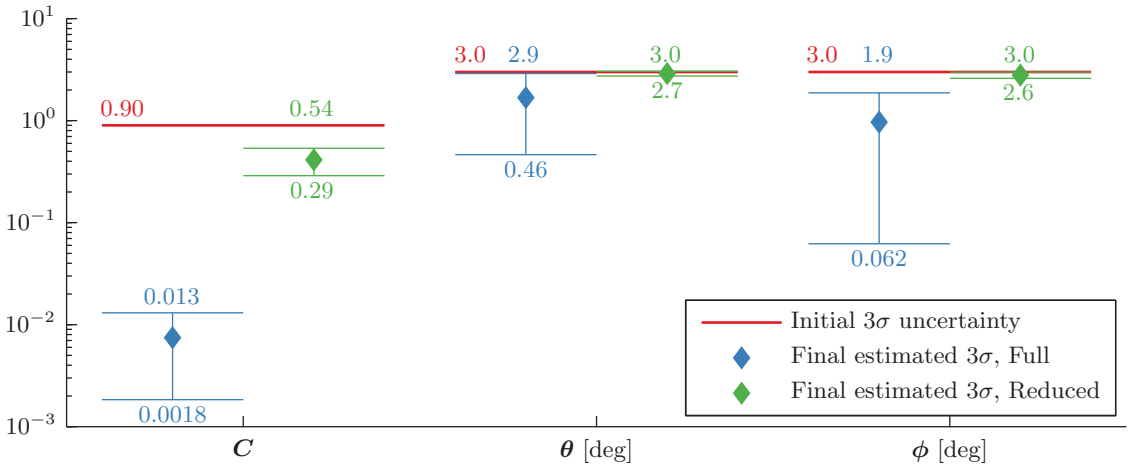

Figure 4.7: Monte Carlo generated statistics of CSS calibration parameter uncertainties for spacecraft using a cube CSS configuration after one orbit.

dual pyramid CSS configuration results. The misalignment angle uncertainties show slightly higher averages, 1.66° and 0.93° compared to 1.05° and 0.9°, but considering the spread of values the results are comparable.

4.4.3 Sensitivity to Albedo Model

The previous section illustrates the significant difference between using the full albedo data set and treating the input due to albedo as a bias. To bridge between these two extremes, the previous results are compared with the full calibration filter run using lower resolution albedo data sets. In particular, the full calibration filter is run using $1° \times 1.25°$, $5° \times 5°$, and $10° \times 10°$ resolution

albedo data sets, which are compared in Figure 4.8, where the lower resolution grids are interpolated from the $1^\circ \times 1.25^\circ$ data. It is found through Monte Carlo analysis that the measurement noise ν_V needs to be increased from 0.05, as dictated by the CSS noise, by 0.01 for the $1^\circ \times 1.25^\circ$ albedo grid, 0.1 for the $5^\circ \times 5^\circ$ albedo grid, and 0.4 for the $10^\circ \times 10^\circ$ albedo grid in order to account for the approximations made in the Jacobians[2].

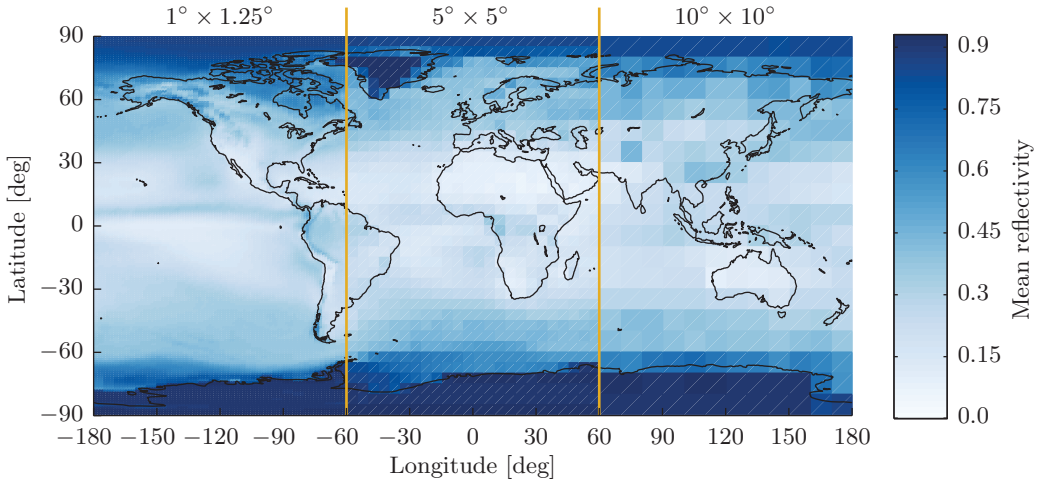

Figure 4.8: Visualization of various albedo resolutions for which calibration filter performance is compared.

The estimation errors and 3σ uncertainty bounds are shown in Figure 4.9. All of the estimates remain bounded by the predicted 3σ uncertainty bounds. Similar to the results of the previous section, the errors in the MRP attitude set and the rate gyro bias estimates are indistinguishable, therefore, these plots are omitted. For brevity, only the calibration estimates for CSS 6 and 2 are shown in Figure 4.9. These sensors are the sensors with the most and least information content based on the particular tumble of the spacecraft; they are in view of the Sun the most and least. The 3σ uncertainty values for all the CSS parameters for the different models are presented in Table 4.3

Using even a very coarse albedo data set in the full estimator provides significant improvement over treating the irradiance due to albedo as a bias. The full filter with $10^\circ \times 10^\circ$ albedo data provides only slightly lower uncertainty in the alignment angles than the reduced filter, but, for some sensors,

[2]To arrive at these values, Monte Carlo analyses are run and values are iterated until the normalized mean estimation error test results, explained in Section 5.1, are satisfactory.

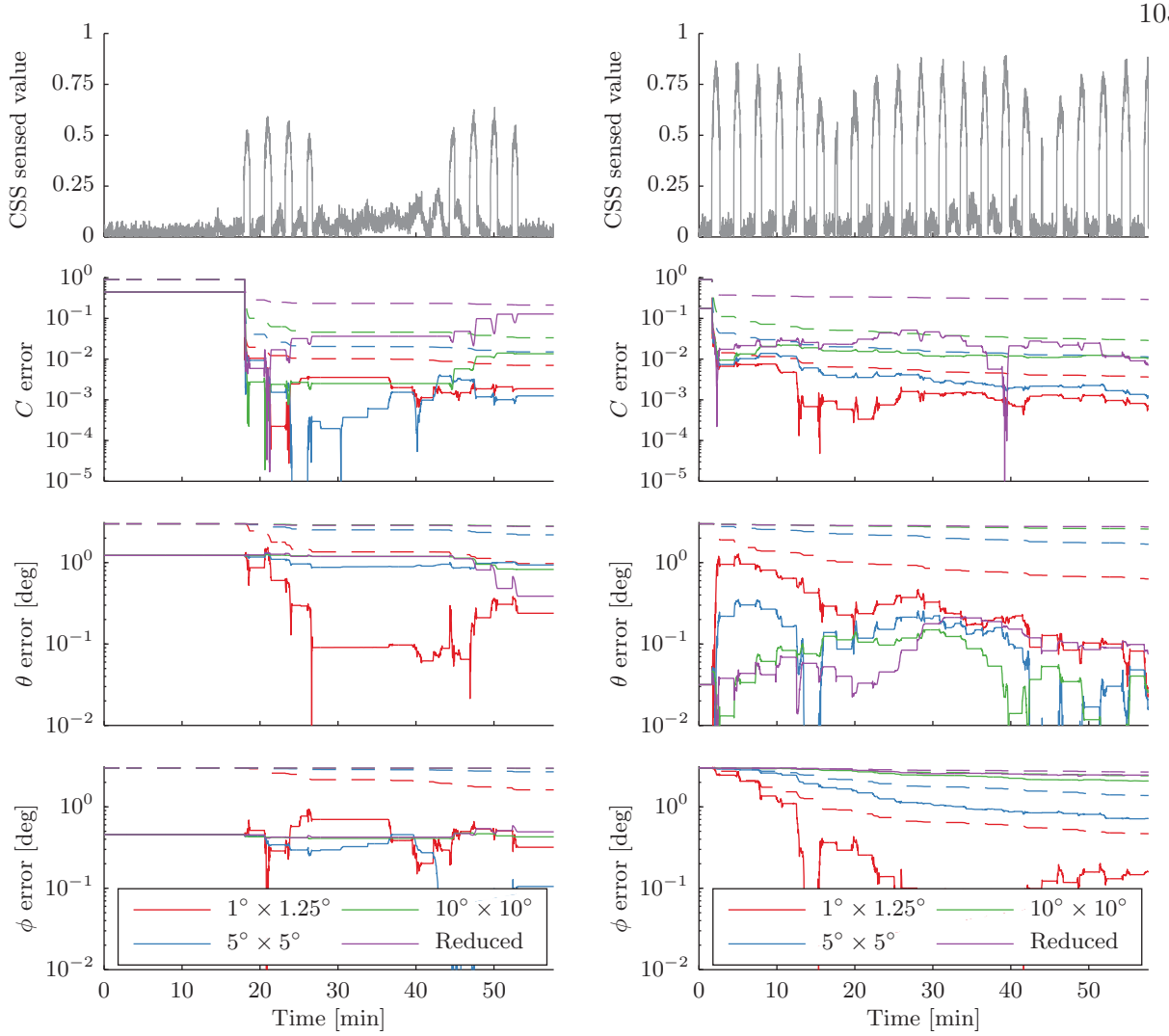

(a) CSS 2.

(b) CSS 6.

Figure 4.9: Calculated mean (solid) and 3σ (dashed) CSS calibration values for full and reduced estimation techniques for CSS 2 and 6.

a full order of magnitude lower uncertainty in the calibration coefficient. In Chapter 3 it is shown that simultaneous coarse sun-direction estimation and control is quickly attainable with calibration coefficient uncertainty of 0.06 3σ, and the full filter is nearly able to attain this accuracy in just one orbit using the $10° \times 10°$ albedo data.

The statistics of the CSS calibration parameter uncertainties after one orbit for a 300 case Monte Carlo are shown in Figure 4.10. The Monte Carlo results confirm the trends seen in the single

Table 4.3: Estimated covariance values after one orbit for various albedo models.

Parameter		Initial	Full Filter $1^\circ \times 1.25^\circ$	Full Filter $5^\circ \times 5^\circ$	Full Filter $10^\circ \times 10^\circ$	Reduced Filter
$3\sigma_C$	max	0.9	0.018	0.043	0.11	0.61
	min		0.0036	0.011	0.029	0.21
$3\sigma_\theta$	max	3.0°	0.97°	2.2°	2.8°	2.9°
	min		0.59°	1.6°	2.6°	2.7°
$3\sigma_\phi$	max	3.0°	1.6°	2.7°	3°	3°
	min		0.47°	1.4°	2.4°	2.6°

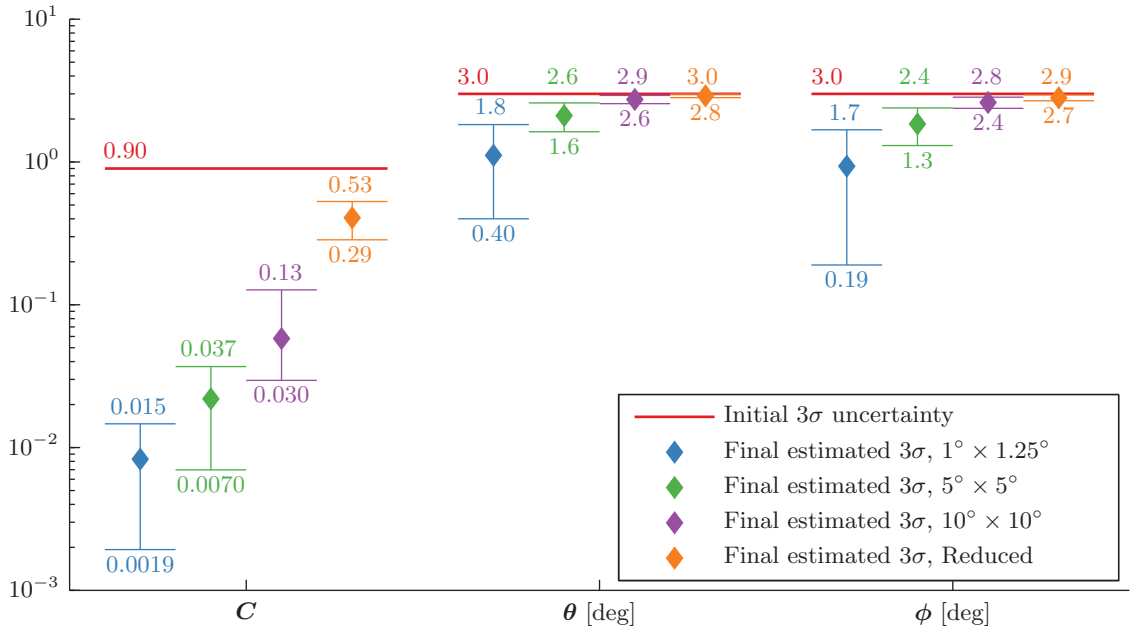

Figure 4.10: Monte Carlo generated statistics of CSS calibration parameter uncertainties for spacecraft using a dual CSS configuration after one orbit for various levels of albedo data resolution.

case, and a steady degradation of accuracy is seen as the albedo resolution is decreased. While the $10^\circ \times 10^\circ$ cases show only slightly better misalignment angle accuracy compared to the reduced filter, there is a significant improvement in the scale factor estimate.

It is important to consider computation time in addition to estimation accuracy. For a 3460 s simulation the computation time for the propagation and measurement update algorithms are timed and recorded; the propagation update is called 34 601 times and the estimation update

6921 times. The averages and standard deviations of the required computation times are shown in Table 4.4. Because no control effort is applied, the simulations follow exactly the same trajectory and experience identical simulated sensor measurements. The propagation algorithms are coded exactly the same except for the size of the bias covariance matrices. The measurement update equations are coded exactly the same with two exceptions: the full calibration filter includes a loop over the albedo data to calculate the expected irradiance due to albedo and the associated uncertainties; and the matrix sizes of the bias covariance matrices have different dimensions. All code is written in C and compiled and run on a Windows i7 2.5 GHz computer. While this is not flight hardware, the relative computation times provide insight into the expected trends.

Table 4.4: Averages and standard deviations of computation times for various filters.

ECKF	Albedo Data	Propagation Update [µs]	Measurement Update [µs]
Full	$1^\circ \times 1.25^\circ$	15.4 ± 2.7	6141 ± 1470
Full	$5^\circ \times 5^\circ$	15.1 ± 2.9	506 ± 101
Full	$10^\circ \times 10^\circ$	15.0 ± 2.9	180 ± 19.7
Reduced	-	18.3 ± 3.8	183 ± 24.5

As expected, the full calibration filter takes significantly more time than the reduced filter, but reducing the density of the albedo grid greatly increases the computation speed. Interestingly, the computation time for the 10×10 albedo grid is lower than that of the reduced calibration filter. This is a result of the total mathematical operations performed. Comparing Equations (4.28) and (4.36) it can be seen that the reduced calibration filter trades the computation of the albedo, and its associated uncertainty, for an increased number of bias parameters, whose uncertainty and correlation with the state must be propagated and updated. For a low resolution albedo data set the number of computations necessary to loop through the albedo data eventually drops below the number of calculations added by accounting for the albedo as a measurement bias in the ECKF formulation. For the current state vector this point occurs near an albedo resolution of $10^\circ \times 10^\circ$.

4.4.4 Sensitivity to Sun-Direction Model

There are several methods available for computing the direction vector from the Earth to the Sun, as required in the full calibration filter, based on only a reference time depending on the computational power available and accuracy desired. When calculating a normalized sun-direction vector, in the body frame of a spacecraft in low Earth orbit, these methods provide a relatively small level of error. Vallado gives an analytic method valid from 1950 to 2050[100]. *Variations Séculaires des Orbites Planétaires* (VSOP) provides a series of periodic terms that can be used to determine the position of the planets[101]. Meeus provides an abbreviated set of VSOP87 tables and associated algorithm[102]. Finally, the NASA Navigation and Ancillary Information Facility (NAIF) SPICE toolkit provides full planetary ephemerids[62].

Vallado provides a simple technique from the Astronomical Almanac. The algorithm gives a mean-equator of date vector in astronomical units with an accuracy of 0.01° that is valid from 1950 to 2050[100]. Starting with the Julian date JD, the normalized sun-direction vector is given by

$$T_{UT1} = \frac{JD - 2\,451\,545.0}{36\,525} \tag{4.39a}$$

$$\lambda_{M_\odot} = 280.460^\circ + 36\,000.771 T_{UT1} \tag{4.39b}$$

$$M_\odot = 357.527\,723\,3^\circ + 35\,999.050\,34 T_{UT1} \tag{4.39c}$$

$$\lambda_{\text{ecliptic}} = \lambda_{M_\odot} + 1.914\,666\,471^\circ \sin\left(M_\odot\right) + 0.019\,994\,643^\circ \sin\left(2M_\odot\right) \tag{4.39d}$$

$$\epsilon = 23.439\,291^\circ - 0.013\,004\,2 T_{UT1} \tag{4.39e}$$

$$r_\odot = 1.000\,140\,612 - 0.016\,708\,617 \cos\left(M_\odot\right) - 0.000\,139\,589 \cos\left(2M_\odot\right) \tag{4.39f}$$

$$\boldsymbol{s}_\oplus = r_\odot \begin{bmatrix} \cos\lambda_{\text{ecliptic}} \\ \cos\epsilon \sin\lambda_{\text{ecliptic}} \\ \sin\epsilon \sin\lambda_{\text{ecliptic}} \end{bmatrix} \tag{4.39g}$$

where universal time T_{UT1} is used instead of barycentric dynamical time T_{TDB} because of the low fidelity of the model.

The planetary theory VSOP87 uses tables of periodic terms to calculate the positions of the planets. The position of the Sun relative to the Earth in astronomical units can be found using

$$\boldsymbol{s}_{\oplus} = \begin{bmatrix} x + 0.000\,000\,440\,360y - 0.000\,000\,190\,919z \\ -0.000\,000\,479\,966x + 0.917\,482\,137\,087y - 0.397\,776\,982\,902z \\ 0.397\,776\,982\,902y + 0.917\,482\,137\,087z \end{bmatrix} \tag{4.40}$$

where

$$x = -\cos B \cos L, \quad y = -\cos B \sin L, \quad z = -\sin B. \tag{4.41}$$

The terms L and B are calculated using

$$\tau = \frac{JD - 2\,451\,545.0}{365\,250.0}$$

$$X(i) = \sum_{j=0}^{N_j} A_j \cos\left(B_j + C_j\tau\right) \; X = X0 + X1\tau + X2\tau^2 + X3\tau^3 + X4\tau^4 + X5\tau^5 \tag{4.42}$$

where A_j, B_j, and C_j correspond to the jth row, of N_j rows, of the A, B, and C columns of the VSOP87 table section $X(i)$. Meeus provides an abbreviated set of tables in Appendix II of Reference 102 that can be used with these same equations. Meeus' solution reduces the total number of row summations necessary from 1586 to 444.

The relative computation times and angular errors for these sun-direction reference models are presented in Table 4.5 where, for this study, the output of the SPICE toolkit is assumed to be truth. The component and total angular errors in the Vallado, Meeus, and VSOP87B methods are shown in Figure 4.11. Also included in Figure 4.11d are the errors resulting from using Vallado and Meeus' methods with an error in the current time of 6 h. The VSOP87 method shows the closest match to the SPICE ephemerids and Vallado's method shows the most difference. All methods exhibit a periodic error with a period equal to half the orbital period of Earth.

The angle error in the sun-direction reference vector can be significantly reduced by moving from Vallado's method to the methods given by SPICE, or Meeus, at the cost of computation time. However, using the SPICE implementation requires the inclusion of a significant library of code, whereas the Meeus algorithm can be implemented with a single function containing several tables.

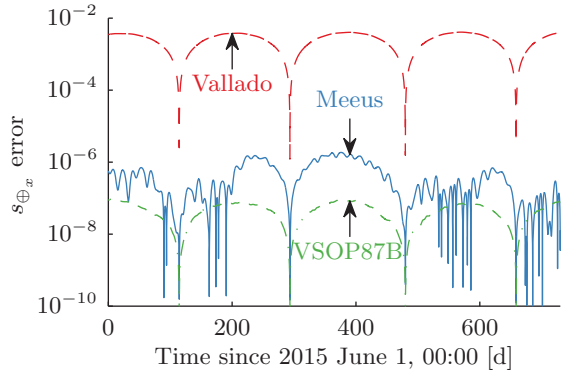

(a) Error in x-component of reference sun-direction vector.

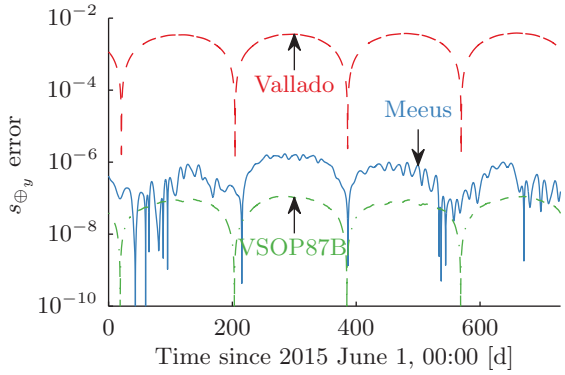

(b) Error in y-component of reference sun-direction vector.

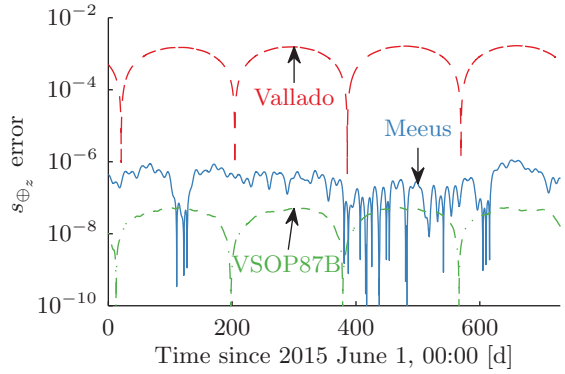

(c) Error in z-component of reference sun-direction vector.

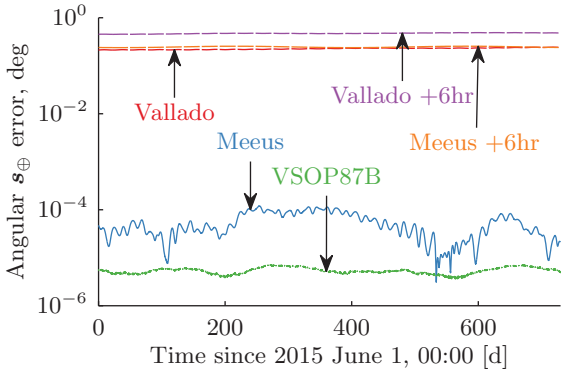

(d) Angular error of sun-direction reference vector.

Figure 4.11: Accuracy of Vallado, Meeus, and VSOP87B methods for calculating reference sun-direction vector relative to SPICE toolkit solution.

Table 4.5: Sun direction approximation methods and their error relative to SPICE.

Method	Normalized mean computation time	Angular error Mean [deg]	Angular error Max [deg]
SPICE	19	–	–
Vallado	1	0.23	0.24
Vallado +6 h		0.47	0.49
Meeus	24	5.2×10^{-5}	1.2×10^{-4}
Meeus +6 h		0.25	0.25
VSOP87B	360	5.4×10^{-6}	7.2×10^{-6}

Interestingly, the angular error in Vallado's method is nearly equal to the angular error incurred from using Meeus' method with a 6 h time error.

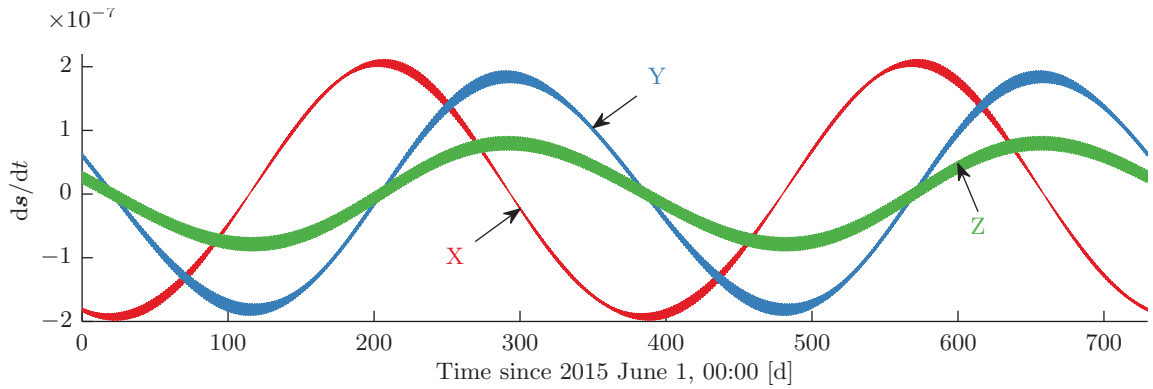

Figure 4.12: Rate of change of inertial sun-direction vector for spacecraft in 400 km polar orbit.

Also of interest is the rate of change of the inertial vector from the spacecraft to the Sun because it is included as a bias term in the ECKF sun-direction estimator developed in Chapter 3. The rate of change of the inertial sun vector, for a spacecraft in a 400 km low Earth polar orbit, is shown in Figure 4.12. The banding seen is a result of the time scales plotted, as the higher frequency movement of the spacecraft around the Earth induces small variations about the lower frequency movement of the Earth around the Sun.

When evaluating these models in the full calibration filter, it is found that there is almost no difference in the estimated state or covariance bounds. Neither is the computation time significantly impacted. The propagation update computation time is unchanged when switching from Meeus' to Vallado's sun-direction model, and the measurement update is only sped up by 10 µs on average, which is small compared to the several hundred microsecond total measurement update time. The minimal impact on the state estimate is in large part due to the discretization of the albedo data. Table 4.5 shows that the maximum angular error in the Earth-Sun vector; even the least accurate Vallado method is below the smallest albedo resolution of $1^\circ \times 1.25^\circ$. Thus, the amount of additional uncertainty in the state estimate for a 0.24° error in the sun-direction vector is dwarfed by the measurement noise added to account for the inaccuracies of the full calibration Jacobians. In fact, the full calibration filter is more likely to develop a bias in the estimated state, due to the Jacobian approximations, before significant differences in the estimated covariance begin to appear.

Therefore, because the fidelity of the albedo model impacts the results most significantly, Monte Carlo analyses must be used prior to flight to characterize the noise necessary to account for albedo model limitations.

Chapter 5

CSS Failure Detection

While CSS have significant flight heritage and are robust sensors, when using an underdetermined configuration, as shown in Figure 2.9, sensor failure is a key concern as it can leave areas without any sensor coverage. Figure 5.1 shows a coverage map for the dual pyramid CSS configuration when CSS 1 fails. Compared to Figure 2.8, a single sensor failure results in a significant area with zero sensor coverage and reduced coverage by three or more sensors. While a single-point estimation scheme will fail when the Sun is this region of zero coverage, a sequential filter based approach is capable of propagating through such dead zones given sufficient prior measurements.

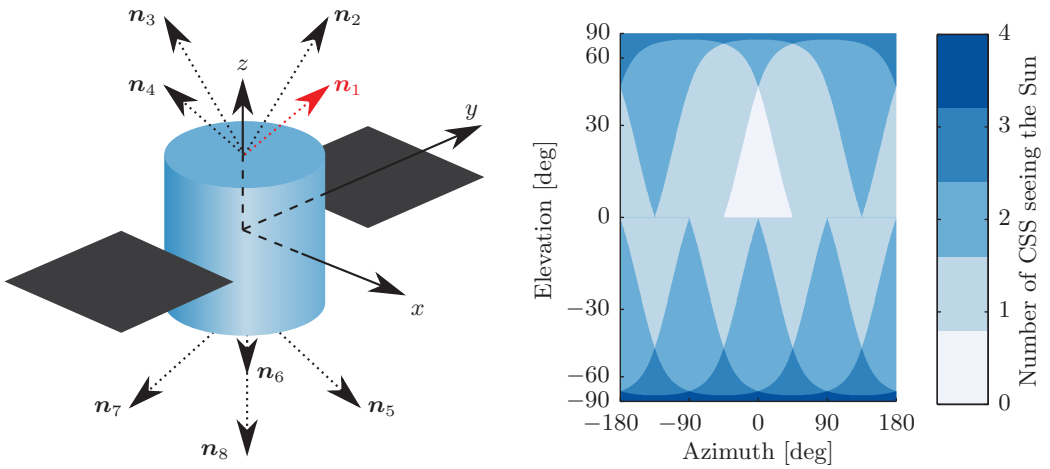

(a) Schematic of spacecraft, $\theta = 45°$.

(b) CSS coverage map.

Figure 5.1: Illustration of spacecraft with CSS unit vectors $\boldsymbol{n}_i$ for a dual pyramid configuration with a single sensor failure and the associated CSS coverage map shown on a cylindrical projection.

There is significant existing research in the field of fault detection[48,49] and a popular approach used to detect sensor failures is to perform statistical tests on the residuals of one or more sequential filters[54,55]. When using a Kalman filter approach on nonlinear problems the linearization can lead to poor detection or high false alarm rates, and, thus, there is much ongoing research into more accurate methods of precise fault detection for nonlinear systems[57–59]. This research focuses on demonstrating how even a simple fault detection scheme, that may be often overlooked, can be used to gain insight with minimal computational overhead. Despite the fact that the problem of detecting failures of coarse sun sensors is highly nonlinear with significant noise, a normalized innovation squared test performed on the output of a calibration filter, as detailed in Chapter 4, is shown to produce acceptable results because of the detailed sensor modeling of Sections 2.1 and 3.2.3. Unfortunately, fault detection using the sun-direction estimators of Chapter 3 is infeasible using this method due to the high level of conservatism used to ensure filter convergence.

5.1 Autonomous Failure Detection Approach

Tests used to tune the noise parameters of statistical filters include the normalized estimate error squared (NEES) test, the normalized mean estimation error (NMEE) test, the normalized innovation error squared (NIS) test, and the averaged NIS test[55]. In addition, autocorrelation tests can be used to test for whiteness. The NEES and NMEE test require the true state to be known and are used during filter development, leveraging Monte Carlo analyses, to tune a filter based on the expected noise values. In contrast, the NIS, and averaged NIS, tests use only the measurement residuals and are suitable for use in real-time applications. The NEES and NMEE tests are reviewed as they are important for filter development, but it is the NIS test that is used for fault detection.

Defining the state error, where the true state $\boldsymbol{x}$ is known from the simulation, as

$$\tilde{\boldsymbol{x}}(t) \equiv \boldsymbol{x}(t) - \hat{\boldsymbol{x}}(t) \tag{5.1}$$

the normalized state estimation error squared is given by

$$\epsilon(t) \equiv \tilde{\boldsymbol{x}}^T(t)\, \boldsymbol{P}^{-1}(t)\, \tilde{\boldsymbol{x}}(t)\,. \tag{5.2}$$

Assuming the system is linear with Gaussian noise, if the null hypothesis H_0, that the filter is consistent, is true then $\epsilon(t)$ is χ^2 distributed, and

$$\mathrm{E}[\epsilon(t)] = n_x \tag{5.3}$$

where n_x is the dimension of the state vector. If $\epsilon_i(t)$ is the NEES of the ith case in a N case Monte Carlo analysis then

$$\bar{\epsilon}(t) = \frac{1}{N} \sum_{i=1}^{N} \epsilon_i(t) \tag{5.4}$$

and $N\bar{\epsilon}(t)$ will have a χ^2 density with Nn_x degrees of freedom[55]. The null hypothesis is accepted if

$$\bar{\epsilon}(t) \in [r_1, r_2] \tag{5.5}$$

where the acceptance interval $[r_1, r_2]$ is based on chosen significance level α such that

$$p\left\{\bar{\epsilon}(t) \in [r_1, r_2]\,|H_0\right\} = 1 - \alpha. \tag{5.6}$$

For a two-sided interval the values of r_1 and r_2 are calculated using inverse χ^2 tables, such as those found in Reference 103, or a software package, such as Reference 104, for $\alpha/2$ and $1.0 - \alpha/2$.

For NEES values outside the acceptance region the null hypothesis is rejected and it is concluded that the estimation errors are not Gaussian with uncertainties equal to the predicted covariance. Unacceptably large values for ϵ and $\bar{\epsilon}$ indicate a bias in the state estimates. In addition, significant simulations show that, for the conservative filters presented here, values consistently below the lower bound indicate a filter with estimate errors that may not be Gaussian, but are bounded by the predicted covariance.

The NEES and averaged NEES results are shown in Figure 5.2 for the full calibration filter using $1^\circ \times 1.25^\circ$ albedo data as an example. The averaged NEES acceptance bounds are calculated using a 1 % significance level for a χ^2 distribution with 30 (states) $\times$ 300 (runs) degrees of freedom,

$$\left[\chi^2_{9000}(0.005)\,, \chi^2_{9000}(0.995)\right] = [8658.17, 9349.34] \quad \longrightarrow \quad [r_1, r_2] = [28.9, 31.2]\,.$$

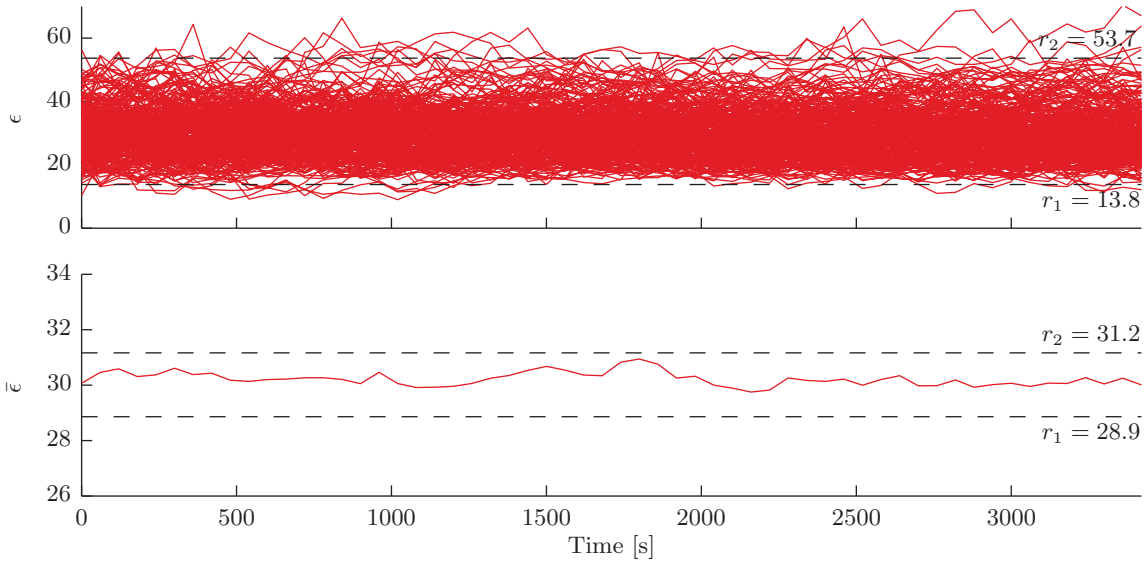

Figure 5.2: NEES and averaged NEES for full calibration filter, run with $1° \times 1.25°$ albedo data, results from Section 4.4.3 at the 1 % significance level.

There are some values of ϵ that fall outside the acceptance bounds, as expected statistically, but the averaged NEES satisfies Equation (5.5) for the entire simulation.

If the NEES test is not satisfied, the normalized mean estimation error (NMEE) test for each component of the state is used to verify if the estimate is zero-mean. The NMEE for the jth component of the state for N Monte Carlo runs is defined as[55]

$$\bar{\mu}_j(t) \equiv \frac{1}{N} \sum_{i=1}^{N} \frac{\tilde{x}_{j,i}}{\sqrt{P_{jj,i}(t)}} \tag{5.7}$$

and ideally will be normally distributed with zero mean and a $1/N$ standard deviation. The null hypothesis, that the estimate is zero-mean, is accepted if

$$\bar{\mu}_j(t) \in [-r, r] \tag{5.8}$$

where the acceptance interval is based on a level of significance α such that

$$p\left\{\bar{\epsilon}(t) \in [-r, r] \,|H_0\right\} = 1 - \alpha. \tag{5.9}$$

For a two-sided interval the value of $r = r_1/\sqrt{N}$ where r_1 is calculated using an inverse normal distribution for $1.0 - \alpha/2$.

While these methods work well for simulated trajectories, the true trajectory is not known in real-time applications. For real-time situations the state estimation error cannot be used to check the consistency of the filter, but the measurement innovations can be used in a similar manner. The normalized innovation squared (NIS) is defined as

$$\epsilon_{y,k} \equiv (\boldsymbol{y}_k - \hat{\boldsymbol{y}}_k)^T \boldsymbol{W}_k^{-1} (\boldsymbol{y}_k - \hat{\boldsymbol{y}}_k) \tag{5.10}$$

where $\boldsymbol{W}_k$ is the innovation covariance from Equation (3.47). Similar to Equation (5.4) an averaged NIS is calculated for a time history of N measurements using

$$\bar{\epsilon}_y = \frac{1}{N} \sum_{i=1}^{N} \epsilon_{y,i}. \tag{5.11}$$

The null hypothesis for the NIS is tested in a similar manner to the NEES.

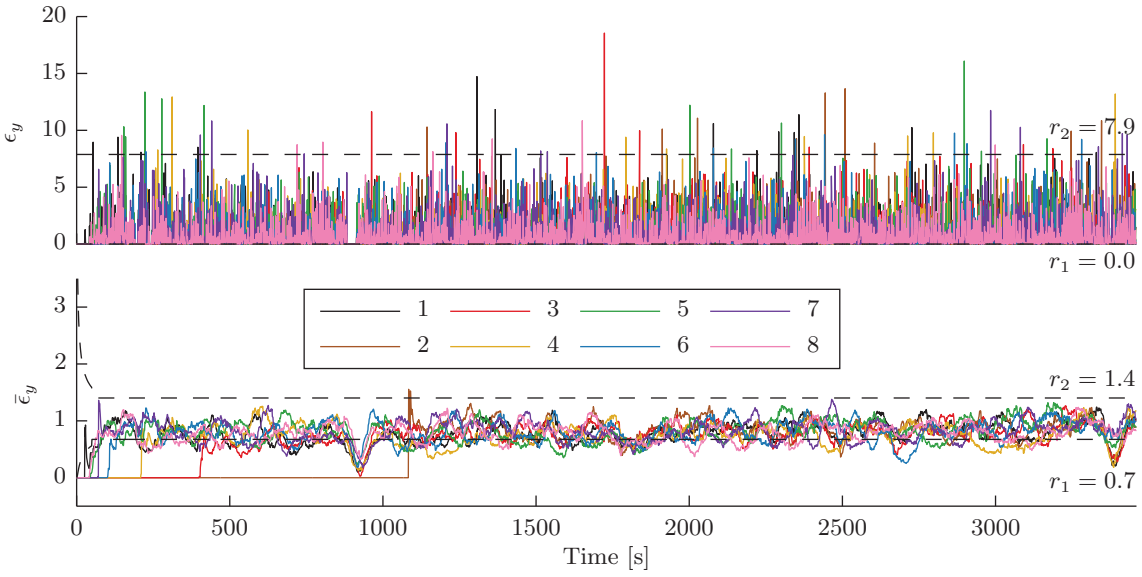

Figure 5.3: NIS and 100 sample averaged NIS for full calibration filter.

Figure 5.3 shows the NIS test for all eight CSS on a simulated dual pyramid equipped spacecraft running the full calibration filter. The acceptance region bounds[1] are shown assuming the

[1]The nominal acceptance region for a χ^2 test is traditionally based on a 5 % or 1 % significance level. This results in an upper bound of 5.02 and 7.88, respectively, for a single value and 1.3 and 1.4, respectively, for a 100 sample averaged value.

sensors begin receiving measurements at the start of the simulation and initially decrease as enough samples are recorded to fill the running average. This is not true for all sensors, for example CSS 2 does not receive a direct sunlight measurement until after 1000 s, but the transient acceptance regions are not shown for all sensors as the focus is on the steady state. After one orbit the averaged NIS, for all eight sensors, is clustered near the low end of the acceptance region. This is because of the additional noise added, as described in Section 4.2, making the filter conservative.

5.2 Numerical Simulation Results

The most expected mode of CSS failure is a slow degradation due to ultraviolet radiation over time, resulting in a darkening of the sensor casing[44]. This failure mode is gradual and is easily identified and quantified through on-orbit calibration, for example with the calibration filters discussed in Chapter 4. Of more interest for failure detection are sudden failures. Three different acute failure modes are simulated to demonstrate the possibility of autonomous failure detection: *a*) a complete loss of signal, resulting in a zero measurement for all subsequent time (off failure); *b*) a stuck fault in which the CSS returns the same measurement from the time of failure for all subsequent time (stuck failure); and *c*) a fault in which the CSS returns random noise for all subsequent time (random failure).

Figure 5.4 illustrates the sensor output of a CSS suffering from each of the three failure modes. A single case with the simulation parameters from Section 2.4 is shown with the sensor failure occurring at 1950 s, during the region of the orbit when the CSS are most affected by Earth's albedo. It is important to note the stuck failure can be varied significantly, with the value at which the CSS remains stuck being set to the current measurement value, the max measurement value, or any random measurement value between.

For a consistent filter, it is expected that the NIS values will fall between the χ^2 acceptance bounds, r_1 and r_2, as shown in Figure 5.3, and they do for the filter using the $1^\circ \times 1.25^\circ$ albedo data set. However, because additional measurement noise is added to the filters using the $5^\circ \times 5^\circ$ and $10^\circ \times 10^\circ$ albedo data sets, their averaged NIS values fall below the lower bound of the χ^2

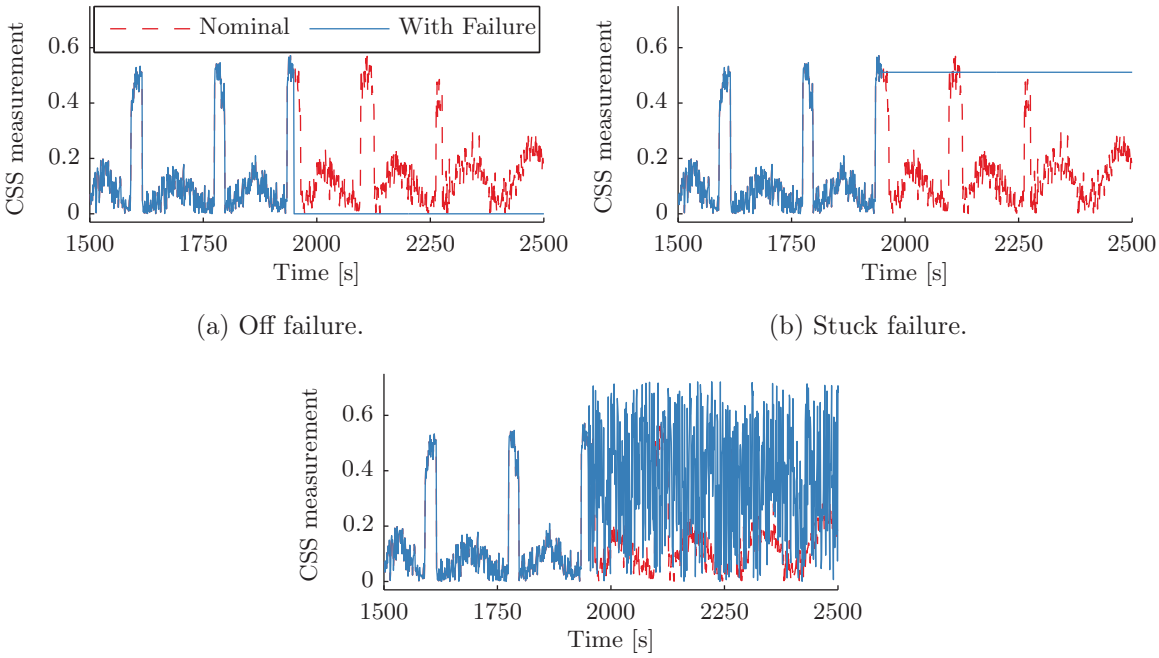

(a) Off failure.

(b) Stuck failure.

(c) Random failure.

Figure 5.4: CSS measurements under each of the failure scenarios studied.

acceptance region. Because of this, different thresholds, determined using numerical Monte Carlo simulations, are used for determining sensor failure.

Figure 5.5 shows the averaged NIS results for a 100 case Monte Carlo analyses run assuming the spacecraft is running a full calibration filter equipped with a $1^\circ \times 1.25^\circ$ and $10^\circ \times 10^\circ$ albedo data set. As can be seen, there is a clear distinction between the nominally operating and failed CSS for a filter using the $1^\circ \times 1.25^\circ$ albedo data set. For a filter using the $10^\circ \times 10^\circ$ albedo data set there is not a clear distinction between nominal operation and failure. Due to the high measurement noise added to account for the system modeling and linearization errors, as discussed in Section 4.2, biases can be seen in the NIS values corresponding to measurements due to Earth's albedo. For this case, choosing a threshold too low leads to high false alarm rates, whereas a value too high leads to poor detection, as traditionally seen when using an EKF approach on a nonlinear problem[56]. In order to avoid false detection, thresholds of 3.0, 1.2, and 1.2 are used for the $1^\circ \times 1.25^\circ$, $5^\circ \times 5^\circ$, and $10^\circ \times 10^\circ$ albedo data sets, respectively. The threshold used for the high resolution albedo grid,

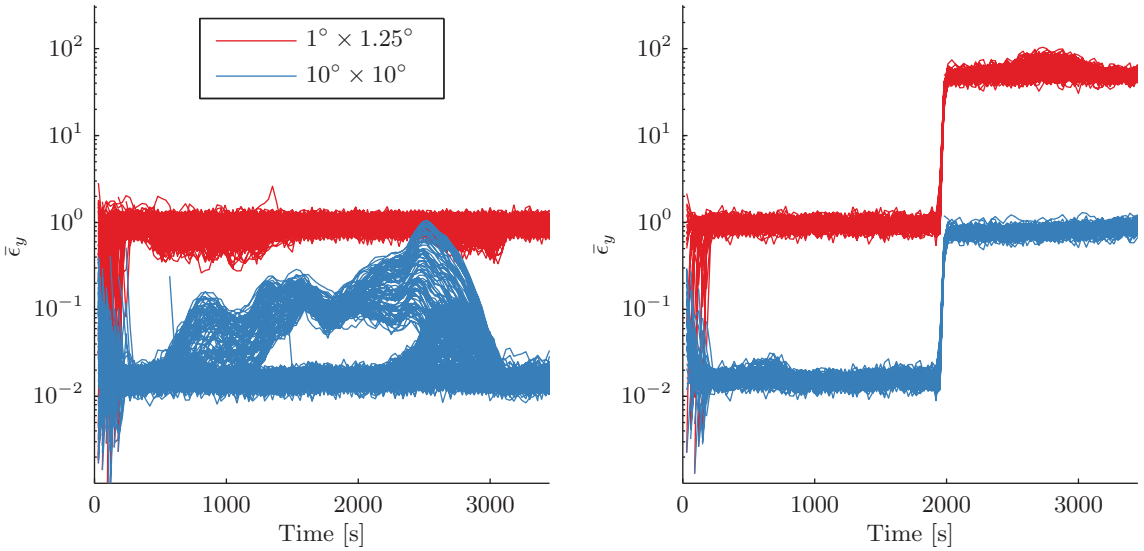

(a) Non-failed CSS.

(b) CSS with random failure.

Figure 5.5: Comparison of nominal and failed CSS averaged NIS values for different albedo resolutions.

while determined empirically, should hold generally because of the accuracy of the albedo model. However, the threshold used for the $10° \times 10°$ albedo grid is more likely to require adjustment for individual missions based on how the albedo grid is evaluated, the maximum albedo expected throughout the orbit, and the desired balance of false detections and missed detections.

Numerical simulations, using the parameters described in Section 2.4, are used to demonstrate the viability of using a NIS test to detect CSS failures. The magnitude of the resulting NIS test results are shown for the off, stuck, and random failure modes of a CSS on-board both a tumbling and controlled spacecraft. It is shown that reliable fault detection can be performed using $1° \times 1.25°$ and $5° \times 5°$ albedo data sets, but using a $10° \times 10°$ results in poor detection.

5.2.1 Fault Detection on Uncontrolled Spacecraft

A single orbit of an uncontrolled spacecraft equipped with a dual pyramid CSS configuration is simulated with CSS 1 experiencing a fault at 1950 s. The spacecraft is assumed to be equipped with a full calibration filter, as described in Section 4.2, with a $1° \times 1.25°$, $5° \times 5°$, or $10° \times 10°$

on-board albedo data set. The expected NIS values, without a failure occurring, are shown as reference.

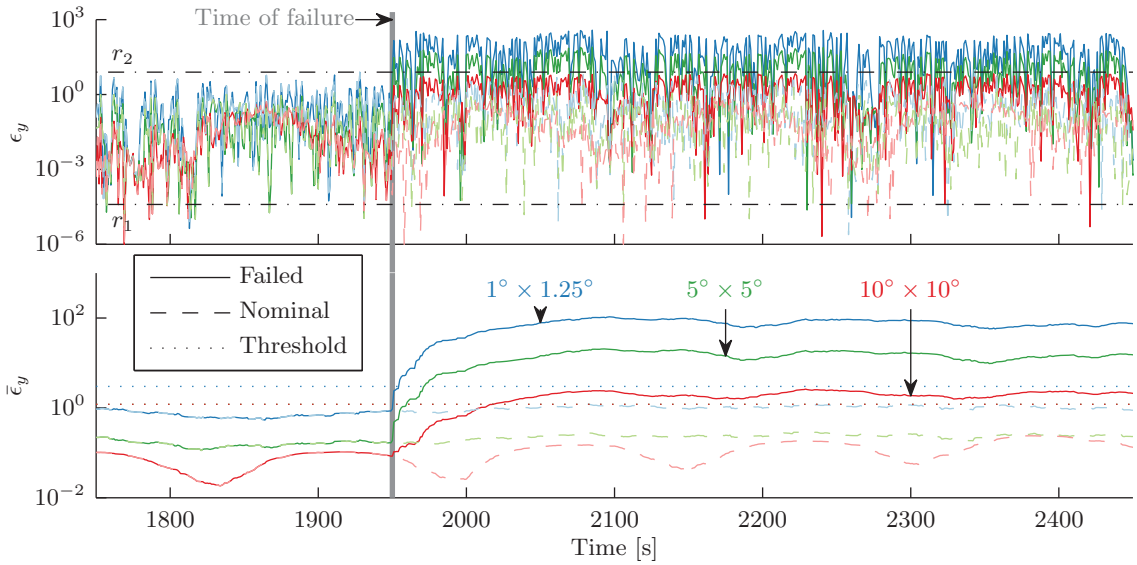

Figure 5.6: NIS and 100 sample averaged NIS for uncontrolled spacecraft running full calibration filter with CSS 1 random failure at 1950 s.

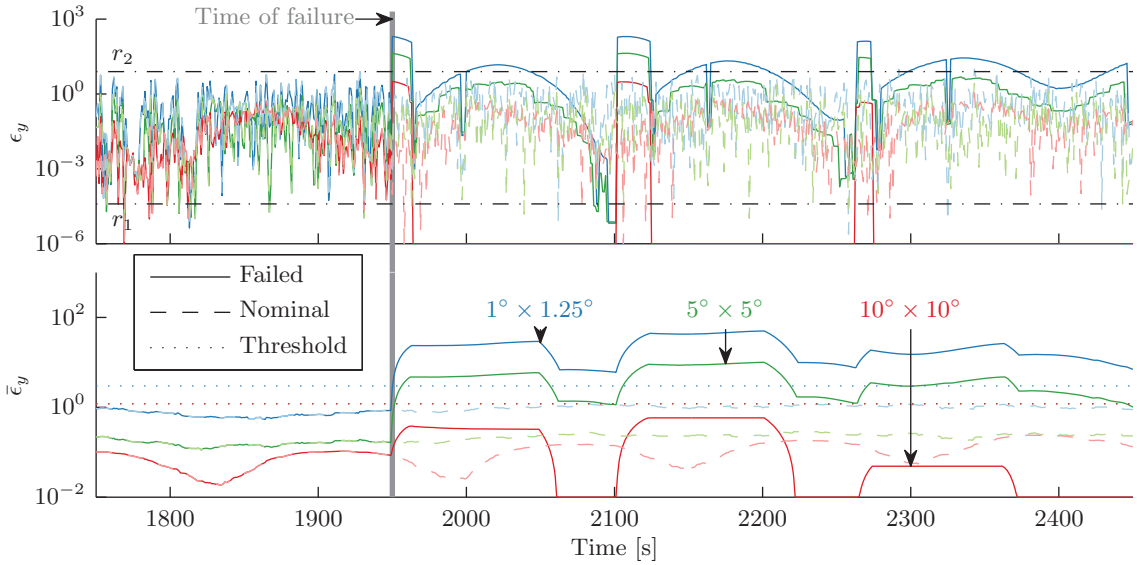

Figure 5.7: NIS and 100 sample averaged NIS for uncontrolled spacecraft running full calibration filter with CSS 1 off failure at 1950 s.

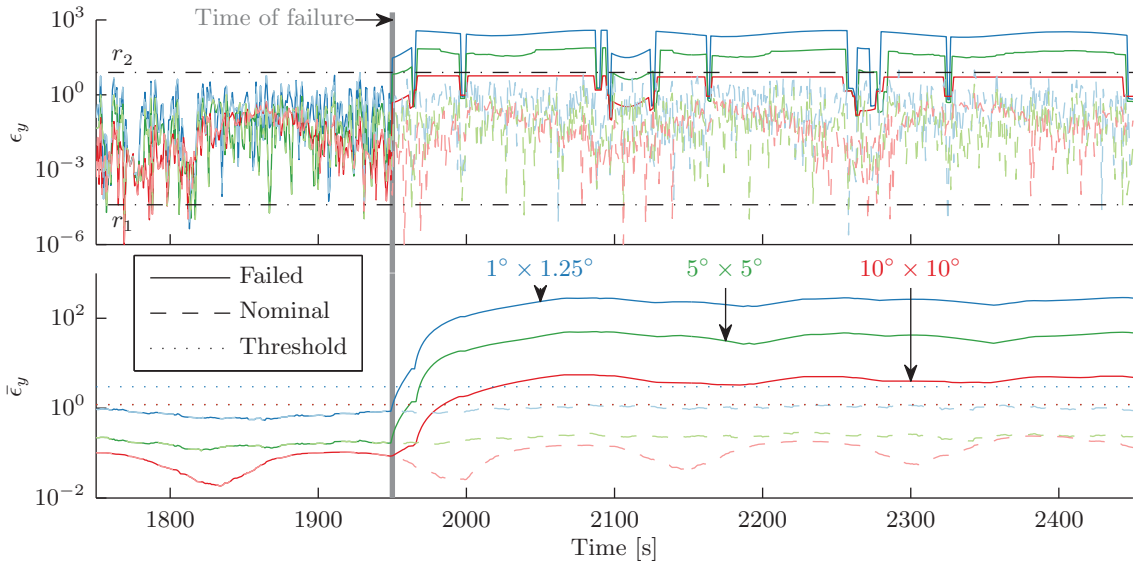

Figure 5.8: NIS and 100 sample averaged NIS for uncontrolled spacecraft running full calibration filter with CSS 1 stuck at max failure at 1950 s.

Figures 5.6 to 5.8 show the NIS, and 100 sample averaged NIS, for random, off, and stuck failures of CSS 1, respectively. The individual timestep NIS values fluctuate significantly, and can be seen to fall outside the χ^2 acceptance bounds even during nominal operation, and within those same bounds after failure. This again illustrates why averaged NIS values are used for fault detection. For the random and stuck failures there is a distinct increase in the averaged NIS value at the time of failure for all three on-board albedo models, with the filters running higher resolution albedo data sets taking less time to increase above the detection threshold. However, the difference between nominal and failure is less distinct for an off failure when using the $10° \times 10°$ albedo data set, and the NIS value of the failed sensor does not increase above the detection threshold for the case shown.

As mentioned previously, a stuck fault may result in a sensor returning any value between its maximum and minimum possible measurements for all subsequent time. Consequently, the NIS value for a stuck sensor returning measurements near the expected nominal measurement may fall within the detection threshold, making it difficult to distinguish between nominal and faulty operation. This is shown in Figures 5.9 and 5.10, where the resulting averaged NIS values are shown for stuck faults in 10 % increments between 0 % to 100 %. For the case shown, CSS 1 does

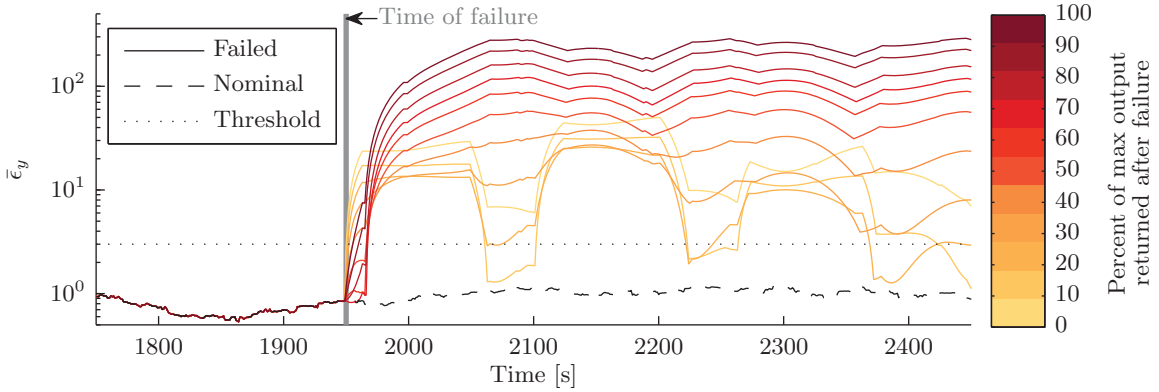

Figure 5.9: 100 sample averaged NIS for uncontrolled spacecraft running full calibration filter with $1° \times 1.25°$ albedo data experiencing a stuck failure of CSS 1 at 1950 s.

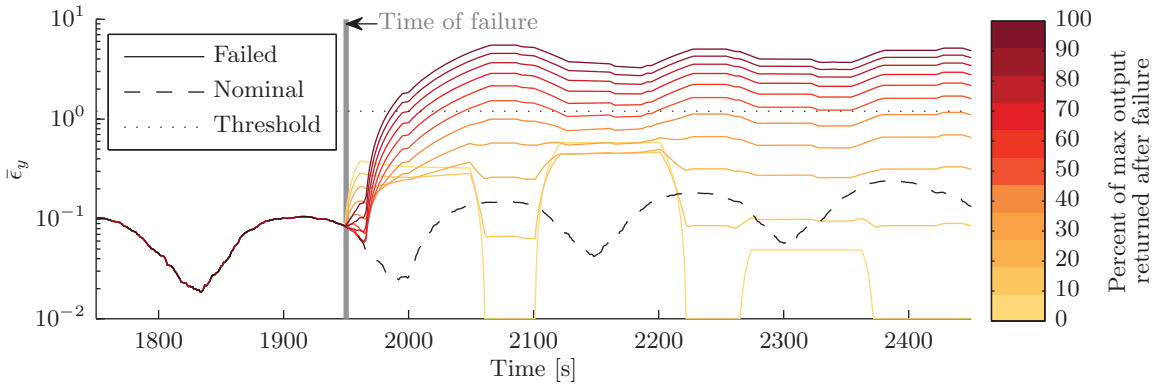

Figure 5.10: 100 sample averaged NIS for uncontrolled spacecraft running full calibration filter with $10° \times 10°$ albedo data experiencing a stuck failure of CSS 1 at 1950 s.

not receive any direct sunlight measurements, but the averaged NIS value for the full albedo data set filter clearly increases above the detection threshold for all values of stuck failures. However, for the low resolution data set it takes an erroneous signal greater than 50 % of the maximum for the averaged NIS to rise above the detection threshold. As expected, decreasing the accuracy of the on-board albedo model increases the conservatism of the filter and trades accuracy for computation time.

Table 5.1 lists the fault detection statistics for a 500 case Monte Carlo analysis, run using the parameters in Section 4.4.3, in which a failure of CSS 1 occurs at 1950 s for an uncontrolled spacecraft attempting calibration. For these results, the cases in which the CSS never registers a

Table 5.1: Fault detection statistics for 500 case Monte Carlo assuming an uncontrolled spacecraft.

Albedo Data	Failure Mode	False Detections		Correct Detections	
$1^\circ \times 1.25^\circ$	Off	6/3686	(0.16 %)	428/428	(100.00 %)
	Random	6/3687	(0.16 %)	428/428	(100.00 %)
	Stuck	6/3686	(0.16 %)	428/428	(100.00 %)
$5^\circ \times 5^\circ$	Off	0/3689	(0.00 %)	431/431	(100.00 %)
	Random	0/3690	(0.00 %)	431/431	(100.00 %)
	Stuck	0/3689	(0.00 %)	427/431	(99.07 %)
$10^\circ \times 10^\circ$	Off	2/3689	(0.05 %)	406/431	(94.20 %)
	Random	2/3690	(0.05 %)	431/431	(100.00 %)
	Stuck	2/3689	(0.05 %)	391/431	(90.72 %)

measurement above the direct sunlight threshold of 0.4, thus becoming initialized in the calibration filter, are removed. False detections are the total number of reported failures amongst CSS 2 through 8, and reported failures of CSS 1 before the time of failure. In all cases, the calibration filters exhibit less than 0.15 % false detection rate. The higher resolution on-board albedo data set filters correctly detect the sensor failure nearly 100 % of the time and the $10^\circ \times 10^\circ$ albedo data set correctly detects the failure greater than 90 % of the time.

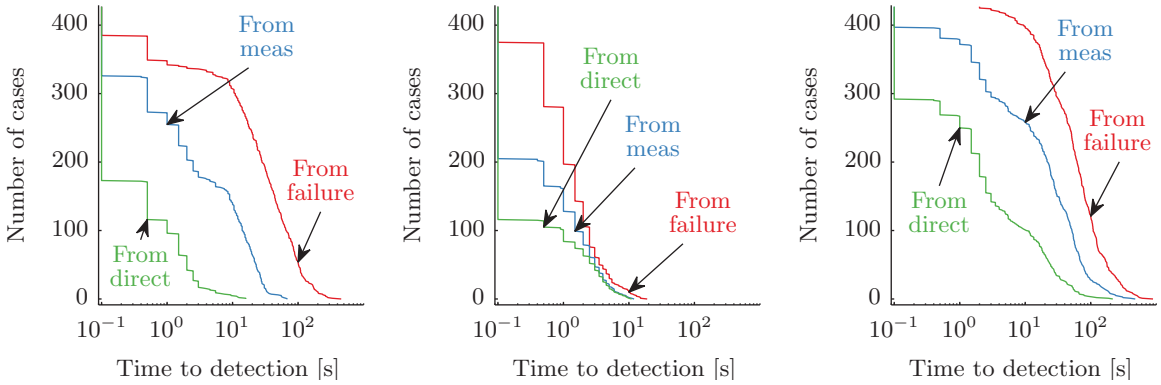

(a) Off failure. (b) Random failure. (c) Stuck failure.

Figure 5.11: Time from failure to detection using $1^\circ \times 1.25^\circ$ albedo data.

Also of importance is how fast the calibration filter is able to identify a sensor failure. Figures 5.11 to 5.13 show the time from failure to detection for each of the albedo data set resolutions

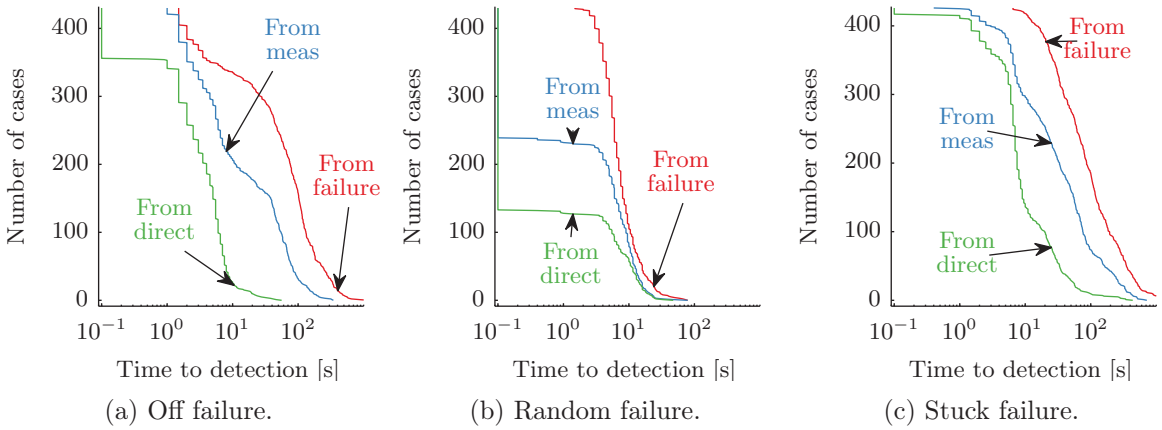

(a) Off failure. (b) Random failure. (c) Stuck failure.

Figure 5.12: Time from failure to detection using $5° \times 5°$ albedo data.

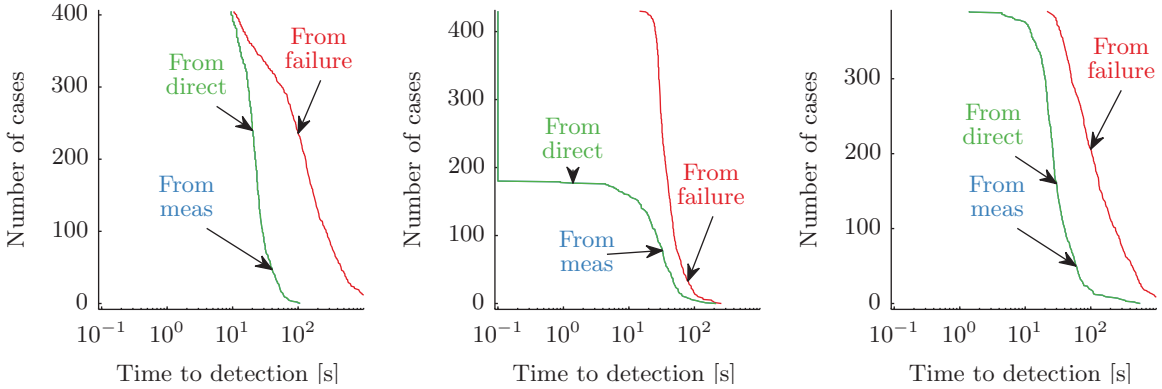

(a) Off failure. (b) Random failure. (c) Stuck failure.

Figure 5.13: Time from failure to detection using $10° \times 10°$ albedo data.

tested. As reference, the time from the first measurement above the specified noise floor, denoted "from meas", and the time from the first direct sunlight measurement, denoted "from direct", to failure detection are also shown. These results illustrate that while some cases may take significant time to detect the sensor failure, the majority of that time is spent without any measurements from the sensor. Once the expected observations for the failed sensor rise above the noise floor the calibration filter is able to quickly identify the faulty sensor. The random failure is the most quickly identified failure, while the stuck failure is, as expected, the most difficult to distinguish. These

results show how even a simple fault detection scheme can be used to identify faulty sensors with minimal computation costs above that of the full calibration filter.

5.2.2 Fault Detection on Controlled Spacecraft

A single orbit of a controlled spacecraft equipped with a dual pyramid CSS configuration is simulated with a fault in CSS 1 occurring at 1950 s. Similar to the previous section, the spacecraft is assumed to be equipped with a full calibration filter, as described in Section 4.2, using a $1^\circ \times 1.25^\circ$, $5^\circ \times 5^\circ$, or $10^\circ \times 10^\circ$ on-board albedo data set. In contrast to the previous section, the spacecraft is actively controlled and maintains the z-axis of the spacecraft pointed at the Sun for the duration of the simulation. This results in sensor measurements that do not change significantly throughout the trajectory, similar to those shown in Figure 2.5.

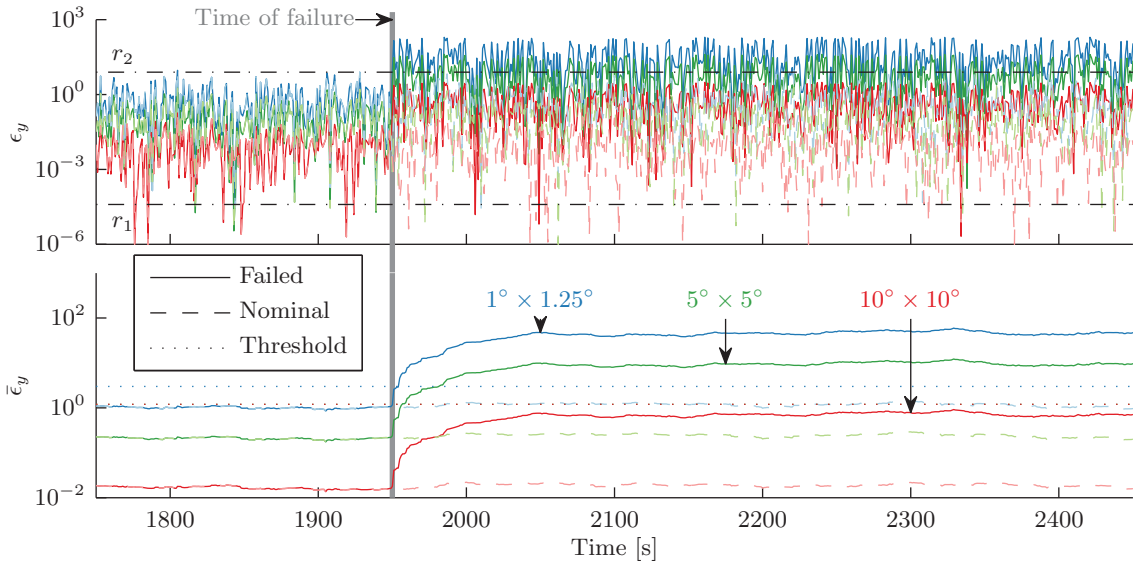

Figure 5.14: NIS and 100 sample averaged NIS for controlled spacecraft running full calibration filter with CSS 1 random failure at 1950 s.

Figures 5.14 to 5.16 show the NIS, and 100 sample averaged NIS, for random, off, and stuck failures of CSS 1, respectively. For the stuck faults, because the spacecraft is actively controlled, the averaged NIS values reach a nearly constant value after a time period equal to the sampling interval. The averaged NIS values for the filters using the $1^\circ \times 1.25^\circ$ and $5^\circ \times 5^\circ$ data set show clear

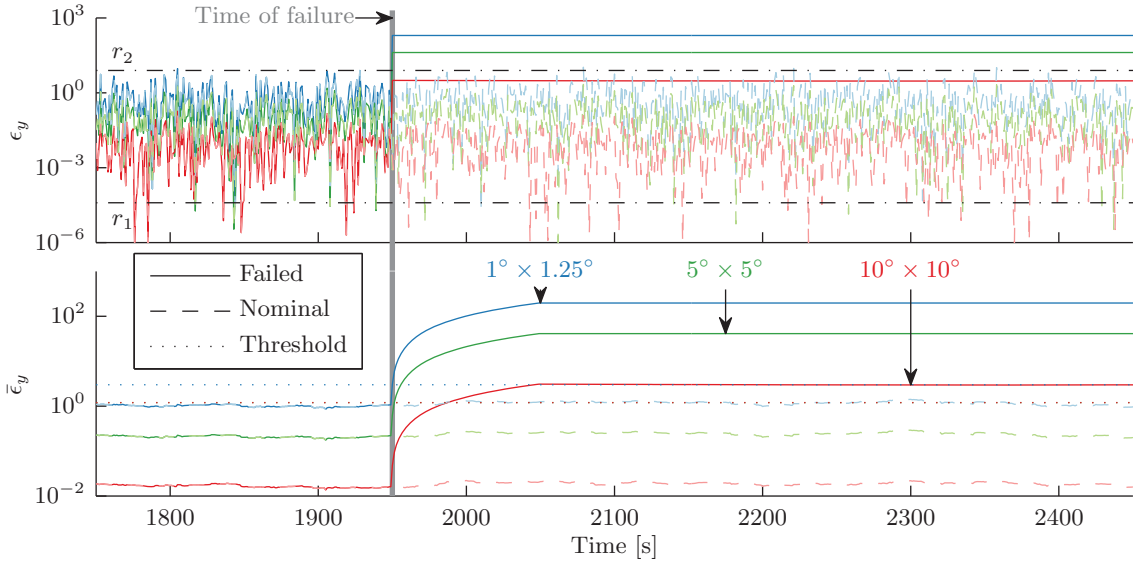

Figure 5.15: NIS and 100 sample averaged NIS for controlled spacecraft running full calibration filter with CSS 1 off failure at 1950 s.

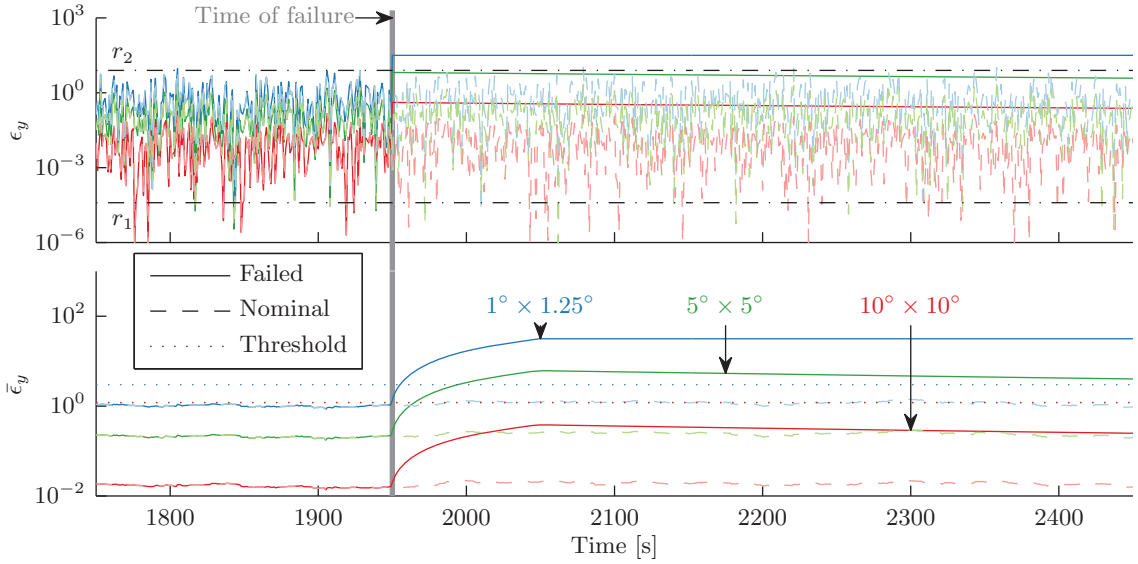

Figure 5.16: NIS and 100 sample averaged NIS for controlled spacecraft running full calibration filter with CSS 1 stuck at max failure at 1950 s.

deviations above the detection threshold for all three failure modes, whereas the $10° \times 10°$ is shown to be too conservative to distinguish random and stuck at max sensor failures.

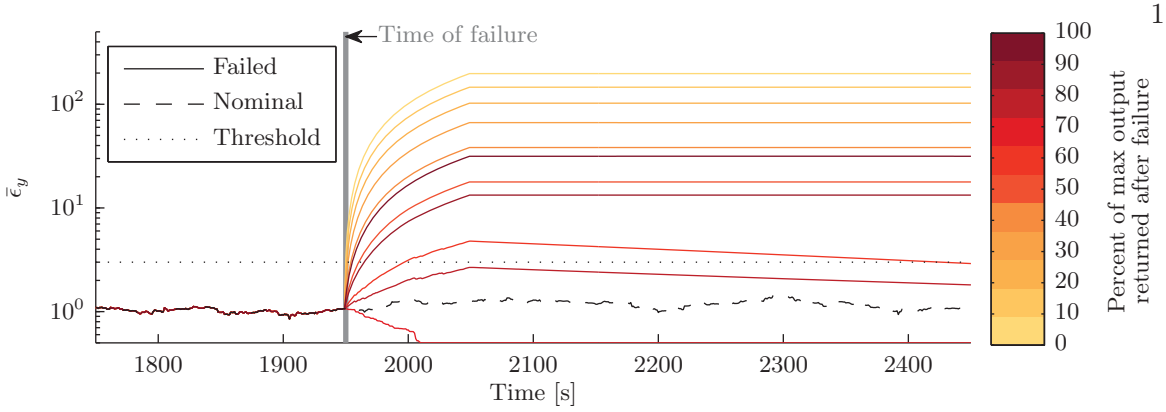

Figure 5.17: 100 sample averaged NIS for controlled spacecraft running full calibration filter with $1° \times 1.25°$ albedo data experiencing a stuck failure of CSS 1 at 1950 s.

The output of the full calibration filter using a $1° \times 1.25°$ albedo resolution, and experiencing different values of stuck faults, is shown in Figure 5.17. All stuck failures, except the ones that return 70 % to 80 % of the maximum output the failure, are clearly marked by an increase of the averaged NIS above the detection threshold. For the time region shown, the expected measurement of CSS 1 is approximately 72 % of the maximum output and the difference between nominal sensor output and that of a stuck sensor is too small to distinguish.

Table 5.2: Fault detection statistics for 500 case Monte Carlo assuming a controlled spacecraft.

Albedo Data	Failure Mode	False Detections		Correct Detections	
$1° \times 1.25°$	Off	1/2427	(0.04 %)	489/489	(100.00 %)
	Random	1/2428	(0.04 %)	490/490	(100.00 %)
	Stuck	1/2427	(0.04 %)	49/489	(10.02 %)
$5° \times 5°$	Off	0/2427	(0.00 %)	489/489	(100.00 %)
	Random	0/2428	(0.00 %)	490/490	(100.00 %)
	Stuck	0/2427	(0.00 %)	0/489	(0.00 %)
$10° \times 10°$	Off	6/2427	(0.25 %)	489/489	(100.00 %)
	Random	5/2428	(0.21 %)	57/490	(11.63 %)
	Stuck	6/2427	(0.25 %)	0/489	(0.00 %)

Table 5.2 shows the fault detection statistics for a 500 case Monte Carlo run using the parameters in Section 4.4.3, in which a failure of CSS 1 occurs at 1950 s for a controlled spacecraft attempting calibration. For these results, the cases in which the CSS never registers a measurement

above the direct sunlight threshold of 0.4, thus becoming initialized in the calibration filter, are removed. Because of how the random numbers are generated, the random failure mode alters the sequence of random numbers used to generate measurements due to Earth's albedo. There is one additional case for the random failure as a result; CSS 1 is randomly assigned a calibration scale factor of 0.43 in the case in question, and without a random faulty measurement of 93 % or higher the CSS is never initialized in the filter. However, with that random measurement the filter is able to identify that something is wrong and flag the sensor as faulty.

As expected, all of the filters have trouble identifying a failure in which the CSS becomes stuck, returning the same measurement from the time of failure for all subsequent time. Both of the filters using higher resolution albedo data sets are reliably able to identify off and random failures, but the calibration filter using a $10^\circ \times 10^\circ$ albedo grid has a very poor detection rate. For a sun-pointing spacecraft, off failures are detected within one measurement update, 0.5 s, using the $1^\circ \times 1.25^\circ$ albedo data set, within 2.5 s using the $5^\circ \times 5^\circ$ albedo grid, and within 20 s using the $10^\circ \times 10^\circ$ albedo data set. For cases suffering a random failure the filter using the $1^\circ \times 1.25^\circ$ albedo data set takes an average of 2.2 s to detect sensor failure and the filter using the $5^\circ \times 5^\circ$ albedo grid takes an average of 11 s. The decreased time to detection is a result of the spacecraft maintaining an orientation with the faulty sensor receiving direct sunlight measurements, but the detection rate of stuck failures suffers as a result of this static attitude.

Chapter 6

Conclusions & Future Work

6.1 Summary of Dissertation

The use of partially underdetermined coarse sun sensor configurations in autonomous satellite attitude, determination, and control systems is examined. A numerical simulation framework is developed and used to test algorithms for sun-direction estimation, on-orbit calibration, and autonomous fault detection. The problems of estimating highly nonlinear systems with significant noise are addressed with emphasis placed on achieving sufficient performance for safe-mode operations while maintaining low sensor and computational requirements.

A simulation framework for testing satellite ADCS algorithms using realistic sensor models is developed. This framework has the ability to perform hardware in the loop tests using actual spacecraft components and visualize the results in real-time. An in depth analysis of cosine-type coarse sun sensor and rate gyroscope models is presented and these models are validated against hardware measurements. Two coarse sun sensor configurations that do not provide sufficient coverage to uniquely determine the sun-direction at any time are presented and analyzed.

Several methods for estimating and controlling a spacecraft's orientation relative to the Sun using only coarse sun sensor and rate gyro measurements are reviewed and compared. Of interest is how to achieve a power positive orientation when little information is available, such as immediately post launch vehicle separation or in a power critical safe-mode situation. All methods perform simultaneous sun-direction estimation and attitude control to achieve a power-positive orientation. Three single-point estimators are presented; the first method uses a simple vector average calculation

and the second and third involve variations on a combination of least squares and minimum norm criteria. Two sequential filter approaches are also presented; the first uses an extended Kalman filter with measurement and process noise inflated to account for measurement inconsistencies, and the second addresses these inconsistencies and the biases present in the system using a consider filter approach. Special attention is given to the nonlinearities of the measurement models that can lead to filter divergence and all methods are evaluated using both a dual pyramid and cube CSS configuration. All of the estimators are shown to provide suitable estimates of the sun-direction vector in the body frame without any knowledge of a spacecraft's inertial position despite significant measurement noise and model biases. Numerical simulations show that sun pointing, to less than 15° accuracy, is quickly achieved even with rate gyroscope performance lower than what is available in mass market commercial electronics MEMS gyroscopes.

Nominally, with rate gyro measurements available, the EKF-based sun-direction estimation method provides the most accurate estimate despite significant dynamic and measurement biases, reducing the 3σ pointing error of the sun-direction estimate below 5°. However, the EKF method's performance is found to be highly sensitive to the process and measurement noise values used, the tuning of which is a highly iterative and time consuming process. A consider Kalman filter approach provides estimation accuracy slightly more conservative than the EKF without the need to adjust measurement and process noise using numerical analysis. Even though the EKF and ECKF methods are non-optimal, by making modifications to how observations are processed, it is shown that these approaches can be made to work even without rate gyro information, thus providing promising performance for safe-mode operation in a situation with few measurement observations.

For underdetermined sensor configurations the positive benefits of simultaneously estimating the sun-direction and controlling the spacecraft are most notable in the single point-estimators. As long as multiple sensor coverage is available in the goal orientation of the control, the spacecraft is able to quickly achieve and maintain sun-direction accuracy on the order of 10° to 15°. This accuracy is sufficient for safe-mode operations in which the aim is to achieve and maintain power

positiveness. Of the single-point estimators, the simple weighted average method provides the best performance.

A MRP-based CSS calibration filter, based on an extended consider Kalman filter, is presented for estimating the calibration coefficient and alignment misalignment angles of CSS on-board a spacecraft in low Earth orbit. The full filter uses orbit knowledge to compute the irradiance contributions to each CSS due to Earth's albedo. A reduced filter is also presented that does not require orbit knowledge and, as a consequence, treats the irradiance due to Earth's albedo as an unmodeled bias. The relative accuracies and computation times of these two methods are computed using numerical simulations. It is shown that estimation using even a very coarse albedo data set is superior, in both accuracy and computation time, to treating the albedo as a bias. CSS calibration scale factors can be estimated to less than 1 % and alignment angles to approximately 1°. Computation time reductions by a factor of 25 can be achieved with only an increase of calibration coefficient accuracies to 2 %, and alignment accuracies to approximately 2°, by reducing the albedo data resolution in the calibration filter. Such a calibration filter could be used on-board a small satellite in order to reduce necessary ground support and increase autonomy.

Finally, the ability to autonomously detect coarse sun sensor failures is investigated. Kalman filters are traditionally not used for fault detection in nonlinear systems due to poor detection or high false alarm rates. However, it is shown that because of the effort placed into accurately modeling the measurement models, a simple method using an averaged normalized innovation squared test can be used to detect sensor failures at little additional computational cost beyond the calibration filters presented earlier. While a calibration filter using a $10° \times 10°$ albedo data set is shown to be incapable of reliably detecting sensor failure, a filter using a higher than $5° \times 5°$ albedo data set resolution is shown to be able to detect sensor failure with above 98 % accuracy and less than 0.2 % false alarms.

All of these areas of investigation provide alternative ADCS algorithms for small satellite missions looking to use inexpensive, small sensors due to size, power, or budget limitations. Throughout this work, emphasis is placed on undetermined sensor configurations that reduce the number of nec-

essary sensors, but might also arise late in the life of larger satellites as sensors fail. In addition, accuracy is balanced against computational costs in an effort to improve spacecraft autonomy and reduce ground testing and support costs.

6.2 Suggestions for Future Work

Throughout this research, emphasis is placed in balancing accuracy with computational costs. To this end, extended Kalman filter approaches are used due to their computational speed to address nonlinearities in the problems examined. Future work should investigate fully nonlinear approaches, such as an unscented Kalman filter or divided difference filter. A comparison of the accuracy gains weighed against the computational increase would be beneficial.

A graduate team at the University of Colorado is currently building a CubeSat for the QB50 mission[105]. The spacecraft is currently planning to fly with magnetometers, but no star tracker. Magnetometer based attitude estimation has been demonstrated, using only magnetometers[106] and in combination with CSS[16]; however, it would be interesting to compare the accuracy of the calibration filter when run using magnetometer, instead of star tracker, measurements.

Throughout this research significant effort is made to make the numerical simulations as real as possible, and sensor models are validated using sensor measurements taken on the ground. However, there is no substitute for actual flight data. There are currently several projects ongoing at the University of Colorado to launch small satellites that will fly coarse sun sensors, and there is interest in incorporating the algorithms developed here into the attitude, determination, and control systems of these vehicles. Future work should continue to investigate the algorithms presented here using actual flight data.

Alternatively, future work could look into terrestrial applications of sun-pointing algorithms. It has been hypothesized that animals, such as the sandhopper, Manx shearwater[107], and Savannah sparrow[108], rely on the position of the Sun for navigation. Because CSS represent a small, inexpensive sensor, through which sun-direction estimation can be calculated quickly, it would be interesting to incorporate them into solar based navigation, such as that explored in Reference 109,

for small robotic platforms. Such a technique could prove useful in environments without access to GPS and, by using solar panels as sensors, could have the added benefit of power generation for small robots.

To improve the accuracy and robustness of the calibration filter, future research could explore more realistic albedo modeling. Currently for the albedo data set, the albedo value for a specific area of the Earth's surface is calculated based on the center of the differential area. Similar to approximations made in numerical integration schemes, examining Figure 4.1a illustrates how this can lead to an under or over representation of the actual albedo input. Different methods for calculating the irradiance due to Earth's albedo could reduce the measurement noise necessary to account for modeling errors. In addition, the values for the Earth's albedo are based on averages and standard deviations of a 5 yr period with each point in the albedo grid being dispersed independently of its neighbors. Global weather patterns tend to result in neighboring regions of the Earth's surface having similar albedo due to cloud cover. Future work could look into these effects significantly impact the accuracy of the calibration filter.

Finally, future work should investigate nonlinear fault detection methods. The fault detection method presented only works with the full calibration filter not the sun-direction estimators. If the accuracy of the sun-direction estimators can be improved through the use of nonlinear filters it may lead to opportunities to perform fault detection and sun-direction estimation simultaneously.

Bibliography

[1] Bouwmeester, J. and Guo, J., "Survey of worldwide pico- and nanosatellite missions, distributions and subsystem technology," Acta Astronautica, Vol. 67, No. 7-8, Oct. 2010, pp. 854–862, ISSN 00945765, 10.1016/j.actaastro.2010.06.004.

[2] Puig-Suari, J., Turner, C., and Twiggs, R. J., "CubeSate: The Development and Launch Support Infrastructure for Eighteen Different Satellite Customers on One Launch," Proceedings of the AIAA/USU Conference on Small Satellites, Logan, UT, 2001, ISBN 6507238651, pp. 1–5.

[3] Rocken, C., Kuo, Y. H., Schreiner, W., Hunt, D., Sokolovskiy, S., and Mccormick, C., "COSMIC System Description," Special Issue of Terrestrial, Atmospheric and Oceanic Science, Vol. 11, No. 1, Mar. 2000, pp. 21–52.

[4] Fong, C.-J., Whiteley, D., Yang, E., Cook, K., Chu, V., Schreiner, B., Ector, D., Wilczynski, P., Liu, T.-Y., and Yen, N., "Space and ground segment performance and lessons learned of the FORMOSAT-3/COSMIC mission: four years in orbit," Atmospheric Measurement Techniques, Vol. 4, No. 6, Jun. 2011, pp. 1115–1132, ISSN 1867-8548, 10.5194/amt-4-1115-2011.

[5] Springmann, J. C., "On-Orbit Calibration of Photodiodes for Attitude Determination," Proceedings of the AIAA/USU Conference on Small Satellites, Logan, UT, Aug. 2013.

[6] Hsiao, F.-y., Chou, W.-T., Cato, T., and Rebelo, C., "Coarse Sun Acquisition Only with Sun Sensors for Micro Satellites," Proceedings of the AAS/AIAA Space Flight Mechanics Conference, Williamsburg, VA, 2015.

[7] Ninomiya, K., Ogawara, Y., Tsuno, K., and Akabane, S., "High Accuracy Sun Sensor Using CCDs," Proceedings of the AIAA Guidance, Navigation, and Control Conference, American Institute of Aeronautics and Astronautics, Minneapolis, MN, 1988.

[8] Rufino, G., Grassi, M., and Rolfi, M., "Preliminary Calibration Results For a High-Precision CMOS Sun Sensor," Proceedings of the AIAA Guidance, Navigation, and Control Conference and Exhibit, Honolulu, HI, Aug. 2011, pp. 1–9.

[9] Wei, M.-S., Xing, F., Li, B., and You, Z., "Investigation of digital sun sensor technology with an N-shaped slit mask." Sensors (Basel, Switzerland), Vol. 11, No. 10, Jan. 2011, pp. 9764–77, ISSN 1424-8220, 10.3390/s111009764.

[10] Chen, F., Feng, J., and Hong, Z., "Digital sun sensor based on the optical vernier measuring principle," Measurement Science and Technology, Vol. 17, No. 9, Sep. 2006, pp. 2494–2498, ISSN 0957-0233, 10.1088/0957-0233/17/9/017.

[11] Ortega, P., López-Rodríguez, G., Ricart, J., Domínguez, M., Castañer, L. M., Quero, J. M., Tarrida, C. L., García, J., Reina, M., Gras, A., and Angulo, M., "A Miniaturized Two Axis Sun Sensor for Attitude Control of Nano-Satellites," IEEE Sensors Journal, Vol. 10, No. 10, 2010, pp. 1623–1632, ISSN 1530-437X, 10.1109/JSEN.2010.2047104.

[12] Xie, N. and Theuwissen, A. J. P., "An autonomous low-power high-resolution micro-digital sun sensor," Proceedings of the International Symposium on Photoelectric Detection and Imaging, Jun. 2011, 10.1117/12.900140.

[13] Flatley, T. W. and Moore, W. A., "An Earth Albedo Model: A Mathematical Model for the Radiant Energy Input to an Orbiting Spacecraft Due to the Diffuse Reflectance of Solar Radiation From the Earth Below," Tech. rep., National Aeronautics and Space Administration, Goddard Space Flight Center, Greenbelt, MD, 1994.

[14] Bhanderi, D. D. V. and Bak, T., "Modeling Earth Albedo for Satellites in Earth Orbit," Proceedings of the AIAA Guidance, Navigation, and Control Conference and Exhibit, American Institute of Aeronautics and Astronautics, San Francisco, CA, Aug. 2005.

[15] Bhanderi, D. D. V., "Modeling Earth Albedo Currents on Sun Sensors for Improved Vector Observation," Proceedings of the AIAA Guidance, Navigation, and Control Conference, Keystone, CO, Aug. 2006.

[16] Appel, P., "Attitude Estimation from Magnetometer and Earth-Albedo-Corrected Coarse Sun Sensor Measurements," Acta Astronautica, Vol. 56, No. 1-2, Jan. 2005, pp. 2–5, ISSN 00945765, 10.1016/j.actaastro.2004.09.001.

[17] Jackson, B. and Carpenter, B., "Optimal Placement of Spacecraft Sun Sensors Using Stochastic Optimization," Proceedings of the IEEE Aerospace Conference, IEEE, Big Sky, MT, Mar. 2004, ISBN 0780381556104, pp. 3916–3923.

[18] Springmann, J. C. and Cutler, J. W., "Optimization of Directional Sensor Orientation with Application to Photodiodes for Spacecraft Attitude Determination," Proceedings of the AAS/AIAA Space Flight Mechanics Conference, Kauau, HI, Feb. 2013, pp. 1–19.

[19] Jung, H. and Psiaki, M. L., "Tests of Magnetometer/Sun-Sensor Orbit Determination Using Flight Data," Proceedings of the AIAA Guidance, Navigation, and Control Conference and Exhibit, American Institute of Aeronautics and Astronautics, Montreal, Canada, Aug. 2001.

[20] Wahba, G., "A Least Squares Estimate of Satellite Attitude," SIAM Review, Vol. 8, No. 3, 1966, pp. 384–386.

[21] Davenport, P. B., "A Vector Approach to the Algebra of Rotations with Applications," Tech. Rep. August, National Aeronautics and Space Adminstration, Goddard Space Flight Center, Greenbelt, MD, 1968.

[22] Shuster, M. D. and Oh, S. D., "Three-Axis Attitude Determination from Vector Observations," Journal of Guidance, Control, and Dynamics, Vol. 4, No. 1, 1981, pp. 70–77, ISSN 0731-5090, 10.2514/3.19717.

[23] Markley, F. L., "Attitude Determination Using Vector Observations: A Fast Optimal Matrix Algorithm," Journal of the Astronautical Sciences, Vol. 41, No. 2, 1993, pp. 261–280.

[24] Black, H. D., "A Passive System for Determing the Attitude of a Satellite," AIAA Journal, Vol. 2, No. 7, 1964, pp. 1350–1351.

[25] Mortari, D., Markley, F. L., and Singla, P., "Optimal Linear Attitude Estimator," Journal of Guidance, Control, and Dynamics, Vol. 30, No. 6, Nov. 2007, pp. 1619–1627, ISSN 0731-5090, 10.2514/1.29568.

[26] Fisher, H. L., Musser, K. L., and Shuster, M. D., "Coarse Attitude Determination From Earth Albedo Measurements," IEEE Transactions on Aerospace and Electronic Systems, Vol. 29, No. 1, Jan. 1993, pp. 22–26, ISSN 0018-9251, 10.1109/7.249110.

[27] Scholz, A., Ley, W., Dachwald, B., Miau, J. J., and Juang, J. C., "Flight results of the COMPASS-1 picosatellite mission," Acta Astronautica, Vol. 67, No. 9-10, Nov. 2010, pp. 1289–1298, ISSN 00945765, 10.1016/j.actaastro.2010.06.040.

[28] Kalman, R. E., "A New Approach to Linear Filtering and Prediction Problems," Journal of Basic Engineering, Vol. 82, No. Series D, 1960, pp. 35–45.

[29] Makovec, K. L., Turner, A. J., and Hall, C. D., "Design and Implementation of a Nanosatellite Attitude Determination and Control System," Proceedings of the AAS/AIAA Astrodynamics Specialist Conference, Quebec City, Canada, Aug. 2001, pp. 1–19.

[30] Sarda, K., Grant, C., Eagleson, S., Kekez, D. D., and Zee, R. E., "Canadian Advanced Nanospace Experiment 2: On-Orbit Experiences with a Three-Kilogram Satellite," Proceedings of the AIAA/USU Conference on Small Satellites, Logan, UT, Aug. 2008, ISBN 1416667792.

[31] Springmann, J. C., Sloboda, A. J., Klesh, A. T., Bennett, M. W., and Cutler, J. W., "The attitude determination system of the RAX satellite," Acta Astronautica, Vol. 75, Jun. 2012, pp. 120–135, ISSN 00945765, 10.1016/j.actaastro.2012.02.001.

[32] Julier, S. J. and Uhlmann, J. K., "A New Extension of the Kalman Filter to Nonlinear Systems," Proceedings of AeroSense: The International Symposium on Aerospace/Defence Sensing, Simulation, and Controls, Orlando, FL, Jul. 1997.

[33] Nørgaard, M., Poulsen, N. K., and Ravn, O., "New Developments in State Estimation for Nonlinear Systems," Automatica, Vol. 36, No. 11, Nov. 2000, pp. 1627–1638.

[34] Karlgaard, C. D. and Schaub, H., "Comparison of Several Nonlinear Filters for a Benchmark Tracking Problem," Proceedings of the AIAA Guidance, Navigation, and Control Conference, American Institute of Aeronautics and Astronautics, Keystone, CO, Aug. 2006.

[35] Schmidt, S. F., "Application of State-Space Methods to Navigation Problems," Advances in Control Systems, Vol. 3, 1966, pp. 293–340.

[36] Friedland, B., "Treatment of Bias in Recursive Filtering," IEEE Transactions on Automatic Control, Vol. 14, No. 4, Aug. 1969, pp. 359–367, ISSN 0018-9286, 10.1109/TAC.1969.1099223.

[37] Jazwinski, A. H., Stochastic Processes and Filtering Theory, Academic Press, Inc., 1970.

[38] Tapley, B., Schutz, B., and Born, G., Statistical Orbit Determination, Elsevier Academic Press, 2004, ISBN 9780126836301.

[39] Woodbury, D. P. and Junkins, J. L., "On the Consider Kalman Filter," AIAA Guidance, Navigation, and Control Conference, American Institute of Aeronautics and Astronautics, Toronto, ON, Aug. 2010, 10.2514/6.2010-7752.

[40] Zanetti, R. and Bishop, R. H., "Kalman Filters with Uncompensated Biases," Journal of Guidance, Control, and Dynamics, Vol. 35, No. 1, Jan. 2012, pp. 327–335, ISSN 0731-5090, 10.2514/1.55120.

[41] Bar-Itzhack, I. Y. and Oshman, Y., "Attitude Determination from Vector Observations: Quaternion Estimation," IEEE Transactions on Aerospace and Electronic Systems, Vol. AES-21, No. 1, Jan. 1985, pp. 128–136, ISSN 0018-9251, 10.1109/TAES.1985.310546.

[42] Tsao, T. and Chiang, R. Y., "Gyroless 3-Axis Sun Acquisition via Sun Sensors Only Unscented Kalman Filter Estimation," Proceedings of the AIAA Guidance, Navigation, and Control Conference, Boston, MA, Aug. 2013, pp. 1–12.

[43] Ahn, H.-s., Member, S., and Lee, S.-h., "Gyroless Attitude Estimation of Sun-Pointing Satellites Using Magnetometers," IEEE Geosscience and Remote Sensing Letters, Vol. 2, No. 1, Jan. 2005, pp. 8–12, ISSN 1545-598X, 10.1109/LGRS.2004.840608.

[44] Springmann, J. C. and Cutler, J. W., "Initial Attitude Analysis of the RAX Satellite," Proceedings of the AAS/AIAA Astrodynamics Specialist Conference, Girdwood, AK, 2011.

[45] Pittelkau, M. E., "Autonomous On-Board Calibration of Attitude Sensors and Gyros," Proceedings of the International Symposium on Space Flight Dynamics, Sep. 2007.

[46] Pittelkau, M. E., "Survey of Calibration Algorithms for Spacecraft Attitude Sensors and Gyros," Proceedings of the AAS/AIAA Astrodynamics Specialist Conference, Mackinac Island, MI, Aug. 2007, pp. 651–705.

[47] Wu, S.-F. and Steyn, W. H., "Modelling and in-orbit calibration practice of a miniature 2-axis analogue sun sensor," Aerospace Science and Technology, Vol. 6, No. 6, Oct. 2002, pp. 423–433, ISSN 12709638, 10.1016/S1270-9638(02)01187-2.

[48] Frank, P. M., "Fault Diagnosis in Dynamic Systems Using Analytical and Knowledge-based Redundancy - A Survey and Some New Results," Automatica, Vol. 26, No. 3, 1990, pp. 459–474.

[49] Betta, G. and Pietrosanto, A., "Instrument Fault Detection and Isolation: State of the Art and New Research Trends," IEEE Transactions on Instrumentation and Measurement, Vol. 49, No. 1, Feb. 2000, pp. 100–107, ISSN 0018-9456, 10.1109/19.836318.

[50] Isermann, R., "Fault Diagnosis of Machines via Parameter Estimation and Knowledge Processing - Tutorial Paper," Automatica, Vol. 29, No. 4, 1993, pp. 815–835.

[51] Isermann, R., "Model Based Fault Detection and Diagnosis Methods," Proceedings of the American Control Conference, Seattle, WA, Jun. 1995, pp. 1605–1609.

[52] Ho, Y. C. and Lee, R. C. K., "A Bayesian Approach to Problems in Stochastic Estimation and Control," IEEE Transactions on Automatic Control, Vol. 9, No. 4, Oct. 1964, pp. 333–339, ISSN 0018-9286, 10.1109/TAC.1964.1105763.

[53] Hussein, I. I., Sorrentino, F., and Erwin, R. S., "Bayesian Hybrid Estimation of LTI Networked Systems using Finite Set Statistics," Proceedings of the American Control Conference, Washington, DC, Jun. 2013.

[54] Mehra, R. K. and Peschon, J., "An Innovations Approach to Fault Detection and Diagnosis in Dynamic Systems," Automatica, Vol. 7, 1971, pp. 637–640, 10.1016/0005-1098(71)90028-8.

[55] Bar-Shalom, Y., Li, X. R., and Kirubarajan, T., Estimation with Applications to Tracking and Navigation, chap. 5, John Wiley & Sons, 2004, pp. 199–266.

[56] Kadirkamanathan, V., Li, P., Jaward, M., and Fabri, S., "A sequential Monte Carlo filtering approach to fault detection and isolation in nonlinear systems," Proceedings of the 39th IEEE Conference on Decision and Control (Cat. No.00CH37187), Vol. 5, No. 1, 2000, pp. 4341–4346, 10.1109/CDC.2001.914586.

[57] Li, J., Chan, C. W., and Zhang, H.-Y., "Asymptotic Local Approach in Fault Detection Based on Predictive Filters," Journal of Guidance, Control, and Dynamics, Vol. 28, No. 6, Nov. 2005, pp. 1112–1122, ISSN 0731-5090, 10.2514/1.12973.

[58] Xiong, K., Chan, C. W., and Zhang, H. Y., "Detection of Satellite Attitude Sensor Faults using the UKF," IEEE Transactions on Aerospace and Electronic Systems, Vol. 43, No. 2, Apr. 2007, pp. 480–491, ISSN 0018-9251, 10.1109/TAES.2007.4285348.

[59] Pirmoradi, F., Sassani, F., and de Silva, C., "Fault detection and diagnosis in a spacecraft attitude determination system," Acta Astronautica, Vol. 65, No. 5-6, Sep. 2009, pp. 710–729, ISSN 00945765, 10.1016/j.actaastro.2009.03.002.

[60] Jasper, L., Nuding, D., Barlow, E., Hogan, E., O'Keefe, S., Withnell, P., and Yunck, T., "CICERO - A Distributed Small Satellite Radio Occultation Pathfinder Mission," Proceedings of the AIAA/USU Conference on Small Satellites, Logan, UT, Aug. 2013.

[61] Lerner, G. M., Spacecraft Attitude Determination and Control, chap. Sun Sensors, D. Reidel Publishing Co., Dordrecht, The Netherlands, 1978, pp. 155–166.

[62] Acton, C., "Ancillary Data Services of NASA's Navigation and Ancillary Information Facility," Planetary and Space Science, Vol. 44, No. 1, 1996, pp. 65–70.

[63] Snyder, J. P., Map Projections: A Working Manual, Geological Survey (U.S.) Professional Paper 1395, 1987, pp. 76–85.

[64] Dobber, M. R., Goede, A. P. H., and Burrows, J. P., "Observations of the Moon by the Global Ozone Monitoring Experiment: Radiometric Calibration and Lunar Albedo," Applied Optics, Vol. 37, No. 33, Nov. 1998, pp. 7832, ISSN 0003-6935, 10.1364/AO.37.007832.

[65] Lucke, R. L., Henry, R. C., and Fastie, W. G., "Far-ultraviolet albedo of the Moon," The Astronomical Journal, Vol. 81, No. 12, Dec. 1976, pp. 1162–1169, 10.1086/112000.

[66] Lane, A. P. and Irvine, W. M., "Monochromatic phase curves and albedos for the lunar disk," The Astronomical Journal, Vol. 78, No. 3, Apr. 1973, pp. 267–277, 10.1086/111414.

[67] Jans, S. J., Hilsenrath, E., Cebula, R. P., and Kelly, T. J., "Observations of the lunar geometric albedo during the ATLAS-3 mission," Geophysical Research Letters, Vol. 23, No. 17, Aug. 1996, pp. 2297–2300, 10.1029/96GL01122.

[68] Farrenkopf, R. L., "Analytic Steady-State Accuracy Solutions for Two Common Spacecraft Attitude Estimators," Journal of Guidance, Control, and Dynamics, Vol. 1, No. 4, 1978, pp. 282–284, ISSN 0731-5090, 10.2514/3.55779.

[69] Crassidis, J., "Sigma-Point Kalman Filtering for Integrated GPS and Inertial Navigation," AIAA Guidance, Navigation, and Control Conference and Exhibit, Aug. 2005, pp. 1–24, 10.2514/6.2005-6052.

[70] Pittelkau, M. E., "Kalman Filtering for Spacecraft System Alignment Calibration," Journal of Guidance, Control, and Dynamics, Vol. 24, No. 6, 2001, ISSN 0731-5090, 10.2514/2.4834.

[71] Pittelkau, M. E., "Everything is Relative in Spacecraft System Alignment Calibration," Journal of Spacecraft and Rockets, Vol. 39, No. 3, 2002, pp. 460–466, ISSN 0022-4650, 10.2514/2.3830.

[72] Grewal, M. S., Weill, L. R., and Andrews, A. P., Global Positioning Systems, Inertial Navigation, and Integration, chap. 6, John Wiley & Sons, Inc., 2001, pp. 131–178.

[73] Grewal, M. and Andrews, A., "How Good Is Your Gyro? [Ask the Experts]," IEEE Control Systems Magazine, Vol. 30, No. 1, Feb. 2010, pp. 12–86, ISSN 1066-033X, 10.1109/MCS.2009.935122.

[74] Riley, W. J. and Howe, D. A., "Handbook of Frequency Stability Analysis," Tech. Rep. 1, National Institute of Standards and Technology, Boulder, CO, Feb. 2008, 10.1016/0148-9062(94)92706-5.

[75] IEEE, "IEEE Standard Specification Format Guide and Test Procedure for Single-Axis Interferometric Fiber Optic Gyros," IEEE Std 952-1997, Vol. 1997, 1998, 10.1109/IEEESTD.1998.86153.

[76] InvenSense, "MPU-6500 Product Specification," Tech. rep., InvenSense, San Jose, CA, 2014.

[77] Choudhary, V. and Iniewski, K., editors, MEMS: Fundamental Technology and Applications, chap. 4, CRC Press, 2013, pp. 69–90.

[78] Knuth, D., "Two Notes on Notation," American Mathematical Monthly, Vol. 99, No. 5, May 1992, pp. 403–422.

[79] Crassidis, J. L. and Junkins, J. L., Optimal Estimation of Dynamic Systems, chap. 5, Chapman and Hall/CRC Press, Boca Raton, FL, 2004, pp. 243–342.

[80] Schei, T. S., "A Finite-Difference Method for Linearization in Nonlinear Estimation Algorithms," Automatica, Vol. 33, No. 11, 1997, pp. 2053–2058.

[81] Simon, D., Optimal State Estimation, chap. 13, John Wiley & Sons, Inc., 2006, pp. 395–432.

[82] Bucy, R. S. and Joseph, P. D., Filtering for Stochastic Processes, John Wiley & Sons, Inc., New York, 1968.

[83] Schaub, H. and Junkins, J. L., Analytical Mechanics of Space Systems, chap. 3, AIAA Education Series, Reston, VA, 2nd ed., October 2009, pp. 79–142.

[84] Van Trees, H. L., Detection, Estimation, and Modulation Theory, Part I, John Wiley & Sons, Inc., 1968.

[85] Tichavský, P., "Posterior Cramér-Rao Bound for Adaptive Harmonic Retrieval," IEEE Transactions on Signal Processing, Vol. 43, No. 5, May 1995, pp. 1299–1302, ISSN 1053-587X, 10.1109/78.382422.

[86] Bierman, G. J., Factorization Methods for Discrete Sequential Estimation, Dover Publications, 2006.

[87] Zanetti, R. and D'Souza, C., "Recursive Implementations of the Consider Filter," Proceedings of the Jer-Nan Juang Astrodynamics Symposium, College Station, TX, Jun. 2012, pp. 1–17.

[88] Willsky, A., "A Survey of Design Methods for Failure Detection in Dynamic Systems," Automatica, Vol. 12, 1976, pp. 601–611, 10.1016/0005-1098(76)90041-8.

[89] Lefebvre, T., Bruyninckx, H., and De Schutter, J., "Kalman filters for non-linear systems: a comparison of performance," International Journal of Control, Vol. 77, No. 7, May 2004, pp. 639–653, ISSN 0020-7179, 10.1080/00207170410001704998.

[90] Hogan, E. A. and Schaub, H., "Three-Axis Attitude Control using Redundant Reaction Wheels with Continuous Momentum Dumping," Proceedings of the AAS/AIAA Spaceflight Mechanics Conference, American Institute of Aeronautics and Astronautics, Kauai, HI, Feb. 2013.

[91] Schaub, H. and Junkins, J. L., Analytical Mechanics of Space Systems, chap. 8, AIAA Education Series, Reston, VA, 3rd ed., 2014, pp. 367–470.

[92] Horn, R. A. and Johnson, C. R., Topics in Matrix Analysis, chap. 5, Cambridge University Press, 1991, pp. 298–381.

[93] Azor, R., Bar-Itzhack, I. Y., and Harman, R. R., "Satellite Angular Rate Estimation from Vector Measurements," Journal of Guidance, Control, and Dynamics, Vol. 21, No. 3, 1998, ISSN 0731-5090, 10.2514/2.4257.

[94] Mortari, D. and Akella, M. R., "Discrete and Continuous Time Adaptive Angular Velocity Estimators," Proceedings of the AAS/AIAA Space Flight Mechanics Conference, Williamsburg, VA, 2015.

[95] Karlgaard, C. D. and Schaub, H., "Nonsingular Attitude Filtering Using Modified Rodrigues Parameters," Journal of the Astronautical Sciences, Vol. 57, No. 4, 2010, pp. 777–791.

[96] Schaub, H. and Junkins, J. L., "Stereographic Orientation Parameters for Attitude Dynamics: A Generalization of the Rodrigues Parameters," Journal of the Astronautical Sciences, Vol. 44, No. 1, 1996, pp. 1–19.

[97] O'Keefe, S. a. and Schaub, H., "Shadow Set Considerations for Modified Rodrigues Parameter Attitude Filtering," Journal of Guidance, Control, and Dynamics, Vol. 37, No. 6, Nov. 2014, pp. 2030–2035, ISSN 0731-5090, 10.2514/1.G000405.

[98] Flanders, H., "Differentiation Under the Integral Sign," The American Mathematical Monthly, Vol. 80, No. 6, 1973, pp. 615–627.

[99] Krivova, N. a., Vieira, L. E. a., and Solanki, S. K., "Reconstruction of solar spectral irradiance since the Maunder minimum," Journal of Geophysical Research, Vol. 115, No. A12, Dec. 2010, ISSN 0148-0227, 10.1029/2010JA015431.

[100] Vallado, D. A., Fundamentals of Astrodynamics and Applications, Microcosm Press, 2nd ed., 2004.

[101] Bretagnon, P. and Francou, G., "Planetary theories in rectangular and spherical variables - VSOP 87 solutions," Astronomy & Astrophysics, Vol. 202, No. 1-2, Aug. 1988, pp. 209–315.

[102] Meeus, J., Astronomial Algorithms, Willmann-Bell, Inc, 2nd ed., 1998.

[103] Krishnan, V., Probability and Random Processes, chap. Appendix D, John Wiley & Sons, Inc, Hoboken, NJ, 2006, pp. 694–700, 10.1002/0471998303.app4.

[104] MATLAB, MATLAB and Statistics Toolbox Release 2014a, The MathWorks, Inc, Natick, Massachusetts, United States, 2014.

[105] Gill, E., Sundaramoorthy, P., Bouwmeester, J., Zandbergen, B., and Reinhard, R., "Formation flying within a constellation of nano-satellites: The QB50 mission," Acta Astronautica, Vol. 82, No. 1, Jan. 2013, pp. 110–117, ISSN 00945765, 10.1016/j.actaastro.2012.04.029.

[106] Psiaki, M. L., Martel, F., and Pal, P. K., "Three-axis attitude determination via Kalman filtering of magnetometer data," Journal of Guidance, Control, and Dynamics, Vol. 13, No. 3, May 1990, pp. 506–514, ISSN 0731-5090, 10.2514/3.25364.

[107] Lockley, R. M., Animal Navigation, Pan Books, 1967.

[108] Moore, F. R., "Solar Cues in the Migratory Orientation of the Savannah Sparrow, Passerculus Sandwichensis," Animal Behaviour, Vol. 28, No. 3, Aug. 1980, pp. 684–704, 10.1016/S0003-3472(80)80129-1.

[109] Shillcutt, K. J., Solar Based Navigation for Robotic Explorers, Doctor of philosophy, Carnegie Mellon University, 2000.

[110] Schaub, H. and Junkins, J. L., Analytical Mechanics of Space Systems, chap. 4, AIAA Education Series, Reston, VA, 2nd ed., October 2009, pp. 143–206.

[111] Cramér, H., Mathematical Methods of Statistics, Princeton University Press, 1946.

[112] Fisher, R. A., Statistical Methods and Scientific Inference, Hafner Press, New York, NY, 3rd ed., 1973.

[113] Taylor, J. H., "The Cramer-Rao estimation error lower bound computation for deterministic nonlinear systems," Proceedings of the IEEE Conference on Decision and Control, San Diego, CA, Jan. 1978, pp. 1178–1181, 10.1109/CDC.1978.268121.

[114] Leven, W. F., Approximate Cramér-Rao Bounds for Multiple Target Tracking, Doctor of philosophy, Georgia Institute of Technology, 2006.

[115] Tichavský, P., Muravchik, C. H., and Nehorai, A., "Posterior Cramér-Rao Bounds for Discrete-Time Nonlinear Filtering," IEEE Transactions on Signal Processing, Vol. 46, No. 5, May 1998, pp. 1386–1396, ISSN 1053-587X, 10.1109/78.668800.

Appendix A

MRP Attitude Filter Shadow Set Considerations

Rigid body attitude estimation algorithms have been previously formulated using Modified Rodrigues Parameter (MRP) attitude sets. These MRP-based attitude estimation algorithms are attractive because they have been shown to have equal accuracy to and faster initial convergence than similar quaternion based filters and they avoid the quaternion constraint problem[95]. These algorithms make use of the fact that two MRP sets describe a particular orientation and singularity avoidance is performed by switching between the original MRP set and the alternate set, known as the shadow set. Unfortunately, the non-uniqueness of MRPs can lead to significant attitude estimation errors through improper calculation of the measurement residual.

Of particular interest for MRP attitude filters is the computation of the measurement residual $\boldsymbol{y}_k$, the difference between the measured $\tilde{\boldsymbol{\sigma}}_k$ and estimated attitude $\hat{\boldsymbol{\sigma}}_k$ at time t_k, which has not previously been discussed in detail. For the additive MRP EKF the measurement residual is given by the numerical difference

$$\boldsymbol{y}_k = \tilde{\boldsymbol{\sigma}}_k - \hat{\boldsymbol{\sigma}}_k. \tag{A.1}$$

Due to the non-uniqueness of MRPs, there are always two MRP sets to describe the same orientation. This can become an issue if the magnitude of the discrete MRP measurement $\|\tilde{\boldsymbol{\sigma}}_k\|$ or estimate $\|\hat{\boldsymbol{\sigma}}_k\|$ is near 1. For example, if $\tilde{\boldsymbol{\sigma}}_k = [1, 0, 0]$ and $\hat{\boldsymbol{\sigma}}_k = [-1, 0, 0]$, which represents the same physical orientation as $\tilde{\boldsymbol{\sigma}}_k^S$, both values describe the same attitude and thus the measurement residual should be $[0, 0, 0]$. However, Equation (A.1) will result in a measurement residual of $[2, 0, 0]$

and the update equations will apply a correction when none is needed, thus degrading the estimate of the attitude.

To avoid this issue, a new approach is proposed where the measurement residual is calculated a second time using

$$\boldsymbol{y}'_k = \tilde{\boldsymbol{\sigma}}_k^S - \hat{\boldsymbol{\sigma}}_k \tag{A.2}$$

where $\tilde{\boldsymbol{\sigma}}_k^S$ is evaluated using Equation (4.2). The quantity $\boldsymbol{y}_k$ or $\boldsymbol{y}'_k$ with the smaller magnitude is then used in the state update and estimation continues. Figure A.1 illustrates graphically the situation where $\|\boldsymbol{y}'_k\| < \|\boldsymbol{y}_k\|$ and Algorithm 1 provides pseudocode for the proposed algorithm. Note that while the measurements $\tilde{\boldsymbol{\sigma}}$ are assumed to be noisy, the measurement at t_k is a discrete value and $\|\tilde{\boldsymbol{\sigma}}_k\|$ is the magnitude of this discrete value.

Algorithm 1 Proposed measurement residual algorithm for additive MRP EKF.

```
y_k = σ̃_k − σ̂_k
if ‖σ̃_k‖ > 1/3 then
    y'_k = σ̃_k^S − σ̂_k
    if ‖y'_k‖ < ‖y_k‖ then
        y_k = y'_k
    end if
end if
```

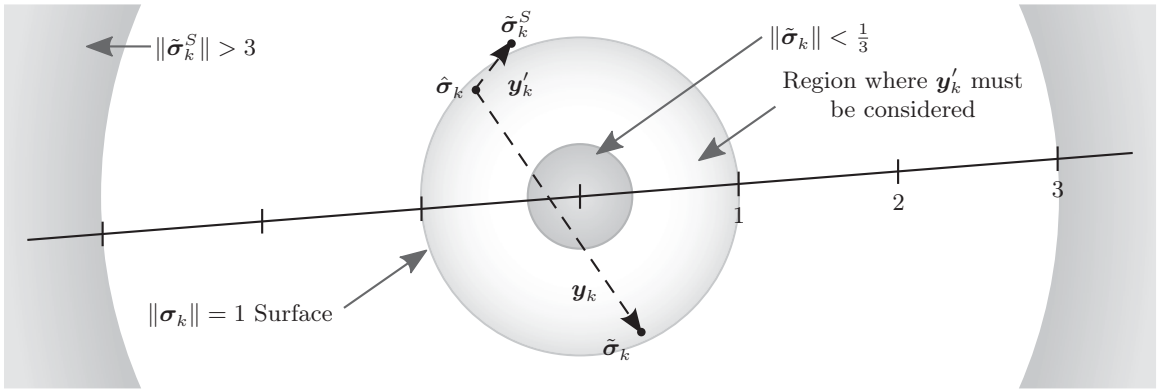

Figure A.1: Illustration of possible measurement residual at a specific time and region where $\boldsymbol{y}'_k$ must be considered.

Performing this additional calculation at every time step does not represent a significant computational burden, however, an issue does develop when a measurement has a magnitude near

zero. When $\|\tilde{\boldsymbol{\sigma}}_k\| \to 0$ the shadow set $\|\tilde{\boldsymbol{\sigma}}_k^S\| \to \infty$ and is ill-defined. In this scenario the magnitude of the original measured MRP $\|\tilde{\boldsymbol{\sigma}}_k\|$ is always less than the magnitude of the shadow MRP set of the measurement $\|\tilde{\boldsymbol{\sigma}}_k^S\|$ and there is no need to evaluate Equation (A.2). For this reason a bound is placed on when to evaluate Equation (A.2). As noted earlier, both $\tilde{\boldsymbol{\sigma}}_k$ and $\hat{\boldsymbol{\sigma}}_k$ are assumed to be constrained with a magnitude less than or equal to 1, which implies at any time t_k

$$\|\boldsymbol{y}_k\| \leq 2.$$

Therefore, conservatively if the magnitude of the measured MRP's shadow set $\tilde{\boldsymbol{\sigma}}_k^S$ at time t_k is greater than 3 the magnitude of $\boldsymbol{y}_k'$ must be greater than $\boldsymbol{y}_k$

$$\|\tilde{\boldsymbol{\sigma}}_k^S\| > 3 \quad \Longrightarrow \quad \|\boldsymbol{y}_k\| < \|\boldsymbol{y}_k'\|$$

and $\boldsymbol{y}_k'$ need not be calculated. By applying Equation (4.2) it is evident that

$$\|\tilde{\boldsymbol{\sigma}}_k^S\| > 3 \quad \Longrightarrow \quad \|\tilde{\boldsymbol{\sigma}}_k\| < 1/3.$$

Thus, a conservative bound on when the calculation of $\boldsymbol{y}_k'$ can be ignored is when $\|\tilde{\boldsymbol{\sigma}}_k\| < 1/3$. Therefore, when $1/3 < \|\tilde{\boldsymbol{\sigma}}_k\| < 1$, as illustrated in Figure A.1, the check described above should be computed.

For a multiplicative MRP EKF, the measurement residual at time t_k is given by the relative orientation difference

$$\boldsymbol{y}_k = \tilde{\boldsymbol{\sigma}}_k \otimes \hat{\boldsymbol{\sigma}}_k^{-1}. \tag{A.3}$$

Using the example provided earlier where $\tilde{\boldsymbol{\sigma}} = [1, 0, 0]$ and $\hat{\boldsymbol{\sigma}} = [-1, 0, 0]$, evaluating Equation (A.3) results in a division by zero and in other cases can lead to an erroneously large residual when the resulting MRP describes a rotation with a principal rotation angle greater than 180°. To avoid this, a similar approach is proposed where the measurement residual is calculated a second time using the shadow set of the measurement

$$\boldsymbol{y}_k' = \tilde{\boldsymbol{\sigma}}_k^S \otimes \hat{\boldsymbol{\sigma}}_k^{-1} \tag{A.4}$$

and the quantity $\boldsymbol{y}_k$ or $\boldsymbol{y}'_k$ with the smaller magnitude is used in the update equations. Algorithm 2 provides pseudocode for a multiplicative MRP EKF. In this case $\|\tilde{\boldsymbol{\sigma}}_k\|$ is compared to a sufficiently small number ϵ to prevent division by zero.

Algorithm 2 Proposed measurement residual algorithm for multiplicative MRP EKF.

```
y_k = σ̃_k ⊗ σ̂_k^{-1}
if ||σ̃_k|| > ε then
    y'_k = σ̃_k^S ⊗ σ̂_k^{-1}
    if ||y'_k|| < ||y_k|| then
        y_k = y'_k
    end if
end if
```

As an alternative, Equation (A.3) could be calculated using direction cosine matrices

$$[C(\boldsymbol{y}_k)] = [C(\tilde{\boldsymbol{\sigma}}_k)]\,[C(-\hat{\boldsymbol{\sigma}}_k)]$$

and extracting the resultant MRP set with the smaller principal rotation angle, but this is found in practice to be significantly more computationally demanding than the proposed algorithm.

A simple numerical simulation is presented to illustrate the performance of the non-singular additive MRP EKF and highlight certain implementation details. The uncontrolled tumbling motion of a small spacecraft is modeled assuming the spacecraft has principle inertia values of $I_1 = 4\,\mathrm{kgm}^2$, $I_2 = 4\,\mathrm{kgm}^2$, and $I_3 = 3\,\mathrm{kgm}^2$. The initial attitude of the spacecraft is given by $\boldsymbol{\sigma}(t_0) = [0.3, 0.1, -0.5]^T$. The initial angular velocity is given by $\boldsymbol{\omega}(t_0) = [-0.2, 0.2, -0.1]^{T\circ}/\mathrm{s}$.

Attitude measurements are simulated at 0.2 Hz with a attitude measurement error covariance of 20 arcsecond. The measurement covariance for the additive filter is set to $\boldsymbol{R} = 0.0004\boldsymbol{I}_{3\times3}$. The angular rate measurements are simulated at 2.0 Hz, assuming bias stability $\boldsymbol{\omega}_r = [-1.0, 2.0, -3.0]^{T\circ}/\mathrm{h}$ and $\sigma_\omega = \sqrt{10}\times10^{-7}\,\mathrm{rad/s}^{1/2}$ and $\sigma_{\omega_d} = \sqrt{10}\times10^{-10}\,\mathrm{rad/s}^{3/2}$. The initial attitude estimate is $\hat{\boldsymbol{\sigma}} = \boldsymbol{0}_{3\times1}$ and the initial angular rate bias estimate is $\hat{\boldsymbol{\omega}}_b = \boldsymbol{0}_{3\times1}$. The initial covariance matrix is given by $\hat{\boldsymbol{P}}_0 = \mathrm{diag}\left[P_\sigma, P_\sigma, P_\sigma, P_{\omega_\beta}, P_{\omega_\beta}, P_{\omega_\beta}\right]$ where $P_\sigma = 0.175\,\mathrm{rad}^2$ and $P_{\omega_\beta} = 0.005\,\mathrm{rad}^2/\mathrm{s}^2$.

The time history of the true attitude and the principal rotation error of the estimate for a 60 min simulation are shown in Figure A.2. It can be seen that not all instances of MRP switching

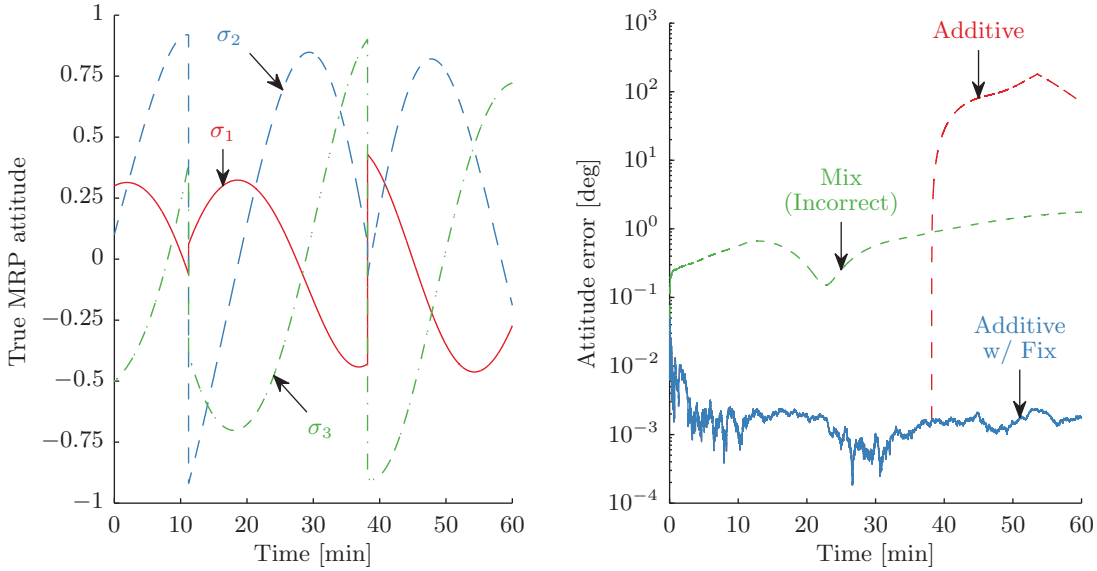

(a) True spacecraft attitude.

(b) Attitude estimate error.

Figure A.2: Results of simulation using additive MRP EKF with and without proposed algorithm illustrating importance.

require the proposed algorithm, for instance the estimator handles the switching at 11.2 min quite well. An example of when $\|\boldsymbol{y}'_k\| < \|\boldsymbol{y}_k\|$ is seen at 38.2 min. At that time simply calculating the vector difference between $\tilde{\boldsymbol{\sigma}}_k$ and $\hat{\boldsymbol{\sigma}}_k$ results in

$$\boldsymbol{y}_k = \begin{bmatrix} 0.85821 & -0.13322 & -1.80039 \end{bmatrix}$$

whereas using the shadow MRP set of the measurement results in

$$\boldsymbol{y}'_k = \begin{bmatrix} -0.00048 & -0.00001 & 0.00097 \end{bmatrix}.$$

Clearly, $\boldsymbol{y}_k$ represents spuriously large error in the attitude estimate and the original additive estimator diverges, whereas by using the shadow MRP set of the measured attitude the magnitude of the measurement residual is very close to zero.

It is important when using an additive filter to use a numerical difference for the measurement residual and when using a multiplicative filter to use a multiplicative residual. Included in Figure A.2b are the results for an additive filter using a multiplicative residual illustrating the poor performance resulting from such an incorrect mixture of methods.

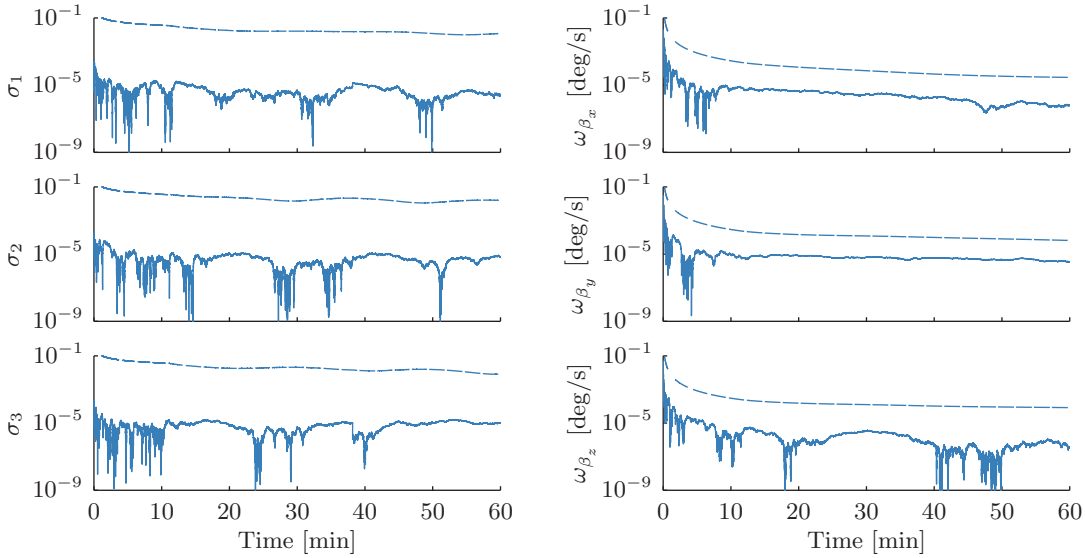

(a) $\boldsymbol{\sigma}$ estimate errors.

(b) $\boldsymbol{\omega}_b$ estimate errors.

Figure A.3: Results of numerical simulation using proposed method showing convergence of all states. Dotted lines indicate 1σ covariance bounds.

The state estimates and their associated covariance bounds for the proposed algorithm are shown in Figure A.3. Both the attitude MRP and rate gyro bias estimates can be seen to quickly converge to the noise level while remaining within the 1σ covariance bounds despite the relatively slow attitude measurement update rate.

Appendix B

MRP Attitude Filter High-Accuracy Considerations

It is assumed in the MRP EKF derivation that the angular velocity is piecewise constant between rate gyro measurements. This assumption is usually good if the spacecraft has near zero angular rates, otherwise, the effect of this assumption manifests itself as a time varying bias in the system dynamics. Therefore, precise attitude determination requires the proper propagation of the angular velocity, using Euler's rotation equations of motion, and accounting for any active control torques.

In this situation, the rotational equations of motion for a spacecraft with several reaction wheels given by[110]

$$\dot{\boldsymbol{\omega}} = [I]^{-1}\left[-\boldsymbol{\omega}\times\left([I]\,\boldsymbol{\omega} + \boldsymbol{G}_s\left\{\boldsymbol{J}_s \circ \left(\boldsymbol{\Omega} + \boldsymbol{G}_s^T\boldsymbol{\omega}\right)\right\}\right) - \boldsymbol{G}_s\boldsymbol{u}_s + \boldsymbol{L}\right] \tag{B.1}$$

are incorporated into the propagation calculations. For maximum benefit, the rate gyro measurement from the previous time step is integrated forward incorporating the rotation equations of motion to arrive at the best estimate of both the state at the current time.

Figure B.1 shows the difference in the MRP estimate for a MRP EKF estimator with and without using Equation (B.1). In this case a spacecraft is simulated in a 400 km circular, polar orbit. The spacecraft is initialized with zero rates and an initial attitude of $\boldsymbol{\sigma} = \left[0, 0, 0\right]$ and commanded to achieve and maintain Sun pointing. The spacecraft is assumed to be equipped with an inertial grade rate gyro and a star tracker with 1σ noise of 20 arcsecond.

The maximum angular velocity of the spacecraft is $0.95\,^\circ/\mathrm{s}$, but it is enough to cause a bias to appear in the estimated attitude. The total bias seen is small, at its maximum the bias equates to a

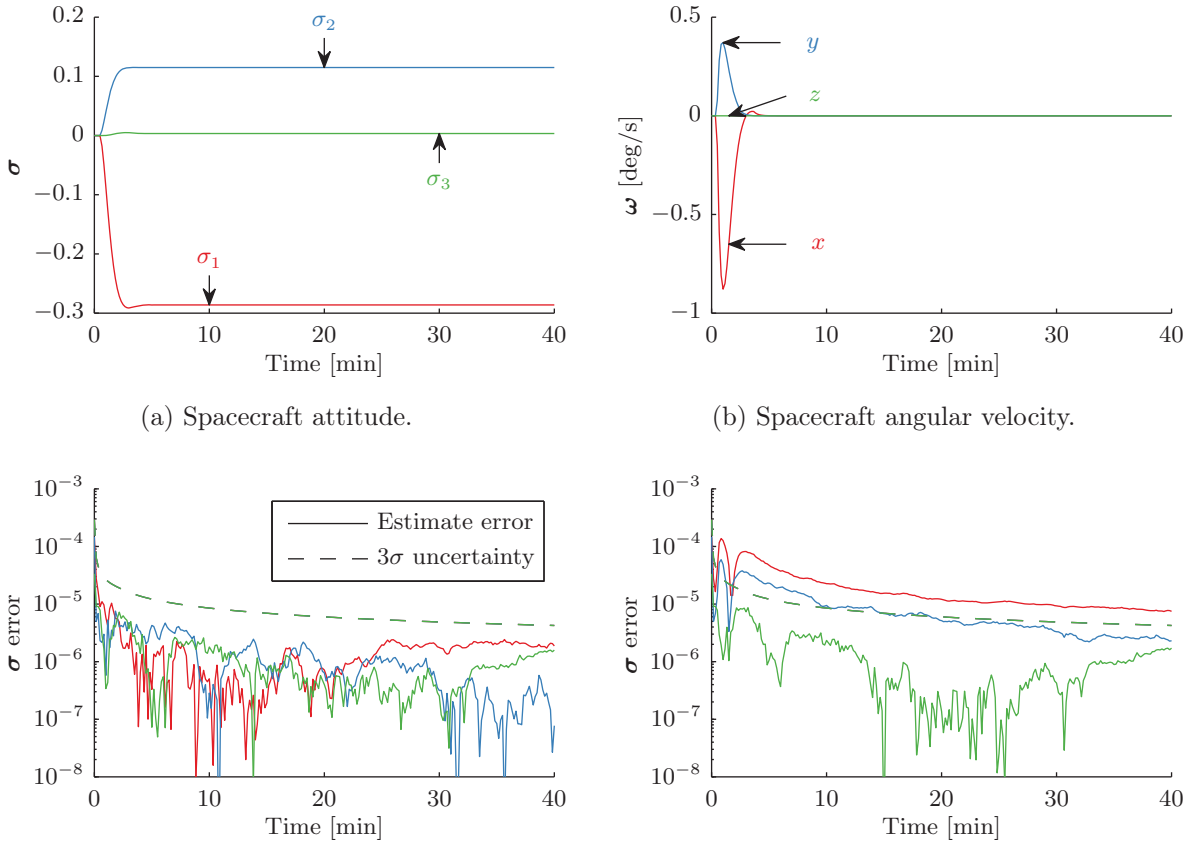

(a) Spacecraft attitude.

(b) Spacecraft angular velocity.

(c) Attitude estimate with Equation (B.1).

(d) Attitude estimate without Equation (B.1).

Figure B.1: Comparison of MRP EKF results with and without including rotational equations of motion in propagation.

total angular error of 0.05°, but is important to be aware of, especially if high accuracy estimation is required. Incorporating the rotational equations of motion into the state propagation alleviates this issue. For lower rate gyro performance grades, without incorporating Equation (B.1) the bias seen is still evident, but only persists as long as the spacecraft's angular rates are non-zero.

Appendix C

Cramér-Rao Lower Bound

The Cramér-Rao lower bound gives a lower bound on the expected errors between an estimated quantity and its true value based on the statistical properties of the given measurements. Methods of calculating the Cramér-Rao lower bound for nonlinear estimation problems are gathered here as a reference.

The Cramér-Rao inequality[111] gives a mean square error (MSE) lower bound, the Cramér-Rao Lower Bound (CRLB), on the variance of an unbiased estimator $\hat{\boldsymbol{x}}$ of an unknown deterministic vector parameter $\boldsymbol{x}$ given measurements $\boldsymbol{y}$ with probability density function p

$$\boldsymbol{P} \equiv E\left\{(\hat{\boldsymbol{x}}-\boldsymbol{x})(\hat{\boldsymbol{x}}-\boldsymbol{x})^T\right\} \geq \boldsymbol{J}^{-1} \tag{C.1}$$

where the $\boldsymbol{J}$ is the Fisher information matrix[112] given by

$$\begin{aligned}\boldsymbol{J} &= E\left\{\left[\frac{\partial}{\partial \boldsymbol{x}}\ln p(\boldsymbol{y};\boldsymbol{x})\right]\left[\frac{\partial}{\partial \boldsymbol{x}}\ln p(\boldsymbol{y};\boldsymbol{x})\right]^T\right\} \\ &= -E\left\{\frac{\partial^2}{\partial \boldsymbol{x}\partial \boldsymbol{x}^T}\ln p(\boldsymbol{y};\boldsymbol{x})\right\}.\end{aligned} \tag{C.2}$$

A singular Fisher information matrix indicates an system that is not fully observable, and in such a case the rank deficiency of the Fisher information matrix indicates the number of unobservable parameters.

C.1 Cramér-Rao Lower Bound for Deterministic Systems

One nonlinear estimation bounding technique based on the CRLB is suggested by Taylor[113]. Consider a deterministic system with continuous-time state dynamics and discrete-time measure-

ments given by

$$\dot{\boldsymbol{x}} = \boldsymbol{f}(\boldsymbol{x}, \boldsymbol{u}, t) \tag{C.3a}$$

$$\boldsymbol{y}_k = \boldsymbol{h}_k(\boldsymbol{x}_k, \boldsymbol{\nu}_k) \tag{C.3b}$$

where $\boldsymbol{x}$ is the state vector, $\boldsymbol{f}$ represents the system dynamics, $\boldsymbol{u}$ is the control input, and $\boldsymbol{y}_k$ is the discrete-time measurement expression. The measurement noise $\boldsymbol{\nu}_k$ is discrete-time white-noise with covariance $\boldsymbol{R}_k$

$$\mathrm{E}[\boldsymbol{\nu}_k] = 0 \tag{C.4a}$$

$$\mathrm{E}\left[\boldsymbol{\nu}_j \boldsymbol{\nu}_k^T\right] = \boldsymbol{R}_{jk}\delta_{jk} \;\forall\; j, k. \tag{C.4b}$$

Taylor shows that the Fisher information matrix for this system propagates recursively according to

$$\boldsymbol{J}\left(\boldsymbol{x}_{k+1}\right) = \left(\boldsymbol{\Phi}^{-1}\right)^T \boldsymbol{J}(\boldsymbol{x}_k)\, \boldsymbol{\Phi}^{-1} + \bar{\boldsymbol{H}}_{k+1}^T \boldsymbol{R}_{k+1}^{-1} \bar{\boldsymbol{H}}_{k+1} \tag{C.5}$$

where

$$\bar{\boldsymbol{H}}_k \equiv \left.\frac{\partial \boldsymbol{h}_k}{\partial \boldsymbol{x}_k}\right|_{\boldsymbol{x}_k} \tag{C.6}$$

and assuming the Jacobian matrix[113]1

$$\bar{\boldsymbol{F}} \equiv \left.\frac{\partial \boldsymbol{f}}{\partial \boldsymbol{x}}\right|_{\boldsymbol{x},\boldsymbol{u}} \tag{C.7}$$

is continuous in $\boldsymbol{x}$ and t, allowing the state transition matrix Φ to be found by integrating

$$\dot{\boldsymbol{\Phi}} = \bar{\boldsymbol{F}}\boldsymbol{\Phi} \tag{C.8}$$

subject to the initial condition $\boldsymbol{\Phi}(k, k) = \boldsymbol{I}$. While this approach provides a simple method for calculating the CRLB, unfortunately, it assumes that the system is deterministic, whereas most real systems are modeled with process noise.

[1]Note the Jacobian matrix is evaluated along the true trajectory, not the best estimate of the trajectory.

C.2 Posterior Cramér-Rao Lower Bound for Discrete Time Systems

For a system with process noise, the unknown vector parameter $\boldsymbol{x}$ is treated as a random variable. Van Trees gives the lower bound for an unbiased estimator of an unknown *random* vector parameter, commonly known as the Posterior Cramér-Rao Bound (PCRB)[85], as[84]

$$\boldsymbol{P}_k \equiv E\left\{\left(\hat{\boldsymbol{x}}_k - \boldsymbol{x}_k\right)\left(\hat{\boldsymbol{x}}_k - \boldsymbol{x}_k\right)^T\right\} \geq \boldsymbol{J}^{-1} \tag{C.9}$$

where

$$\begin{aligned}\boldsymbol{J} &= E\left\{\left[\frac{\partial}{\partial \boldsymbol{x}} \ln p\left(\boldsymbol{Y}_k; \boldsymbol{X}_k\right)\right]\left[\frac{\partial}{\partial \boldsymbol{x}} \ln p\left(\boldsymbol{Y}_k; \boldsymbol{X}_k\right)\right]^T\right\} \\ &= -E\left\{\frac{\partial^2}{\partial \boldsymbol{x} \partial \boldsymbol{x}^T} \ln p\left(\boldsymbol{Y}_k; \boldsymbol{X}_k\right)\right\}\end{aligned} \tag{C.10}$$

and

$$\boldsymbol{X}_k = \begin{bmatrix}\boldsymbol{x}_0 & \boldsymbol{x}_1 & \cdots & \boldsymbol{x}_k\end{bmatrix} \tag{C.11a}$$

$$\boldsymbol{Y}_k = \begin{bmatrix}\boldsymbol{y}_0 & \boldsymbol{y}_1 & \cdots & \boldsymbol{y}_k\end{bmatrix}. \tag{C.11b}$$

The PCRB differs from the CRLB, and Taylor's implementation, in that the expectation in Equation (C.10) is taken over both the random parameter $\boldsymbol{X}_k$ and measurements $\boldsymbol{Y}_k$, as opposed to just over the measurements. Thus, instead of the bound being a function of a single deterministic path, the PCRB averages over all possible paths[114].

Consider a system with discrete-time state dynamics and measurements given by

$$\boldsymbol{x}_{k+1} = \boldsymbol{f}(\boldsymbol{x}_k, \boldsymbol{u}_k, \boldsymbol{w}_k) \tag{C.12a}$$

$$\boldsymbol{y}_k = \boldsymbol{h}_k(\boldsymbol{x}_k, \boldsymbol{\nu}_k) \tag{C.12b}$$

where $\boldsymbol{w}$ is discrete-time white-noise with covariance $\tilde{\boldsymbol{Q}}_k$

$$\mathrm{E}[\boldsymbol{w}_k] = 0 \tag{C.13a}$$

$$\mathrm{E}\left[\boldsymbol{w}_j \boldsymbol{w}_k^T\right] = \tilde{\boldsymbol{Q}}_{jk}\delta_{jk} \;\forall\; j, k \tag{C.13b}$$

and the measurement noise $\boldsymbol{\nu}_k$ is discrete-time white-noise with covariance $\boldsymbol{R}_k$

$$\mathrm{E}[\boldsymbol{\nu}_k] = 0 \tag{C.14a}$$

$$\mathrm{E}\left[\boldsymbol{\nu}_j \boldsymbol{\nu}_k^T\right] = \boldsymbol{R}_{jk}\delta_{jk} \;\forall\; j,k. \tag{C.14b}$$

Tichavský et al. show the Fisher information matrix for this system propagates recursively according to[115]

$$\boldsymbol{J}_{k+1} = \boldsymbol{D}_k^{22} - \boldsymbol{D}_k^{21}\left(\boldsymbol{J}_k + \boldsymbol{D}_k^{11}\right)^{-1}\boldsymbol{D}_k^{12} \tag{C.15}$$

where

$$\boldsymbol{D}_k^{11} = \mathrm{E}\left[-\frac{\partial^2}{\partial \boldsymbol{x}_k \partial \boldsymbol{x}_k^T}\ln p\left(\boldsymbol{x}_{k+1}|\boldsymbol{x}_k\right)\right] \tag{C.16}$$

$$\boldsymbol{D}_k^{12} = \mathrm{E}\left[-\frac{\partial^2}{\partial \boldsymbol{x}_k \partial \boldsymbol{x}_{k+1}^T}\ln p\left(\boldsymbol{x}_{k+1}|\boldsymbol{x}_k\right)\right] \tag{C.17}$$

$$\boldsymbol{D}_k^{21} = \mathrm{E}\left[-\frac{\partial^2}{\partial \boldsymbol{x}_{k+1} \partial \boldsymbol{x}_k^T}\ln p\left(\boldsymbol{x}_{k+1}|\boldsymbol{x}_k\right)\right] = \left[\boldsymbol{D}_k^{12}\right]^T \tag{C.18}$$

$$\boldsymbol{D}_k^{22} = \mathrm{E}\left[-\frac{\partial^2}{\partial \boldsymbol{x}_{k+1} \partial \boldsymbol{x}_{k+1}^T}\ln p\left(\boldsymbol{x}_{k+1}|\boldsymbol{x}_k\right)\right] + \mathrm{E}\left[-\frac{\partial^2}{\partial \boldsymbol{x}_{k+1} \partial \boldsymbol{x}_{k+1}^T}\ln p\left(\boldsymbol{z}_{k+1}|\boldsymbol{x}_{k+1}\right)\right] \tag{C.19}$$

initialized with

$$\boldsymbol{J}_0 = \mathrm{E}\left[-\frac{\partial^2}{\partial \boldsymbol{x}_0 \partial \boldsymbol{x}_0^T}\ln p\left(\boldsymbol{x}_0\right)\right]. \tag{C.20}$$

A special form of Equation (C.15) can be found for a linearized system model with additive Gaussian noise. Linearizing Equation (C.12) and assuming $\boldsymbol{w}_k$ and $\boldsymbol{\nu}_k$ are additive white Gaussian noise gives

$$\boldsymbol{x}_{k+1} = \boldsymbol{\Phi}_k \boldsymbol{x}_k + \boldsymbol{\Gamma}_k \boldsymbol{w}_k \tag{C.21}$$

$$\boldsymbol{y}_k = \bar{\boldsymbol{H}}_k \boldsymbol{x}_k + \bar{\boldsymbol{M}}_k \boldsymbol{\nu}_k \tag{C.22}$$

Plugging this into Equation (C.15) gives

$$\boldsymbol{J}_{k+1} = \left(\boldsymbol{\Phi}_k \boldsymbol{J}_k^{-1} \boldsymbol{\Phi}_k^T + \boldsymbol{\Gamma}_k \tilde{\boldsymbol{Q}}_k \boldsymbol{\Gamma}_k^T\right)^{-1} + \bar{\boldsymbol{H}}_{k+1}^T \bar{\boldsymbol{M}}_k \boldsymbol{R}_{k+1}^{-1} \bar{\boldsymbol{M}}_k^T \bar{\boldsymbol{H}}_{k+1}. \tag{C.23}$$

Initializing with Equation (C.20) gives a method for computing the Fisher information matrix, and subsequently the PCRB, for all time.

C.3 Posterior Cramér-Rao Lower Bound for Hybrid Systems

The propagation of the Fisher information matrix given in Equation (C.23) can be broken down into a propagation step

$$\boldsymbol{J}_{k+1}^{-} = \left(\boldsymbol{\Phi}_k \boldsymbol{J}_k^{-1} \boldsymbol{\Phi}_k^T + \boldsymbol{\Gamma}_k \tilde{\boldsymbol{Q}}_k \boldsymbol{\Gamma}_k^T\right)^{-1} \tag{C.24}$$

and a measurement update step

$$\boldsymbol{J}_{k+1}^{+} = \boldsymbol{J}_{k+1}^{-} + \bar{\boldsymbol{H}}_{k+1}^T \bar{\boldsymbol{M}}_k \boldsymbol{R}_{k+1}^{-1} \bar{\boldsymbol{M}}_k^T \bar{\boldsymbol{H}}_{k+1}. \tag{C.25}$$

Through some rearranging it can be shown that the propagation step for the inverse of the Fisher information matrix is of the same form as the traditional propagation update of the Kalman filter state covariance. Thus, for systems with continuous-time dynamics it can be shown that the Fisher information matrix can be propagated using

$$\dot{\boldsymbol{J}}(t)^{-1} = \bar{\boldsymbol{F}}(t)\, \boldsymbol{J}(t)^{-1} + \boldsymbol{J}(t)^{-1}\, \bar{\boldsymbol{F}}(t)^T + \bar{\boldsymbol{G}}(t)\, \boldsymbol{Q}(t)\, \bar{\boldsymbol{G}}(t)^T \tag{C.26}$$

where the partials

$$\bar{\boldsymbol{F}} \equiv \left.\frac{\partial \boldsymbol{f}}{\partial \boldsymbol{x}}\right|_{\boldsymbol{x},\boldsymbol{u}}, \quad \bar{\boldsymbol{G}} \equiv \left.\frac{\partial \boldsymbol{f}}{\partial \boldsymbol{\eta}}\right|_{\boldsymbol{x},\boldsymbol{u}} \tag{C.27}$$

are evaluated along the true trajectory instead of the best estimate of the trajectory.

Appendix D

Propagation of Uncertainty

In many cases the parameters being estimated by an estimator are not the only values of interest. For these secondary parameters it is valuable to estimate an associated uncertainty bound. For example, the sun-direction estimators of Chapter 3 estimate a sun-direction vector, but of particular importance is the angle between this vector and the true sun-direction. If these secondary parameters can be formulated as a function of the estimator states, a first-order estimate of the secondary parameter covariance can be calculated using the properties of the covariance matrix.

The covariance matrix $\boldsymbol{\Sigma}$ for a random vector $\boldsymbol{x}$ is given by

$$\begin{aligned}\boldsymbol{\Sigma}(\boldsymbol{x}) &= \mathrm{E}\Big[(\boldsymbol{x} - \mathrm{E}[\boldsymbol{x}])^2\Big] \\ &= \mathrm{E}\Big[(\boldsymbol{x} - \mathrm{E}[\boldsymbol{x}])\,(\boldsymbol{x} - \mathrm{E}[\boldsymbol{x}])^T\Big]\end{aligned} \tag{D.1}$$

and the covariance matrix of some constant matrix $\boldsymbol{A}$ multiplied by a random vector $\boldsymbol{x}$ plus a constant vector $\boldsymbol{\beta}$ is given by

$$\begin{aligned}\boldsymbol{\Sigma}(\boldsymbol{A}\boldsymbol{x} + \boldsymbol{\beta}) &= \mathrm{E}\Big[(\boldsymbol{A}\boldsymbol{x} + \boldsymbol{\beta} - \mathrm{E}[\boldsymbol{A}\boldsymbol{x} + \boldsymbol{\beta}])^2\Big] \\ &= E\left[(\boldsymbol{A}\,(\boldsymbol{x} - \mathrm{E}[\boldsymbol{x}]))\,(\boldsymbol{A}\,(\boldsymbol{x} - \mathrm{E}[\boldsymbol{x}]))^T\right] \\ &= \boldsymbol{A}E\left[(\boldsymbol{x} - \mathrm{E}[\boldsymbol{x}])\,(\boldsymbol{x} - \mathrm{E}[\boldsymbol{x}])^T\right]\boldsymbol{A}^T \\ &= \boldsymbol{A}\boldsymbol{\Sigma}(\boldsymbol{x})\,\boldsymbol{A}^T.\end{aligned} \tag{D.2}$$

Taking the Taylor series expansion of some function $\boldsymbol{f}(\boldsymbol{x})$ about the current instantiation $\boldsymbol{x}$ gives

$$\boldsymbol{f}(\boldsymbol{x}) \approx \boldsymbol{f}(\mathrm{E}[\boldsymbol{x}]) + \boldsymbol{J}(\mathrm{E}[\boldsymbol{x}])\,(\boldsymbol{x} - \mathrm{E}[\boldsymbol{x}]) + \frac{1}{2}\,(\boldsymbol{x} - \mathrm{E}[\boldsymbol{x}])\,\boldsymbol{H}(\mathrm{E}[\boldsymbol{x}])\,(\boldsymbol{x} - \mathrm{E}[\boldsymbol{x}])^T + \ldots \tag{D.3}$$

where $\boldsymbol{J}$ is the Jacobian matrix and $\boldsymbol{H}$ is the Hessian matrix. Noting that $\boldsymbol{f}(\mathrm{E}[\boldsymbol{x}])$ is a constant, the covariance of the function $\boldsymbol{f}(\boldsymbol{x})$ to first order is given by

$$\begin{aligned}
\boldsymbol{\Sigma}(\boldsymbol{f}(\boldsymbol{x})) &\approx \mathrm{E}\Big[\{\boldsymbol{f}(\mathrm{E}[\boldsymbol{x}]) + \boldsymbol{J}(\mathrm{E}[\boldsymbol{x}])\,(\boldsymbol{x} - \mathrm{E}[\boldsymbol{x}]) - \mathrm{E}[\boldsymbol{f}(\mathrm{E}[\boldsymbol{x}]) + \boldsymbol{J}(\mathrm{E}[\boldsymbol{x}])\,(\boldsymbol{x} - \mathrm{E}[\boldsymbol{x}])]\}^2\Big] \\
&\approx \mathrm{E}\Big[\{\boldsymbol{J}(\mathrm{E}[\boldsymbol{x}])\,\boldsymbol{x} - \mathrm{E}[\boldsymbol{J}(\mathrm{E}[\boldsymbol{x}])\,\boldsymbol{x}]\}^2\Big] \\
&\approx \boldsymbol{J}(\mathrm{E}[\boldsymbol{x}])\,\boldsymbol{\Sigma}(\boldsymbol{x})\,\boldsymbol{J}(\mathrm{E}[\boldsymbol{x}])^T .
\end{aligned} \tag{D.4}$$

D.1 CSS Sun-Direction Angular Uncertainty

Several of the CSS estimators developed in Chapter 3 give an estimate of the scaled sun-direction vector and associated covariance. Of interest for a control algorithm, and for pointing accuracy considerations, is the angle α between the current scaled sun-direction vector $\boldsymbol{d}$ and a desired unit direction vector $\boldsymbol{c}$.

$$\alpha = \arccos\left(\boldsymbol{c}^T \frac{\boldsymbol{d}}{\|\boldsymbol{d}\|}\right) \tag{D.5}$$

The uncertainty of such an angle can be calculated from the covariance of the sun-direction estimate using

$$\boldsymbol{\Sigma}(\alpha) \approx \boldsymbol{J}(\alpha)\,\boldsymbol{\Sigma}(\boldsymbol{d})\,\boldsymbol{J}(\alpha)^T \tag{D.6}$$

where

$$\boldsymbol{J}(\alpha) = \frac{1}{\sqrt{1 - \left(\boldsymbol{c}^T \frac{\boldsymbol{d}}{\|\boldsymbol{d}\|}\right)^2}} \left[\frac{\boldsymbol{d}^T}{\|\boldsymbol{d}\|}\left(\boldsymbol{c}^T \frac{\boldsymbol{d}}{\|\boldsymbol{d}\|}\right) - \boldsymbol{c}^T\right]. \tag{D.7}$$

D.2 MRP Angular Uncertainty

A MRP-based attitude estimator gives an estimate of the spacecraft's attitude expressed as a MRP set. Of interest is the principle rotation angle Φ between the current attitude and the true

attitude as it represents the total angular error of the estimate. The principle rotation angle can be found from an MRP using

$$\Phi = 4 \arctan(\|\boldsymbol{\sigma}\|) \tag{D.8}$$

and the uncertainty of this angle can be calculated from the covariance of the MRP estimate using

$$\boldsymbol{\Sigma}(\Phi) \approx \boldsymbol{J}(\Phi)\, \boldsymbol{\Sigma}(\boldsymbol{\sigma})\, \boldsymbol{J}(\Phi)^T \tag{D.9}$$

where

$$\boldsymbol{J}(\Phi) = \frac{4\boldsymbol{\sigma}^T}{\sqrt{\boldsymbol{\sigma}^T\boldsymbol{\sigma}}\,(1+\boldsymbol{\sigma}^T\boldsymbol{\sigma})}. \tag{D.10}$$

D.3 Total Angular Rate Uncertainty

A MRP-based attitude estimation gives an estimate of the spacecraft's rate gyro's bias components in the body frame. In order to condense the information, a total angular rate bias uncertainty is calculated using the vector norm of the rate gyro bias using

$$\|\boldsymbol{\omega}_\beta\| = \sqrt{\omega_{\beta_x}^2 + \omega_{\beta_y}^2 + \omega_{\beta_z}^2}. \tag{D.11}$$

The uncertainty in this quantity can be calculated from the covariance of the rate gyro bias estimate using

$$\boldsymbol{\Sigma}\big(\|\boldsymbol{\omega}_\beta\|\big) \approx \boldsymbol{J}\big(\|\boldsymbol{\omega}_\beta\|\big)\, \boldsymbol{\Sigma}\big(\boldsymbol{\omega}_\beta\big)\, \boldsymbol{J}\big(\|\boldsymbol{\omega}_\beta\|\big)^T \tag{D.12}$$

where

$$\boldsymbol{J}\big(\|\boldsymbol{\omega}_\beta\|\big) = \frac{\boldsymbol{\omega}_\beta^T}{\|\boldsymbol{\omega}_\beta\|}. \tag{D.13}$$